Rupture of Wrinkled Steel Pipelines under Monotonic Bending

by

Nima Mohajerrahbari

A thesis submitted in partial fulfillment of the requirements for the degree of

Doctor of Philosophy

in

STRUCTURAL ENGINEERING

Department of Civil and Environmental Engineering
University of Alberta

ABSTRACT

Buried steel pipelines are widely used in transportation and distribution of oil/gas products over long distance. The changing geo-environmental conditions over the line may subject the pipelines to unforeseen load combinations and prompt the failure and loss of containment of the pipelines that can pose a serious threat to the environment and public safety.

Monotonic ground movements commonly impose axial strain and bending curvature on buried pipelines that provoke local buckling of the steel pipes on the compressive side of the wall. Preceding studies have shown that the rupture of compressive wrinkled wall is unlikely to occur under monotonic ground excitations unless due to the formation of rare changing boundary conditions for the deflected segment of the line which is accompanied by a reversal regime of deformations toward the tearing of the pipe wall. However, limited experiments have shown that the monotonically-increasing curvature can trigger the rupture of the tensile wall on the opposite side of the wrinkling.

Rupture of steel pipelines is the ultimate failure of the material under the applied stress fields that is a catastrophic consequence of ductile fracture initiation and propagation. The present study concentrates on the rupture of wrinkled buried pipelines on the tensile side of the cross-section due to a monotonic increase of curvature.

In order to understand this material behavior, a series of dogbone coupons, notched round bars, and plain strain grooved plate specimens made of API X65 steel grade were designed and tested to study the post-necking plasticity and the ductile fracture of material in steel pipelines. The experimental results indicated the dependence of the fracture strain on the stress triaxiality and Lode angle. Finite element analysis (FEA) of the experiments was then performed to calibrate the ductile fracture toughness in the form of equivalent plastic strain as a function of stress triaxiality and Lode angle. The results of this hybrid experimental-numerical analysis also revealed that the power law could be successfully used to extrapolate the post-necking stress-strain curve of the material through solving an optimization problem.

Moreover, the finite element simulations of four pertinent full-scale tests of steel pipes were conducted to examine the material model and simulation techniques. It was demonstrated that the finite element models fairly simulated the post-buckling behavior of the full-scale specimens and closely predicted the rupture of the wall. The verified finite element models were used to study the effect of key factors that were responsible for the rupture of the tensile wall on the opposite side of the wrinkling. The internal pressure, Y/T (yield strength/tensile strength) ratio, and axial tension were found as the dominant design parameters that affected the final failure mode of the wrinkled pipelines and directly increased the chance of post-buckling rupture. In addition, it was explored that the formation of the "pinned-pinned" condition at the boundaries of the deflected line due to immoderate frictional forces was the most critical scenario which dramatically precipitated the rupture of pipe wall by restraining the axial displacement of the line undergoing monotonically-increasing curvature.

Lastly, the coupled effect of key design variables was examined through an extensive parametric study. The critical design factor term was introduced to limit the internal pressure as the transitional state from the compressive failure to the post-buckling rupture failure mode due to an increasing curvature. The parametric study showed that the diameter of the pipe had little effect on the ultimate post-buckling failure mode, whereas, the D/t ratio slightly affected the critical design factor. Therefore, a critical design factor envelope was developed as a sigmoid function of the Y/T ratio for the pinned-pinned boundary conditions. This design criterion serves as the minimum rupture limit state for the wrinkled buried pipelines. Finally, the critical design factor was obtained as a surface versus the Y/T ratio and normalized axial tension for the simply-supported boundary conditions to accommodate the impact of the axial tensile load.

To my wonderful parents

&

Mina, my beloved sister

ACKNOWLEDGEMENTS

First and foremost, my deepest appreciation goes to my parents and my dearest sister, Mina, for their endless love, kindness, and support throughout my entire life. It would have been impossible to pass the up-and-downs without them.

I would like to express my sincerest gratitude to my supervisor, Dr. Roger Cheng, who offered his continuous advice, encouragement, and paternal support throughout the course of my studies. I have been highly privileged and honoured to have the opportunity of knowing him and working with him.

I also wish to warmly thank Dr. Samer Adeeb. This project would not have materialized without his valued insight and constant support. I am also truly thankful to the other committee members, Dr. Sreekanta Das from the University of Windsor, Dr. Weixing Chen, and Dr. Alireza Bayat for reading the previous draft of this dissertation and drawing constructive comments to the improvement of the contents.

I gratefully acknowledge the valuable assistance from the EVRAZ Inc. which provided this project with the full-scale pipe specimens. I also thank the JFE steel corporation for sharing their test data with this research. In addition, I would like to thank the lab technicians, Mr. Greg Miller and Mr. Cameron West for their technical brilliance and help.

Thanks are extended to all of those individuals who supported me during my attendance to the University of Alberta, especially my great friend, Tom Kirdeikis.

TABLE OF CONTENTS

LIST OF TABLES

LIST OF FIGURES

LIST OF SYMBOLS AND ABBREVIATIONS

A	=	Material constant in power law equation
a	=	Defect height
A_0	=	Initial cross-sectional area of specimen
A_D	=	Dilatational amplification factor of spherical voids
A_{imp}	=	Amplitude of initial imperfection
A_{imp}^{offset}	=	Amplitude of initial imperfection at girth weld
A_N	=	Proportionality constant in porous plasticity
A_{r0}	=	Initial reduced cross-sectional area of speciemn
B3	=	2-node linear beam element
b_j	=	Major radius of the elliptical void
BC	=	Boundary Conditions
C	=	Material Constant for cumulative fracture criterion
c	=	Half of defect length
$C_{1\sim2}$	=	Constants of void nucleation
$c_{1\sim4}$	=	Constants in *Mohr-Coulomb* equation
C3D8R	=	8-node brick element with reduced integration
CAX8R	=	8-node axisymmetric element with reduced integration
CBS	=	Critical Buckling Strain
C_{ij}	=	Cummulative damage parameter in *McClintock* model
CTOD	=	Crack Tip Opening Displacement
CWP	=	Curved Wide Plate
D	=	Outside diameter of pipe
d	=	Depth of buried defect

$D_{1\sim5}$	=	Material constants in *Johnson-Cook* equation
D_d	=	Damage variable
D_{dc}	=	Critical damage variable to fracture
DIC	=	Digital Image Correlation
DSAW	=	Double Submerged Arc Welded
DUCTCRT	=	Fracture Index in Abaqus
df_{gr}	=	Change of the void volume fraction due to void growth
df_{nucl}	=	Change of the void volume fraction due to void nucleation
E	=	Modulus of elasticity
EL	=	Elongation to fracture
f	=	Microscopic void volume fraction
$f^*(f)$	=	Void volume fraction function
f_0	=	Initial void volume fraction
f_c	=	Critical void volume fraction
f_{mass}	=	Material density factor in explicit FEA
FE	=	Finite Element
FEA	=	Finite Element Analysis
f_F	=	Void volume fraction to fracture
F_{ij}	=	Relative void growth factor
F^f_{ij}	=	Relative void growth factor to fracture
F_N	=	Void volume fraction of nucleated voids
F_u	=	Tensile/ultimate strength
F_y	=	Yield strength
$g(\sigma_{ij})$	=	Weighting function
GP	=	Grooved Plate

HAZ	=	Heat Affected Zone
HSS	=	High Strength Steel
I	=	Vector of internal force in FEA
I_1	=	First stress invariant
ICA	=	Imperialist Competitive Algorithm
J_{1D}	=	First deviatoric stress invariant
J_{2D}	=	Second deviatoric stress invariant
J_{3D}	=	Third deviatoric stress invariant
K	=	Accelerated void growth factor
k	=	Shape constant in *Xue*'s equation
$k_{1\sim5}$	=	Constants of sigmoidal logistic function
L_0	=	Initial length of specimen
l_0^{EXT}	=	Initial gauge length
L_{Collar}	=	Length of collar
l_e	=	Moment arm eccentricity
l_j	=	Mean distance between parallel elliptical voids
L_s	=	End-to-end straight length of pipe
LCF	=	Low Cycle Fatigue
L_{imp}	=	Length of imperfection
M	=	Matrix of nodal lumped mass in FEA
m_b	=	Bending moment
MPC	=	Multi-Point Constraint
MSE	=	Normalized mean square error
n	=	Strain-hardening constant in power law equation
N_E	=	Number of discrete experimental data

n_I	=	Hardening index in *McClintock* model
NPS	=	Nominal Pipe Size
NRB	=	Notched Round Bar
n_{RS}	=	Strain hardening constant in the *Ramberg-Osgood* equation
P	=	Vector of external force in FEA
p	=	Internal pressure
p/p_y	=	Design factor
$(p/p_y)_{\text{cr}}$	=	Critical design factor
$P_{1\sim6}$	=	Constants of quadratic surface
P_c	=	Compressive axial load exerted by MTS
p_e	=	Minimum external hydrostatic pressure
P^{MTS}	=	MTS load
p_y	=	Yield internal pressure
$q_{1\sim3}$	=	Void interaction parameters in porous plasticity
R	=	Notch radius
r	=	Reduced radius of bar at notch root
R_0	=	Initial radius of spherical voids in void growth model
RA	=	Reduced area to fracture
RB	=	Round Bar
R_{imp}	=	Radius of pipe at imperfect cross-section
r_m	=	Radius of spherical volume element of porous material
RMV	=	Representative Material Volume
R_{pin}	=	Reaction force of the pinned end
r_v	=	Radius of concentric spherical void in porous material
S	=	Gross area under stress

$\widetilde{S}$	=	Effective area under stress
S_0	=	Temperature constant in damage mechanics
s_0	=	Material constant in damage mechanics
S4R	=	4-node quadrilateral shell element with reduced integration
S4RS	=	S4R element with small membrane strains
SEM	=	Scanning electron microscope
SENT	=	Single-Edge-Notched Test
SMYS	=	Specified Minimum Yield Strength
s_N	=	Standard deviation of void nucleation
$s^2_{\sigma_E}$	=	Variance of the experimental stress values
T	=	Tensile/ultimate strength
t	=	Wall thickness of pipe
T_A	=	Tensile axial load
$(T_A/T_{Ay})_{\min}$	=	Normalized minimum design tension load
T_{Ay}	=	Yield tensile axial load
T_m	=	Homologous temperature
T_p	=	Tensile axial load due to internal pressure
t_r	=	Reduced thickness of plate at notch root
U	=	Displacement
$\ddot{u}_{(t)}$	=	Vector of nodal acceleration in explicit FEA
u^{EXT}	=	Displacement of knife edge
UTS	=	Uniaxial Tensile Strength
U_x	=	Horizontal displacement
u_x	=	Transitional degree of freedom in x direction

u_y	=	Transitional degree of freedom in y direction
u_z	=	Transitional degree of freedom in z direction
x_{imp}	=	Position of imperfection
Y	=	Yield strength
y_c	=	Critical energy release rate
δ	=	CTOD toughness
ΔA	=	Change of cross-sectional area in specimen to fracture
ΔL	=	Change of length in specimen to fracture
Δ_{roller}	=	Horizontal displacement of the roller end
Δt	=	Time increment in explicit FEA
Δ_{vFEA}	=	Vertical deflection of the middle of the pipe from FEA
ε	=	True strain
$\bar{\varepsilon}$	=	Equivalent strain
ε_1	=	Major principal strain
ε_2	=	Intermediate principal strain
ε_3	=	Minor principal strain
ε_c^{crit}	=	Critical buckling strain
ε^{ENG}	=	Engineering strain
$\bar{\varepsilon}_f$	=	Equivalent strain to fracture
$\bar{\varepsilon}_f^p$	=	Equivalent plastic strain to fracture
$\bar{\varepsilon}_f^{(\xi=-1)}$	=	Fracture strain curve versus stress triaxiality at ξ=-1
$\bar{\varepsilon}_f^{(\xi=0)}$	=	Fracture strain curve versus stress triaxiality at ξ=0
$\bar{\varepsilon}_f^{(\xi=1)}$	=	Fracture strain curve versus stress triaxiality at ξ=1

ε_{kk}^{p}	=	Plastic volumetric strain
ε_N	=	Mean strain of void nucleation
$\bar{\varepsilon}^{p}$	=	Equivalent plastic strain
$\dot{\bar{\varepsilon}}^{p}$	=	Rate of equivalent plastic strain
ε_u	=	Uniform/necking strain
ζ	=	Ratio of defect length to wall thickness
η	=	Stress Triaxiality
η_{ave}	=	Average stress Triaxiality
θ	=	Lode angle
$\bar{\theta}$	=	Lode angle parameter
θ_{cb}	=	Central Angle of cold bend pipe
θ_{FEA}	=	Average angle of pinned and roller ends
θ_{pin}	=	Rotation of pinned end
θ_{roller}	=	Rotation of roller end
θ_x	=	Rotational degree of freedom about x axis
θ_y	=	Rotational degree of freedom about y axis
θ_z	=	Rotational degree of freedom about z axis
λ	=	Y/T ratio
ν_θ	=	Lode variable
ξ	=	Normalized third deviatoric stress invariant
ξ_{ave}	=	Average normalized third deviatoric stress invariant
σ	=	True stress
$\bar{\sigma}$	=	Equivalent stress (Von Mises Stress)
$\tilde{\sigma}$	=	Effective stress
σ_1	=	Major principal stress

σ_2	=	Intermediate principal stress
σ_3	=	Minor principal stress
σ_E	=	Experimental true stress
σ^{ENG}	=	Engineering stress
σ_{ij}	=	Stress tensor
σ_m	=	Hydrostatic pressure
σ_p	=	Proportional limit strength
σ_{PL}	=	Predicted stress by power law
σ_{ym}	=	Equivalent plastic stress flow in the damage-free matrix
υ	=	Poisson's ratio
φ	=	Damage potential function
Φ_S	=	Fracture Index
χ	=	Ratio of defect height to wall thickness
ψ	=	Ratio of defect depth to wall thickness
ϕ_g	=	Global curvature

CHAPTER 1: INTRODUCTION

1.1 Foreword

Underground energy pipelines work as the earth arterial vessels that transmit the oil and gas products for thousands of kilometers from remote refineries and production sites to the consumption units. Playing this vital role, buried pipelines are being subjected to the primary loads due to the internal pressure of the contents and soil overburden. Pipelines also experience secondary loads (i.e. axial force and bending moment) on their long path being imposed by the geo-environmental excitations (Figure 1-1), such as ground movements and temperature gradients. These combined loading conditions can progressively impair the structural integrity of the steel pipelines to the level of instability or final collapse and the loss-of-containment which ultimately may be accompanied by property damage or fatal accidents. Therefore, any premature failure of buried pipelines should be well understood and considered in the design stage and during the operating mode.

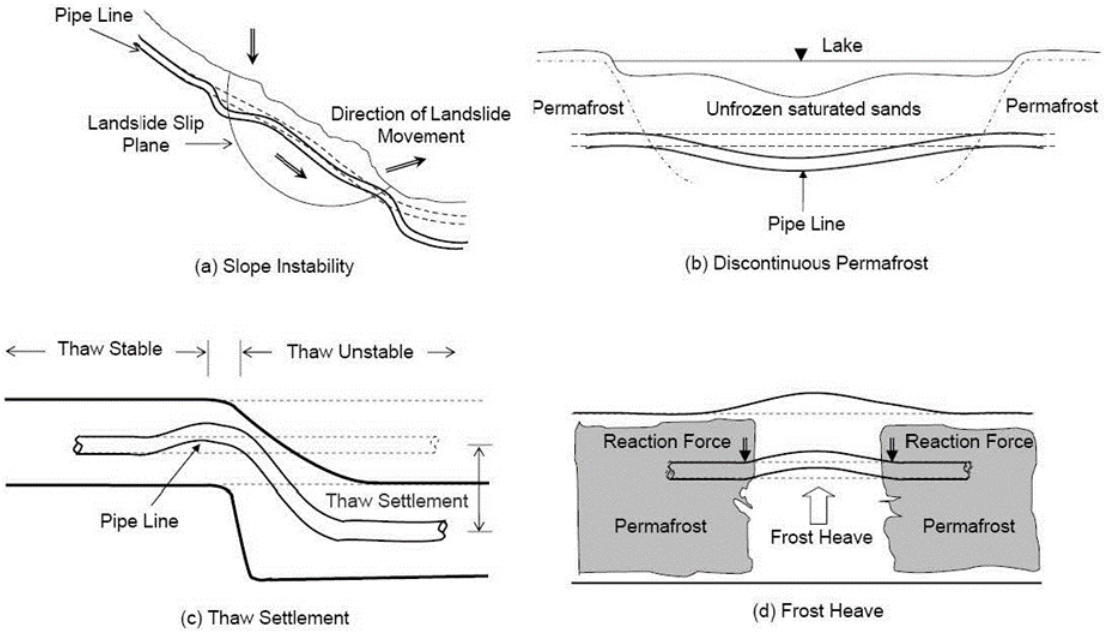

Figure 1-1: Schematic display of some geo-environmental excitations (Ahmed 2011)

1.2 Problem Statement

Ground movements monotonically increase the local curvature in buried steel pipelines that initially forms a local buckling (or the so-called wrinkling) on the compressive side of the wall. Global buckling is unlikely due to the continuous circumferential support of the surrounding soil medium (Dorey 2001). Once a pipe locally buckles, it may loose its serviceability, however, the major concern is that the catastrophic burst of the wall may be initiated from that softening point under the on-going geotechnical perturbations. Rupture of energy pipelines leads to environmental contamination and is extremely hazardous to the public safety and property. Therefore, the common practice to avoid the post-buckling rupture is that the pipeline operators try to trace and replace any buckled portion of the pipelines which is a highly expensive remedy but may be dispensable (Ahmed 2011). On the other hand, there is a considerable risk that a wrinkling is not identified by monitoring a pipeline which is the reason behind the rupture of many buried piplines in the field.

Experimental observations and numerical analyses (Ahmed 2011; Das et al. 2002; Sen 2006; DelCol 1998; Mohareb 1995; Zhou and Murray 1995; Chiou and Murray 1993) have shown that steel pipelines are so ductile and can accommodate relatively large post-buckling deformations beyond the maximum bending capacity without the loss of their operational safety (Figure 1-2). This matter is one of the main cornerstones of the idea of using the strain-based (limit state) design approach for the pipelines to benefit from the high deformability feature of the steel pipes over the plastic region.

Also, the critical rupture strain due to the pre-existing defects in the girth weld area of the pipelines, which is currently the only rupture limit state in the codes (CSA-Z662 2015), is unlikely to be reached in the case of pressurized wrinkled pipes under monotonic curvature even for the pipelines with relatively large weld defects (Igi et al. 2011; Igi and Suzuki 2007).

Therefore, in the situations where the wrinkling does not disrupt any specific serviceability requirements of the line, the wrinkled pipes can theoretically still be kept in service. However, further limit states should be identified to safeguard the wrinkled pipelines against the post-buckling rupture of the wall. The JGA code specifies the

rupture that happens after the peak moment (at the buckling strain) as the limit of the steel pipes (JGA 2001; Mitsuya and Sakanoue 2015; Mitsuya and Motohashi 2013). But, the rupture limit of the wrinkled pipes is presently missing from the codes.

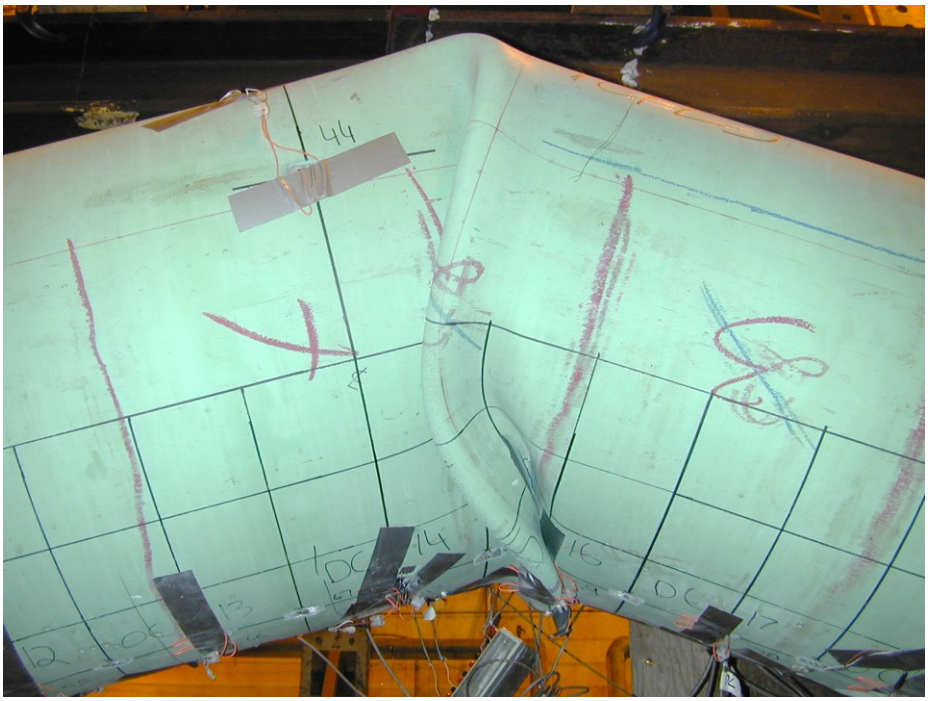

Figure 1-2: Excessive cross-sectional deformations under monotonic curvature without burst of the wall (Sen 2006)

It was postulated that the rupture of wrinkled pipelines under a monotonic loading condition is a quite significant issue that needs to be identified and understood through the study of post-buckling behavior. It has been demonstrated that the fracture of the bulging buckle on the compressive side of the wrinkled location is out of question once the pipe is subjected to monotonic increase of deformations, as shown in Figure 1-2, and such a fracture limit is only likely to be reached under a cyclic loading condition where the strain reversals initiate the low cycle fatigue (LCF) fracture (Das 2003). The only scenario for the fracture of the wrinkle under monotonic loading condition is the so-called tearing failure that occurs only at the telescoping wrinkles under very rare circumstances due to the changing boundary conditions (BC) and extremely large deformations (Ahmed 2011; Das et al. 2002). However, the fracture of the pipe wall on

the opposite side of the bulging wrinkle on the tensile side of the cross-section has been observed in many experiments due to monotonic increase of the curvature as shown in Figure 1-3 (Sen 2006; Tajika et al. 2011; Igi et al. 2011; Tajika and Suzuki 2009; Mitsuya et al. 2008; Mitsuya and Motohashi 2013; Mitsuya and Sakanoue 2015). This mode of failure seems very likely to be the rupture limit of the wrinkled pipes as it occurs due to the extension of the same regime of monotonic curvature and corresponding deformations that have previously made the pipe buckle. Now, the experimental observations bring up an open question as to what are the conditions under which the wrinkled pipes would be actuated to burst on the tension side and how to protect the wrinkled pipes against this undesirable catastrophic failure when they are going to be in service.

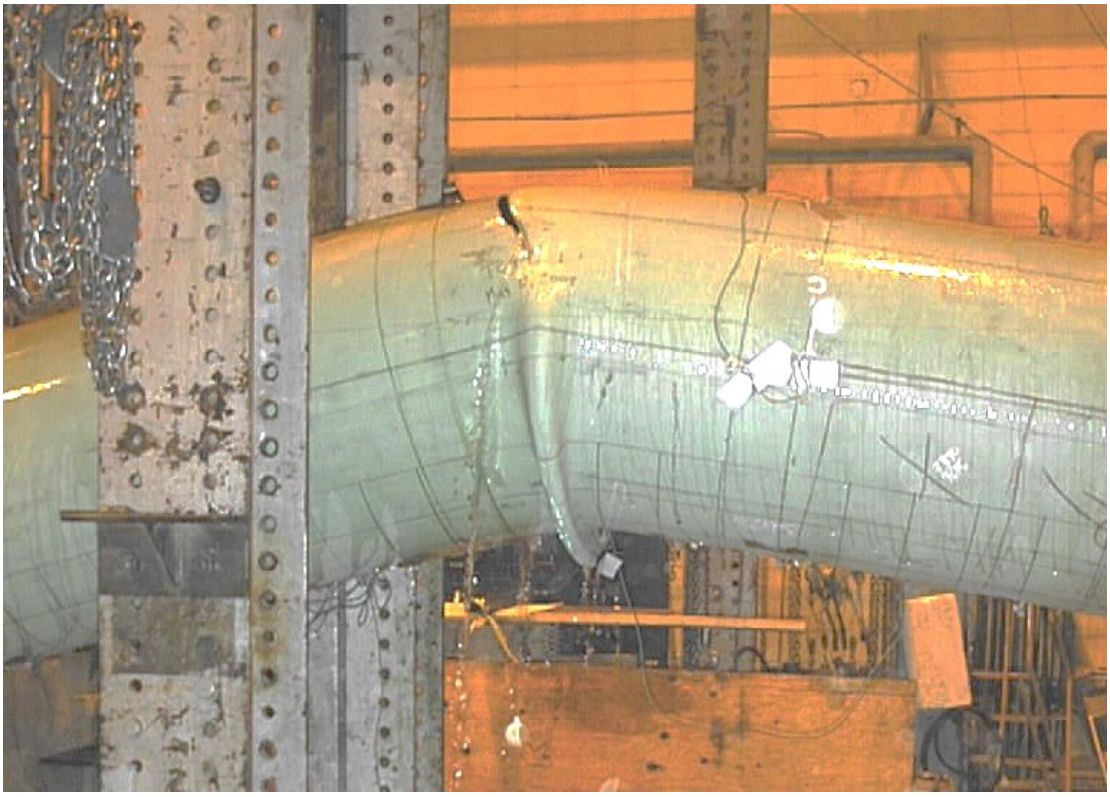

Figure 1-3: Tensile fracture of cold bend pipe at the wrinkled region (Sen 2006)

1.3 Research Objectives

This research program aims at studying the post-buckling rupture of the plain steel line pipes on the tension side of the wrinkled location under monotonically-increasing curvature which leads to the catastrophic burst of the pipe wall. The evaluation of the structural integrity of pressurized buried pipelines after wrinkle formation will be studied with a particular emphasis on developing design criteria to safeguard against the post-buckling fracture initiation on the tensile side of the pipe wall to retain the operational safety of the wrinkled steel pipelines. The main objective falls into the following itemized subcategories:

1) Calibration of a proper material model that is capable of simulating the post-necking behavior of steel material and predicting the ductile fracture initiation as the final material failure;

2) Finite element (FE) analysis of the applicable full-scale pipe tests to verify the validity of the simulation techniques and material model by predicting the pre-existing experimental results;

3) Employment of the verified FE models to identify the key factors and critical BC that are responsible for rupture of the wrinkled buried pipelines on the tension side of the wrinkled cross-section;

4) Parametric study on the design parameters that are contributing to the rupture of wrinkled pipes to develop the interactive limiting bounds and design guidelines for safe operation of the in-service buckled pipelines and to safeguard against the catastrophic rupture on the tensile side of the wall due to an ongoing increase of monotonic curvature.

1.4 Research Methodology

The procedure required to be followed in order to attain the aforementioned objectives of the project could be categorized into five major steps as follows.

The primary stage of any research project is to learn from the relevant works conducted by the predecessors. In this regard, a comprehensive literature review was conducted in pursuing three main goals: first, to understand the post-buckling behavior of the wrinkled steel pipes; second, to identify the significant parameters that govern the existing rupture limit states of the steel pipelines; and third, to comprehend the mechanism of the ductile fracture initiation in steel material.

In the second phase, a number of small-scale experiments were conducted in order to calibrate an appropriate material model for API X65 or CSA Z245 Gr 448 steel grade. A series of conventional dogbone tensile coupons were tested to adjust the stress-strain relationship of the material. Also, a set of smooth and notched round bars (NRB) plus grooved plates (GP) with various notch radii were designed and tested under tensile load to examine the dependence of the fracture strain on triaxial stresses in the uniaxial and plane strain loading conditions. Comparison of the results for these two loading conditions examined the functionality of the fracture strain to the so-called Lode angle parameter. Afterward, the FEA of all experiments were conducted using ABAQUS software and verified by the test results to calibrate the material plasticity (true stress-strain curve) using the power law model and to obtain the ductile fracture toughness as a surface of equivalent fracture strain (Bai 2007; Bai and Wierzbicki 2010; Xue 2007a; Xue 2007b) versus stress triaxiality and Lode angle variables.

The calibrated true stress-strain curve simulates the post-yielding behavior of the material through von Mises isotropic hardening until the fracture strain in conjunction with the cumulative fracture criterion (Johnson 1980; Bao 2003; Bai and Wierzbicki 2008) predict the onset of ductile fracture initiation. An important advantage of using such material model is that both effects of high triaxial stresses and biaxial loading conditions, which can be developed in the pipe wall, are considered in the prediction of ductile fracture.

The third step of this research program was assigned to simulate a number of full-scale tests using ABAQUS software. The experimental data were selected from previous research works on two pairs of similar specimens (four specimens in total) with the nominal pipe size (NPS) of 30” (Sen 2006; Dorey 2001) and 48” (Tajika et al. 2011),

out of which the post-buckling rupture was observed for only one of the two specimens at each pair. The FE models attempted to exactly simulate the physical test conditions including the magnitude and sequence of the loadings, as well as the BC. The load-deformation behavior and the prediction of fracture obtained from the FEA were compared to those of experiments in order to verify the simulation techniques and the material model implemented in the FE models.

The fourth part of the procedure, the verified FE models were employed to investigate different failure modes and highlight the key factors that are responsible for triggering the post-buckling rupture of the pipe wall due to increasing curvature. Also, the verified FE models were engaged to examine different BC that can be developed for the deflected segments of buried pipelines to discover the most critical BC that precipitates the wrinkled pipes into the tensile rupture.

In the final stage, the matrix of the key design variables identified in the previous section is designed to cover a wide range of geometry, primary loads and material properties applicable to the common energy pipelines and numerous FE models are constructed and analysed based on each combination of the parameters to assess the final failure mode. The results from this stage suggest some useful interactive design curves that can be used by the pipeline engineers in order to benefit from the ductile quality of the steel pipes and maintain the wrinkled pipelines in a safe operating mode in lieu of changing the wrinkled portion.

1.5 Organization of the Thesis

The current dissertation is categorized into eight chapters. Chapter 2 includes a wide-ranging literature review on different failure modes of steel pipelines with attention to three main studies on the critical buckling strain (CBS), rupture of the local buckle on the compressive side, and rupture strain limits due to pre-existing defects in the girth-welded areas.

In Chapter 3, the physical mechanism of the ductile fracture phenomenon and associated theories are systematically studied through reputable mechanical models. Chapter 4 represents the description of the small-scale fracture experiments on X65

steel grade and test results. In this chapter, material model and ductile fracture toughness are calibrated through using a hybrid experimental-numerical approach.

Details of the full-scale tests and development of their corresponding FE simulations are discussed in Chapter 5. The results of the FEA of the full-scale tests are presented in Chapter 6. Also in this chapter, the verified FE models are used to identify the critical BC and the key design parameters that are responsible for the post-buckling rupture of steel pipes.

Description of the parametric study is provided in Chapter 7 where the final results are demonstrated through design curves and equations. Lastly, the concluding remarks of the current research program and the recommendations for future studies are summarized in Chapter 8.

CHAPTER 2: LITERATURE REVIEW OF FAILURE MODES FOR STEEL PIPELINES

2.1 Introduction

In this chapter, the existing knowledge that helps to understand the rupture of wrinkled pipes is discussed and studied through a comprehensive literature review to build a general background that directs the present research project. Taking the rupture of buckled pipes into consideration, it is essential to cover two most important failure limits of steel pipes, namely wrinkling and rupture.

To begin with, an overview of previous studies on local buckling of steel pipes conducted at the University of Alberta is highlighted. The experimental simulation of loading mechanism on the buried pipelines as well as the effect of different design variables that can precipitate the formation of the wrinkle is briefly reviewed. Afterward, the rupture limit of steel pipes due to pre-existing defects in the girth-welded area is investigated from the literature as one of the growing concerns in the design of structural integrity to find an understanding of the crucial factors that are responsible for rupture. Moreover, the rupture of wrinkle on the compressive side of the cross-section is studied as a failure scenario that could trigger the rupture of buckled pipelines. Lastly, a state-of-the-art review of the experimental research works in which the rupture of wrinkled pipes has been reported is provided as the intrinsic motivations for this research.

2.2 Local Buckling of Steel Pipes

Many research works have been conducted to address the critical buckling strain (CBS) of the steel pipelines in association with the strain-based design approach. Figure 2-1 schematically shows the general full-scale test set-up that has been used for experimental studies on CBS. As it can be seen, the pipe specimen is subjected to simply-supported boundary conditions without any restraints on the axial deformations which simulates the critical field conditions.

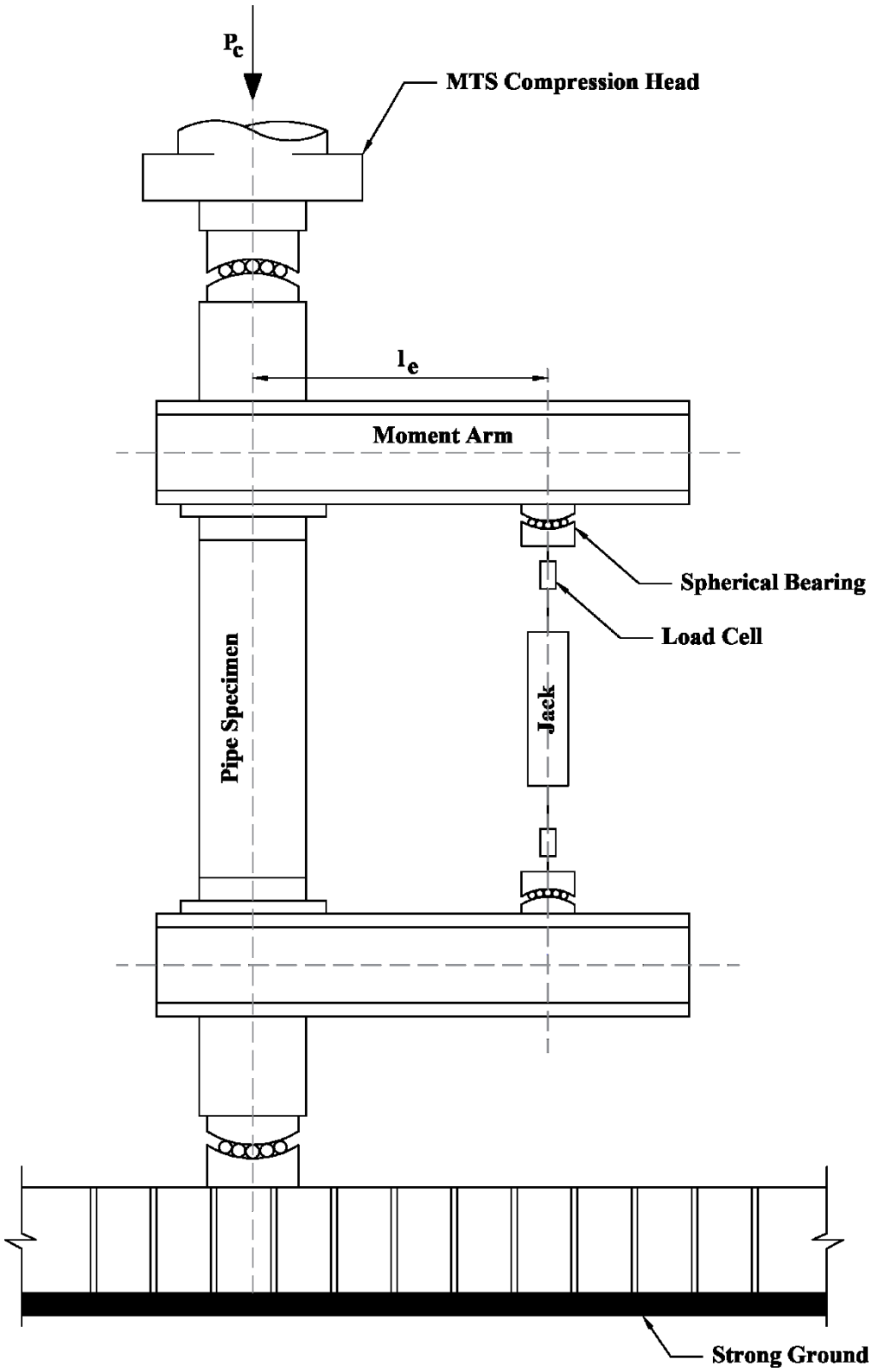

Figure 2-1: Schematic representation of test set-up and boundary conditions for CBS studies

Mohareb et al. (1995; 2001) conducted a number of full-scale tests on the steel line pipe specimens with outside diameter (D) to the wall thickness (t) ratio of 51 and 64 under combined loading conditions. It was found that the higher D/t ratio dramatically decreases the moment capacity and buckling strain of steel pipes. Numerical simulations were developed and verified by the experimental results to examine the effect of various load combinations. Deformation limiting criteria were introduced by developing an empirical equation for CBS by means of numerical parametric study and π-dimensional analysis theorem. The so-called "bulge" shaped and "diamond" shaped buckles (as shown in Figure 2-2) were observed for specimens with and without internal pressure respectively. In this study, CBS was found as a function of hoop stress, axial force, and D/t ratio. However, *(DelCol 1998)* simulated the pre-buckling and post-buckling behavior of both plain and girth-welded steel pipes under different combination of monotonic loads and it was shown that the pre-existing geometric imperfections is another key parameter in the CBS of the steel pipes.

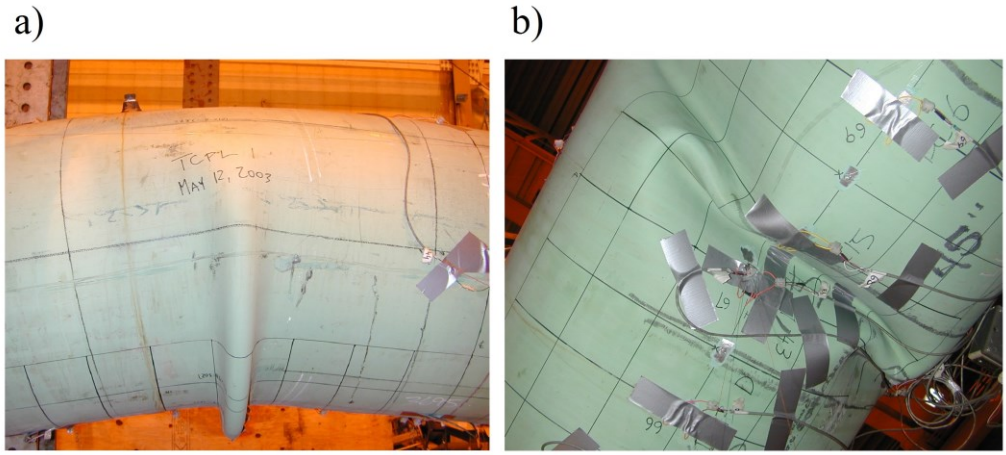

Figure 2-2: Different types of local buckling (Sen 2006)

a) Bulging buckle for pressurized pipe;
b) Diamond wrinkle for pipes with low internal pressure

Dorey (2001) implemented the available experimental database at the University of Alberta by testing both girth-welded and plain line pipe specimens with the D/t ratio of 92. First, a useful technique was developed to introduce the initial geometric

imperfections of the pipe segments in the analytical analysis to simulate the experimental results (Dorey et al. 2006b). For plain pipes, three types of imperfections (ring, half-ring and blister) were considered in the FEA. A cosine function was used to introduce the amplitude of maximum imperfection (measured in the laboratory) at the mid-height of the pipe in the circumferential direction. It was found that the blister imperfection results in a closer prediction of CBS in comparison to the experimental data. For girth-welded pipes, however, it was proposed to introduce an "offset" equal to the measured offset at girth weld between upper and bottom cans (this offset acts similar to a ring imperfection) and neglect the other pre-existing imperfections in the cans.

Afterward, a comprehensive parametric study was conducted to study the CBS of the line pipes through finite element analyses (Dorey et al. 2006a). Initial imperfections were found to be one of the most influential factors particularly for the pipes with higher D/t ratios which significantly affect load-carrying capacity as well as the location of the buckles. Internal pressure was found to have a significant influence on load-carrying capacity, global curvature, CBS and slope of the post-buckling branch in the moment-curvature diagram. It was observed that by increasing the internal pressure, the moment capacity decreases and global curvature at the initiation of local buckling increases. It was also found that the higher D/t ratio results in lower ultimate moment and deformation. Study on the CBS for different steel grades with different specified minimum yield strength (SMYS) showed that the higher the steel grade (higher yield stress), results in the lower CBS.

The following design parametric equations were derived as a function of internal pressure (p), D/t ratio, the amplitude of initial imperfection (A_{imp}), yield strength (F_y), and modulus of elasticity (E) to predict the CBS (ε_c^{crit}) of the plain pipes [Eq. (2-1)] and girth-welded pipes [Eq. (2-2)].

$$\varepsilon_c^{crit} = \left(\frac{2.94}{D/t}\right)^{1.59} \times \left(\frac{1}{1-0.868\left(\frac{p}{p_y}\right)}\right) \times \left(\frac{E}{F_y}\right)^{0.854} \times \left(1.27 - \left(\frac{\left(A_{imp}\right)_{\max}}{100t}\right)^{0.15}\right) \quad (2\text{-}1)$$

$$\varepsilon_c^{crit} = \left(\frac{8.99}{D/t}\right)^{1.72} \times \left(\frac{1}{1-0.892\left(\frac{p}{p_y}\right)}\right) \times \left(\frac{E}{F_y}\right)^{0.701} \times \left(1.09 - \left(\frac{A_{imp}^{offset}}{t}\right)^{0.0863}\right) \quad (2\text{-}2)$$

in which, p_y denotes the yield internal pressure.

Sen (2006) studied the CBS and post-buckling behavior of cold bend pipes pressurized up to 80% of the SMYS under combined loading. Three *D*/*t* ratio of 44, 69 and 93 were examined experimentally and analytically. The initial intention of the research program was to study the critical buckling strain (Sen et al. 2004; Cheng et al. 2004; Sen and Cheng 2010) and the mechanical properties of the cold bend pipes (Sen et al. 2008). In this study, it was found that the CBS of the cold bend pipes is significantly decreased compared to their corresponding straight pipe. It was also revealed that the buckle on the compression side of the cold bend pipes are susceptible to low cycle fatigue (LCF) since leakage occurred at the buckle location in two specimens after 3 to 6 loading-unloading cycles. Furthermore, one of the X65 cold bend pipe specimens with *D*/*t* ratio of 93 which was pressurized to 80% of the SMYS unexpectedly ruptured on the tensile side of the wrinkled location while increasing the monotonic curvature. Therefore, it was found that the rupture of pipe wall at the tensile side of the buckled cross-section is possible to happen due to high internal pressure and largely imposed curvature.

Fathi (2012) implemented a combination of kinematic hardening model with isotropic von Mises yield criterion and introduced a combined hardening anisotropic material model which accounts for the material anisotropy (Bauschinger's effect) of high strength steel (HSS) pipes due to the extension stage in UOE pipe manufacturing

process. In this study, the CBS of HSS pipes were studied by experiments and finite element simulations and it was found that internal pressure significantly decreases the effects of anisotropy on CBS.

2.2.1 CSA–Z662 Standard for CBS

The CSA-Z662 Standard provides the following regression equations as the limit state for the CBS of steel pipelines corresponding to the peak moment capacity of the pipe (CSA-Z662 2015).

$$\varepsilon_c^{crit} = \begin{cases} 0.5\dfrac{t}{D} - 0.0025 + 3000\left(\dfrac{(p-p_e)D}{2tE}\right)^2 & for \quad \dfrac{(p-p_e)D}{2tF_y} < 0.4 \\ 0.5\dfrac{t}{D} - 0.0025 + 3000\left(\dfrac{0.4F_y}{E}\right)^2 & for \quad \dfrac{(p-p_e)D}{2tF_y} \geq 0.4 \end{cases} \qquad (2\text{-}3)$$

in which, p_e denotes the minimum external hydrostatic pressure acting on the pipe in MPa unit.

2.3 Rupture of Steel Pipes Due to Defects

The ductile fracture initiation and propagation from the flaws in the girth weld or its heat affected zone (HAZ) which results in the final rupture of the pipe wall is currently known as the most critical ultimate limit state in the design of steel pipelines. Therefore, recent research in this area has been mostly focused on the study of critical tensile strain limit state of the steel pipes possessing defects in their girth welds or HAZ. These studies are based on introducing an artificial notch in the weld metal or HAZ and measuring the critical strain at a remote location that coincides the initiation of ductile crack propagation. The majority of these studies are based on tensile testing of the curved wide plate (CWP) specimens cut from a girth-welded segment of a steel pipe which ignores the effect of internal pressure on critical rupture strain.

Wang et al. (2002) conducted a series of FE analyses on the axisymmetric girth-welded pipe with surface cracks in the weld centerline to study the relationship between crack driving CTOD (crack tip opening displacement) toughness and remote tensile strain for a wide range of defect sizes and weld strength mismatch. It was found that the relationship between crack driving CTOD and applied strain can be categorized into three regions of stable linear, stable nonlinear and unstable based on the defect size and weld strength mismatch (Figure 2-3a). It can be observed that as the depth of defect increases, the plastic strain concentration at the crack tip becomes larger and accelerates the transmission of plastic strain to the back of the surface which results in a sharp increase of crack driving CTOD due to a small increase in tensile strain. Also, the lower weld strength mismatch leads to more unstable behavior of the weld defect subjected to tensile strain (Figure 2-3b). Crack driving CTOD was set to a range of assumed values of fracture toughness CTOD for different crack sizes to derive three parametric equations for predicting the critical strain limit as a function of defect size, weld strength mismatch and fracture toughness CTOD. The proposed rupture criterion was shown to be very conservative in predicting the critical rupture strain of the CWP tensile tests and full-scale pipe bending tests.

Wang et al. (2004b) studied the relationship between the crack driving CTOD and tensile strain for various material properties and surface weld defect. Stress-strain curves with various Y/T (yield strength to tensile strength) ratio were constructed for each pipe steel grades using the *Ramberg-Osgood* equation (Ramberg and Osgood 1943) given in the CSA-Z662 standard. Defect length and pipe geometry were taken into account as other effective factors. Rupture strain limit for girth-welded pipes was obtained and presented in a tabular format by equating the crack driving CTOD from FEA and the apparent fracture toughness CTOD for a large range of material properties, defect size, pipe grade, geometry. To validate these numerical results, *Wang et al.* (2004c) conducted a series of CWP tensile tests made of X80 and X100 steel materials. The tensile strain limit of girth weld of the experiments was found to be predicted with a reasonable accuracy. In a similar study, *Wang et al.* (2004a) carried out a series of FE analyses of pipeline structure possessing buried defects (e.g. lack-of-side wall fusion defects) in their girth weld and subjected to increasing tensile strain. Tensile strain limit

values of buried defect were developed for a wide range of material properties, defect size, pipe grade, and geometry by limiting the crack driving CTOD from FEA to apparent fracture toughness.

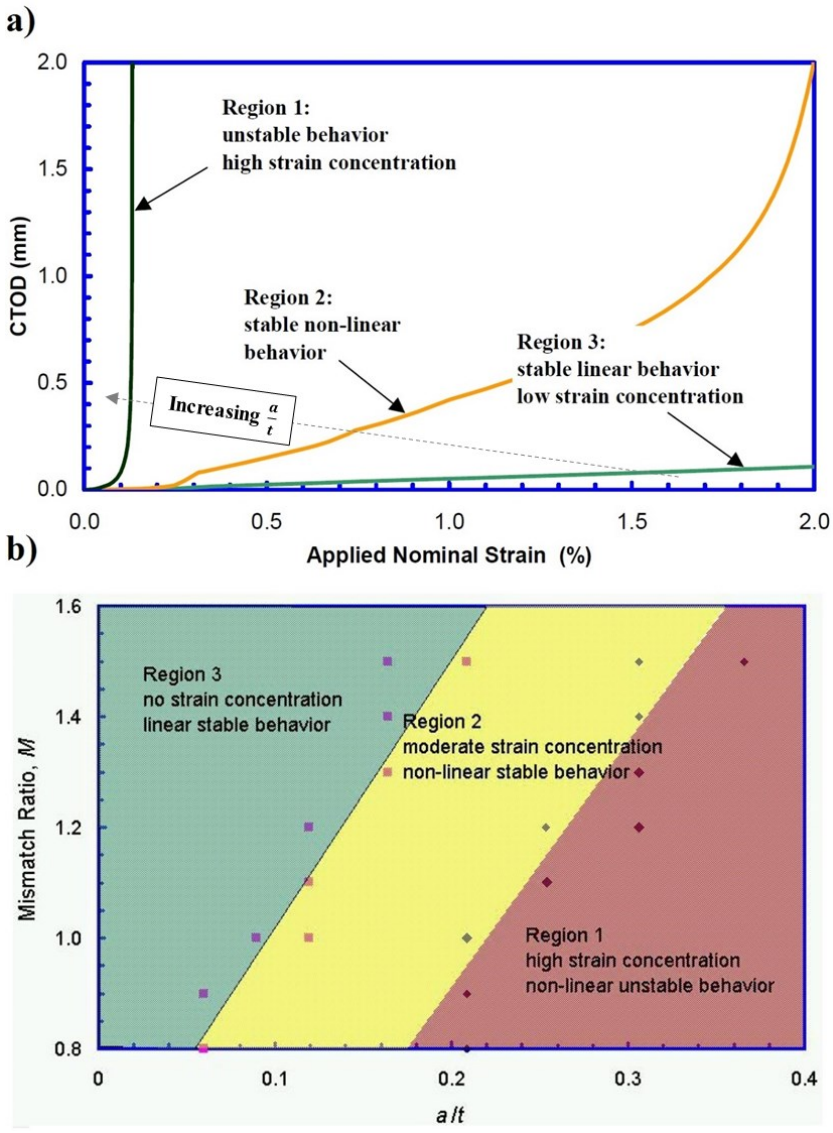

Figure 2-3: The three-region strain design diagram based on defect size and weld strength mismatch (Wang et al. 2002)

Sadasue et al. (2004) studied the ductile crack initiation and the final rupture of the girth weld joints of X80 and X100 steel line pipes using single-edge-notched test (SENT), notched round bars test and CWP test. The SENT and CWP tests were

conducted by introducing an artificial notch at the centerline of weld metal. Comparison between the results of the SENT and CWP tests revealed that the fracture toughness could be fairly stated in either form of CTOD or critical equivalent plastic strain. The critical equivalent plastic strain to fracture obtained from SENT test was found to acceptably predicting the fracture of CWP. The results from NRB tests with different notch radii (R) were also used to obtain the critical equivalent plastic strain to crack propagation of CWP considering the triaxial stress condition at the crack tip (Figure 2-4a). It was found that the critical equivalent plastic strain obtained from the NRB tests can also provide a good prediction of crack propagation and fracture initiation (Figure 2-4b). Moreover, a simplified method was proposed to predict the onset of crack propagation based on obtaining the fracture toughness from SENT test and limiting the crack driving force of notched CWP obtained from FEA. The corresponding critical strain limit at this point is estimated as rupture limit state for the imperfect weld material of girth-welded pipes. A parametric study was conducted using the proposed method and it was postulated that a lower Y/T ratio for the base material will considerably decrease the plastic strain concentration at the crack tip and consequently delays the ductile crack propagation in the girth weld.

Igi and Suzuki (2007) conducted small-scale tensile tests on girth-welded SENT and notched CWP specimens made of X80 steel material and obtained the critical equivalent plastic strain at notch tip corresponding to the critical CTOD to crack growth (fracture toughness). The critical equivalent plastic strain was used as the limit in FEA of a full-scale notched girth-welded pipe subjected to axial tensile and bending loads to study the effect of internal pressure and Y/T ratio on the tensile strain limit. It was found that the critical remote tensile strain for ductile crack growth (associated with the critical equivalent plastic strain at notch tip) decreases with the increase of internal pressure and Y/T ratio of the base material once the pipe is subjected to the axial tensile loading condition (Figure 2-5). However, in the case of pure bending deformation (Figure 2-6), it was observed that an increase of internal pressure reduces the critical remote tensile strain for base material with high Y/T ratio and conversely increases the critical remote tensile strain for base material with low Y/T ratio. The reason is that the

local buckling occurs on the compressive side under bending deformations prior to the crack growth on the tensile side.

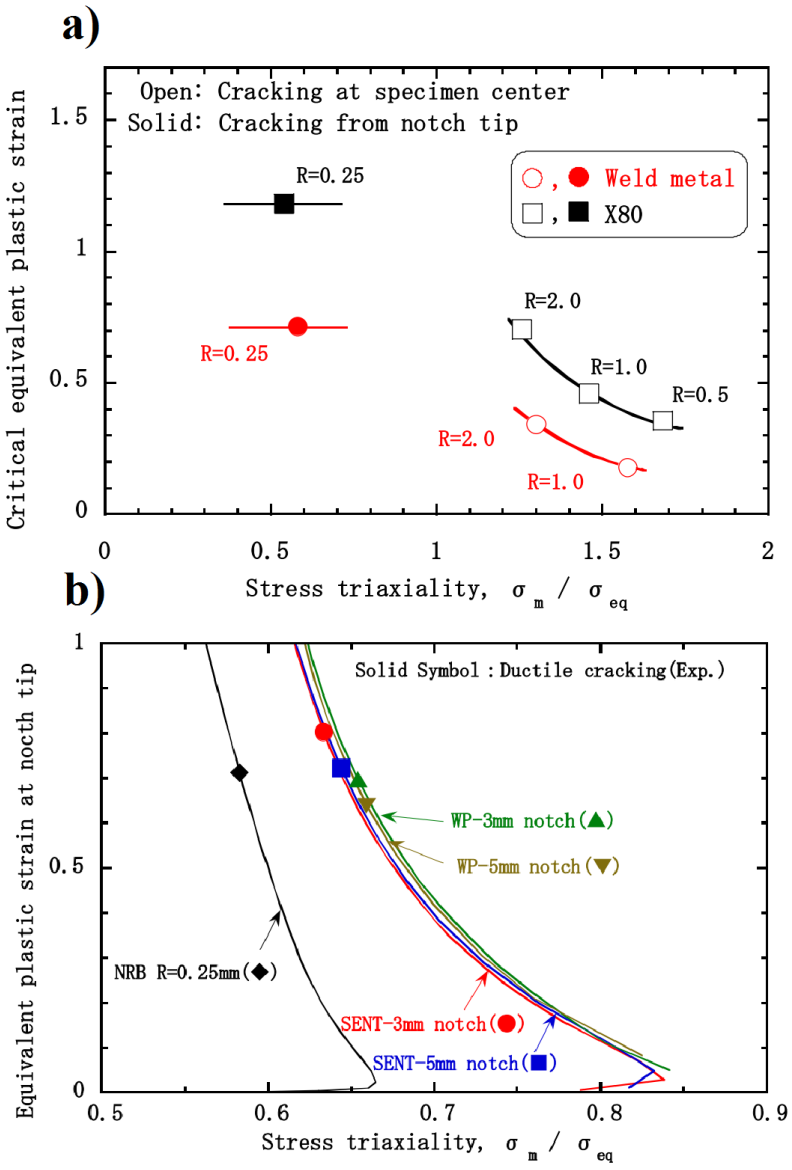

Figure 2-4: Prediction of crack propagation using critical equivalent plastic strain (Sadasue et al. 2004)
a) Equivalent plastic strain to fracture as a function of triaxial stress from NRB tests;
b) Comparison of critical equivalent plastic strain from SENT, CWP and NRB tests

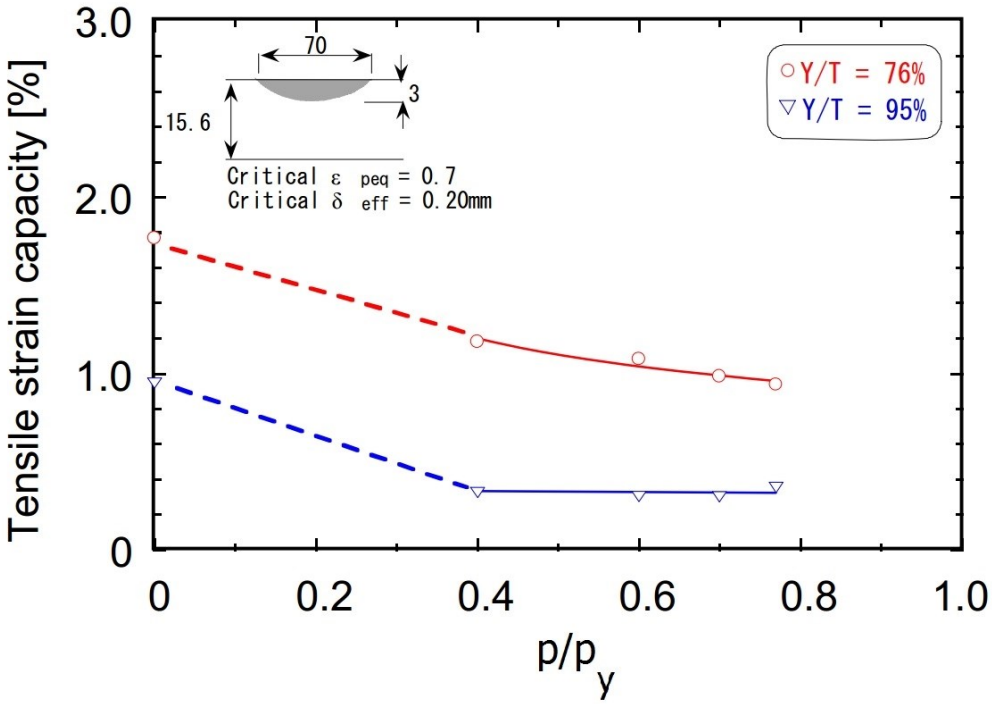

Figure 2-5: Effect of internal pressure and *Y*/*T* ratio on rupture strain limit due to axial tensile loading (Igi and Suzuki 2007)

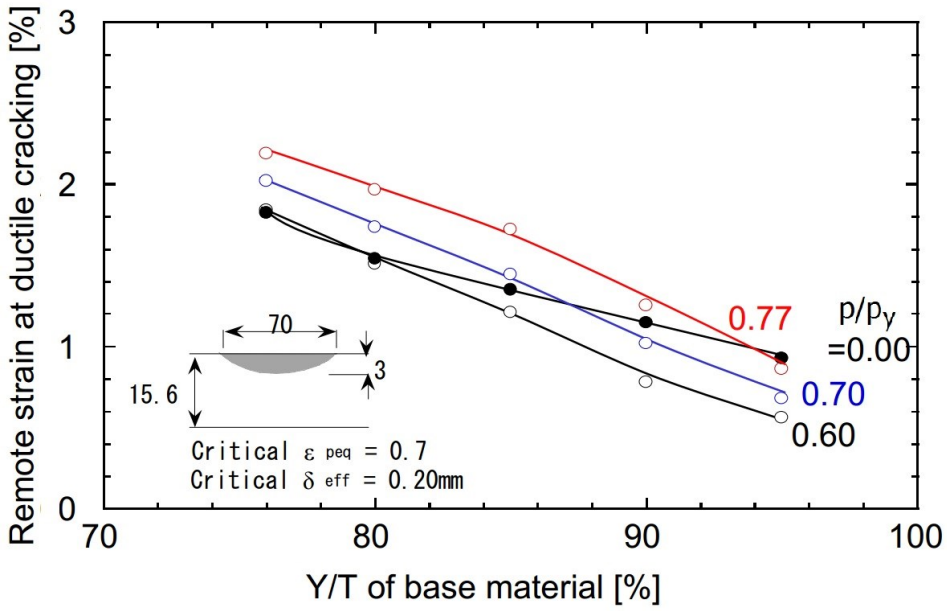

Figure 2-6: Effect of internal pressure and *Y*/*T* ratio on rupture strain limit due to pure bending loading (Igi and Suzuki 2007)

Gioielli et al. (2007) conducted tensile full-scale tests on pressurized and unpressurized girth-welded pipes of X65 material with machined flaws to study the influence of internal pressure on the tensile capacity of steel pipelines. Internal pressure corresponding to 80% of SMYS was applied to the pressurized pipes. Artificial notches were introduced in the base material and girth weld material. It was found that for the specimens with failure initiated from the artificial notch, the failure strain for the pressurized pipes decreases by 44% to 47% in comparison to that of unpressurized specimens. And, the decrease in failure strain was about 16% for the pipe specimens failed away from the notch.

Igi et al. 2010 (Igi and Sakimoto 2010; Igi et al. 2010) conducted tensile tests on small-scale notched girth-welded CWP and full-scale notched girth-welded pipe specimens made of X80 steel material. Semi-elliptical notches were introduced in weld material and HAZ for the CWP specimens and it was observed that final rupture occurred in the base material away from the artificial notch for the case of the notched weld, however, ductile crack growth from the artificial notch triggered the rupture for the specimen with a notch in the HAZ. Therefore, a same size artificial notch was machined in the HAZ of the girth-welded pipe to study the effect of internal pressure in tensile strain capacity of steel line pipes. The pipe was pressurized to 72% of SMYS hoop stress and examined under tensile axial load. Comparing the results from the CWP test (with no internal pressure effect) and the pressurized pipe test revealed a considerable reduction of 50% in global critical tensile strain due to the presence of internal pressure. It was also found that the rate of change of crack driving force in the case of pressurized pipe test is considerably higher than that of CWP test. In other words, the final rupture will be more catastrophic due to internal pressure.

2.3.1 CSA Code Specifications for Rupture Limit State

According to the latest version of CSA-Z662 standard published in 2015, the tensile strain capacity or rupture limit state of the steel pipelines shall be determined by sound or proven methods that have been validated by physical tests and account for the effect of defects, metallurgical damage, and changes in mechanical property of the welds and

HAZ. Actual stress-strain relations of the steel material shall be obtained from standard test methods and used for the analysis instead of nominal tensile properties. The effect of internal and external pressure on the buried steel pipes shall be considered in the analysis (CSA-Z662 2015).

However, the previous versions of this standard (CSA-Z662 2011) allowed using the second approach to determine the tensile strain capacity of the steel pipes in case of lacking detailed information. This approach is based on the study of crack driving CTOD and fracture mechanic concepts (Wang et al. 2002; Wang et al. 2004a; Wang et al. 2004b; Wang et al. 2004c) and suggests using the following parametric equations, which are adopted from *Wang et al.* (2006), to estimate the ultimate tensile strain for different kinds of pre-existing defects (Figure 2-7).

$$
\begin{aligned}
&a)\ \ surface-bracking\ \ defects \\
&\varepsilon_t^{crit} = \delta^{(2.36-1.58\lambda-0.101\xi\chi)}\left(1+16.1\lambda^{-4.45}\right)\left(-0.157+0.239\zeta^{-0.241}\chi^{-0.315}\right) \\
&b)\ \ buried\ \ defects \\
&\varepsilon_t^{crit} = \delta^{\left(1.08-0.612\chi-0.0735\zeta+0.364\ \psi\right)}\left(12.3-4.65\sqrt{t}+0.495t\right)\left(11.8-10.6\lambda\right) \\
&\left(-5.14+\frac{0.992}{\psi}+20.1\psi\right)\left(-3.63+11.0\sqrt{\chi}-8.44\chi\right) \\
&\left(-0.836+0.733\chi+0.0483\zeta+\frac{3.49-14.6\chi-12.9\psi}{1+\zeta^{1.84}}\right)
\end{aligned}
\qquad (2\text{-}4)
$$

in which, δ is the CTOD toughness in millimeters $[0.1 \le \delta \le 0.3]$; λ is Y/T ratio $[0.7 \le Y/T \le 0.95]$; ζ is the ratio of defect length to wall thickness ($2c/t$) $[1 \le \xi \le 10]$; χ is the ratio of defect height to wall thickness (a/t and $2a/t$ for surface-breaking and buried defects respectively) $[\chi \le 0.5]$; and ψ is the ratio of defect depth to wall thickness (d/t). In most cases, these equations provide conservative estimations in comparison with CWP test results (Wang et al. 2004c).

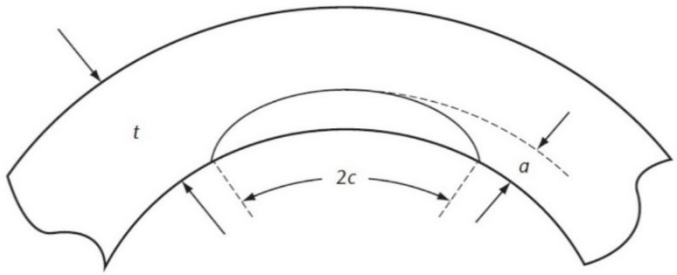

A planar surface-breaking defect in the pipe wall

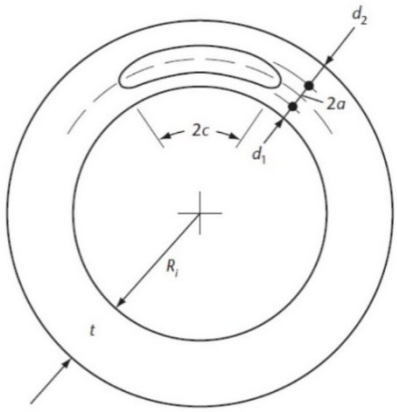

A planar buried defect in the pipe wall

Figure 2-7: Definition of surface-breaking and buried defects (CSA-Z662 2011)

2.4 Rupture of Buckled Pipe at the Wrinkle Location

The most significant ultimate limit state in pipeline practice is the rupture limit. It was found from the experimental research conducted by *Sen* (2006) that LCF can trigger the rupture of the buckle on the compression side of the wrinkled cold bend pipes subjected to a few loading cycles.

Das (2003) conducted full-scale tests on NPS12 steel pipe specimens with *D*/*t* ratio of 45 under combined monotonic loading, and cyclic loading which can be developed due to the temperature variation, operating pressure fluctuation, and seismic movements in the field. It was found that the high ductility of the pipe specimens avoids failure due to monotonically-increasing axisymmetric compressive axial load and the "accordion" type wrinkles (Figure 2-8a) are anticipated to form (Das et al. 2002). However, it was found that the strain reversals due to cyclic loading history would result in a fracture at

the crest of the bulge-type wrinkles (Figure 2-8b) in very few cycles of loading due to LCF phenomenon (Das et al. 2007a; Das et al. 2007b; Das et al. 2007c). Both of these failures are shown in Figure 2-8. The maximum strain values obtained in this study were found to be much higher than permissible strain values given in the design standards.

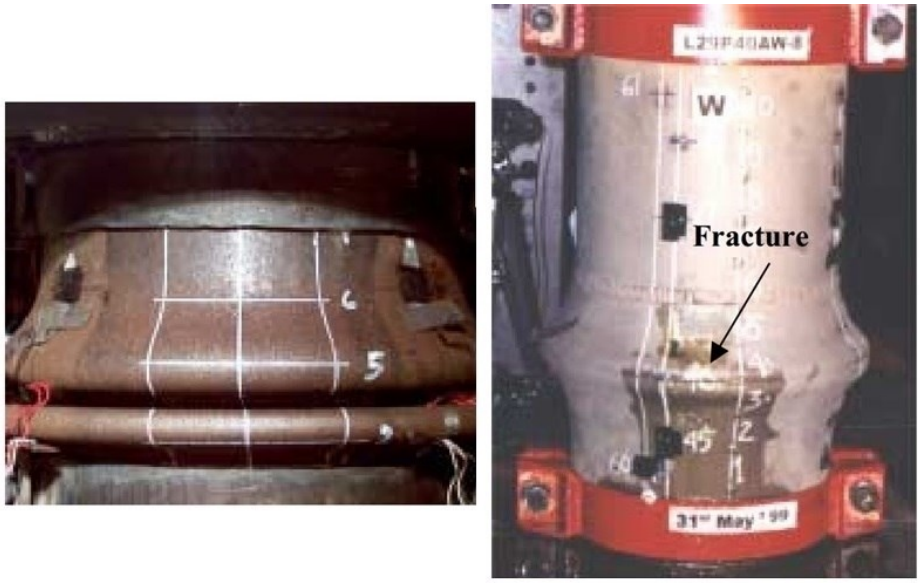

a) b)

Figure 2-8: Failures of pressurized steel pipes due to axial load
a) Accordion wrinkle due to monotonic load (Das et al. 2002);
b) Fracture of wrinkle due to cyclic load (LCF) (Das et al. 2007b)

Armen et al. (Ahmed et al. 2010a; Ahmed 2011; Ahmed et al. 2011) studied the tearing failure of the steel pipes with D/t ratio of 34 and 79, pressurized up to 80% of the SMYS, and subjected to monotonically-increasing axial displacement while keeping a constant curvature. The initial bulging wrinkle was developed by initial curvature and axial displacement, and then, the pipe was squashed by secondary axial force not aligned with its axis to the point that the interior surfaces of the pipe wall came into contact with itself at the wrinkle location and the wrinkle became flat. Continuing axial deformation led the top side to slip inside the bottom can in a telescoping manner which

resulted in tearing failure at the sharp fold of the "telescopic" wrinkles, as shown in Figure 2-9. The boundary conditions were changed from pinned to fixed ends during the experiment in order to apply axial load not aligned with the pipe axis while keeping constant curvature. Numerical results showed that significant localized strain reversal occurs at the wrinkle fold under the monotonic axial deformations which is the key parameter in the development of tearing failure. From FE simulations, a double design criterion based on checking the strain reversal and critical equivalent plastic strain limit was proposed to prevent the tearing fracture of wrinkled pipes subjected to monotonic loading (Ahmed et al. 2010b). It was postulated that the possibility of tearing failure occurrence is decreased by the increase of internal pressure and D/t ratio. For low internal pressure and D/t ratio, tearing failure was observed to be one of the possible failure scenarios.

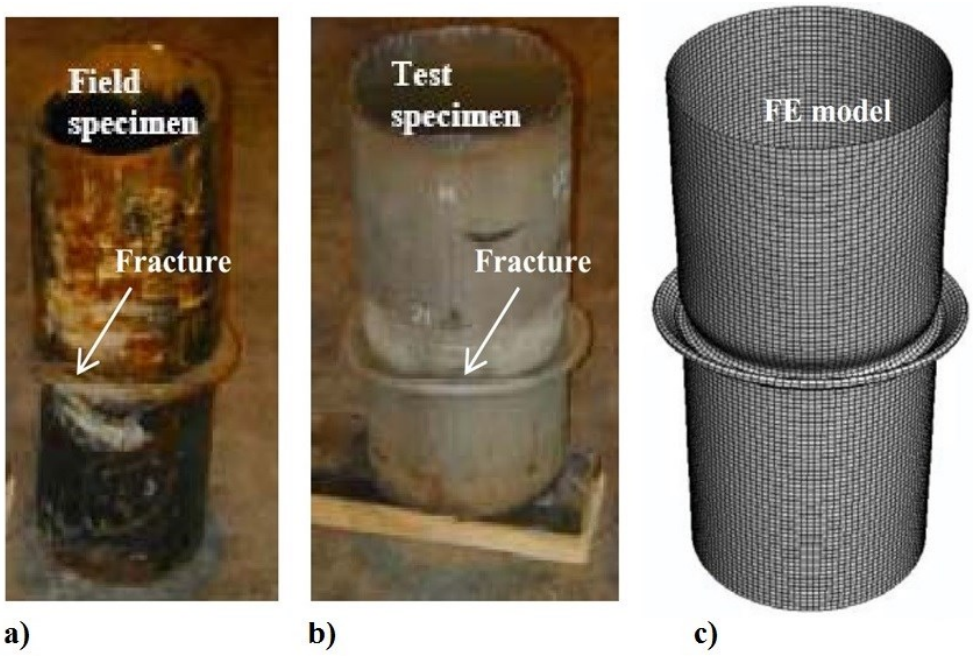

Figure 2-9: Telescopic wrinkle and tearing fracture of the buckle
a) Field (Das et al. 2002); b) Test (Das et al. 2002);
c) Numerical simulation (Ahmed 2011)

2.5 Rupture of Buckled Pipes on the Tension Side

Herein, the rupture of pressurized pipes on the tensile side of the wrinkled cross-section due to monotonically-increasing loading condition, which is the subject of current research, is outlined from the up-to-the-minute research works.

As discussed earlier, one of the pressurized cold bend pipe specimens of *Sen* (2006) tested at the University of Alberta unexpectedly ruptured on the tensile side of the buckled region while under the increased monotonic curvature along the post-buckling loading path (Figure 1-3). This pipe had the D/t ratio of 93 and was made of steel grade X65 with Y/T ratio of 94%. The rupture occurred under an internal pressure corresponding to 80% of SMYS hoop stress and a monotonic increase of closing curvature. It should be noted that the effect of internal hydrostatic pressure on the confining end plates also created tensile axial stresses by approximately 32% of the SMYS. No rupture failure was observed for the similar specimen that was pressurized to the 80% of the SMYS. Figure 2-10 illustrates the fracture surface after the rupture. A small necking of pipe wall (reduced wall thickness) was observed at the tensile fibers of the cross-section where the fracture initiated. This observation shows the occurrence of ductile fracture in steel material on the tension side. As shown in Figure 2-10, the fracture surface was found to be fibrous which means that not a lot of voids nucleated before the fracture happened (Khoo 2000). Fracture surface propagated to the sides of the pipe and inclined with an angle of 45° from the longitudinal axis which can be interpreted as shear fracture mode.

Three quite similar failures have been reported in the literature for the buckled line pipes tested by JFE Steel Corporation in Japan. *Tajika* et al. (2011) tested two high-stain and one conventional line pipes under monotonically-increasing curvature while pressurized up to 60% of the SMYS as hoop stress. The tensile axial stress due to the internal pressure pushing against the end plates was about 27% of the SMYS. All three pipe specimens had the same geometry with the D/t ratio of 54 and were made of X80 steel grade. However, the Y/T ratio for the material of the high-strain pipes and the conventional pipe were roughly 83% and 90% respectively. It was found that the conventional pipe (with Y/T=90%) started to wrinkle at much lower curvature due to

the high value of *Y*/*T* ratio and finally ruptured on its tensile side close to the bulging buckle as depicted in Figure 2-11. Over 7% tensile strain was captured by strain gauges at the rupture.

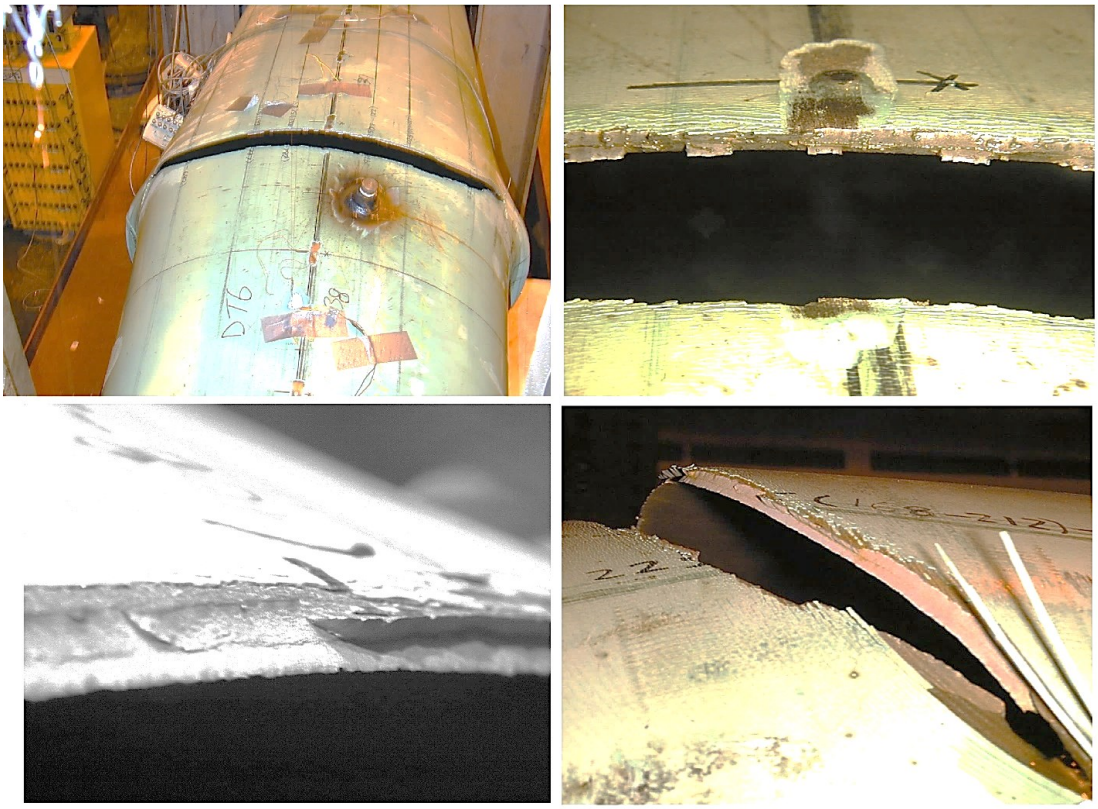

Figure 2-10: Necking in fibrous fracture surface and crack propagation (Sen 2006)

Igi et al. (2011) tested a girth-welded line pipe specimen of the same size and steel grade with *Y*/*T* equal to 80% and the *D*/*t* ratio of 55 under a constant internal pressure corresponding to 60% of the SMYS hoop stress and monotonically-increasing curvature. The initial intention was to study the tensile fracture of pressurized steel pipes due to weld flaws while subjected to bending curvature. Hence, a large artificial notch with the length of 80 mm and depth of 20% of wall thickness was introduced on the outer surface on the tensile side of girth weld's HAZ region, since it was known from previous studies (Igi et al. 2010) that the HAZ is more vulnerable to tensile fracture than weld material itself. It was found that after certain deformations, several small consecutive wrinkles formed in the vicinity of the girth weld showing a periodic

compressive strain. One of the wrinkles located about one wavelength (400 mm) far from the girth weld began to swell and finally an unexpected rupture occurred on the tensile side of the bulging wrinkle cross-section which not only did not have any initial defects but also was 400 mm away from the artificial notch and the HAZ (Figure 2-12). The crack growth from the artificial notch was propagated to 40% of the wall thickness but no rupture occurred at that location. Visual investigation of the fracture surface revealed that the fracture surface was fibrous and normal to the direction of bending stress on the tensile side of the cross-section and decreased wall thickness due to necking was observed in this region. The shear fracture was the case of failure by propagation of fracture surface towards bending neutral axis.

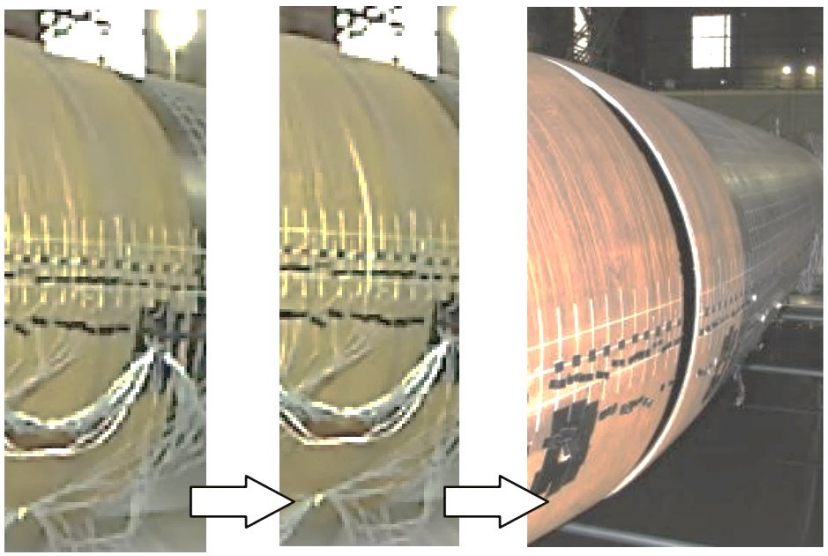

Figure 2-11: Tensile fracture of conventional line pipe at wrinkle location (Tajika et al. 2011)

Tajika and Suzuki (2009) tested three line pipe specimens with D/t ratio of 32 and made of X65 steel grade with Y/T ratio of 88%. The specimens were tested under increasing curvature while being pressurized by three different internal pressure rates equal to 40%, 60%, and 66% of the yield pressure which also created tensile axial stress equal to 17%, 25%, and 28% of the SMYS respectively (since the internal pressure pushing against the end plates at both ends of the pipes). It was found that the specimen with the highest rate of internal pressure, and accordingly axial tensile load, failed in rupture

on the opposite side of the buckled area (Figure 2-13) while experiencing post-buckling deformations. Excessive distortion of the buckled cross-section without any leakage was reported as the failure mode of the other two specimens which had the lower rate of internal pressure and axial stress.

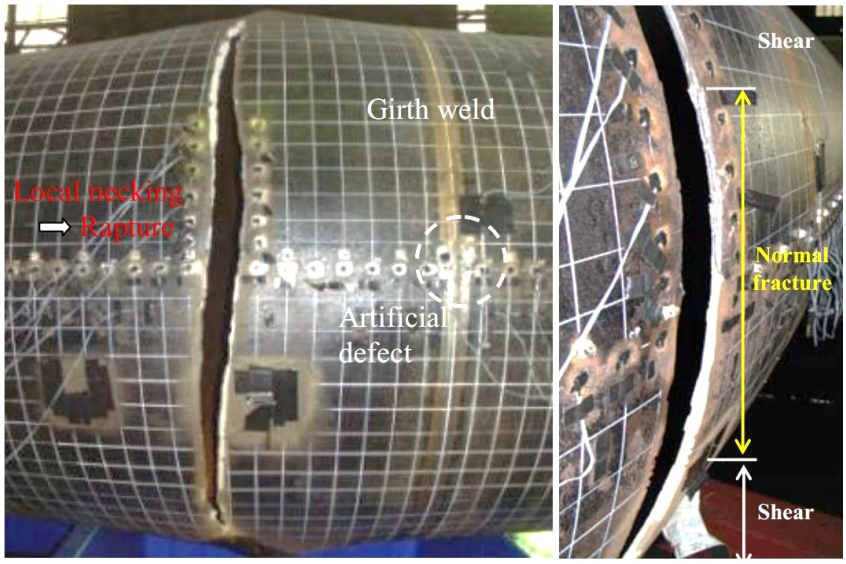

Figure 2-12: Tensile fracture of notched girth-welded line pipe at wrinkled cross-section away from the artificial notch (Igi et al. 2011)

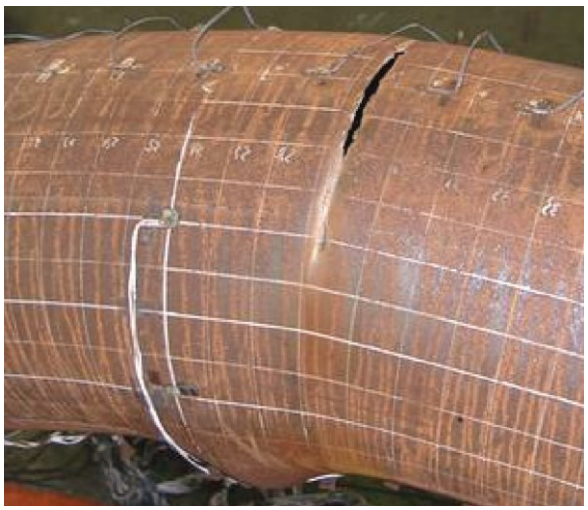

Figure 2-13: Rupture of the pressurized pipe on the tensile side of the buckled region (Tajika and Suzuki 2009)

Mitsuya et al. (2008; 2013; 2015) conducted experimental research on pressurized cold bend pipes under both closing and opening monotonic curvature to study the rupture limit state of the buried pipelines due to liquefaction. The specimens were made of X80 steel grade with the Y/T ratio of around 90% and had the average D/t ratio of 35 (material stress-strain curve and wall thickness were quite different on intrados and extrados sides due to large cold bend action). The hydrostatic internal pressure was imposed in the pipes to develop a constant hoop stress equal to 40% of SMYS during the test which also developed axial tensile load equal to 15% of the yield load. Under opening curvature, a bulging wrinkle was developed on the extrados of the cold bend specimen (with a central bend angle of 45°), where the bend and straight segments meet, and a rupture occurred on the intrados of bend exactly on the opposite side of the wrinkle, as shown in Figure 2-14. High wall thickness reduction (more than 57%) was observed at the rupture location due to strain localizations and necking.

Figure 2-14: Rupture of pressurized cold bend pipe on tensile side of the wrinkled location under opening curvature (Mitsuya et al. 2008)

2.6 Summary

Studies on the CBS of steel pipelines show that,

1) the simply-supported boundary condition is the critical boundary conditions for CBS;

2) not only does the internal pressure change the shape of the buckle and the post-buckling behavior of the steel pipes, but also an increase of internal pressure significantly reduces the CBS;

3) the increase of D/t and Y/T ratios considerably decreases the CBS;

Also, it was learnt from the literature review on the rupture strain that,

1) the equivalent plastic strain to fracture is decreased by the growth of triaxial stress condition and can be used to predict the fracture initiation at the crack tip;

2) the higher Y/T ratio precipitates the plastic strain localization and decreases the rupture strain;

3) the higher the internal pressure, results in the lower the rupture limit.

And more importantly, in case of the rupture of the wrinkled pipes, it was discovered that,

1) the rupture strain limits that have been developed for the weld defects are unlikely to be the failure mode for the pressurized wrinkled pipes under monotonically increased curvature;

2) rupture of the wrinkled pipes only occurs due to strain reversal and LCF;

3) rupture normally will not occur under monotonic loading, except the tearing failure due to low internal pressure and fixed boundary conditions;

3) the increase of internal pressure, tensile stress, and Y/T ratio precipitate the rupture of buckled pipelines on the tension side.

4) necking occurs before the rupture of pipe wall on the tension side which represents the occurrence of ductile fracture phenomenon.

CHAPTER 3: BACKGROUND ON DUCTILE FRACTURE

3.1 Introduction

Current research investigates the post-buckling rupture of buried steel pipes under internal pressure and monotonically-increasing curvature. Study of the fracture surface revealed that the reduction of the wall or the so-called necking occurred on the tensile side of the local buckling area due to plastic strain localization which clearly indicates the ductile crack formation in the steel material that ultimately triggers the rupture. In this chapter, the ductile fracture phenomenon will be studied through a comprehensive review of well-established models and methodologies to comprehend the mechanism and prediction of macro-crack formation in steel material.

3.2 Ductile Fracture

Ductile fracture due to positive hydrostatic pressure loading condition involves void nucleation at the location of inclusions or second-phase particles, growth, and linkage due to large plastic deformations (necking) which eventually leads to form macro-cracks and the final fracture in the material matrix (Figure 3-1). Despite brittle fracture which is only dependent on the state of stress at fracture point, the whole history of stress state affects the void nucleation and growth in ductile fracture (McClintock 1968). *Rogers* (1960) found that the so-called cup-and-cone failure of the ductile materials in the necking region of tensile specimens is produced by increasing the coalescence of voids inside the material due to large plastic deformations which is influenced by triaxial stress condition.

Many theoretical models have been developed to predict the ductile fracture of metals in macro-scale due to various loading conditions and large deformations based on phenomenological studies of the nucleation, growth, and coalescence of assumed homogeneous cavities in the media of ductile material. Following sections introduce the most widely used ductile fracture models that have been verified and validated by experimental and numerical studies.

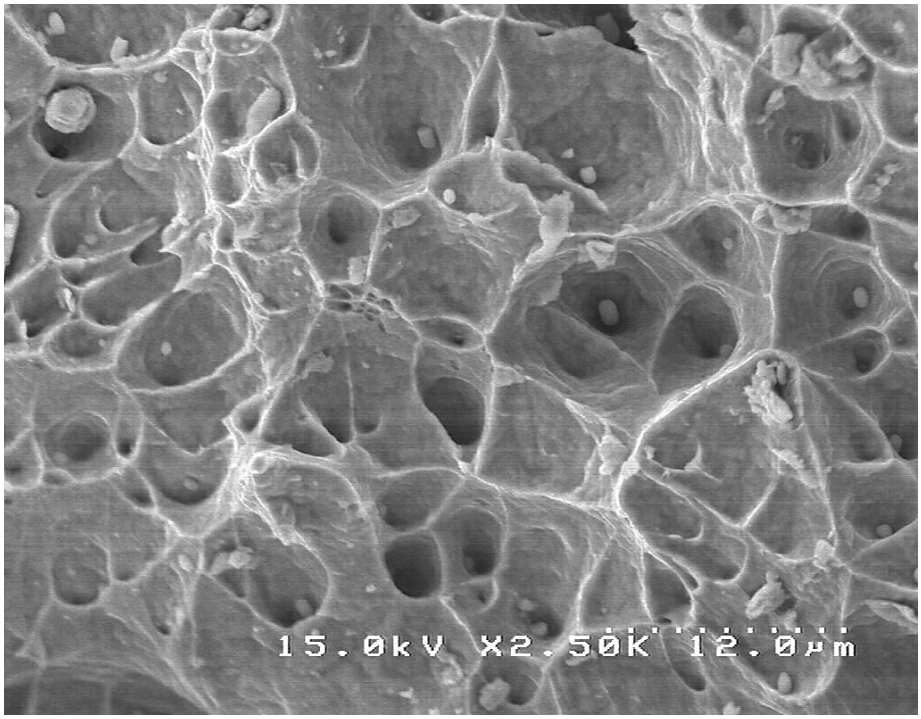

Figure 3-1: Scanning electron microscope (SEM) fractograph of microvoid nucleation originated from the small contaminants and coalescence in 304 Stainless Steel due to triaxial stress (Photography by Dr. James Wittig; provided with author's permission)

3.3 Void Growth Models

McClintock (1968) modeled the growth and coalescence of the voids by cylindrical holes which elliptical cross-section in a plastic incompressible media (Figure 3-2) and developed a criterion for the fracture of ductile materials. The material was assumed to contain three mutually perpendicular sets of holes, parallel to the axes of applied principal stresses which do not rotate relative to the material. The holes are considered to be in a cylindrical cell whose dimensions are of the order of the mean spacing between the holes and deform in-plane strain mode. In this case, fracture happens once the growth of the holes leads each hole to touch a pair of its cell walls. Hence, the relative growth factor is defined as

$$F_{ij} = \frac{b_j / l_j}{b_j^0 / l_j^0} \qquad (3\text{-}1)$$

in which, b_j and l_j are the current dimension of the elliptical hole and mean spacing between two parallel holes in the j^{th} direction of growth, respectively. The "0" superscript implies the initial condition. In fact, the fracture occurs once b_j/l_j=0.5.

To account for the stress-varying condition (history of stress), the following cumulative damage criterion was developed based on the relative growth factor definition so that fracture happens once the measure of damage accumulates to unity.

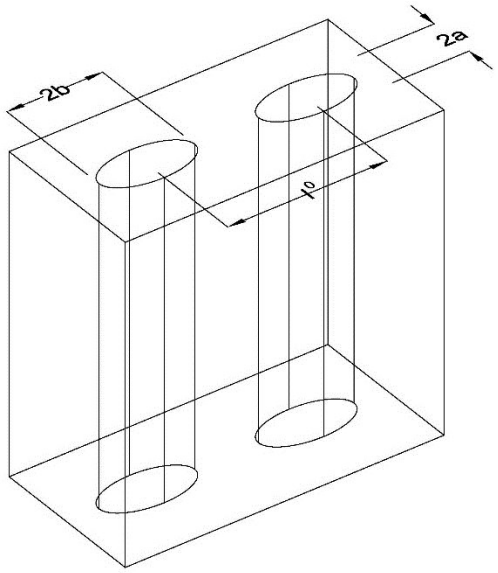

Figure 3-2: Cylindrical void growth model (McClintock 1968)

$$dC_{ij} = \frac{d\left(\ln F_{ij}\right)}{\ln F_{ij}^f} = \frac{d\left(\ln F_{ij}\right)}{\ln\left(\dfrac{0.5}{b_j^0 / l_j^0}\right)} \qquad (3\text{-}2)$$

where the "^{f}" superscript implies the final fracture condition. It was observed that the triaxial stress has a strong effect in decreasing the equivalent strain to fracture and exponentially correlates the damage growth to the state of stress as follows

$$dC_{ij} = \frac{1}{\ln F_{ij}^{f}}\left[\frac{\sqrt{3}}{2(1-n_I)}\sinh\left(\frac{\sqrt{3}(1-n_I)(\sigma_1+\sigma_2)}{2\bar{\sigma}}\right)+\frac{3(\sigma_1-\sigma_2)}{4\bar{\sigma}}\right]d\bar{\varepsilon} \qquad (3\text{-}3)$$

in which, n_I , is the hardening index (e.g. n_I=0 for non-hardening material; and, n_I=1 for linearly hardening material) to be defined from stress-strain graph by $n_I = \frac{\bar{\sigma}^{@\max(\bar{\varepsilon})}}{\left[\bar{\sigma}\right]^{upto\ \max(\bar{\varepsilon})}} - 1$. σ_1 and σ_2 are the major and minor principal stresses (in transverse directions of the holes) respectively, and, $\bar{\sigma}$ and $\bar{\varepsilon}$ are equivalent stress (Von Mises Stress) and equivalent strain which are determined as functions of principal stress ($\sigma_{1\sim3}$) and principal strain ($\varepsilon_{1\sim3}$) values as follows

$$\bar{\varepsilon} = \left\{\frac{2}{9}\left[(\varepsilon_1-\varepsilon_2)^2+(\varepsilon_2-\varepsilon_3)^2+(\varepsilon_3-\varepsilon_1)^2\right]\right\}^{\frac{1}{2}} \qquad (3\text{-}4)$$

$$\bar{\sigma} = \left\{\frac{1}{2}\left[(\sigma_1-\sigma_2)^2+(\sigma_2-\sigma_3)^2+(\sigma_3-\sigma_1)^2\right]\right\}^{\frac{1}{2}} = \sqrt{3J_{2D}} \qquad (3\text{-}5)$$

where J_{2D} denotes the second deviatoric stress invariant. It is noteworthy to restate Eq. (3-3) as follows

$$\int_0^{\bar{\varepsilon}_f}\left[\frac{\sqrt{3}}{2(1-n_I)}\sinh\left(\frac{\sqrt{3}(1-n_I)(\sigma_1+\sigma_2)}{2\bar{\sigma}}\right)+\frac{3(\sigma_1-\sigma_2)}{4\bar{\sigma}}\right]d\bar{\varepsilon} = \ln\left(\frac{0.5}{b_j^0/l_j^0}\right) \qquad (3\text{-}6)$$

in which, $\bar{\varepsilon}_f$ denotes the final equivalent strain at fracture.

Rice and Tracey (1969) studied the growth of spherical voids inside a non-hardening elastic-perfectly plastic and incompressible medium (Figure 3-3) subjected to a remote uniform stress and strain rate field. It was postulated that on a tensile remote field, the spherical voids symmetrically dilate when the hydrostatic stress is large. It was found that the dilatational amplification factor is exponentially increasing versus stress triaxiality. In this study, the obtained results for the tensile field were generalized for the compressive and shear fields by introducing the concept of equivalent strain quantity, and dilatational amplification factor (A_D) was formulated as follows

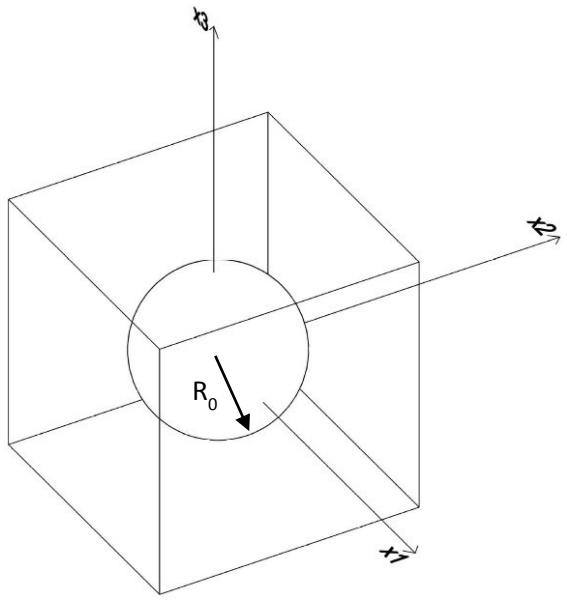

Figure 3-3: Spherical void growth model (Rice and Tracey 1969)

$$A_D = 0.558 \sinh\left(\frac{3}{2}\eta\right) + 0.008 \quad \nu_\theta \cosh\left(\frac{3}{2}\eta\right) \qquad (3\text{-}7)$$

in which, Lode variable, $\nu_\theta = -\frac{3\dot{\varepsilon}_2}{\dot{\varepsilon}_1 - \dot{\varepsilon}_3}$, is equal to -1, 0 and 1 for incompressible material in the cases of remote simple tension (load applied in one direction), shear and compression loads respectively. η denotes the stress triaxiality which incorporates the effect of the stress components through including the first and second deviatoric stress invariant (hydrostatic pressure and Von Mises stress). The stress triaxiality is given by Eq. (3-8). It is readily understood that the stress triaxiality increases by moving along the diagonal of principal stress spatial axes towards the direction illustrated in Figure 3-4.

$$\eta = \frac{\sigma_m}{\bar{\sigma}} \qquad (3\text{-}8)$$

in which, hydrostatic stress, σ_m, is obtained from

$$\sigma_m = \frac{\sigma_1 + \sigma_2 + \sigma_3}{3} = \frac{I_1}{3} = \frac{J_{1D}}{3} \qquad (3\text{-}9)$$

where, I_1 and J_{1D} are the first stress invariant and first deviatoric stress invariant, respectively.

The results suggest that the fracture ductility sharply decreases with the increase of stress triaxiality. The physical interpretation of the dilatational amplification factor is described as

$$\frac{dR_0}{dt} = A_D R_0 \frac{d\bar{\varepsilon}}{dt} \qquad (3\text{-}10)$$

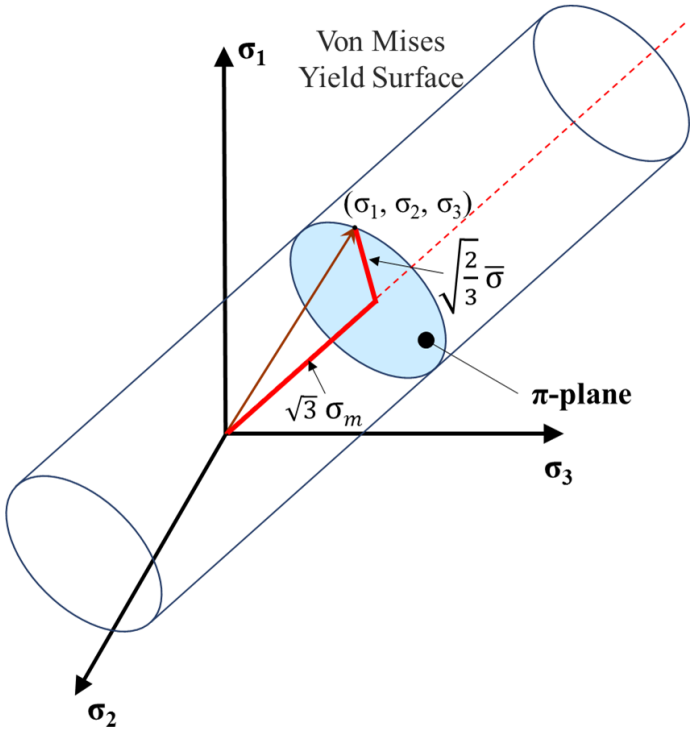

Figure 3-4: The hydrostatic pressure and equivalent stress in principal stress space

where R_0 is the initial spherical void radii. From this equation, it is revealed that dilatational amplification factor is equal to the inverse of the equivalent strain. By integrating Eq. (3-10) up to the fracture point, fracture criterion could be rewritten as

$$\int_0^{\bar{\varepsilon}_f} A_D R_0 d\bar{\varepsilon} = R_f - R_0 \qquad (3\text{-}11)$$

In void growth models, it is assumed that the ductile fracture occurs once the surface of adjacent (nucleated) voids meet each other due to the void growth. These studies show that the stress triaxiality and equivalent strain are the most determining factors in ductile fracture phenomenon. Paying attention to the essence of Eqs. (3-6) and (3-11) reveals that the crack formation phenomenon and ductile fracture in macro-scale could be stated by the following cumulative damage criterion which is dependent on the state of stress and change in the equivalent strain at each loading step.

$$\int_0^{\bar{\varepsilon}_f} g(\sigma_{ij}) d\bar{\varepsilon} = C \qquad (3\text{-}12)$$

where g is a weighting function, σ_{ij} represents the stress tensor components and C is a material property. A number of simple empirical ductile fracture criteria have been proposed in the form of Eq. (3-12) based on observations and simple assumptions (Bao 2003; Bao and Wierzbicki 2004a). A comparative study of some of these models and the presented void growth models in predicting fracture of 2024-T351 aluminum alloy obtained from experiments shows that most of the empirical models fail to acceptably predict the ductile fracture under both positive and negative hydrostatic pressure (tensile and compression) loading conditions. Although McClintock and Rice-Tracey criteria give a fairly good prediction for the tensile tests, however, they fail to predict the fracture under negative stress triaxialities. This is quite comprehensible since the void growth models were developed based on the mechanism of crack formation due to the tensile field (Bao 2003; Bao and Wierzbicki 2004a).

3.4 Fracture Strain Models

Dividing Eq. (3-12) by the material constant C gives the ductile fracture criterion as (Bao 2003)

$$\int_0^{\bar{\varepsilon}_f} f(\sigma_{ij}) d\bar{\varepsilon} = 1 \qquad (3\text{-}13)$$

Herein, the ductile crack initiates when this integral value accumulates to unity. The weighting function that makes the integral equal to unity could be readily stated as $f(\sigma_{ij}) = 1/\bar{\varepsilon}_f(\sigma_{ij})$ (Bao 2003). *Johnson* (1980) proposed the following cumulative damage criterion

$$\int_0^{\bar{\varepsilon}_f^p} \frac{d\bar{\varepsilon}^p}{\bar{\varepsilon}_f^p} = 1 \qquad (3\text{-}14)$$

in which, $\bar{\varepsilon}^p$ is the equivalent plastic strain and $\bar{\varepsilon}_f^p$ refers to the final equivalent plastic strain at fracture. Now, the problem is simply reduced to finding the fracture toughness in the form of equivalent strain as a function of stress components.

Johnson and Cook (1985) used the strength model for large deformations and high-temperature conditions and postulated that for the stress triaxialities less than 1.5, the equivalent plastic strain to fracture could be related to the stress triaxiality, equivalent plastic strain rate ($\dot{\bar{\varepsilon}}^p$) and homologous temperature (T_m) as follows

$$\bar{\varepsilon}_f^p = \left[D_1 + D_2 \exp\left(D_3 \eta\right)\right]\left[1 + D_4 \ln\left(\dot{\bar{\varepsilon}}^p\right)\right]\left[1 + D_5 T_m\right] \qquad (3\text{-}15)$$

where $D_{1\sim5}$ are five material constants. Considering a static loading condition and neglecting the effect of temperature ($D_4 = D_5 = 0$), Eq. (3-15) reduces to the first bracket. In this case, the fracture strain is an exponential function of stress triaxiality as shown in Figure 3-5. The other three constants ($D_{1\sim3}$) were calibrated using notched tensile bar tests plus torsion test for three different metals (Johnson and Cook 1985).

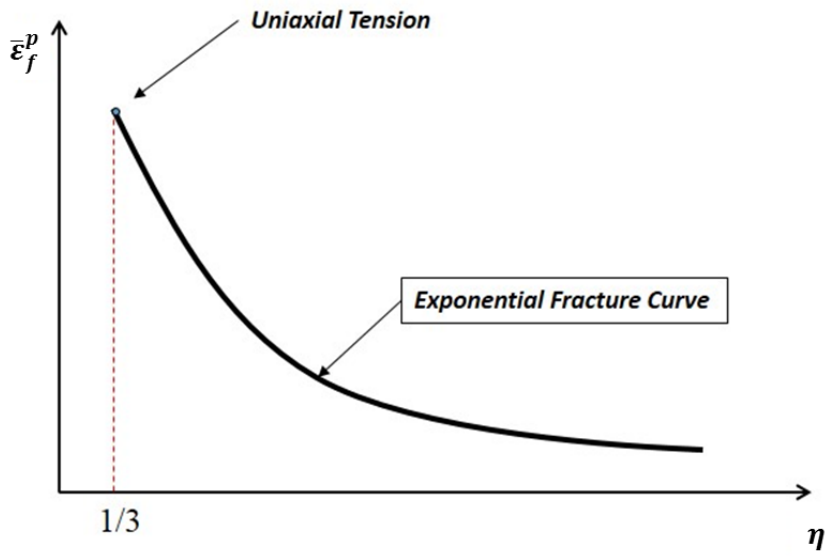

Figure 3-5: Schematic view of fracture toughness in the form of equivalent plastic strain to fracture as a function of stress triaxiality

Bao and Wierzbicki (2003; 2004b) carried out a series of fracture tests on 2024-T351 aluminum to find a correlation between a wide range of stress triaxiality and equivalent strain to fracture. Upsetting compression tests were carried out on cylindrical specimens designed with various height to study the fracture strain in the range of negative stress triaxiality. Shear specimens were designed and examined to achieve results for fracture due to very small (around zero) stress triaxialities. To obtain the results for a range of high stress triaxiality (higher hydrostatic pressure), smooth and circumferentially notched round bars were tested under tension. A hybrid method was used by engaging parallel FEA to recreate the test results and obtain equivalent fracture strain for all experiments. It was demonstrated that the equivalent strain to fracture is a function of stress triaxiality and there are three entirely distinct branches of this function with possible slope discontinuities in the transition regions (Bao 2003) as shown in Figure 3-6. From this plot, it can be understood that a cut-off triaxiality value of -1/3 was found under which no fracture will be initiated (from upsetting tests) and the equivalent crack initiation strain tends to infinity. Also, once the triaxiality is high (NRB tests) the equivalent crack formation strain is exponentially decreasing. It was postulated that there are two types of ductile crack formation namely “shear fracture”

that occurs in the cases of negative triaxialities, and "void nucleation, growth, and linkage" that is developed in the high triaxial stress conditions. There is a transition zone in which a combination of these two scenarios will happen (Bao 2003).

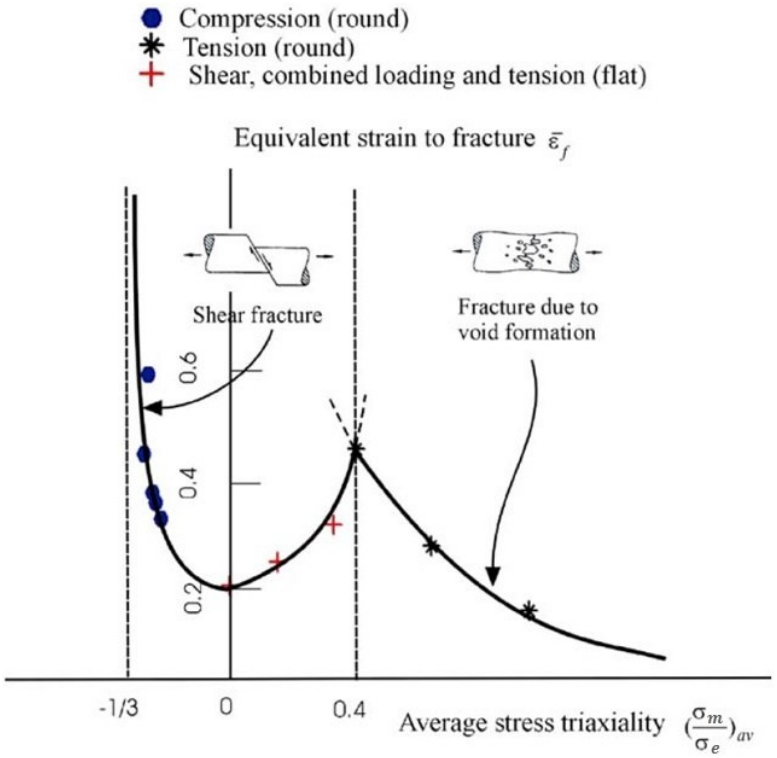

Figure 3-6: Fracture locus in equivalent strain and stress triaxiality plane (Bao and Wierzbicki 2004b)

Wilkins et al. (1980) postulated that not only is the fracture strain a function of stress triaxiality, but the maximum deviatoric stress ratio could also affect the final strain to fracture. This is associated with the change in the so-called Lode angle parameter (Xue 2007a; Xue 2007b) which is defined as the angle between the position vector of the state of stress and the maximum principal stress axes on π-plane as shown in Figure 3-7. A physical perception could be achieved by saying that the equivalent strain to fracture is affected by hydrostatic pressure and also by the type of loading scenario, e.g. uniaxial/biaxial tension or compression, shear, plane strain, plane stress, etc.

(Figure 3-8). Lode angle is a function of the normalized third deviatoric stress invariant (ξ) and can be obtained from the following formula

$$\theta = \frac{1}{3}\arccos(\xi), \qquad 0° \le \theta \le 60° \tag{3-16}$$

where

$$\xi = \frac{27}{2}\frac{J_{3D}}{\bar{\sigma}^3} = \frac{3\sqrt{3}}{2}\frac{J_{3D}}{J_{2D}^{3/2}}, \qquad -1 \le \xi \le 1 \tag{3-17}$$

in which, J_{3D} is the third deviatoric stress invariant as follows

$$J_{3D} = (\sigma_1 - \sigma_m)(\sigma_2 - \sigma_m)(\sigma_3 - \sigma_m) \tag{3-18}$$

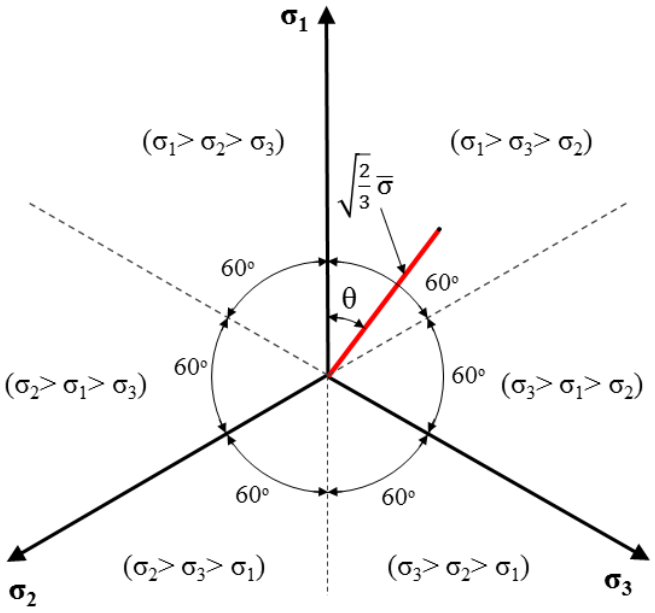

Figure 3-7: Lode angle definition on π-plane

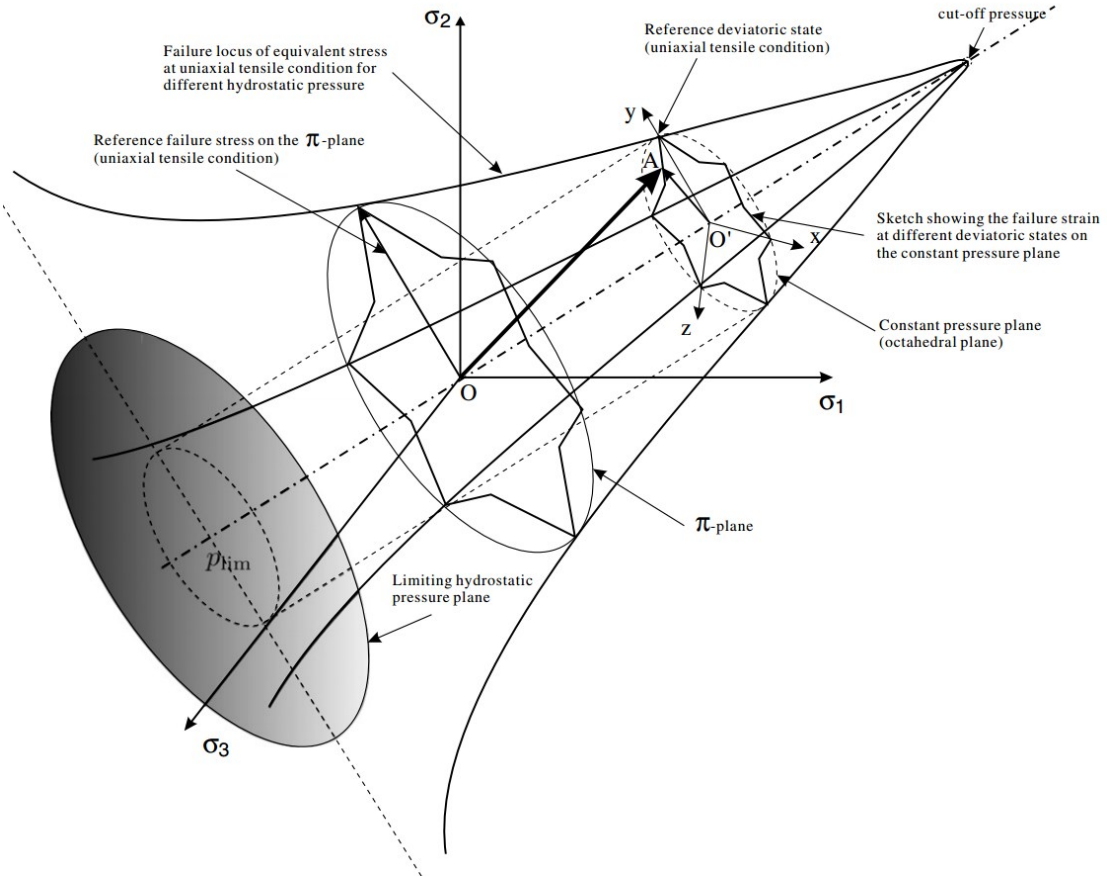

Figure 3-8: Effect of stress triaxiality and Lode angle on fracture envelope (Xue 2007a)

Xue (2007b) conducted tests on a set of smooth and notched round bars, compression cylinders, flat grooved plates and three-point bending specimens made of Aluminum alloy 2024-T351 and studied the effect of stress triaxiality and Lode angle on fracture strain. *Wierzbicki et al.* (2005; 2005b) assumed that the fracture strain is a symmetric and concave function of Lode angle and a family of elliptic functions was used to model the change of fracture strain versus Lode angle parameter. The following envelope for equivalent strain to fracture was proposed as a function of stress triaxiality and the normalized third invariant as

$$\bar{\varepsilon}_f(\eta,\xi) = \bar{\varepsilon}_f^{(\xi=1)} - \left(\bar{\varepsilon}_f^{(\xi=1)} - \bar{\varepsilon}_f^{(\xi=0)}\right)\left[1-\xi^k\right]^{\left(1/k\right)} \qquad (3\text{-}19)$$

in which, $\bar{\varepsilon}_f^{(\xi=1)}$ and $\bar{\varepsilon}_f^{(\xi=0)}$ are the fracture strain as an exponential function of stress triaxiality corresponding to ξ=1 (tensile test of smooth and notched round bars) and ξ=0 (shear test or tensile test of plane strain grooved plates) loading conditions, respectively. *k* is the shape constant that adjusts the rate of fracture strain dependence on Lode angle.

Bai and Wierzbicki (2007; 2008) studied the fracture locus obtained by *Bao and Wierzbicki* (2003; 2004b) in three-dimensional space of fracture strain, stress triaxiality, and Lode angle, and postulated that the fracture envelope for some materials can be asymmetric with respect to the Lode angle parameter. Tests were carried out on a set of smooth and notched round bars, compression cylinders, and grooved plates made of Aluminum alloy 2024-T351 and the following asymmetric fracture envelope was proposed

$$\bar{\varepsilon}_f\left(\eta,\bar{\theta}\right)=\left[\frac{1}{2}\left(\bar{\varepsilon}_f^{(\xi=1)}+\bar{\varepsilon}_f^{(\xi=-1)}\right)-\bar{\varepsilon}_f^{(\xi=0)}\right]\bar{\theta}^2+\frac{1}{2}\left(\bar{\varepsilon}_f^{(\xi=1)}-\bar{\varepsilon}_f^{(\xi=-1)}\right)\bar{\theta}+\bar{\varepsilon}_f^{(\xi=0)} \qquad (3\text{-}20)$$

in which, $\bar{\varepsilon}_f^{(\xi=-1)}$ is the lower band of fracture strain as an exponential function of stress triaxiality corresponding to ξ=-1 obtained from compression cylinder tests and/or equi-biaxial tension tests. $\bar{\theta}$ denotes the Lode angle parameter (normalized Lode angle) and defined as

$$\bar{\theta}=1-\frac{6\theta}{\pi},\qquad -1\le\bar{\theta}\le 1 \qquad (3\text{-}21)$$

Butterfly-shaped specimens (Wierzbicki et al. 2005b) made of A710 steel material were also tested as an alternative method for classical tensile, shear and compressive tests to calibrate the proposed asymmetric model. Figure 3-9 compares the symmetric and asymmetric fracture envelope proposed by *Xue* and *Bai*.

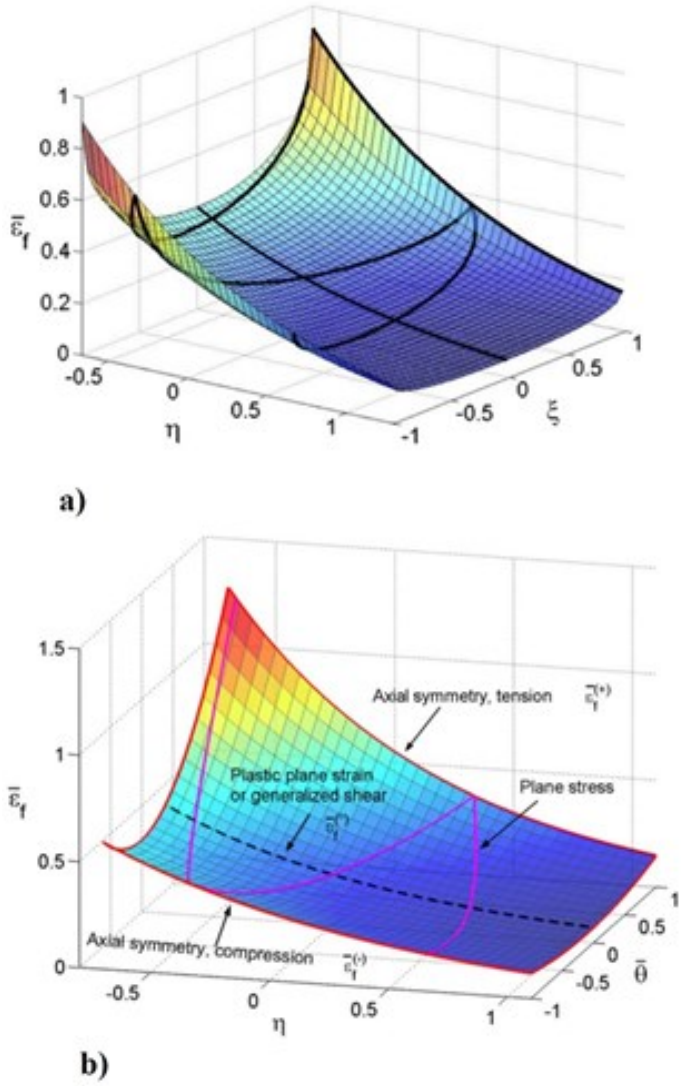

Figure 3-9: Comparison between symmetric and asymmetric fracture surfaces (Bai and Wierzbicki 2008)

a) *Xue*'s symmetric model; b) *Bai*'s asymmetric model

Gao and Kim (2006) studied the void-containing RMV (representative material volume) in FE analysis simulation (Faleskog et al. 1998; Gao et al. 1998) and postulated that the fracture surface of the 2024-T3 aluminum alloy is an asymmetric function of the stress triaxiality and Lode angle parameters. It was found that these two parameters characterize the void growth and linkage in the RMV due to macroscopic state of stress.

Bai and Wierzbicki (2007; 2010) postulated that the *Mohr-Coulomb* (M-C) fracture criterion, which is widely used for prediction of the failure in soil and rock, can be rearranged and related to stress triaxiality and Lode angle. The M-C fracture criterion reformulated as a function of stress triaxiality and Lode parameter is as follows

$$\bar{\varepsilon}_f\left(\eta,\bar{\theta}\right)= \left\{\frac{A}{c_2}\left[c_3+\frac{\sqrt{3}}{2-\sqrt{3}}\left(c_\theta^{ax}-c_3\right)\left(\sec\left(\frac{\bar{\theta}\pi}{6}\right)-1\right)\right]\left[\frac{\sqrt{1+c_1^2}}{3}\cos\left(\frac{\bar{\theta}\pi}{6}\right)+c_1\left(\eta+\frac{1}{3}\sin\left(\frac{\bar{\theta}\pi}{6}\right)\right)\right]\right\}^{-\frac{1}{n}} \quad (3\text{-}22)$$

in which, A and n are material constant and strain-hardening parameters in power law relation for calibration of plasticity in stress and strain which is defined as

$$\bar{\sigma}=A\bar{\varepsilon}^n \quad (3\text{-}23)$$

and, c_θ^{ax} constant is defined as

$$c_\theta^{ax}=\begin{cases}c_4 & for\ \bar{\theta}<0\\ 1 & for\ \bar{\theta}\geq 0\end{cases} \quad (3\text{-}24)$$

$c_{1\sim4}$ are the M-C fracture criterion constants mostly affecting hydrostatic pressure dependence, the general height of fracture envelope, Lode dependence, and asymmetry of the fracture surface respectively. These constants need to be calibrated from test results. This M-C fracture envelope calibrated and validated by test results on 2024-T351 Aluminum and TRIP690 high strength steel. M-C criterion introduces an asymmetric fracture surface with respect to Lode angle parameter. It was postulated that M-C model predicts the exponential decrease of material ductility with an increase

of stress triaxiality and also predicts the Lode angle dependence of the fracture strain by a family of parabolic functions.

3.5 Damage Mechanic Model

The equations of continuum damage mechanic were developed to predict the progressive failure of material due to continuous degradation. These equations include variables that are continuously related to the density of the micro-scale defects in the material to predict fracture occurrence due to the initiation and growth of macro-cracks (Zhang and Cai 2010). *Lemaitre* (Lemaitre 1984; Lemaitre 1985; Lemaitre 1992) assumed that the voids in a ductile material are equally distributed in all directions and developed an evolutionary ductile damage criterion by introducing an isotropic damage variable. The damage variable is defined as the area of voids per unit surface under the traction force as

$$D_d = \frac{S - \widetilde{S}}{S} \qquad (3\text{-}25)$$

where S and $\widetilde{S}$ denote the gross section area and the effective resisting area respectively. The non-damaged condition is associated with D_d=0 and rupture occurs when D_d=1. In this case, the effective stress ($\widetilde{\sigma}$) experienced by the damaged matrix is defined as

$$\widetilde{\sigma} = \frac{\sigma}{1 - D_d} \qquad (3\text{-}26)$$

in which, σ is the nominal stress. It is assumed that the strain modification is only dealt with by replacing the effective stress for nominal stress in the constitutive equations e.g. for the case of one-dimensional linear elasticity (infinitesimal strains), the nominal

strain is calculated from $\varepsilon = \sigma/(1-D_d)E$. Thus, it can be interpreted that damage variable progressively degrades the stiffness of the material.

Using the damage potential function and *Ramberg-Osgood* material hardening law, the damage evolution is given as

$$dD_d = \frac{D_{dc}}{\varepsilon_R - \varepsilon_D}\left[\frac{2}{3}(1+\upsilon)+3(1-2\upsilon)\eta^2\right]\bar{\varepsilon}^{\frac{2}{n_{RO}}}d\bar{\varepsilon} \qquad (3\text{-}27)$$

in which, n_{RO} is the hardening constant in the *Ramberg-Osgood* model, υ is Poisson's ratio, and D_{dc} denotes to the critical damage variable at which the macro-crack initiates. ε_D is the damage threshold strain below which the damage evolution is zero (D_d=dD_d=0), and, ε_R is the fracture strain in correspondence with the critical damage variable (D_d=D_{dc}) to be defined using the uniaxial test. Considering spherical and uniformly distributed voids, *Khoo* (2000) assumed that void nucleation and void growth both involve dilation in the material and developed a modified damage limit as a function of hydrostatic pressure based on the continuum damage mechanics law to predict the ductile fracture of steel. In this model, material dilation is assumed to be a function of the state of stress. Parameters used in this model can be calibrated from the uniaxial tensile test.

3.6 Porous Plasticity Model

Modeling a ductile material as a homogenous porous media, *Gurson* (1975; 1977a; 1977b) developed an associated flow rule and proposed a plasticity model which is dependent on the hydrostatic pressure and void volume fraction. This plasticity model was modified by the *Tvergaard* (1981; 1982a; 1982b), and *Tvergaard and Needleman* (1984) which is known as the GTN model. In this model, the void volume fraction (the volume of porosity) is increased under the applied stress due to the nucleation of new voids and the growth of the existing voids. The void nucleation is the material property, however, the void growth increases by the increase of the volumetric plastic strain. The

final failure of material is predicted by the final void volume fraction which is a material property. The most demanding task in the application of the GTN model is that there are almost nine different parameters that are required to be calibrated for a given material. Whereas, no solid approach has been introduced for calibrating each individual parameter. The derivation and formulations of the porous plasticity model and research works on its calibration are studied in Appendix A.

3.7 Summary

Study of the ductile fracture phenomenon in metals shows that the ductile crack formation is a function of the state and history of the stress field and is progressively precipitated by the increase of equivalent plastic strain. It has been shown that the increase of hydrostatic pressure (or the first stress invariant) exponentially decreases the fracture strain. The type of stress field (weather it is tensile/compressive uniaxial/biaxial, etc.) could also affect the fracture strain which can be correlated to the second and third deviatoric stress (or Lode angle parameter).

Ductile fracture toughness can be expressed as the equivalent fracture strain which is a function of stress triaxiality and Lode angle parameter. Theoretical and experimental studies indicate that the initiation of ductile fracture could be predicted by cumulatively integrating the inverse of equivalent fracture strain over the increase of equivalent strain until unity is reached.

CHAPTER 4: FRACTURE EXPERIMENTS AND MATERIAL MODEL

4.1 Introduction

Looking at the ultimate failure of a structure always demands a reasonably validated approach to predict and capture the final collapse due to the applicable loading scenario. Mechanical properties, plasticity, ductility, and failure mechanism of the material shall be carefully determined from appropriate test results for the safe design of the steel pipelines. Buried pipelines are normally subjected to internal pressure and large deformations due to ground movements which can develop hoop and axial stresses in the pipe wall. This biaxial stress condition may apply a high triaxial stress (hydrostatic pressure) and cause premature rupture. Therefore, to deal with the rupture of buckled pipes, a suitable fracture model needs to be used which accounts for both stress triaxiality and biaxial stress condition to predict the onset of ductile fracture.

Fracture strain model (surface of fracture strain) in conjunction with the cumulative damage criterion (Section 3.4) is used in the current study because of its solid theoretical background (Section 3.3), good agreement with experimental data for monotonic loading (Bao 2003; Bao and Wierzbicki 2004a; Bai 2007), being uncoupled from constitutive law, being compatible with well-established von Mises plasticity model and isotropic hardening, ease of calibration (Wierzbicki et al. 2005b; Bai and Wierzbicki 2008), and applicability to engineering problems (Bao 2003; Lee 2005). Moreover, fracture strain model is capable of accounting for the effect and history of hydrostatic pressure and biaxial stress field in the pipe wall.

In this chapter, the description of material tests on API X65 steel grade is provided. The effect of stress triaxiality and Lode angle parameters on the fracture strain envelope (ductile fracture toughness) is experimentally studied through conducting tension tests on a set of smooth and notched round bars as well as flat grooved plane strain plates with various notch radii. Afterward, material plasticity is calibrated by using the experimental data from standard material test and incorporated into parallel FEA of the experiments. A hybrid experimental-numerical method is used to find the ductile

fracture toughness in the form of equivalent plastic strain to fracture which will be dependent on both stress triaxiality and Lode angle.

4.2 Test Variables and Methodology

The theoretical and experimental studies show that stress triaxiality is a key parameter in controlling the magnitude of the fracture strain for ductile metals. Notched round bar specimens are commonly used to quantify the dependence of the ductile fracture strain on stress triaxiality. *Oh et al.* (2007a; 2007b) conducted a series of tensile tests on smooth and NRBs with various notch radii (to develop stress triaxiality between 0.5 to 1.5) and used parallel FEA of experiments to calibrate the parameters of *Johnson-Cook* model given by Eq. (3-15) for API X65 steel grade. In this study, the equivalent plastic strain to fracture is given as an exponential function of stress triaxiality as follows

$$\bar{\varepsilon}_f^p = 3.29\exp\left[-1.54\eta\right] + 0.1 \qquad (4\text{-}1)$$

In addition to the stress triaxiality, it has been postulated that the normalized third stress invariant (i.e. Lode angle) can also affect the fracture strain by bringing the effect of different types of loading condition into account. In this case, fracture locus is a surface in the space of fracture strain, stress triaxiality and third stress invariant (or Lode angle) and various kinds of experiments are required to be tested to achieve different parts of this surface as shown in Figure 4-1 (Bai and Wierzbicki 2008). As mentioned in the earlier chapter, alternatively, butterfly-shaped specimens could be tested under tension at different angles to accommodate the Lode dependence of fracture locus (Wierzbicki et al. 2005a; Bai and Wierzbicki 2008).

Experimental results show that the fracture strain of DH36 steel is independent of the Lode angle (Bai 2007; Bai et al. 2009). However, A710 steel (Bai and Wierzbicki 2008) and 1045 steel (Bai et al. 2009) materials show asymmetric fracture locus with respect to the Lode angle. *Kofiani* (2013) conducted a series of different tests on various types of specimens including tensile tests on NRBs (ξ=1 & high η), tensile tests on notched

flat plates (ξ=1 & low η), tensile tests on butterfly-shaped specimens that is associated with plane strain condition (ξ=0 & η=1/√3), tensile tests on flat plates with central hole (ξ=0 & η=1/3), and punch tests on circular disk specimens that is associated with equi-biaxial tension condition (ξ=-1 & η=2/3), to study the plasticity and fracture strain envelope of API X100 (Kofiani et al. 2012) and API X70 (Kofiani et al. 2013) pipeline steel materials. All tests were modeled by parallel FE simulations and the M-C fracture criterion defined by Eq. (3-22) was calibrated using an inverse curve fitting technique. Table 4-1 reports the obtained optimal parameter values of the power law and M-C equation for X100 and X70. The calibrated model successfully used in FEA to predict the fracture initiation of SENT tests.

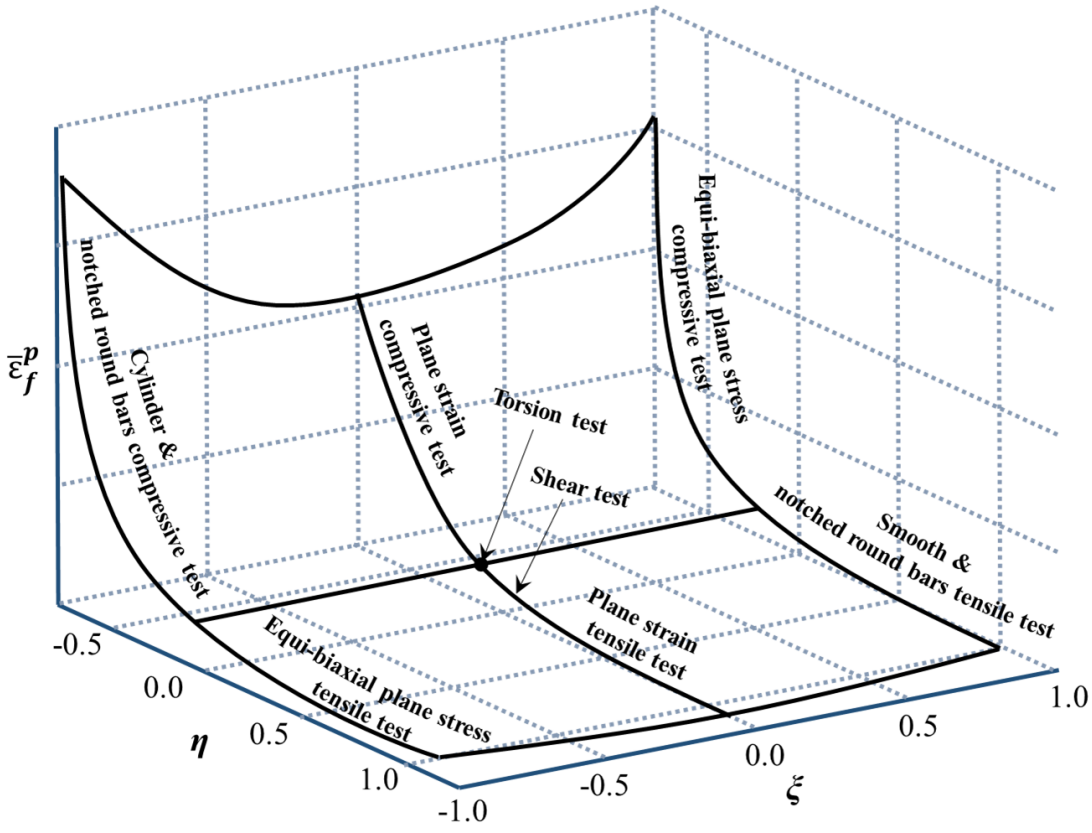

Figure 4-1: Schematic view of the fracture surface related to stress triaxiality and Lode angle parameters; and required tests to obtain fracture locus of different parts

Table 4-1: Values of the parameters of M-C model for X100 and X70 steel grades (Kofiani 2013)

Steel Grade	A	n	c_1	c_2	c_3	c_4
	Power Law Constants		-	[MPa]	-	-
API X100	1006.5	0.0384	0.029	535	0.9	1
API X70	844.6	0.0984	0.050	454	0.91	1

Attention to the values given in Table 4-1 reveals that the fracture strain for pipeline's steel is Lode dependent which is controlled by c_3 parameter. Also, it can be understood that the fracture surface is almost symmetric since the c_1 value is so close to zero and the c_4 parameter, which adjusts the asymmetry of the surface, was initially set to unity (Bai and Wierzbicki 2010). This matter was also double checked by comparing the fracture locus at ξ equal to -1 and 1 for both materials. It was found that the fracture strain was slightly higher at ξ=-1 (this can be also due to ignoring the c_4 in curve fitting process and setting it to unity).

In the current research, the fracture locus for pipeline steel is assumed to be a function of stress triaxiality and Lode angle. By providing the above explanations, the fracture strain is assumed to be symmetric with respect to the Lode Angle. Thus, a set of smooth and notched round bars are designed and tested under axial tensile load to find the fracture locus on ξ=1 (zero Lode angle). The various ratios of notch radius to the ligament diameter (the diameter at the most reduced cross-section) are designed to develop different hydrostatic pressure in the reduced area during the test. The higher the ratio, the lower the stress triaxiality. Similarly, a series of flat grooved plates with various ratio of notch radius to ligament thickness (the most reduced thickness) are designed to develop different stress triaxiality values in the plane strain loading condition i.e. ξ=0 (θ=30°). As the reduced thickness of the GP specimens is extremely smaller than the width, no strain is expected in the width direction under tension test.

Subsequently, parallel FE analyses of all experiments are conducted and load-deformation response of each simulation is verified to match that of the corresponding test. Through employing a hybrid experimental-numerical method, the equivalent

plastic strain to fracture for each specimen is obtained from the FE model right at the fracture point specified by the test. Therefore, the fracture locus on ξ equal to 0 and 1 are obtained for a variety of stress triaxialities. Considering a symmetric fracture surface, obtained results for ξ=1 are also assumed to conservatively serve for ξ=-1 (θ=60°); and M-C fracture surface is calibrated through solving an optimization problem.

4.3 Test Specimens

This section provides all the information about the material, design, and specifications of the test specimens used in the current experimental program.

4.3.1 Steel Grade and Specimen Cuts

All specimens were cut from an NPS30 seam-welded DSAW (Double Submerged Arc Welded) pipe joint provided to this research program by EVRAZ Inc. The outside diameter (D) and wall thickness (t) of the pipe were 762 mm and 11.5 mm respectively. Table 4-2 includes material test results on the yield strength (F_y) and tensile strength (F_u) of the pipe obtained from the mill certificate. The steel grade is recognized as either API-5L X65 (API-5L 2012), or CSA-Z245.1 GR448 (CSA-Z245.1 2014). Table 4-3 provides the chemical composition of the X65 material.

Table 4-2: Material strength obtained from mill certificate (EVRAZ Inc. 2015)

F_y [MPa]	F_u [MPa]	Y/T ($=F_y/F_y$) [%]
552	642	86.0

The general cross-sectional dimensions of the specimens were specified to fit in the thickness and curved cross-section of the pipe as illustrated in Figure 4-2a. Specimens were machined out of the mid-thickness of the pipe wall. Equally important to note that

all specimens were cut from a portion of the pipe which was deviated by 90° from the seam weld to exclude the Bauschinger's effect from material properties as much as possible (Figure 4-2b) which is caused by the UOE process of seam-welded pipe production.

Table 4-3: Chemical composition of the X65 steel material (EVRAZ Inc. 2015)

C	Mn	P	S	Si	Cu	Ni	Cr
0.08	1.50	0.011	0.002	0.27	0.02	0.02	0.02
V	**Nb**	**Ti**	**Al**	**B**	**N**	**Ca**	**C.E.**
0.01	0.06	0.014	0.020	0.001	0.003	0.0011	0.24

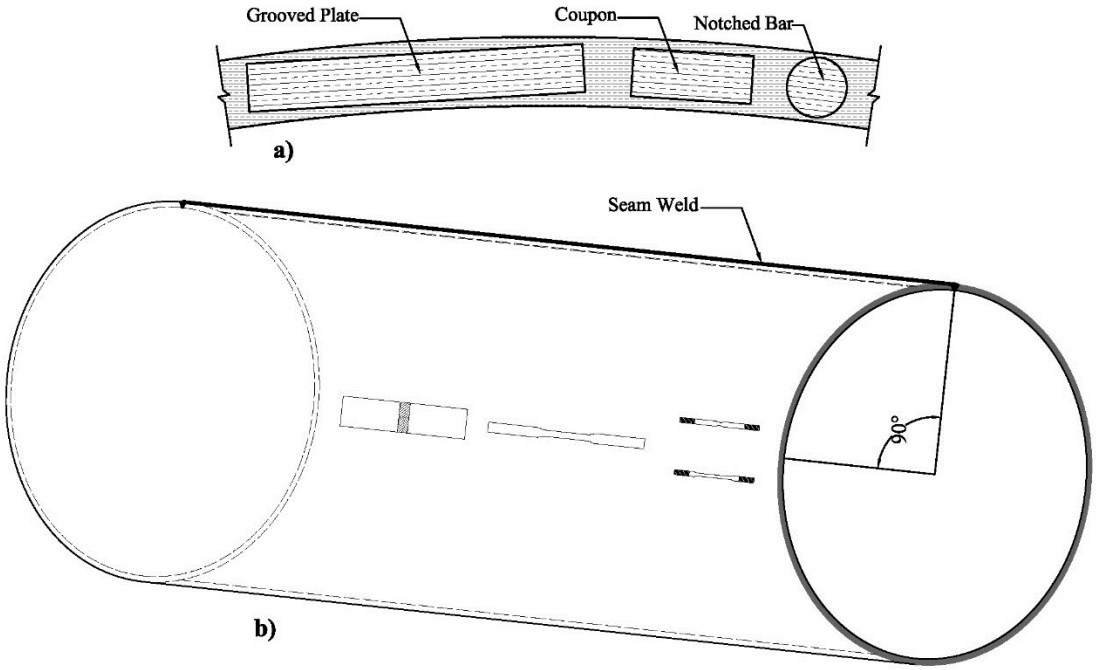

Figure 4-2: Specimens cut schema
a) Cross-sectional; b) Longitudinal

4.3.2 Coupon Specimens

Three standard flat dogbone coupon specimens were designed according to the ASTM-A370 standard specifications (ASTM-A370 2014) for the material tension test to calculate the mechanical properties and calibrate the plasticity of the material under examination. The detailed of a typical coupon specimen is shown in Figure 4-3.

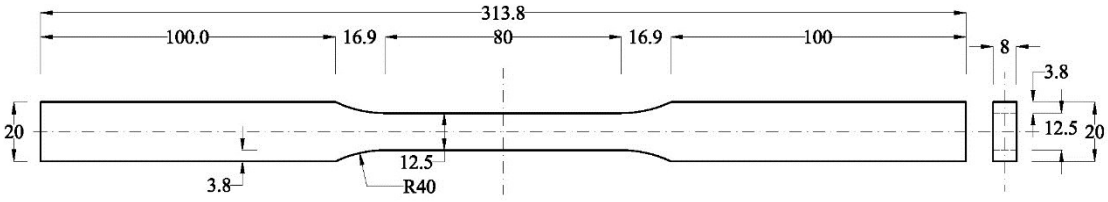

Figure 4-3: Details of the dogbone coupon specimens (all dimensions are in mm)

4.3.3 Round Bar Specimens

A series of smooth and notched round bars were designed to measure the degree of dependence of the fracture locus on the stress triaxiality in the ξ=1 plane. The smooth bar was designed according to the ASTM-A370 standard specifications (ASTM-A370 2014). Smooth bar specimen is assumed to simulate the uniaxial loading condition for which the stress triaxiality is equal to 1/3. Depending on the geometry of the notch, notched round bars are subjected to higher stress triaxialities due to superimposed tensile hydrostatic tension toward the center (Bao 2003) at the reduced cross-section.

Bridgman (1952) studied the stress field developed in the necked cross-section of the tensile round bars which exactly act like notched bars. From this study, the following formula can be derived to calculate the stress triaxiality at the center of the most reduced cross-section (Bao 2003) where the fracture is expected to be initiated from.

$$\eta = \frac{1}{3} + \ln\left(1 + \frac{r}{2R}\right) \qquad (4\text{-}2)$$

where R is the notch radius and r denotes the most reduced radius of the bar at notch root.

Bridgman's formula was further revised to accommodate the post-necking increase of stress triaxiality according to the FEA results and the following amplified formula was proposed to calculate the final stress triaxiality of the notched round bars (Bao 2003)

$$\eta = \frac{1}{3} + \sqrt{2}\ln\left(1 + \frac{r}{2R}\right) \qquad (4\text{-}3)$$

Keeping the radius of the cross-section at notch root constant (r=6), Eq. (4-3) was used to design the notch radius of the bars to cover a wide range of stress triaxiality (between 0.33 and 1). Table 4-4 includes the nominal notch dimensions and corresponding theoretical values of the stress triaxiality for the NRB specimens. Figure 4-4 indicates the details of round bar specimens. All round bars were threaded at both ends to be screwed in the fixtures that fit in the loading machine. Three units of each kind of specimens were prepared to be tested for back-up and validation purposes (Figure 4-5).

Table 4-4: Nominal notch dimensions of the RB specimens

Specimen	Reduced Radius (r) [mm]	Notch Radius (R) [mm]	Stress Triaxiality (η) Eq. (4-3) -	Third Normalized Invariant (ξ) -	Unit
SB	6.0	∞	0.33	1.0	3
NB25		25	0.49		3
NB10		10	0.70		3
NB5		5	1.00		3

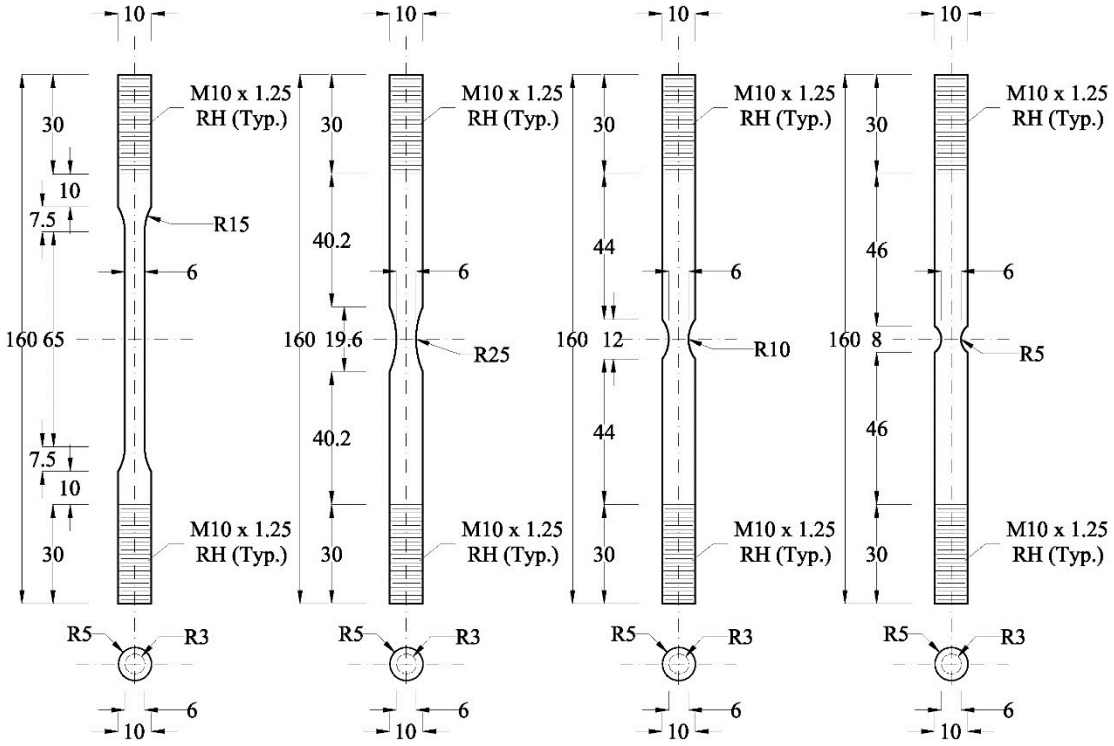

Figure 4-4: Details of NRB specimens with various notch geometry
(all dimensions are in mm)

Figure 4-5: Picture of NRB specimens machined out of the pipe wall

4.3.4 Grooved Plate Specimens

A set of flat grooved plate specimens were designed to explore the functionality of the fracture strain to stress triaxiality in the plane of ξ=0 which is associated with plane strain loading condition. The lower the ratio of notch radius to the reduced thickness, the higher the stress triaxiality.

Bai et al. (2007; 2009) obtained the following closed-form equation to calculate the stress triaxiality at the centroid of the reduced cross-section of the grooved plates as a function of notch geometry

$$\eta = \frac{\sqrt{3}}{3}\left[1 + 2\ln\left(1 + \frac{t_r}{4R}\right)\right] \qquad (4\text{-}4)$$

in which, t_r is the most reduced thickness of the GP. By setting the t_r of all specimens equal to the constant value of 2.6, notch radii of GPs were designed based on Eq. (4-4) to accommodate an adequate range of stress triaxialities (Table 4-5). Three units of each type of specimens were made to be tested. Figure 4-6 and Figure 4-7 illustrate the details and picture of GP specimens respectively.

Table 4-5: Nominal notch dimensions of the GP specimens

Specimen	Reduced Thickness (t_r) [mm]	Notch Radius (R) [mm]	Stress Triaxiality (η) Eq. (4-4) -	Third Normalized Invariant (ξ) -	Unit
GP40	2.6	40	0.60	0.0	3
GP20		20	0.61		3
GP8		8	0.67		3
GP4		4	0.75		3

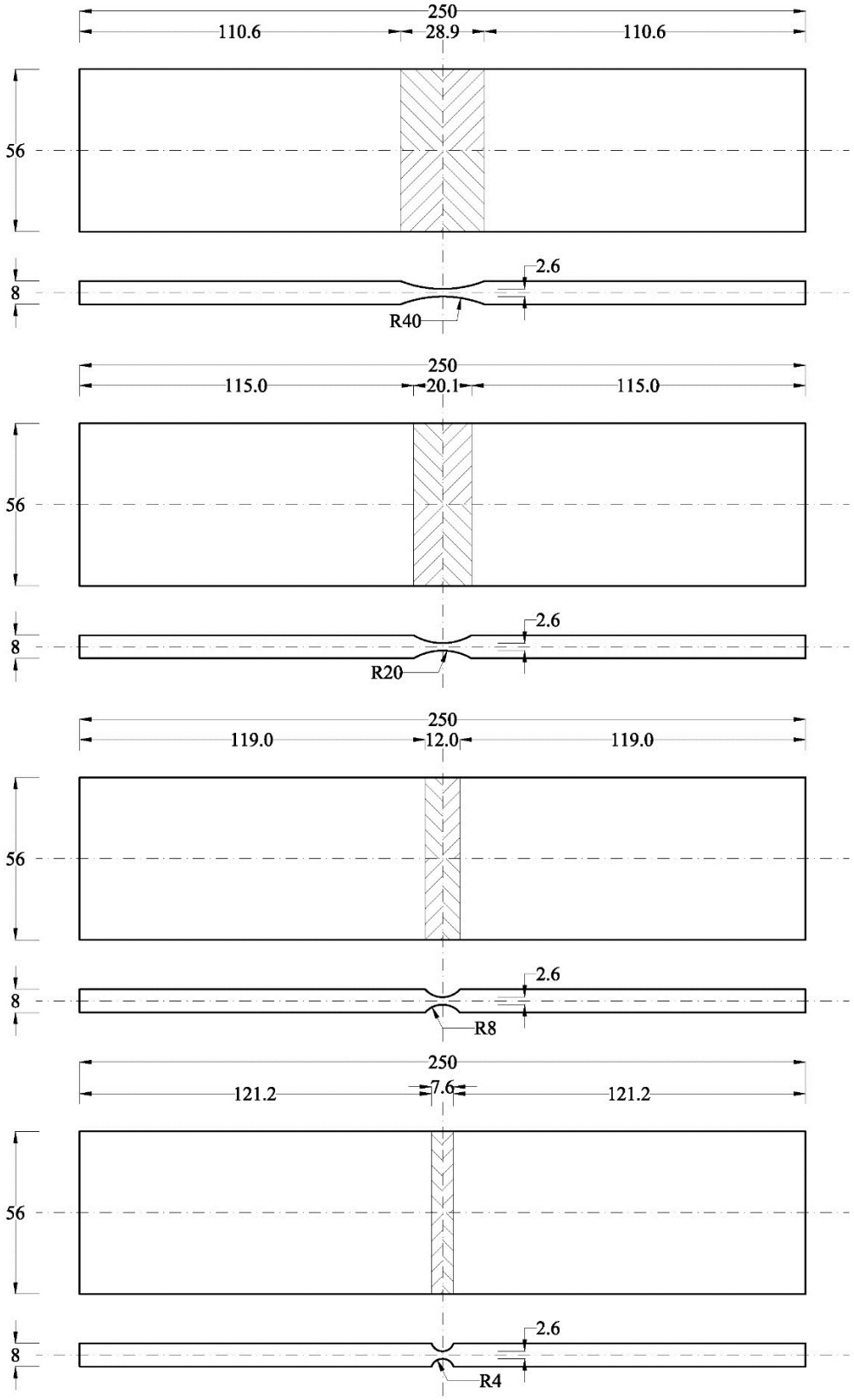

Figure 4-6: Details of the GP specimens with various notch geometry
(all dimensions are in mm)

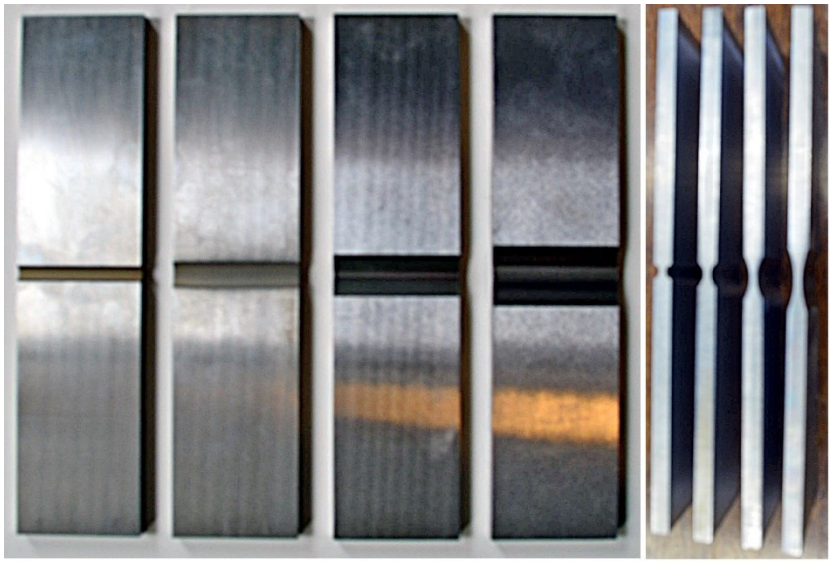

Figure 4-7: Picture of GP specimens machined out of the pipe wall

4.4 Test Set-up and Procedure

Figure 4-8 demonstrates the test set-up. An MTS 1000 loading machine was used to impose tension in the longitudinal direction of the test specimens and to monitor the amount of tensile load at each loading step. An extensometer (linear displacement sensor) was symmetrically mounted on the critical regions (reduced cross-sections) of the test specimens to measure the local tensile displacement in the length of 50 mm. The VIC-3D digital image correlation (DIC) system was used to measure the displacement and strain fields in the critical areas of the coupon and GP specimens. And, a digital data acquisition system was employed to simultaneously record the readings of MTS and extensometer and synchronize image correlation data at each loading step.

Prior to test initiation, dimensions of all test specimens were accurately measured. Specimens were painted white and made speckled by black dots all around the critical areas to calibrate and activate the image correlation system. All test specimens were

installed into the MTS machine and loaded under displacement-controlled monotonic tension until they ruptured and were split into two pieces.

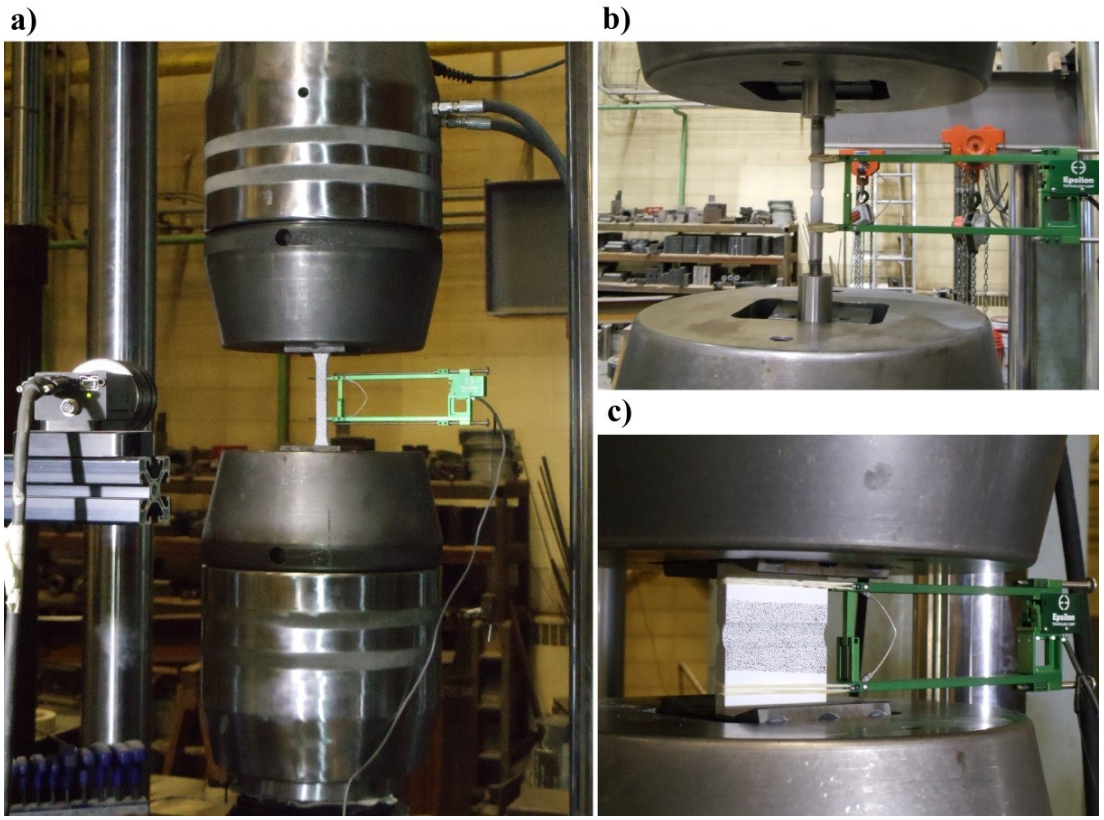

Figure 4-8: Test set-up
a) Coupon; b) NRB; c) GP

Three tests for each type of specimens were carried out to assure the robustness of the obtained results. Since the static behavior was critically important in this experimental program, the MTS machine was regularly shut down during each test while the specimen was experiencing plastic deformations. This technique unloaded the experiment to the static load level. Therefore, small sudden load drops would appear in the load-displacement plot (if the strain rate is high) which represent the static points. Specimens were started to reload after stabilization reached. The following procedure was pursued to achieve the static loading condition for all specimens.

1) Strain rate for the first test was selected by experience.

2) The second test was run at relatively slower strain rate based on the amount of load drop observed in the first test. If no load drops are observed while shutting down the MTS machine, it means that the strain rate is slow enough to be considered as static.
3) The last test was run at a significantly slower strain rate (based on observations from the second test). No static point obtained in the load-displacement plot of the third tests during the shutdowns.

Also, it is noteworthy that for coupon and GP specimens that have negligible dimensional tolerances, the load-displacement plot at the static rate passes through the static points obtained from the faster tests.

4.5 Test Results

Figure 4-9 shows the engineering stress-strain plot for coupon material tests. Engineering stress and strain are calculated based on initial geometry of the specimens as

$$\begin{cases} \sigma^{ENG} = \dfrac{P^{MTS}}{A_{r0}} \\ \varepsilon^{ENG} = \dfrac{u^{EXT}}{l_0^{EXT}} \end{cases} \quad (4\text{-}5)$$

where, P^{MTS} is MTS load, and A_{r0} is the initial reduced cross-sectional area of the speciemns. u^{EXT} and l_0^{EXT} respectively denote the displacement of knife edges and the initial gauge length (=50 mm) of extensometer.

It can be seen from Figure 4-9 that specimen B and C show static behavior as they showed no load drops at the shutdowns while connecting the static points obtained by testing specimen A. Static specimens showed round-house type stress-strain behavior which is typical of pipelines steel (due to the cold forming in UOE process). And, the coupons loaded statically showed less ductility but higher final load at fracture in

comparison to Coupon A. It is also worthy of attention that the static point method cannot predict the static load level of the specimen after necking occurs (ultimate load).

Figure 4-10 and Figure 4-11 depict the engineering stress-strain curves for round bar and GP specimens respectively. It was understood that the specimens with lower notch radius require lower strain rate to reach the static behavior. As mentioned earlier, static tests show no load drops on MTS shutdowns. In the case of GPs, the load-deformation of static specimens perfectly connect the static points of their corresponding first tests.

Ductile fracture initiates where the sudden load drop takes place. From Figure 4-10 and Figure 4-11, it is clearly apparent that reducing the notch radius raises the ultimate stress (stress triaxiality); and, the final engineering strain (fracture strain) markedly decreases. That is, the higher the stress triaxiality, the lower the fracture strain. Comparing Figure 4-10 and Figure 4-11 shows that the fracture strain for the plane strain GP specimens is generally less than that of NRBs. For instance, although both NB5 and GP4 specimens show almost the same ultimate stress (about 800 MPa), the engineering strain to fracture of GP4 (about 18000 μmm/mm) was found to be considerably less than that of NB5 (about 40000 μmm/mm). In other words, for the same level of stress triaxiality, GP plain strain specimens indicate less ductility compared to NBs. This clearly reflects the effect of Lode angle parameter on fracture strain for the tested X65 steel material.

Figure 2-10 and Figure 2-11 show the fracture surface of RB and GP specimens respectively. Necking was observed with the cup-and-cone fracture mode for the RBs.

Reduction of width from the sides and thickness particularly in the middle of GP specimens occurred due to necking and ductile fracture. The pattern of thickness reduction is increasing from the sides to the mid-width of the specimens where plane strain stress condition governs and fracture initiation occurs.

Figure 4-14 demonstrates the distribution of horizontal strain in the width direction of the GP40 specimen obtained by image correlation system after a considerable necking took place and right before the paints flaked off due to the big reduction of the cross-section. Plane strain loading condition is fully apparent from this picture as the strain in the width direction is decreasing by moving from the sides (where the horizontal

strain is maximum) to the mid-width of the specimen where the in-width strain is pretty close to zero.

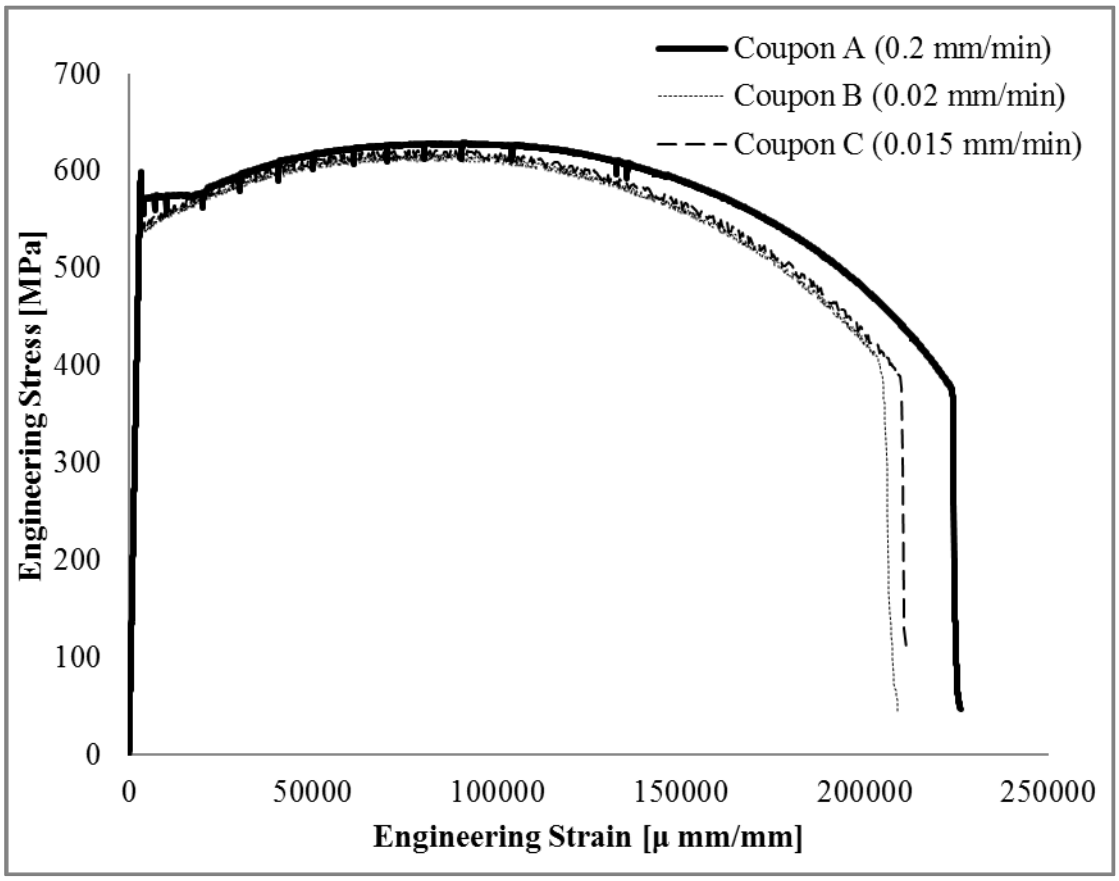

Figure 4-9: Engineering stress-strain plot for coupon tests

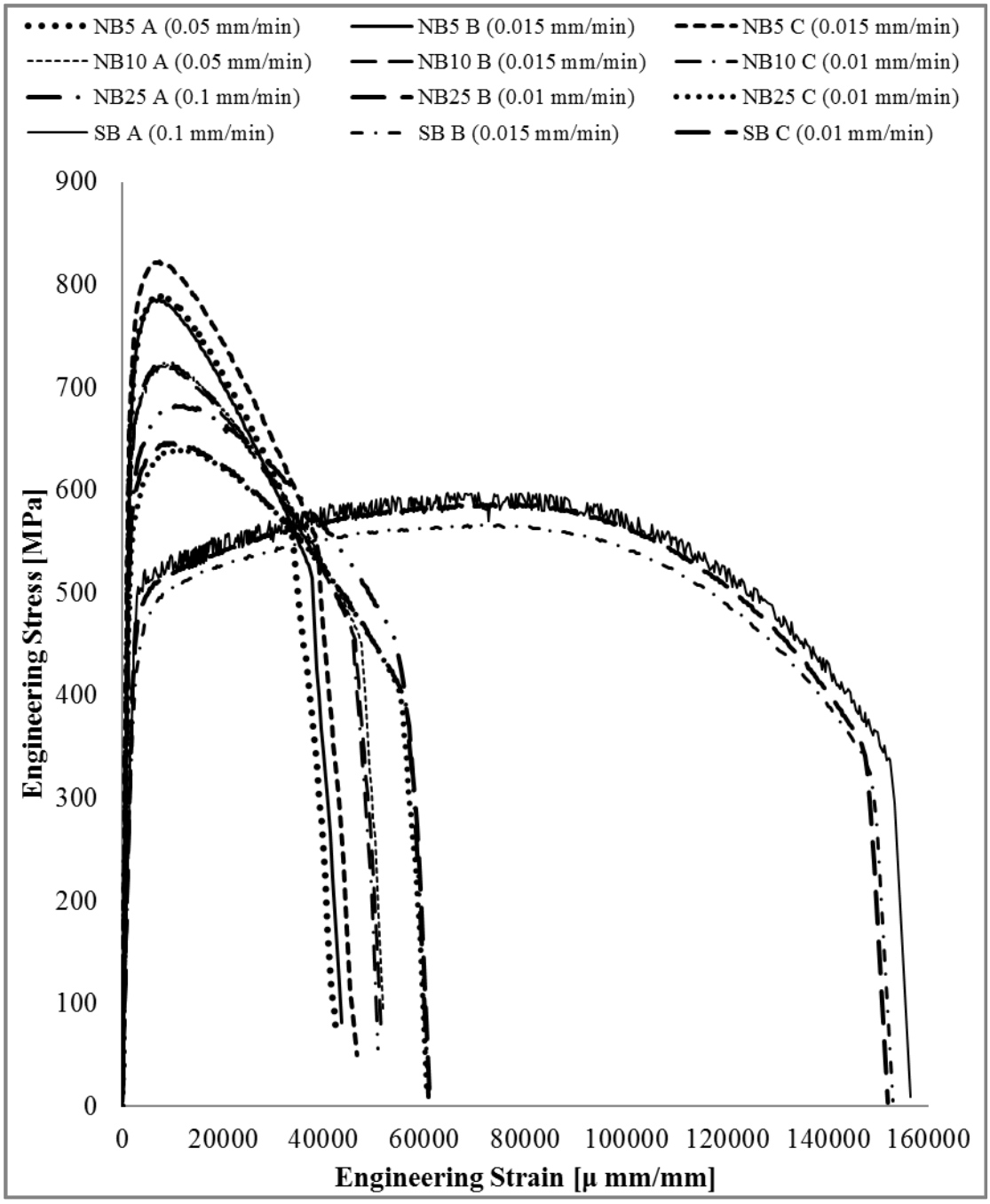

Figure 4-10: Engineering stress-strain plot for RB tests

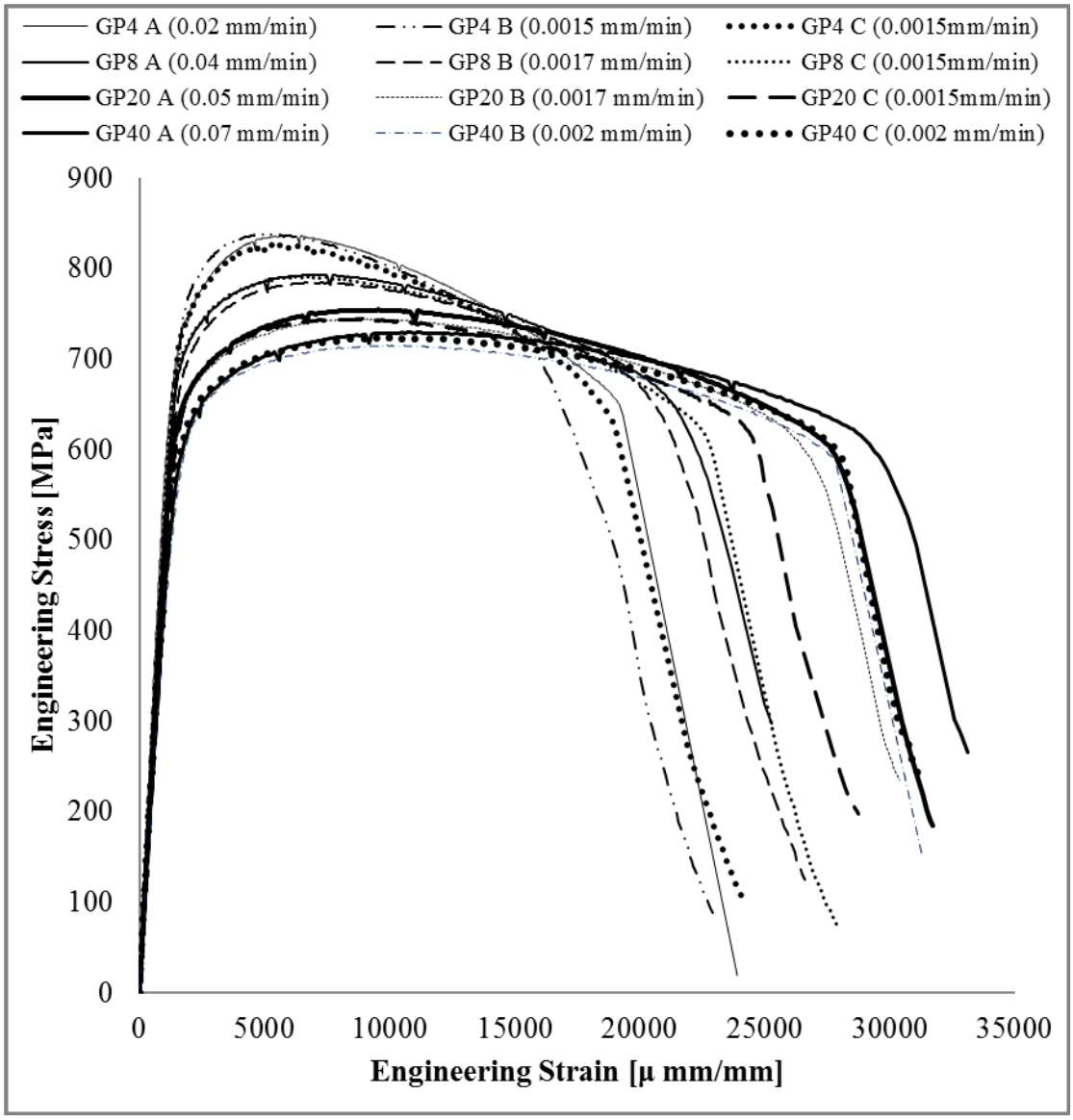

Figure 4-11: Engineering stress-strain plot for GP tests

Figure 4-12: Failure mode of RB specimens

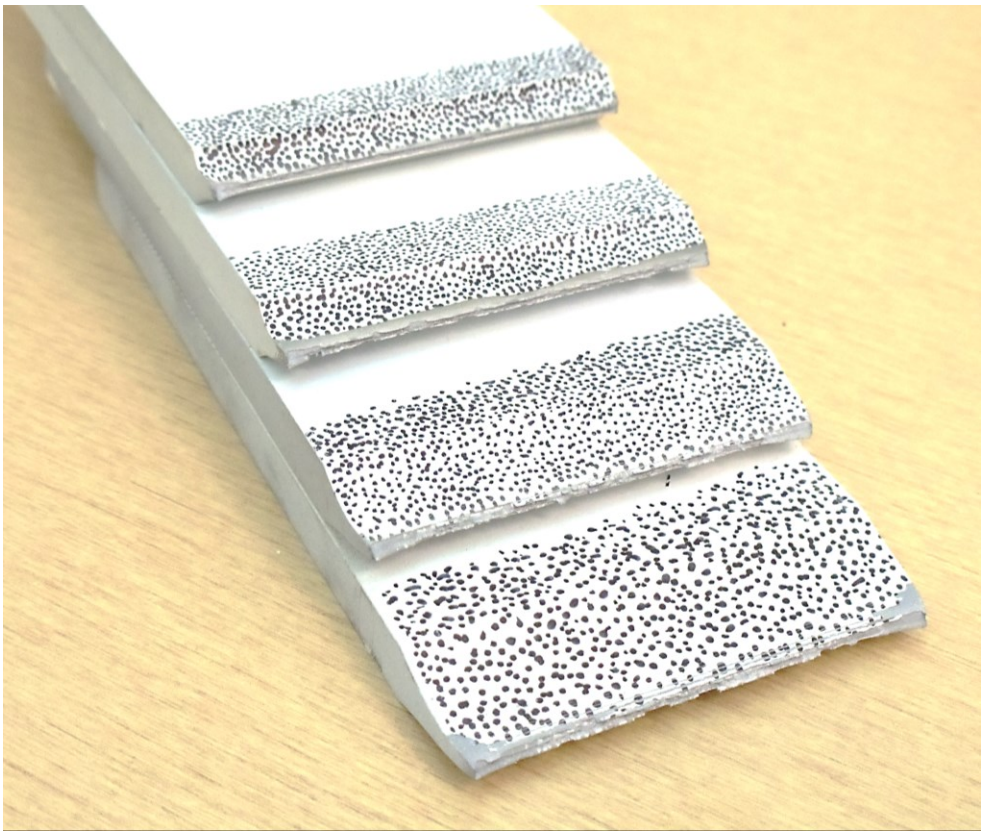

Figure 4-13: Failure mode of GP specimens

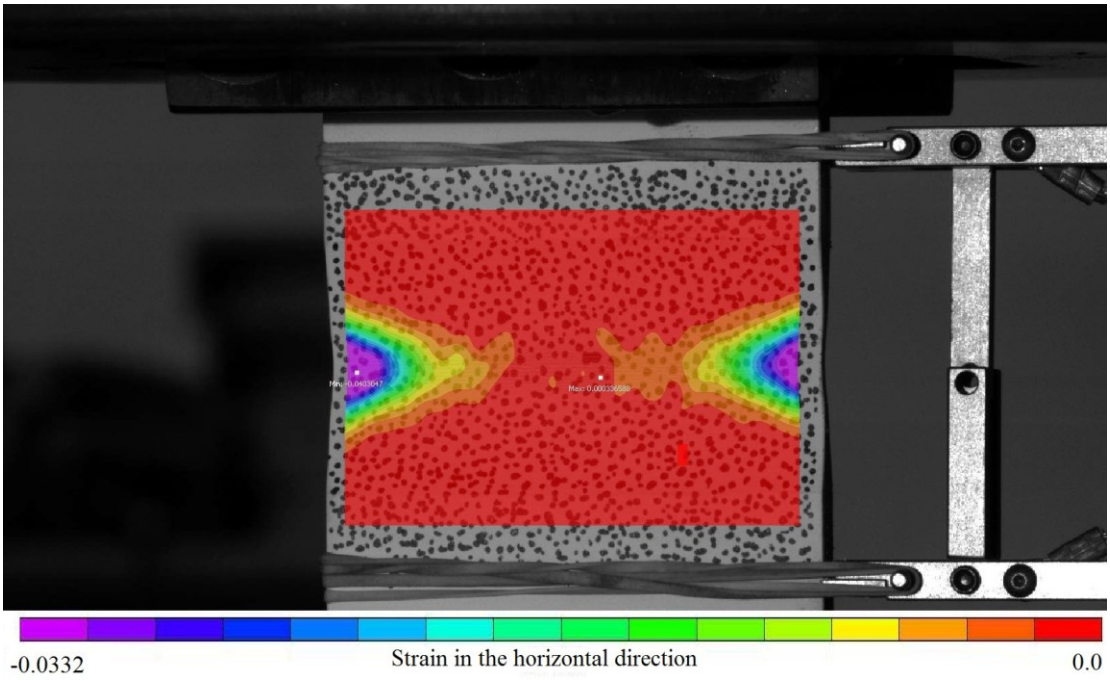

Figure 4-14: The distribution of post-necking in-width strain in GP40 specimen close to the fracture obtained by image processing (MTS load=100.6kN & (ε^{ENG}, σ^{ENG})=(21545.84 μmm/mm, 691.03 MPa)

4.6 Material Properties and Plasticity Calibration

Table 4-6 summarizes the mechanical properties of the tested X65 steel obtained from the stress-strain plot of the tensile coupon tests. The yield strength was obtained by reading the stress value corresponding to the 0.5% strain (CSA-Z662 2015). Material possesses a relatively high Y/T ratio equal to 87.5%.

To evaluate the ductile fracture of a structure, which is associated with the final stress-carrying capacity of the material, a plastic analysis is required to be conducted by taking the material plasticity into account. Hence, it is extremely important to acquire the true stress-strain behavior of the material which is verified by experimental data to be inverted into the plastic analysis of ductile fracture.

Table 4-6: Mechanical properties of the tested X65 material

Yield Strength @ 0.5% Strain, F_y	Tensile Strength at Necking (UTS), F_u	Y/T
[MPa]	[MPa]	[%]
549	628	87.5
Elastic Modulus, E	Poisson's Ratio, υ	Proportional Limit Strength, σ_p
[MPa]	-	[MPa]
200000	0.3	440
Uniform Strain (Necking Strain), ε_u	Reduced Area at Fracture ($\Delta A/A0$), RA	Elongation at Fracture ($\Delta L/L_0$), EL
[mm/mm]	[%]	[%]
0.09	0.50	0.19

The engineering stress in the stress-strain plot of the material shown in Figure 4-9 is calculated based on the initially reduced area of the coupon specimens, and the engineering strain is based on the initial gauge length covered by the extensometer (Eq. (4-5)). Nevertheless, the true stress-strain behavior should be calculated based on the current deformed shape of the specimen at each loading step. To address this issue, the following equations are used to calculate the true logarithmic strain and the true stress of the material directly from the engineering stress and strain values.

$$\varepsilon = \ln\left(1 + \varepsilon^{ENG}\right) \qquad (4\text{-}6)$$

$$\sigma = \sigma^{ENG}\left(1+\varepsilon^{ENG}\right) \qquad (4\text{-}7)$$

However, the above equations are only valid to obtain the true stress-strain curve up to the ultimate load where the diffuse necking takes place at the uniform strain. At this point, large localized plastic deformations and strains start to develop in the specimen and excessive local cross-sectional reduction is observed accompanying by the load drop in the load-deformation plot (Figure 4-9). In this regard, a verified technique is needed to produce the actual stress-strain curve of the material after the onset of diffuse necking.

Bao (2003) proposed a hybrid experimental-numerical method to calibrate the true stress-stain curve after necking occurrence. In this method, a parallel FEA of the material test is carried out and the stress-strain values inverted into the analysis are changed by trial and error until the load-displacement responses of the FEA fairly reproduce the experimental data. *Lee* (2005) used the power law for the initial guess and used a similar trial and error method to construct the stress-strain curve after diffused necking. In the same way, *Kofiani* (2013) used an iterative process starting with the power law and swift law stress-strain fits to extrapolate the post-necking stress-strain curve. Iterations continued until the response of the parallel FE models acceptably followed the experimental load-displacement behavior. *Mitsuya and Sakanoue* (2015) proposed linear and nonlinear extrapolations to extend the stress-strain curve beyond the uniform strain. For the linear method, it was proposed to linearly extrapolate the curve by the slope of the line that connects the stress associated with 1% strain less than uniform strain to uniform strain. In the nonlinear method, it was suggested to fit the swift law to the stress-strain curve from the yield to ultimate strength and use that for post-necking extrapolation.

In the current study, the closest half of the true stress-strain data to the uniform strain between the end of the round part of the curve (where the slope rate of the post-yield stress-strain curve becomes relatively moderate) and the ultimate stress was used to calibrate the constant parameters of the power law in Eq. (3-23) and consider as the initial assumption to extrapolate the stress-strain plot beyond the diffused necking.

Imperialist Competitive Algorithm (ICA) optimization technique (Talatahari and Mohajer Rahbari 2015) was engaged to fit the power law to the experimental data. In order to obtain the optimal parameters, the following normalized mean square error (MSE) was used as the fitness function (penalty function) to be minimized through the optimization process.

$$\mathrm{MSE}(\boldsymbol{A},\boldsymbol{n}) = \frac{\sum_{i=1}^{N_E} \left(\sigma_E(\varepsilon_i) - \sigma_{PL}(\varepsilon_i \mid \boldsymbol{A},\boldsymbol{n})\right)^2}{N_E s_{\sigma_E}^2} \qquad (4\text{-}8)$$

in which, $\boldsymbol{A}$ and $\boldsymbol{n}$ are the parameters of the power law that are changed at each iteration until the optimum values are found. $\sigma_E(\varepsilon_i)$ and $\sigma_{PL}(\varepsilon_i \mid \boldsymbol{A},\boldsymbol{n})$ signify the experimental stress values and power law stress associated with i^{th} strain value (ε_i), respectively. N_E denotes the number of discrete experimental stress-strain data points that are fed into the curve fitting process; and $s_{\sigma_E}^2$ is the variance of the experimental stress values.

Optimum values of A and n were found to be 830.96 and 0.083 respectively. Figure 4-15 shows the full stress-strain curve which is extrapolated by the power law in the post-necking region. As mentioned earlier, the pre-necking true stress-strain was calculated from experimental data using Eqs. (4-6) and (4-7).

Parallel static FEA of the coupon tests was conducted using Abaqus/Standard V.6-13 finite element platform (Simulia Corp. 2013) to assess the stress-strain curve obtained by the plasticity calibration process. 8-node brick elements with reduced integration (C3D8R) was used to model the coupon's body, and only a half of specimens were modeled due to symmetry. Figure 4-16 illustrates the mesh description of the FE model.

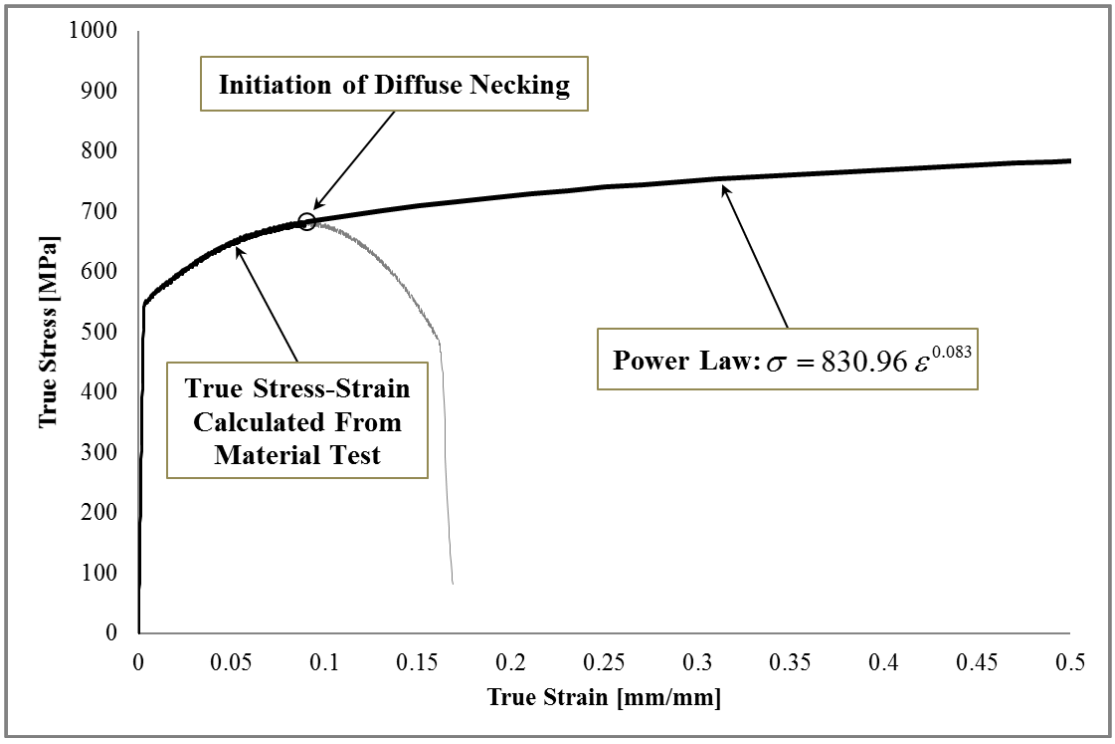

Figure 4-15: True stress-strain curve of the tested X65 steel material obtained by plasticity calibration

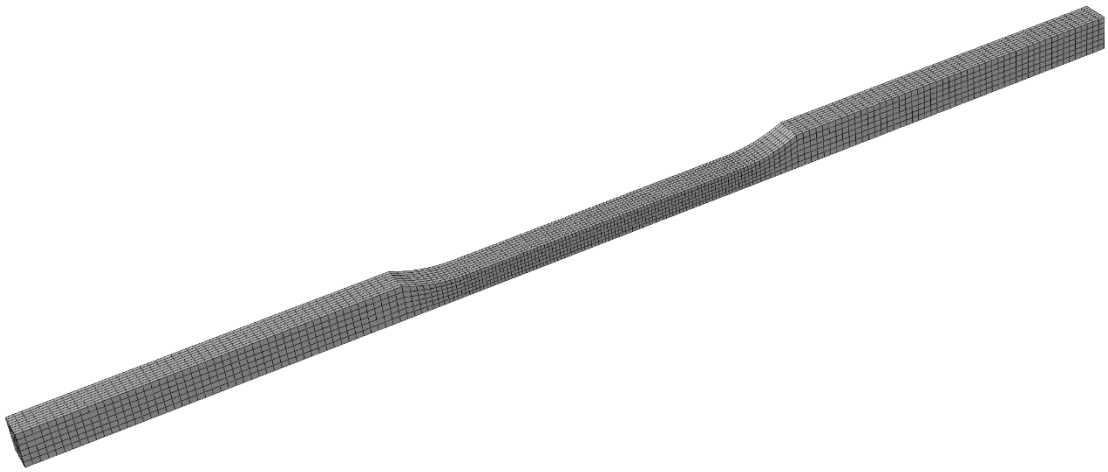

Figure 4-16: Mesh description and FE model of the coupon specimens

Figure 4-17 compares the load-displacement response of the FEA with that of the coupon tests. It is observed that the FE model using the calibrated stress-strain curve (Figure 4-15) acceptably recreates the experimental load-displacement curve up to the

fracture initiation. Also, Figure 4-18 examines the deformed shape and horizontal displacement field of the coupon obtained from FEA in comparison with test data acquired by image correlation system at a post-necking frame exactly before the paints flaked out due to the reduction of the cross-section. It is clear that the FE model almost predicts the same deformed shape and displacements as image processing system. Hence, it can be concluded that the assumed stress-strain curve can fairly represent the actual material behavior and no further iteration is required.

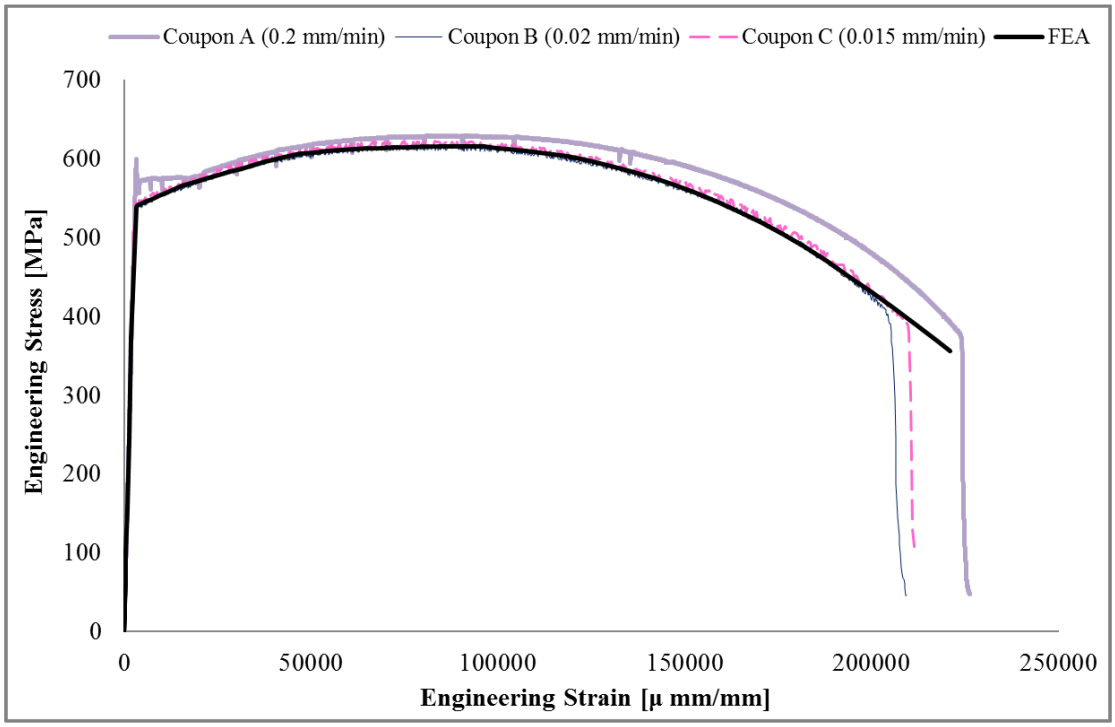

Figure 4-17: Comparison between the load-displacement response of FE model and test results for coupon specimens

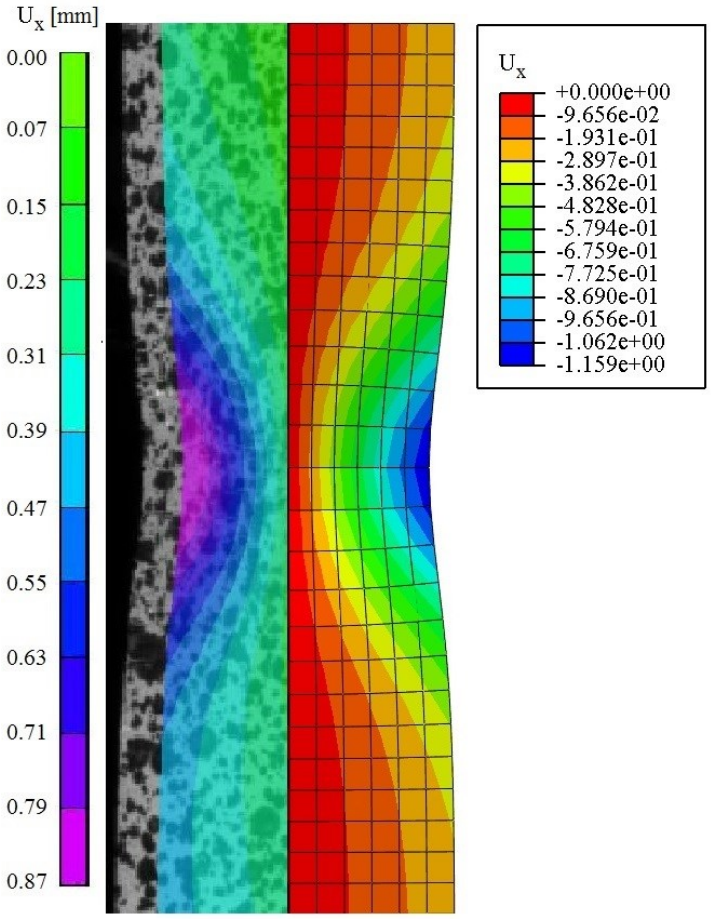

Figure 4-18: Comparison of post-necking horizontal displacement obtained from FEA (right) and image correlation system (left) in coupon specimen close to the fracture point (MTS load=54.9kN & (ε^{ENG}, σ^{ENG})=(160967.9 μmm/mm, 549.3 MPa)

4.7 Parallel FEA of RB and GP Experiments

As mentioned before, the ductile fracture toughness is usually defined by the equivalent plastic strain as a function of stress triaxiality and Lode angle. Therefore, it is required to somehow capture the history of principal stress and strain values at the fracture location for each specimen. However, it is very impractical to rigorously monitor this information during the experiments. Alternatively, parallel FEA of the tests could be conducted to collect the actual stress and strain fields developed in the specimens during the test provided that the FE model can faithfully reproduce the experimentally obtained load-displacement behavior (Bao and Wierzbicki 2004a).

FE simulation of RB and GP specimens were carried out using the calibrated material stress-strain curve demonstrated in Section 4.6 (Figure 4-15) to obtain the equivalent plastic strain to fracture, history of stress triaxiality and Lode angle parameter through a hybrid experimental-numerical technique. Figure 4-19 to Figure 4-22 compare the load-displacement response of the RB specimens obtained from FEA and tests. FE simulations acceptably follow the experimental results up to the fracture point. Herein, the fracture is assumed to coincide with the ductile macro-crack initiation that appears as a sudden load drop in the load-displacement plot of specimens. The average of displacements to fracture obtained from the static tests was assumed as the final displacement in FEA. Figure 4-23 illustrates the mesh description, final deformed shapes and equivalent plastic strain to fracture of the RBs from FEA. 8-node axisymmetric element type with reduced integration (CAX8R) was used to model the RB specimens and the half of geometry were modeled due to symmetry.

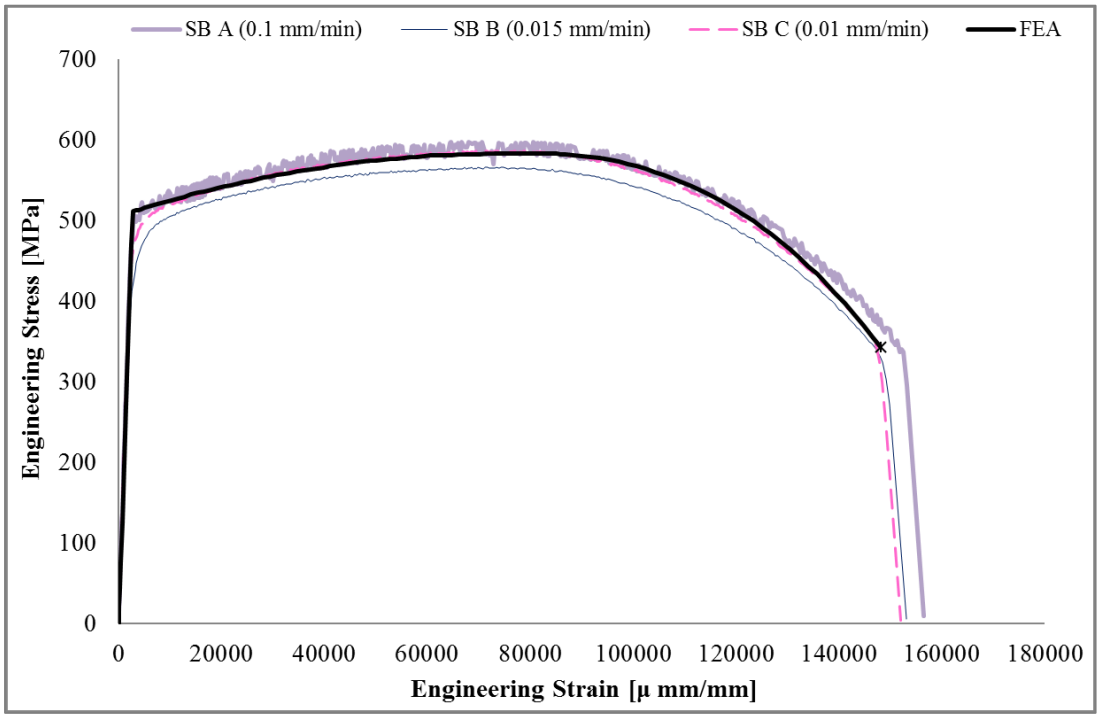

Figure 4-19: Comparison between the load-displacement response of FE model and test results for smooth RB specimens

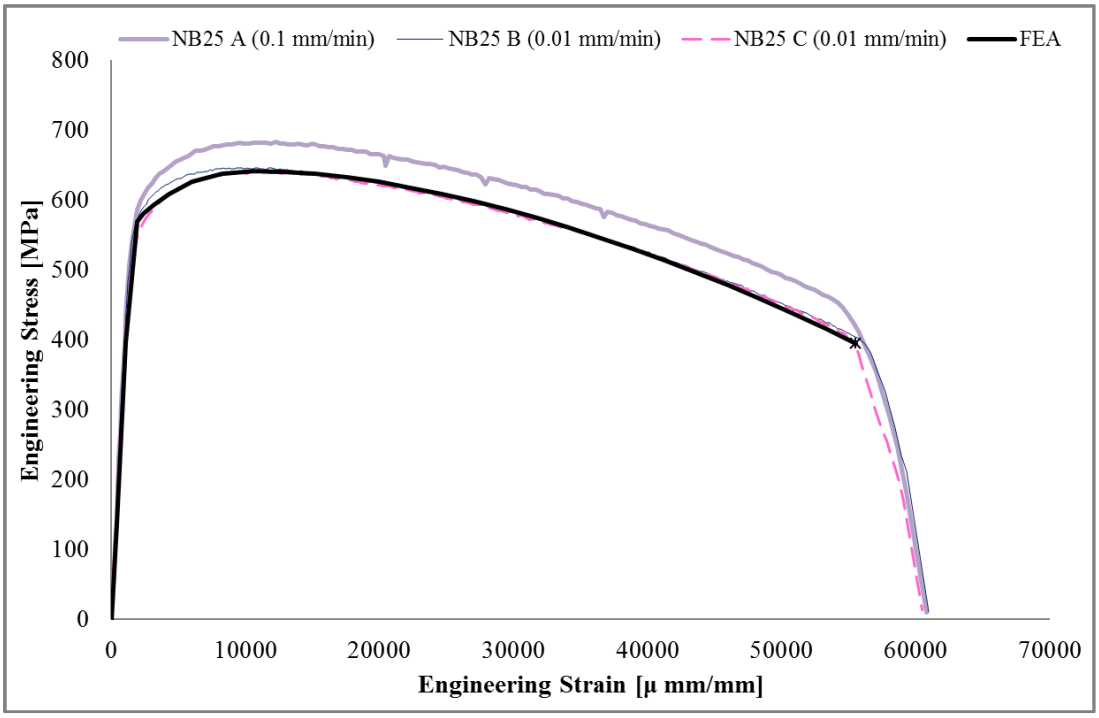

Figure 4-20: Comparison between the load-displacement response of FE model and test results for NB25 specimens

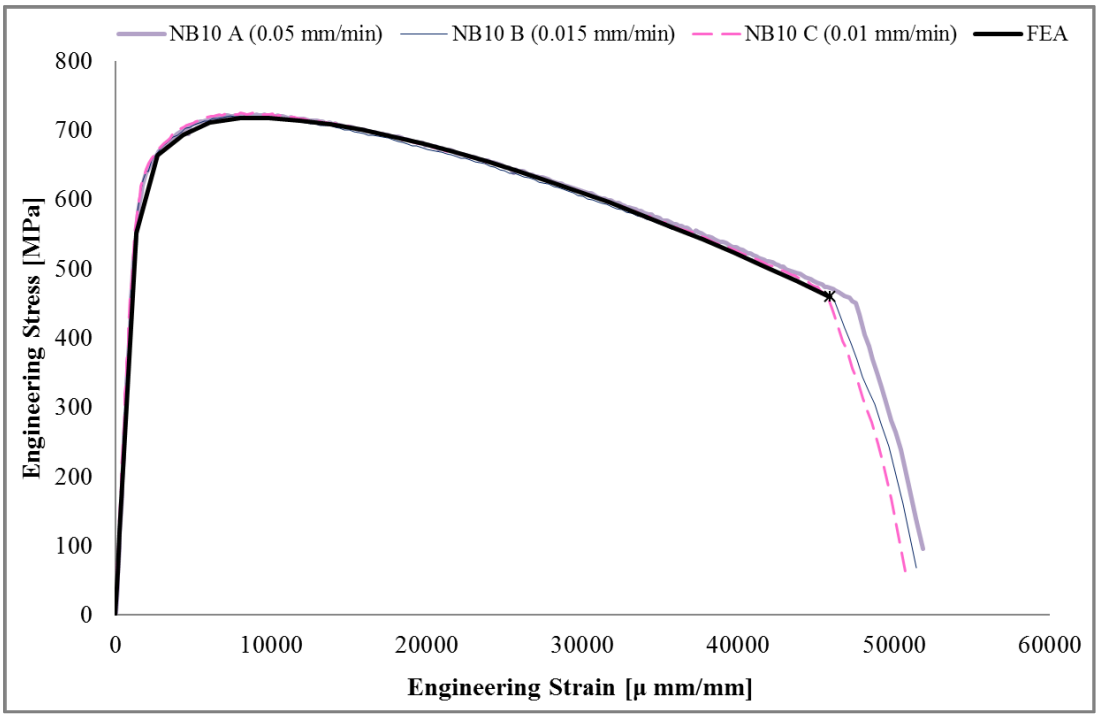

Figure 4-21: Comparison between the load-displacement response of FE model and test results for NB10 specimens

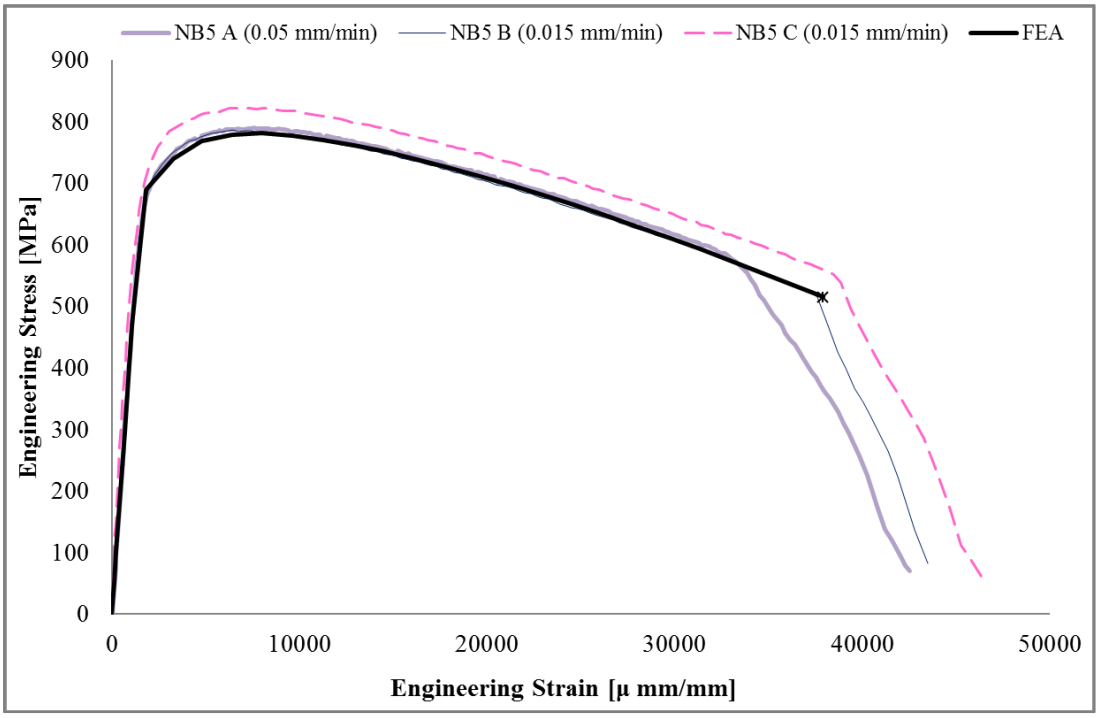

Figure 4-22: Comparison between the load-displacement response of FE model and test results for NB5 specimens

A similar approach was used for the GP specimens. Figure 4-24 to Figure 4-27 describe the load-displacement plots from FEA in comparison to experiments. The FEA results are in a very good agreement with static tests data. Figure 4-28 depicts the mesh pattern and equivalent plastic strain to fracture on the final deformed shapes of the specimens obtained from FEA. One eighth of specimens' geometry were modeled in FE simulations due to their symmetry about three perpendicular axes. C3D8R solid elements were used to form the body of the specimens in FE models.

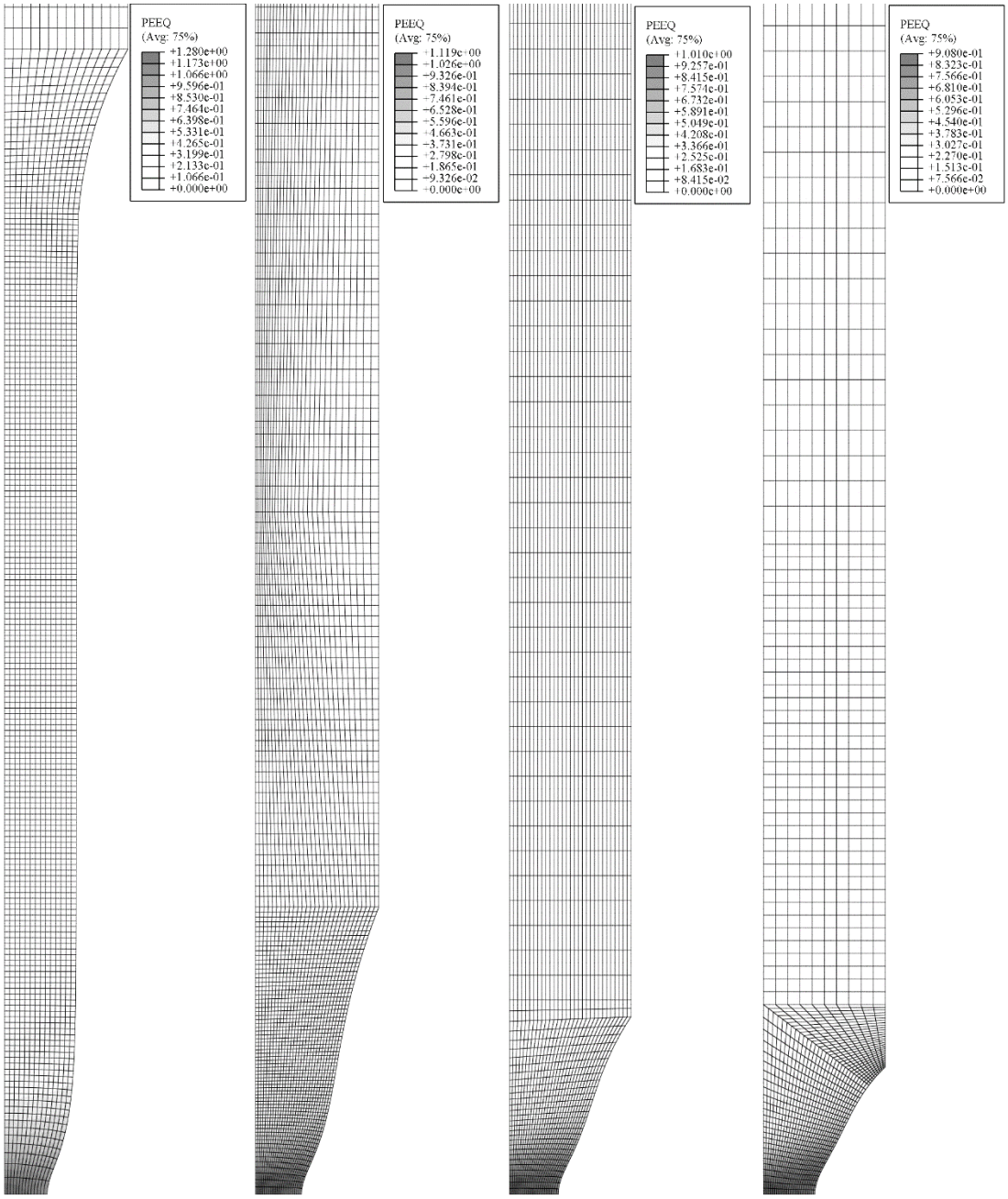

Figure 4-23: Mesh description, final deformed shape and equivalent plastic strain to fracture of the RB specimens obtained from FE model

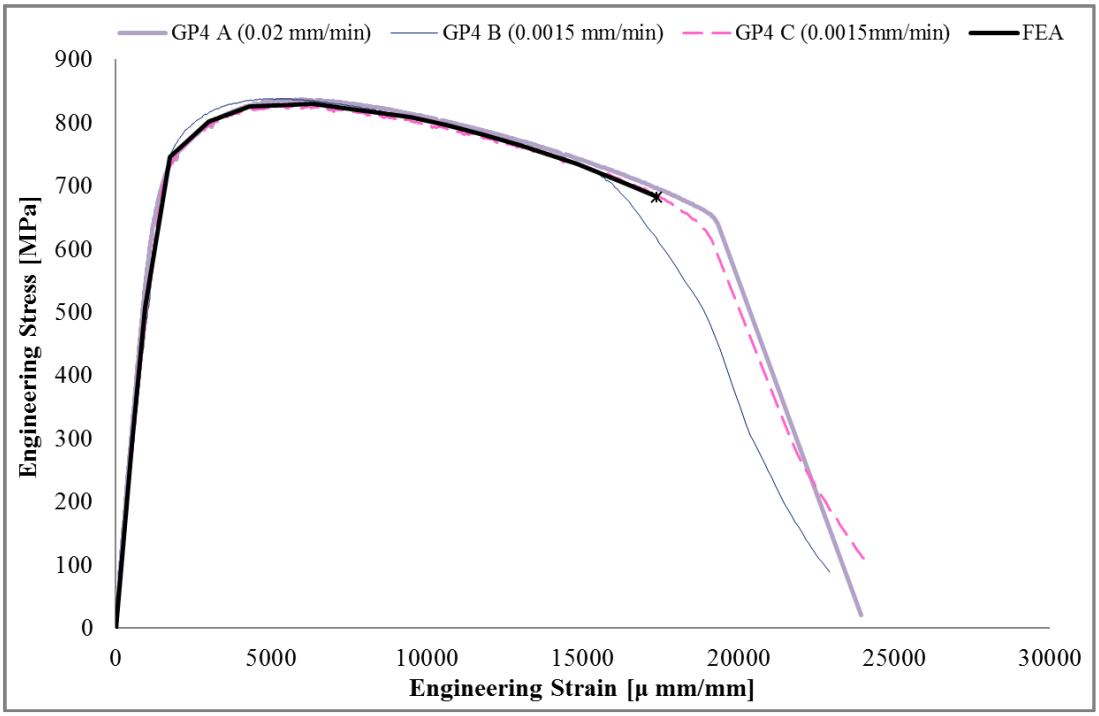

Figure 4-24: Comparison between the load-displacement response of FE model and test results for GP4 specimens

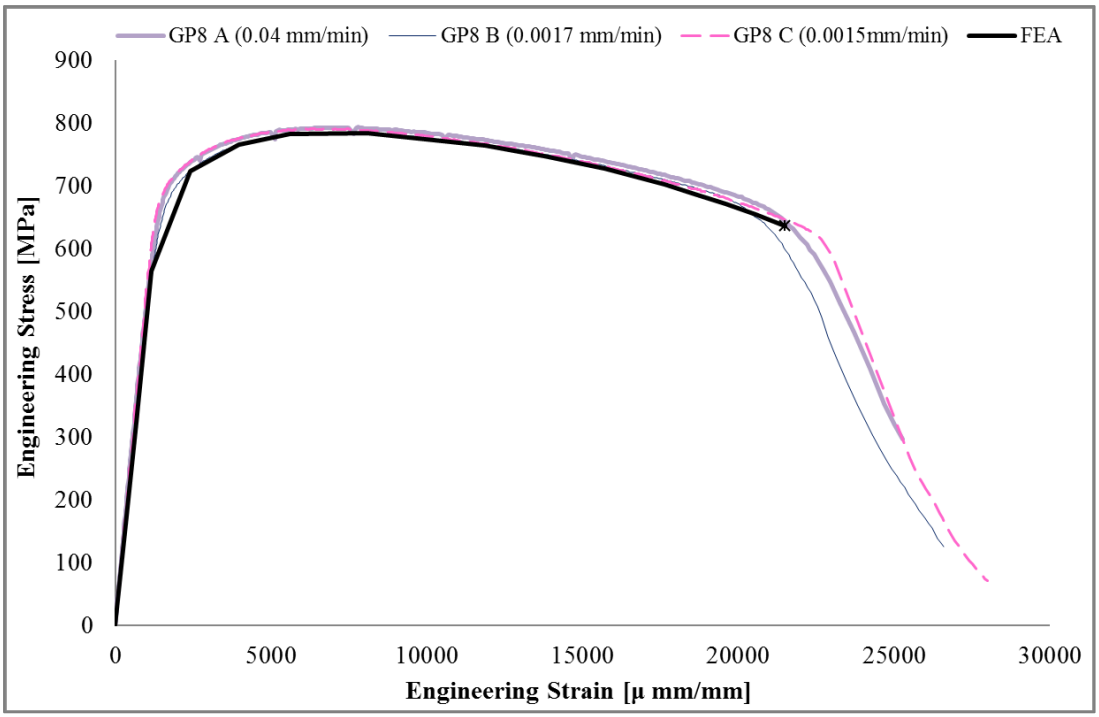

Figure 4-25: Comparison between the load-displacement response of FE model and test results for GP8 specimens

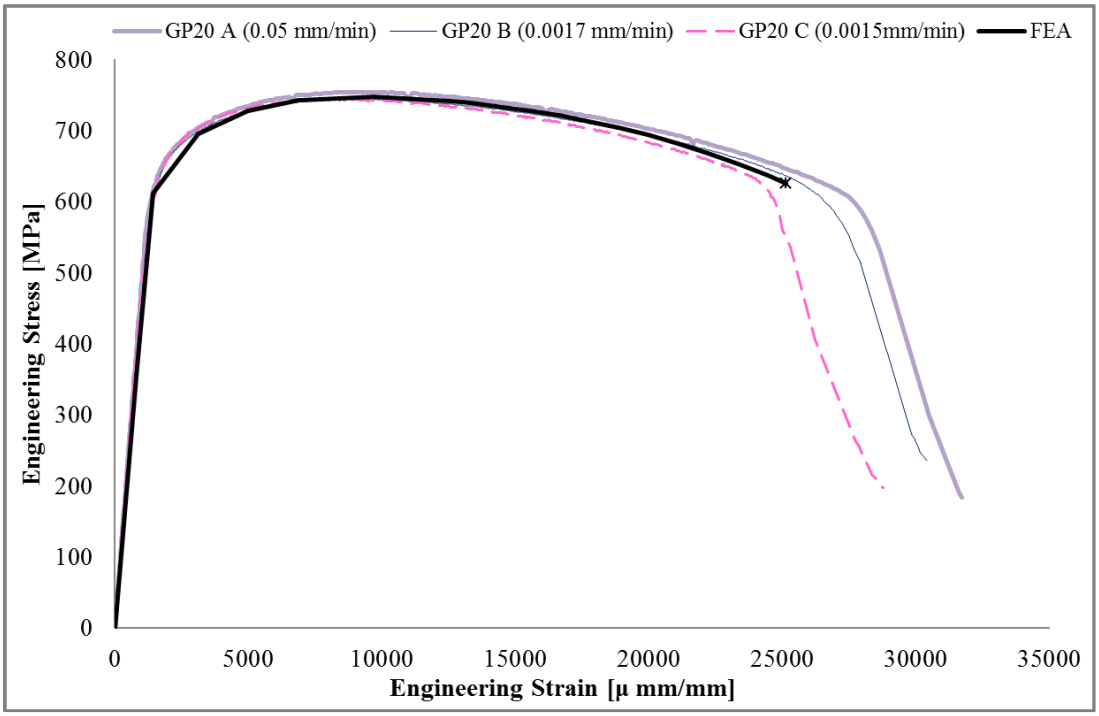

Figure 4-26: Comparison between the load-displacement response of FE model and test results for GP20 specimens

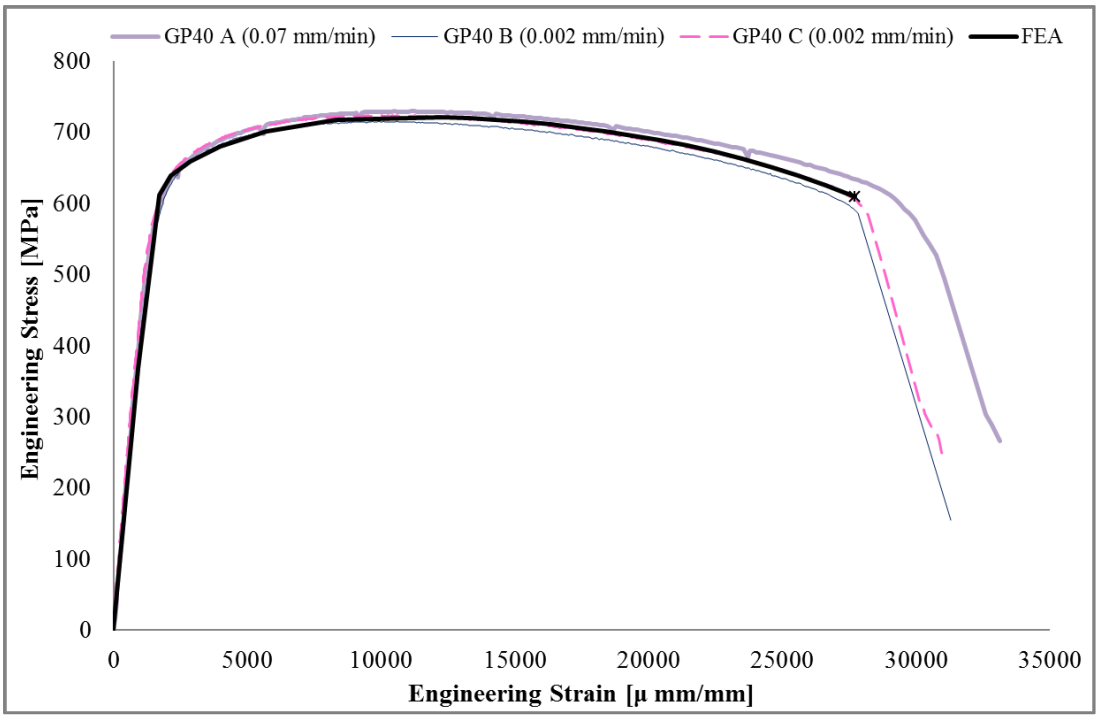

Figure 4-27: Comparison between the load-displacement response of FE model and test results for NB40 specimens

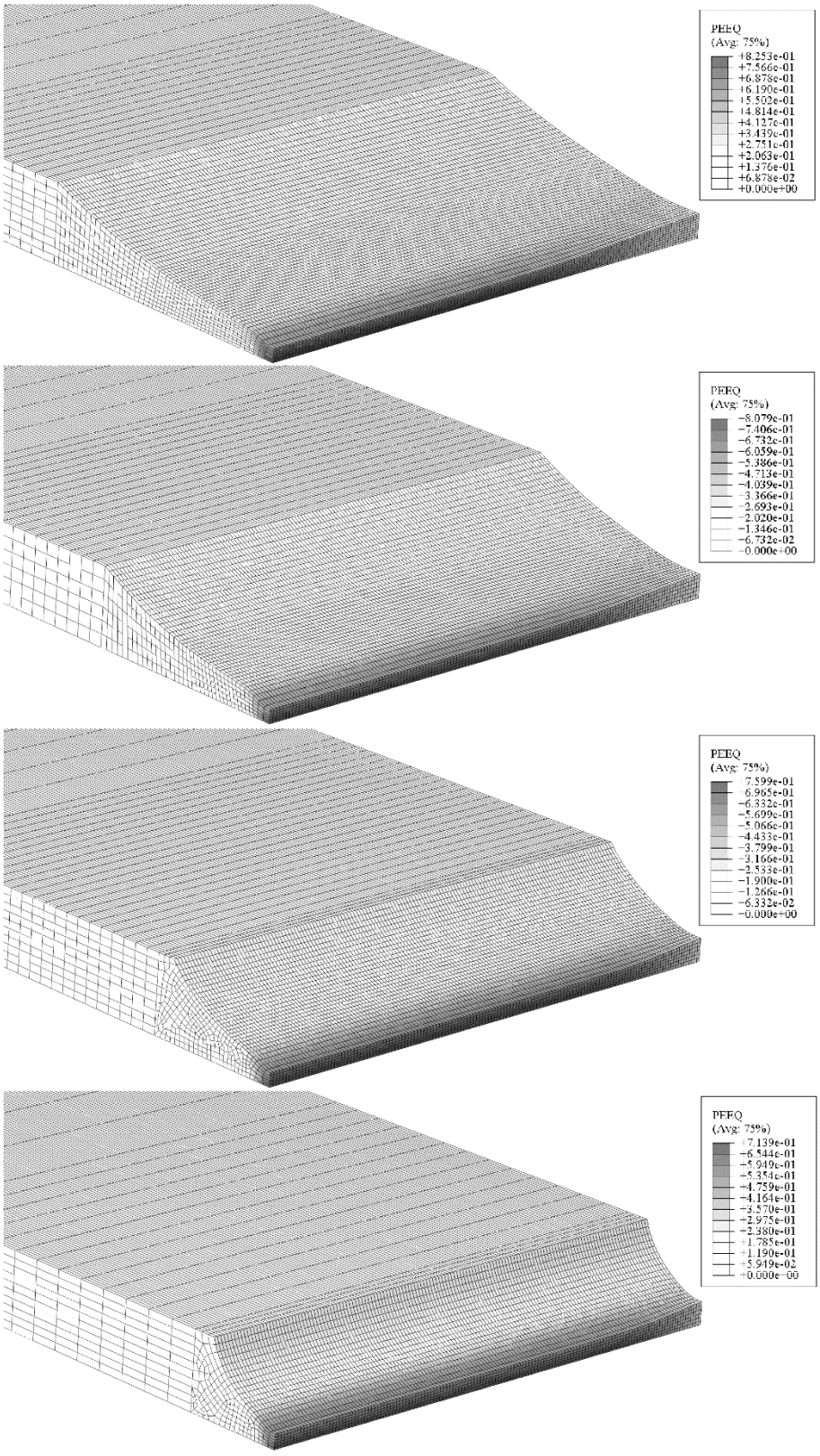

Figure 4-28: Mesh description, final deformed shape and equivalent plastic strain to fracture of the GP specimens obtained from FE model

4.8 Ductile Fracture Toughness

In the previous section, the parallel FEA of the test specimens were conducted and verified to match the load-displacement behavior of the experiments up to the fracture point. Final equivalent plastic strain to fracture was readily obtained from FE simulations for each specimen at the centroid of the reduced cross-section where the ductile crack initiates. As well, the history of principal stresses was red at the fracture location to calculate the history of the stress triaxiality through Eq. (3-8), and normalized third deviatoric stress invariant via Eq. (3-17) during the loading process. The average stress triaxiality (η_{ave}) and normalized third deviatoric stress invariant (ξ_{ave}) are calculated for each specimen using the following equations (Wierzbicki et al. 2005b) to account for the history of hydrostatic pressure and Lode angle parameters on the fracture strain.

$$\eta_{ave} = \frac{1}{\bar{\varepsilon}_f^p} \int_0^{\bar{\varepsilon}_f^p} \eta\left(\bar{\varepsilon}^p\right) d\bar{\varepsilon}^p \qquad (4\text{-}9)$$

$$\xi_{ave} = \frac{1}{\bar{\varepsilon}_f^p} \int_0^{\bar{\varepsilon}_f^p} \xi\left(\bar{\varepsilon}^p\right) d\bar{\varepsilon}^p \qquad (4\text{-}10)$$

Figure 4-29 and Figure 4-30 demonstrate the history of stress triaxiality with respect to equivalent plastic strain and average stress triaxiality for RB and GP specimens respectively. It is observed that the stress triaxiality is almost constant in a small portion of the diagram and then it is rapidly ascending. That is because of the occurrence of necking and cross-sectional reduction that causes an increase in the ratio of ligament dimension to notch radius in Eqs. (4-3) and (4-4). As it was expected, the average normalized third deviatoric stress invariant were found to be extremely close to 1 for RBs and 0 for GPs.

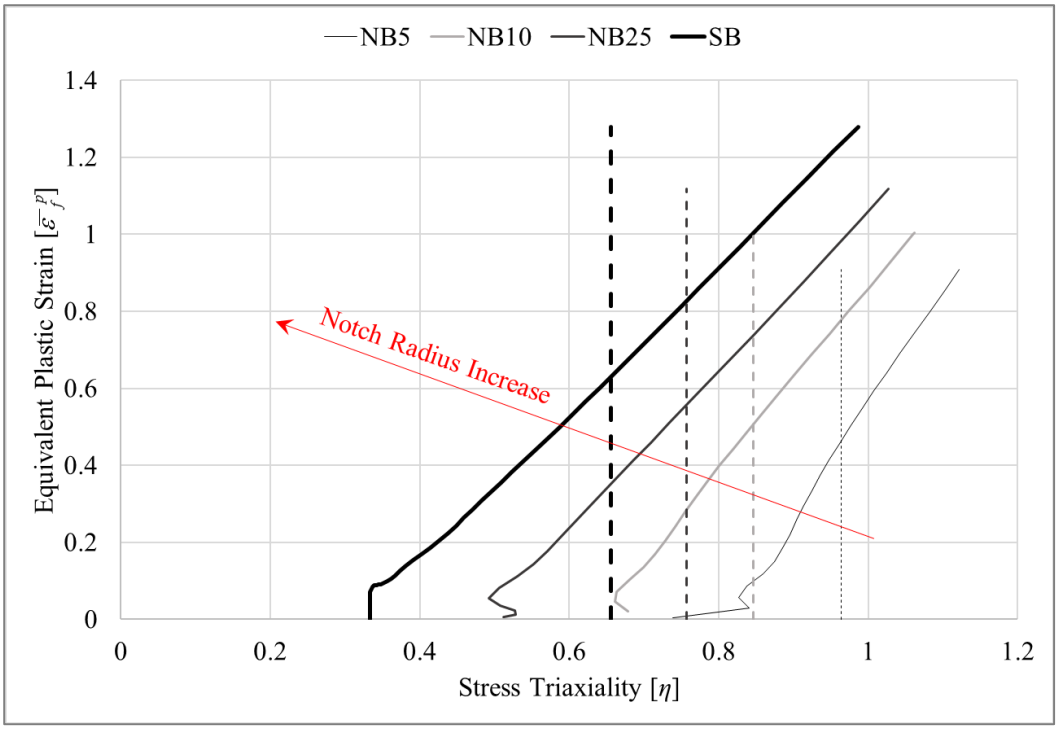

Figure 4-29: $\left(\eta - \bar{\varepsilon}_f^p\right)$ diagram and average stress triaxiality for RB specimens

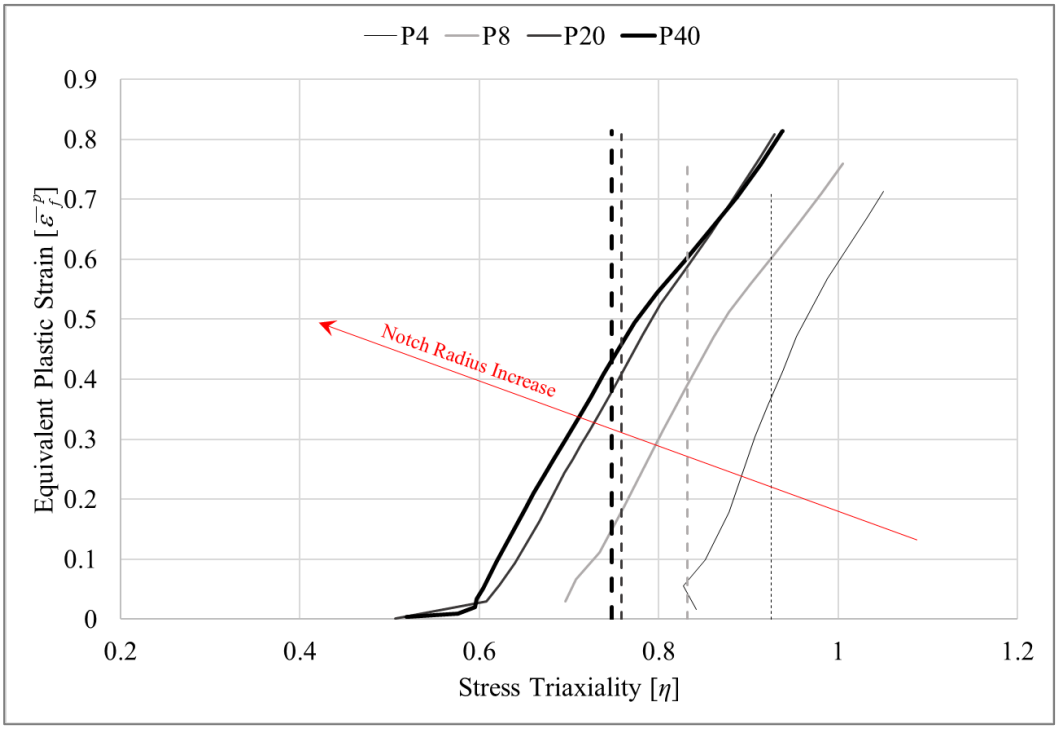

Figure 4-30: $\left(\eta - \bar{\varepsilon}_f^p\right)$ diagram and average stress triaxiality for GP specimens

Figure 4-31 demonstrates the plot of equivalent plastic fracture strain versus stress triaxiality obtained from the experimental-numerical analysis. It is noticeable that the fracture strain for RBs and GPs form two distinct exponentially decreasing pattern with respect to stress triaxiality. Furthermore, the fracture strain plot obtained by the RBs (ξ=1) is higher than that of the GPs (ξ=0) specimens which indicates the Lode dependence of the fracture strain. Similar to the stress-strain extrapolation procedure explained in Section 4.6, ICA optimization algorithm was used to minimize the MSE function described in Eq. (4-8) to calibrate the *Johnson-Cook* model for the RB and GP specimens as follows

$$\begin{cases} \bar{\varepsilon}_f^{p\ (\xi=1)} = 3.70\exp\left[-2.59\eta\right] + 0.6 & \text{for RBs} \\ \bar{\varepsilon}_f^{p\ (\xi=0)} = 1.63\exp\left[-2.20\eta\right] + 0.5 & \text{for GPs} \end{cases} \qquad (4\text{-}11)$$

The fracture locus obtained by the hybrid experimental-numerical method was also engaged to minimize the MSE penalty function using ICA optimization and find the optimal values for the parameters of the M-C fracture surface criterion presented by Eq. (3-22). Table 4-7 summarizes the optimum values of the power law and M-C model for the X65 steel grade. Figure 4-32 illustrates the fracture locus with respect to stress triaxiality and the normalized third deviatoric stress invariant for X65 steel. Fracture locus forms a surface which is exponentially decreasing with respect to stress triaxiality and is concave in terms of the Lode dependence. Black stars in Figure 4-32 represent the experimental data used in the calibration procedure.

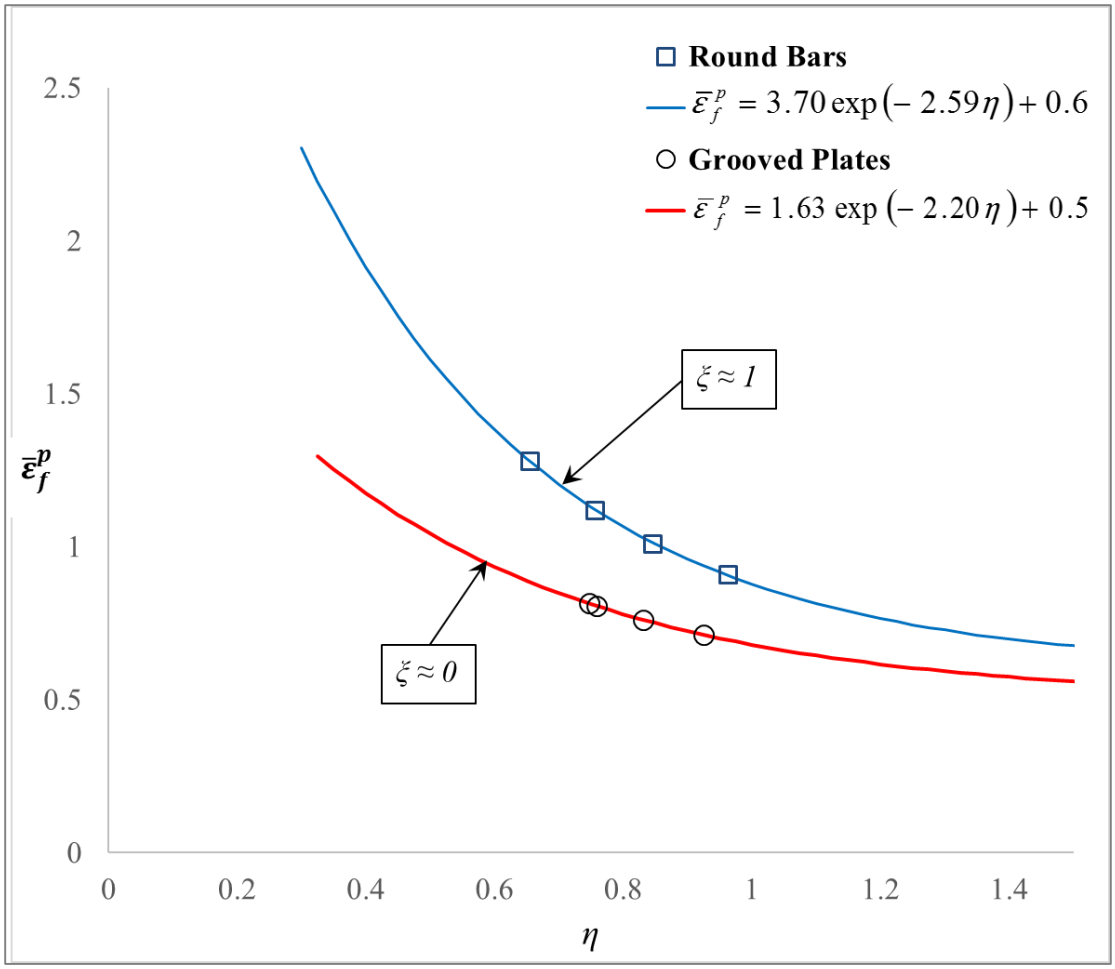

Figure 4-31: $\left(\eta_{ave} - \bar{\varepsilon}_f^p\right)$ plots and exponentially fitted curves obtained from hybrid experimental-numerical approach for RB and GP specimens

Table 4-7: Optimal values of the parameters of M-C model for X65 steel grade

Steel Grade	***A***	***n***	c_1	c_2	c_3	c_4
	Power Law Constants		[MPa]	-	-	-
API X65	830.96	0.0834	0.0499	458.98	0.912	1.031

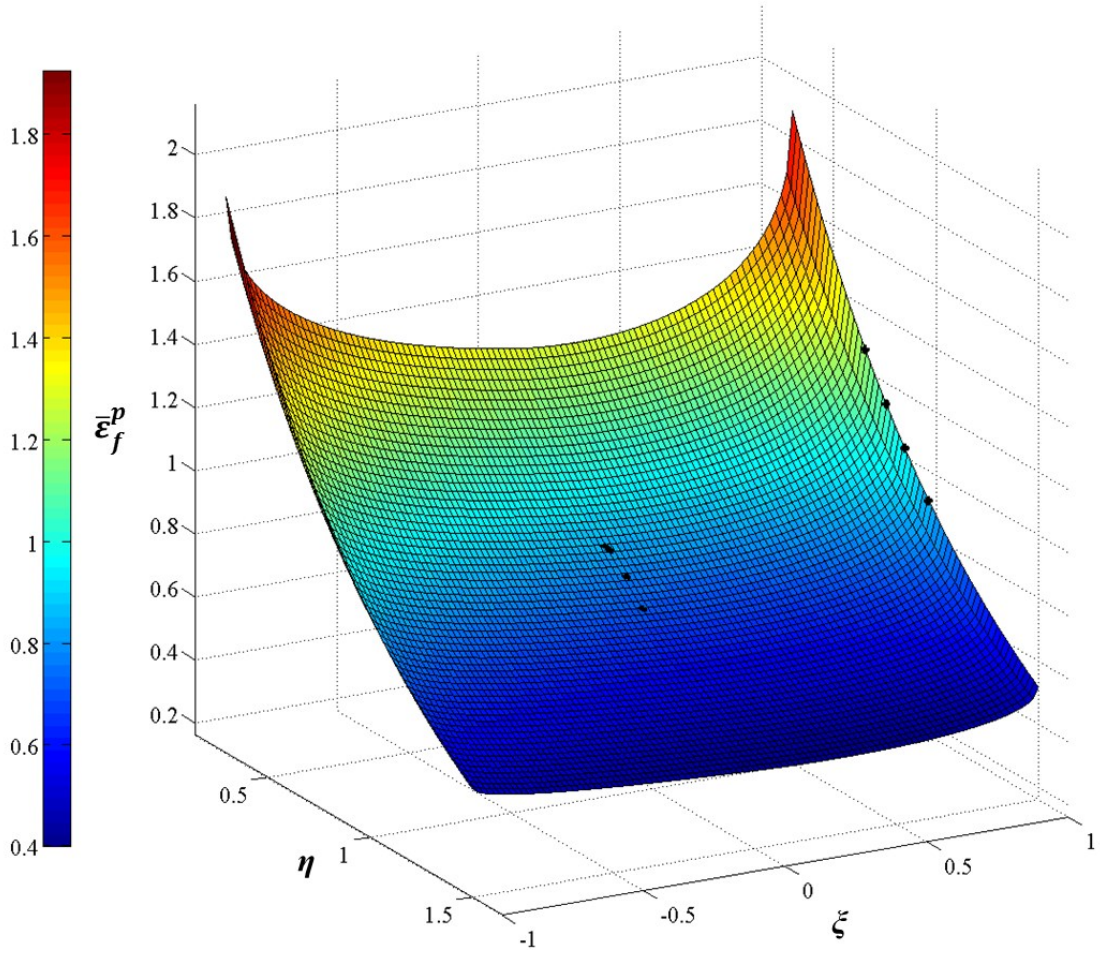

Figure 4-32: M-C fracture surface envelope calibrated for X65 steel

It is beneficial to combine the previous database on fracture strain of the steel pipelines reported in Table 4-1 with the results obtained in the current research to develop a general fracture toughness for high-strength steel pipelines. To do so, it is reasonably assumed that the equivalent plastic strain to fracture calculated by FEA is almost equal to the equivalent fracture strain as $\bar{\varepsilon}_f^p \approx \bar{\varepsilon}_f$ (Bai and Wierzbicki 2008). According to the studied from the FE modeling, this assumption will introduce an error less than 0.4% which is quite negligible.

Figure 4-33 compares the equivalent plastic strain to fracture versus stress triaxiality on ξ=0, 0.7, 0.85 and 1 planes for X65, X70, and X100. It is understood that the fracture strain is irregular and cannot be related to the steel grades. Therefore, the average of

curves are calculated for different values of ξ as shown in Figure 4-33. The average curves are imported into an optimization process to minimize the MSE function and calibrate the *Xue*'s model given in Eq. (3-19) as follows:

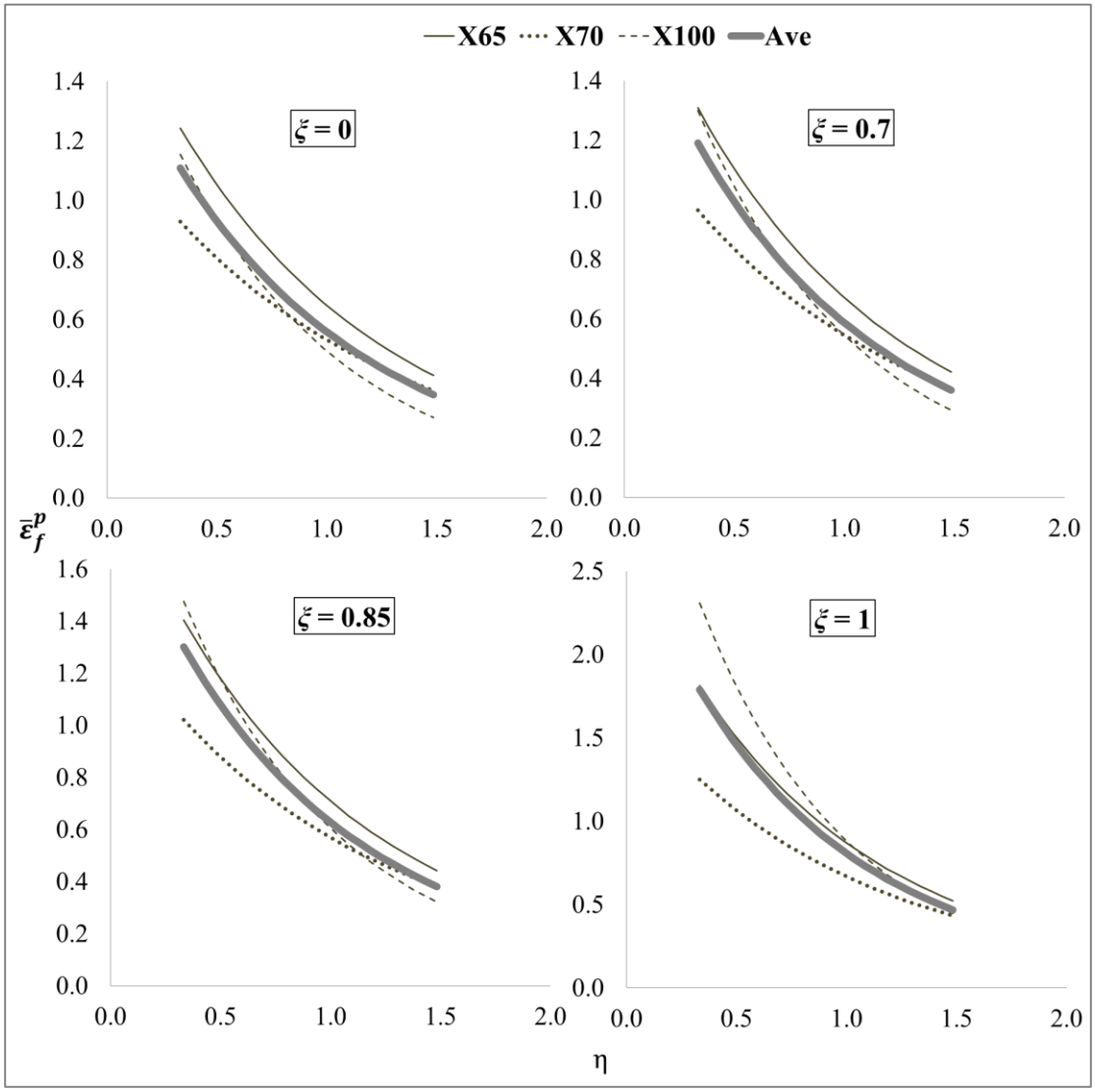

Figure 4-33: $\left(\eta_{ave} - \bar{\varepsilon}_f^p\right)$ curves at ξ=0, 0.7, 0.85 and 1 planes for X65, X70 and X100 and the average curves

$$\begin{cases} \bar{\varepsilon}_f^{p\ (\xi=1)} = 2.64\exp\left[-1.18\eta\right], \\ \bar{\varepsilon}_f^{p\ (\xi=0)} = 1.54\exp\left[-1.02\eta\right] \\ \& \\ k = 2.97 \end{cases} \qquad (4\text{-}12)$$

Figure 4-34 illustrates the average fracture toughness in the form of equivalent plastic strain generalized for high-strength steel pipelines obtained by calibrating symmetric *Xue*'s model.

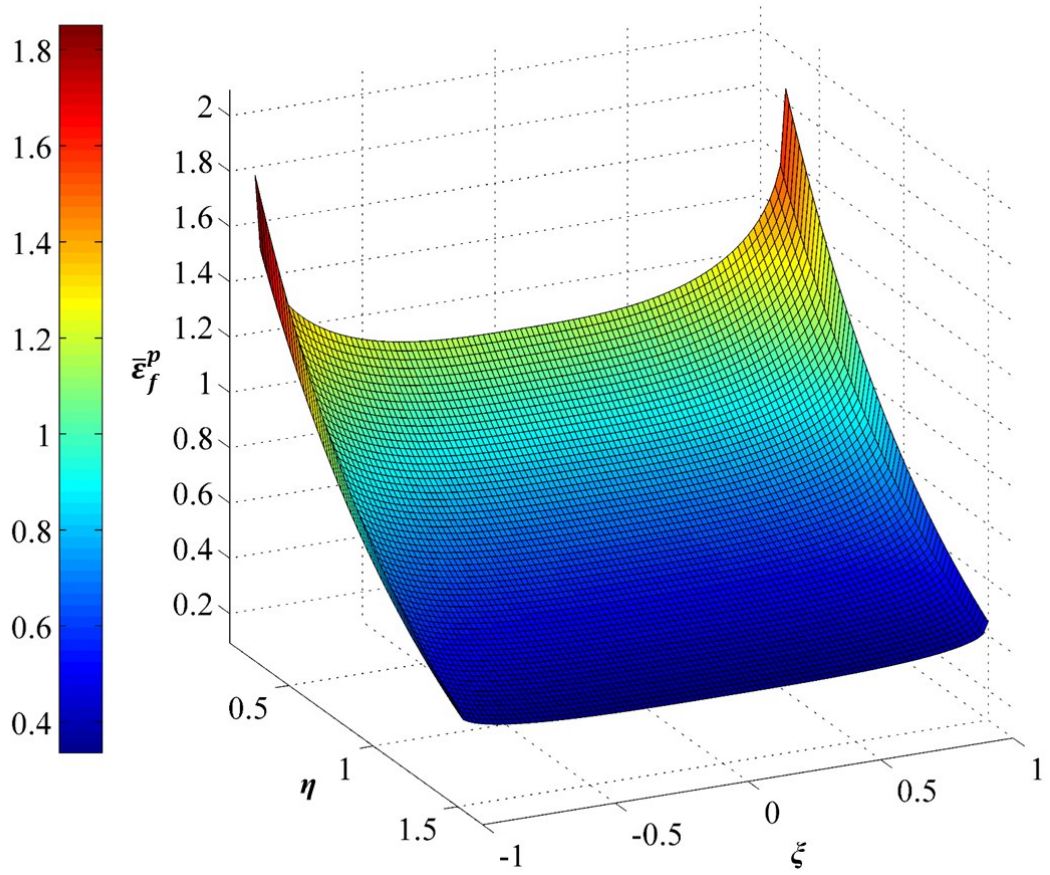

Figure 4-34: Averaged fracture surface envelope for high-strength steel pipelines using *Xue*'s model

4.9 Fracture Strain for Plane Stress Loading Condition

The D/t ratio of energy pipelines is usually sufficiently large to reasonably assume that no radial stress is developed in the pipe wall. This assumption reduces the constitutive relations to the plane stress configuration. In case of plane stress condition, *Wierzbicki and Xue* (2005) postulated that the normalized third deviatoric invariant can be nonlinearly related to the stress triaxiality as follows

$$\xi = -\frac{27}{2}\eta\left(\eta^2 - \frac{1}{3}\right) \qquad (4\text{-}13)$$

Therefore, the fracture locus can be only expressed as a function of stress triaxiality if the equation of fracture surface is known provided that one of the principal stresses in any direction is zero. Figure 4-35 depicts the equivalent plastic strain to fracture versus stress triaxiality in the case of plane stress loading condition for X65, X70, X100 and general HS steel pipeline (developed in Section 4.8).

4.10 Summary

A set of dogbone specimens, RB specimens and GP specimens with different notch radii were made of X65 steel grade and tested under axial tensile load. The test results suggest a remarkable dependence of the ductile fracture of X65 steel on both stress triaxiality and Lode angle.

Parallel FE simulation of all experiments was conducted to calibrate the plasticity and fracture models. It was shown that the best fit of the power law to the post-yield experimental stress-strain data can be successfully used to model the post-necking stress-strain relation of the steel. Furthermore, the equivalent plastic strain to fracture was obtained from the parallel FEA of the RB and GP experiments at the experimentally observed fracture points. And, the average stress triaxiality was calculated from the FEA results. It was shown that the equivalent fracture strain of the RB and GP tests resulted in two distinct exponentially decreasing functions with

respect to the stress triaxiality where the fracture strain for the plane strain GPs is decreased in comparison to that of RBs (Lode effect). Therefore, the ductile fracture toughness was calibrated as a surface of the equivalent plastic strain to fracture versus the average stress triaxiality and the third deviatoric stress invariant using the M-C fracture criterion. Lastly, the obtained results were combined with the available database from previous studies and a general fracture surface was derived for the steel pipelines using *Xue*'s model.

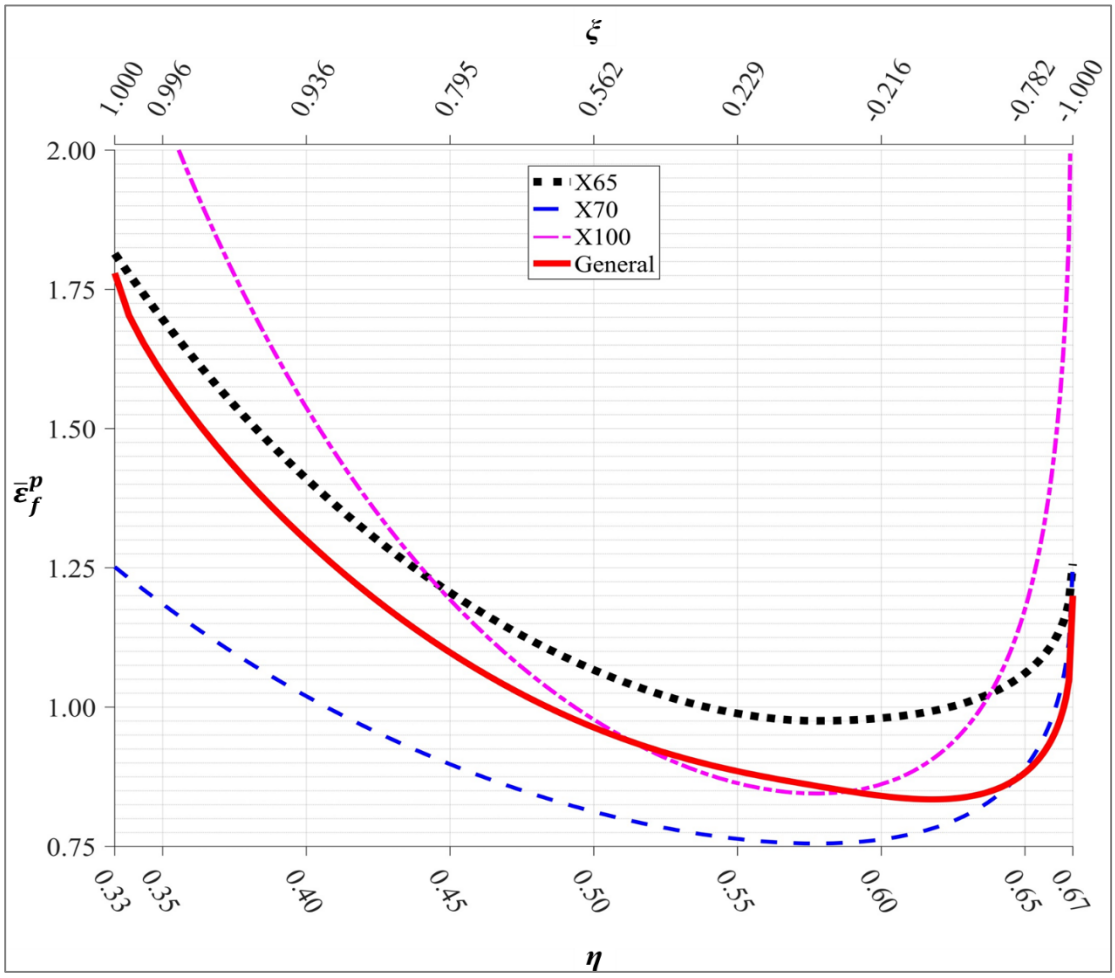

Figure 4-35: Fracture locus for plane stress loading condition

CHAPTER 5: FULL-SCALE TESTS AND FE SIMULATION

5.1 Introduction

Since conducting full-scale tests always demands considerable efforts and cost, normally a few of them are only considered in a research program to study the problem of interest. However, FE simulations can be reliably used as an efficient tool to study a wide variety of load combinations, material properties or boundary conditions (BC) which are not examined by the full-scale tests provided that the credibility of FE models and simulation techniques are verified by the experimentally observed behavior.

Four different full-scale tests are selected from the previous pertinent works to be studied in the current research. The specimens mutually have similar characteristics and are tested under internal pressure, axial load and monotonically-increasing curvature. The first specimen was obtained from the experimental program on X65 cold bend pipes conducted by *Sen* (2006) at the University of Alberta. Next two ones were taken from the tests on X80 line pipes conducted by JFE steel corporation (Tajika et al. 2011). And, the last test was one of the X70 experiments tested by *Dorey* (2001) at the University of Alberta. Rupture of the buckled cross-section at tension side was only the case of failure for the first and second tests. The next two tests were decided to be examined due to their similar geometry, boundary conditions, and loading in comparison to the first and second tests, however, they did not show the same failure as the first couple since those tests were stopped after the formation of local buckling.

In this chapter, the description of the experiments is provided. Afterward, the FE simulation of all four tests is described. The simulation techniques and features used in the FE models are comprehensively elaborated.

5.2 Description of Full-Scale Experiments

In this section, a general description of the full-scale tests including the details of specimens, the test set-up, and procedure are provided and the final experimental results are presented in graphic forms. It should be noted that the test information was

obtained from three different experimental research programs (Sen 2006; Tajika et al. 2011; Dorey 2001) in which the initial objectives were to study the CBS of the pressurized steel pipes due to increasing monotonic curvature.

5.2.1 Test Specimens

Table 5-1 summarizes the material and geometry details of the full-scale test specimens. The first specimen is only a cold bend pipe and the rest are line pipes. The specimens are from two categories: 1) NPS 30 with D/t ratio of 92 (No.1 & 4); and, 2) NPS48 (No.2 & 3) with D/t ratio of 54. The specimens are of different steel grades as shown that are covering a range of Y/T ratio between 83 to 94.

The nomenclature of the specimens is set based on the following pattern

$$X\ \#_1\ D\ \#_2\ Y\ \#_3\ p\ \#_4\ T\ \#_5$$

where the numbers reflect the following quantities

$\#_1$: steel grade based on API 5L specifications

$\#_2$: D/t ratio

$\#_3$: Y/T ratio

$\#_4$: p/p_y ratio (Table 5-2)

$\#_5$: T_A/T_{Ay} ratio (Table 5-2)

5.2.2 Tests Set-Up and Loading Procedure

Since the intention of all three experimental programs was to investigate the buckling strain, all experiments were conducted following similar boundary conditions and loading steps. Figure 5-1 schematically demonstrates the test set-up that was used for the X65 and X80 specimens (Figure 5-2 and Figure 5-3). However, the test set-up shown in Figure 2-1 was used for the last X70 specimen in which an extra MTS 6000 loading machine was set along the pipe axis to axially load the specimen and modify the axial internal force developed in the pipe specimen during the test (Dorey 2001).

Moment arms were used to apply the bending curvature to the pipe specimens by introducing an eccentricity to the influence line of the applied load. A hydraulic jack was engaged in all experiments to apply force against the moment arm. And, collars were mounted on all the specimens to avoid the formation of so-called elephant leg buckles at the ends of specimens due to the effect of boundary conditions.

Table 5-1: Summary of the full-scale specimens

No	Specimen Name	Grade	NPS*	D	t	D/t	L_s **	Y/T
				mm	mm	-	mm	%
1 [1]	X65D92Y94p80T32	X65	30"	762	8.3	92	7391	94
		L_{v0}*** = 152.81mm				θ_{cb}**** = 8.04°		
2 [2]	X80D54Y90p60T27	X80	48"	1220	22.5	54	8000	90
3 [2]	X80D54Y83p60T26	X80	48"	1219	22.6	54	8000	83
4 [3]	X70D92Y89p80T18	X70	30"	762	8.3	92	2700	89

* Nominal Pipe Size

** The End-to-end straight length of pipe specimen

*** The initial Middle deflection due to cold bend

**** Cold bend Central Angle

[1] Sen (2006)

[2] Tajik at al. (2011)

[3] Dorey (2001)

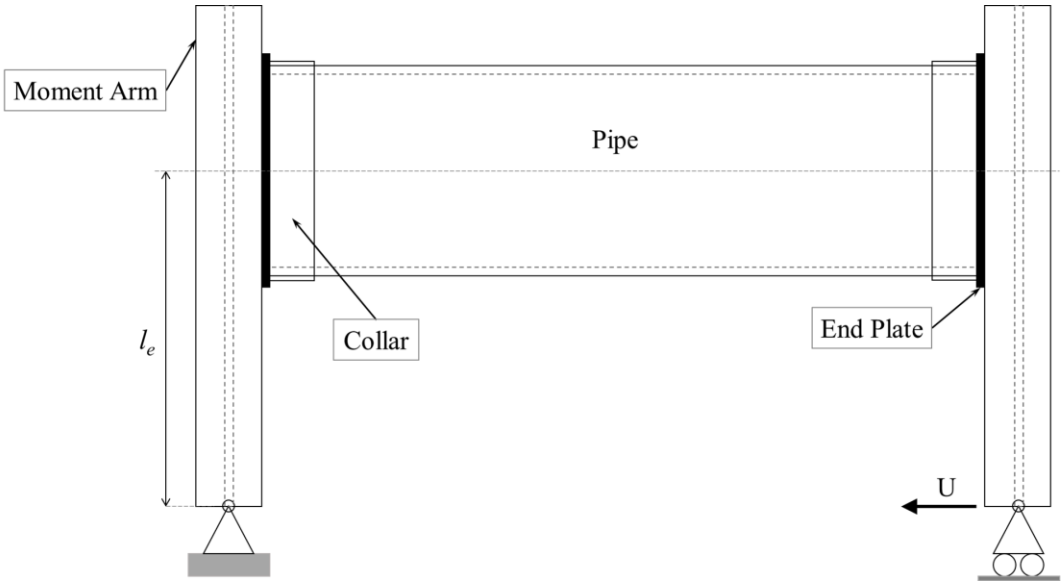

Figure 5-1: Schematic view of test set-up for X65 and X80 specimens

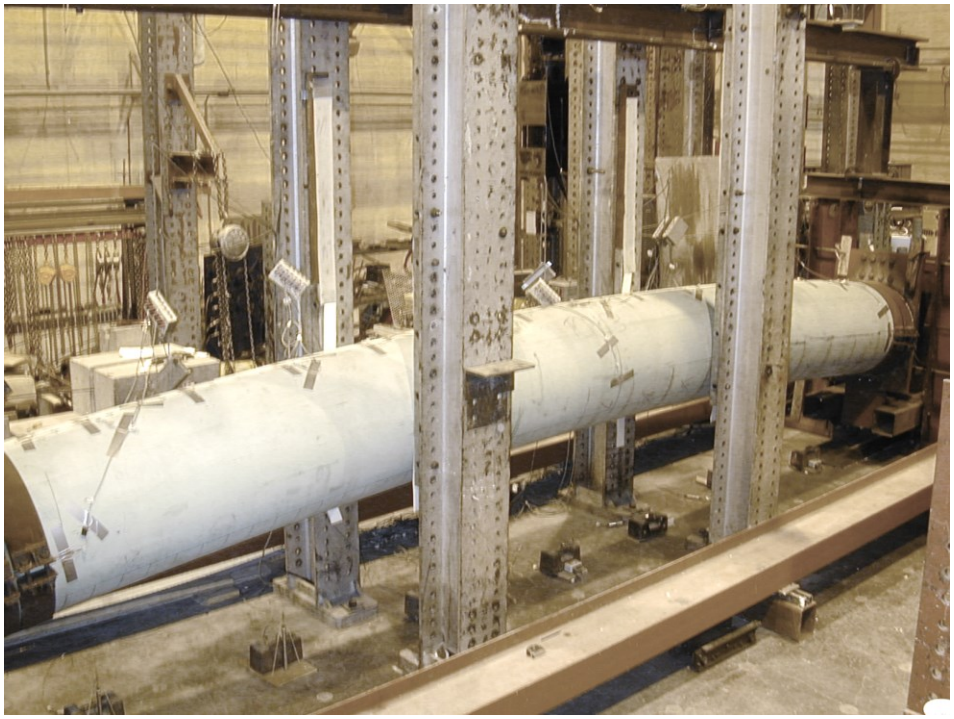

Figure 5-2: *Sen*'s test set-up (Sen 2006)

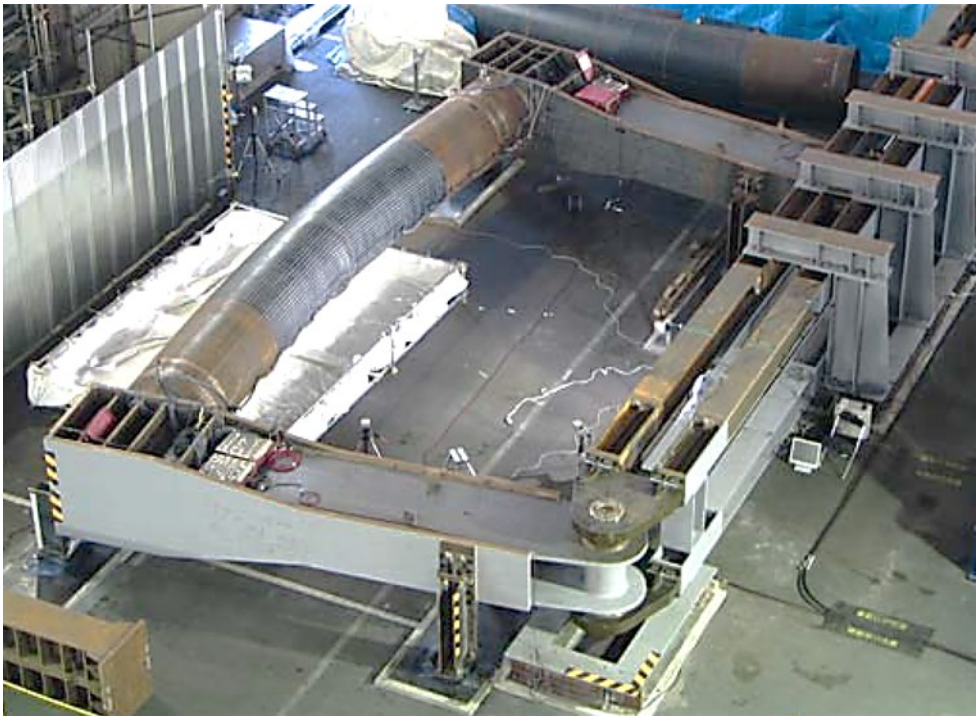

Figure 5-3: JFE test set-up (Tajika et al. 2011)

Table 5-2 reports the amount of internal pressure and axial tension that each specimen was subjected to during the test as well as the eccentricity of the applied load on moment arms with respect to the axis of pipe specimens (l_e). The sequence of loads that were applied to the specimens could be itemized as follows

1- The internal pressure was developed in all the specimens by using hydrostatic pressure to reach the values specified in Table 5-2. The internal pressure was monitored and kept constant through the next loading steps. It is important to be noted that other than radial pressure in the pipe cross-section, axial tensile load (T_p) is also applied to the specimen at this stage by the internal pressure acting on the end plates which is inevitable but considerable (Table 5-2). The collars are installed after internal pressure
2- Only for the last specimen, an MTS machine was used to apply a compressive axial load (P_c) in a force control manner to reduce the axial tension force developed in the specimen (by internal pressure) to approximately 18% of the yield force. The MTS was set to auto stroke control mode to monitor and keep

the total internal axial force (T_A) constant even in the post-buckling loading path.

3- In a displacement control loading manner, monotonic bending curvature was imposed to all the specimens by a loading jack eccentrically forcing against the moment arm. This eccentric load applies a bending moment about the pivot point on the pipe axis. In addition, it is worthy of notice that an axial force is also developed in the pipe specimen at this stage due to the jack load. Only for the last test, this axial load was counteracted by monitoring and maintaining the axial load constant to the desired value. However, jack load inserted a compressive axial load in other specimens (e.g. cold bend specimen which was loaded in closing mode) for which no loading machine had been considered in the set-up along the axis of the pipe specimens. For the first and second experiments, the monotonic curvature was increased in the post-buckling region until rupture occurred on the opposite side of the bulging buckle. This process spent four days to be implemented for the cold bend specimen, and accordingly, the specimen had to be unloaded and reloaded again three times. In the case of the third and fourth specimens, tests were stopped and the specimen were unloaded after the local buckling took place.

5.2.3 Test Results

Figure 5-4 to Figure 5-6 illustrate the final load-deformation plots of the X65 (No.1), X80 (No.2 &3), and X70 (No.4) specimens respectively. Middle moment versus global curvature measured from the test is chosen to verify FEA model for the cold bend specimen as it accommodates the secondary moment due to initial deflection. Load-displacement of the hydraulic jack and End moment versus global curvature was respectively picked as the representation of the load-deformation response of the X80 and X70 line specimens. As it is seen from the Figure 5-4. the X80 line pipe with Y/T ratio of 83 was unloaded after buckling. So was the X70 specimen (Figure 5-5).

Table 5-2: Details of radial, axial and bending loadings

Specimen Name	p	p/p_y[1]	T_p[2]	P_c[3]	T_A[4]	T_A/T_{Ay}[1]	l_e
	MPa	%	kN	kN	kN	%	mm
X65D92Y94p80T32	7.7	80	3338	0	3338	32	600
X80D54Y90p60T27	12.0	60	13003	0	13003	27	6000
X80D54Y83p60T26	12.0	60	12976	0	12976	26	6000
X70D92Y89p80T18	8.6	80	3757	-1859	1898	18	1500

[1] The subscript "y" denotes to the load that is associated with yield in the specimen

[2] T_p is the axial tensile load developed due to internal pressure acting on end plates

[3] P_c reflects the axial compressive load imposed by the loading machine

[4] T_A denotes the total tensile axial force developed in the specimen

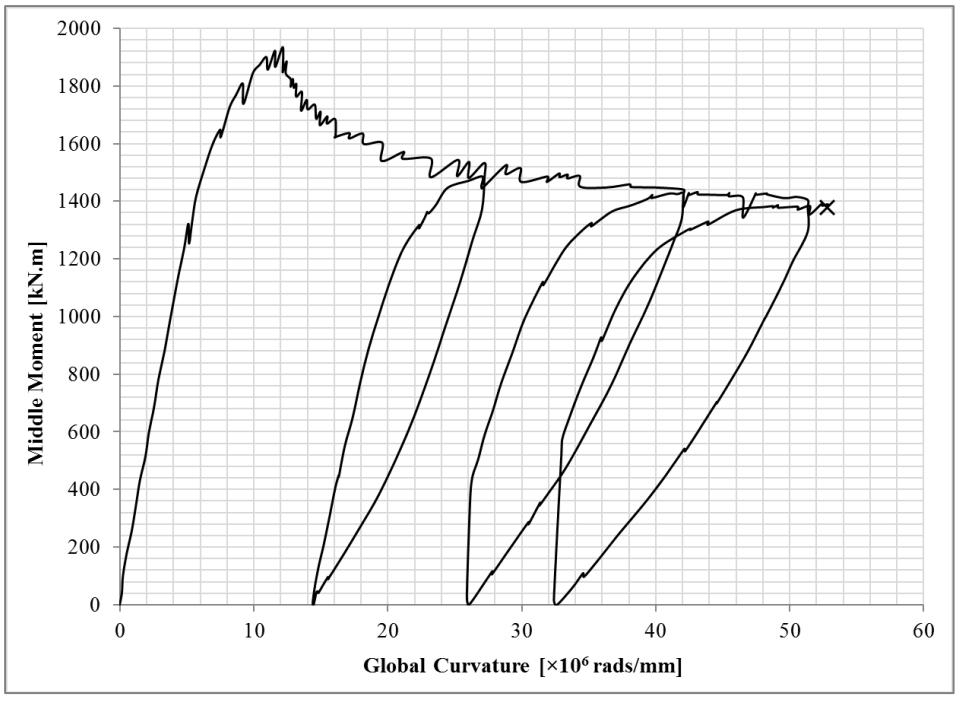

Figure 5-4: The end moment-curvature plot for X65 cold bend specimen obtained from *Sen* (2006)

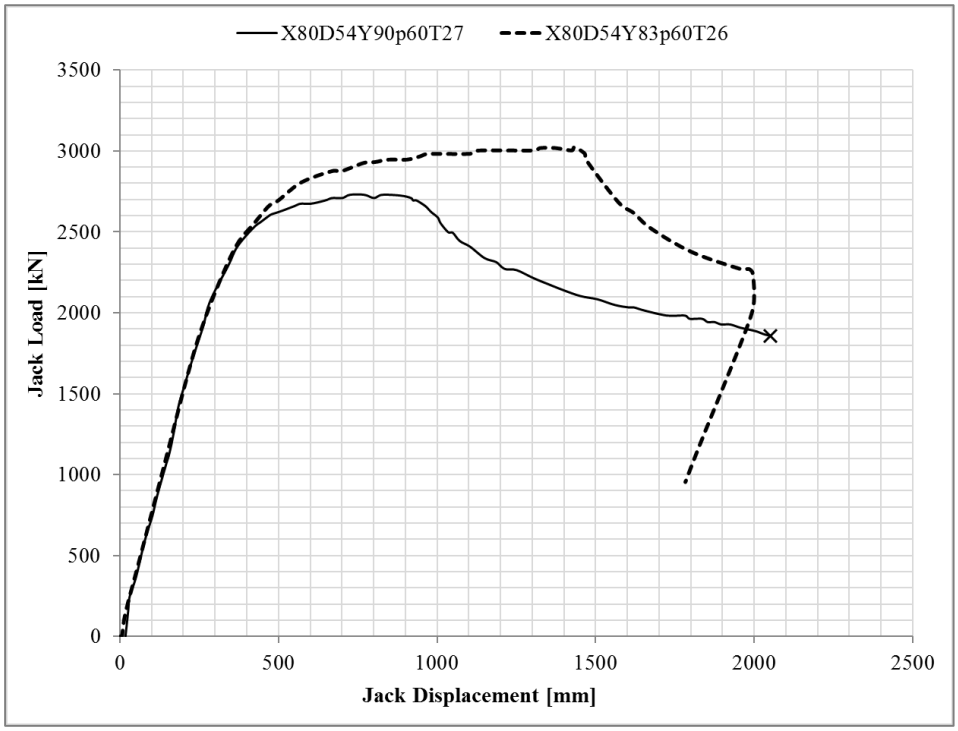

Figure 5-5: The plot of load-displacement of the loading jack for X80 specimens obtained from *Tajika et al.* (2011)

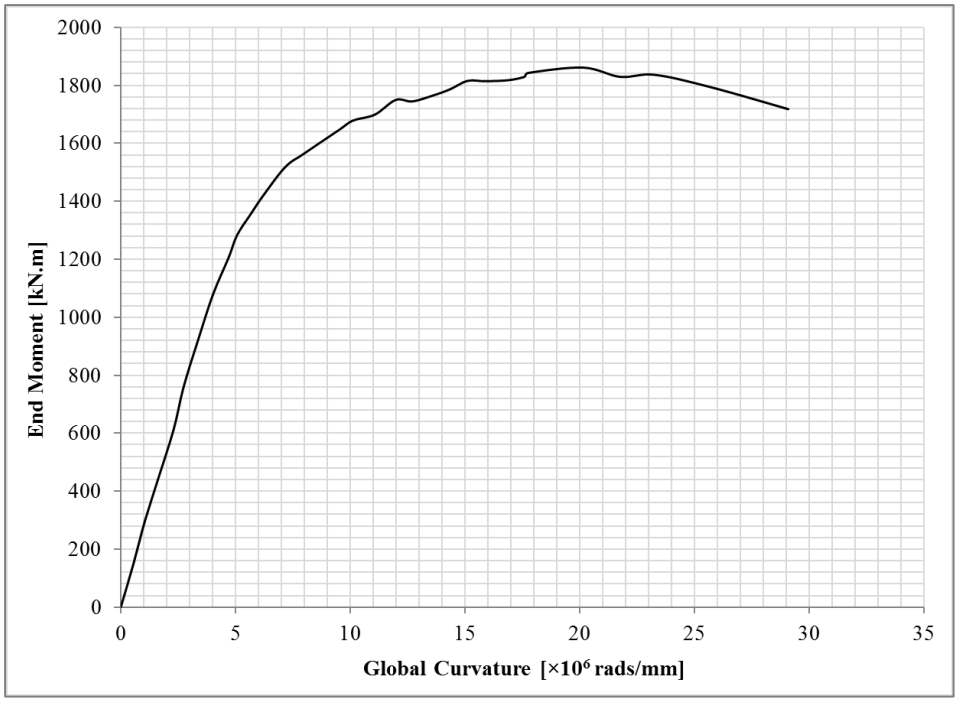

Figure 5-6: The end moment-curvature plot for X70 specimen obtained from *Dorey* (2001)

5.3 Development of FE model

Herein, Abaqus/Explicit V.6-13 (Simulia Corp. 2013) FE platform was used to model all 4 full-scale tests described in the previous section. Simulations were tried to exactly match the real situations governed in the physical tests. Abaqus software provides a complete three-dimensional FE modeling package that includes all the features required to conduct successful simulations of the experiments. For instance, having an extensive element library for different applications, ability to simulate the pressure and follower forces, ability to apply displacement control loads, capability of the plastic analysis using constitution law and isotropic hardening, dealing with material and geometric nonlinearity, and handling material failure and ductile fracture simulation (using the models discussed in the previous chapter) are highlighted as some of the built-in features of the Abaqus software that make it suitable for usage in the current research. Explicit solution method was engaged due to its capability to model the material failure and because of its robustness in dealing with high nonlinear three-dimensional static problems that involve large deformations and solution discontinuity like local buckling and wrinkling.

5.3.1 Pipe Modeling

A program was developed by which the geometry of the pipes' body was constructed as a surface in AutoCAD V.2014 and imported into Abaqus. This was done to include the initial geometric imperfections of the line pipes. The following sections provide the simulation details of the pipe specimens.

5.3.1.1 Initial Imperfection

Initial imperfection was introduced to the mid-length of the line pipe specimens using the so-called half-ring model. Since the half-ring model was found unrealistically increasing the effect of initial imperfections in FEA (Dorey 2001), the half of the maximum amplitude of the experimentally measured imperfections were considered in the analytical simulations (Tajika et al. 2011; Dorey 2001). Table 5-3 includes the

maximum amplitude and length of the geometric imperfections used for line pipes. No initial imperfections were modeled for the cold bend pipe.

Table 5-3: Imperfection of the line pipe specimens

Specimen Name	$(A_{imp})_{max}$	L_{imp}
	mm	mm
X80D54Y90p60T27	0.4	500.0
X80D54Y83p60T26	0.2	250.0
X70D92Y89p80T18	1.0	300.0

Figure 5-7 schematically shows an imperfect pipe and the definition of variables used to develop the initial imperfection in the geometry. The radius of the pipe at each imperfect half of the cross-section (R_{imp}) is defined as

$$R_{imp} = R_{Pipe} + A_{imp}\sin(\theta) \qquad 0 \le \theta \le 180^{\circ} \tag{5-1}$$

in which, the amplitude of imperfection (A_{imp}) varies between the imperfect length (L_{imp}) (Figure 5-7) as follows

$$A_{imp} = \left(A_{imp}\right)_{\max} \sin\left[\frac{x_{imp}}{L_{imp}}\pi\right] \qquad 0 \le x_{imp} \le L_{imp} \tag{5-2}$$

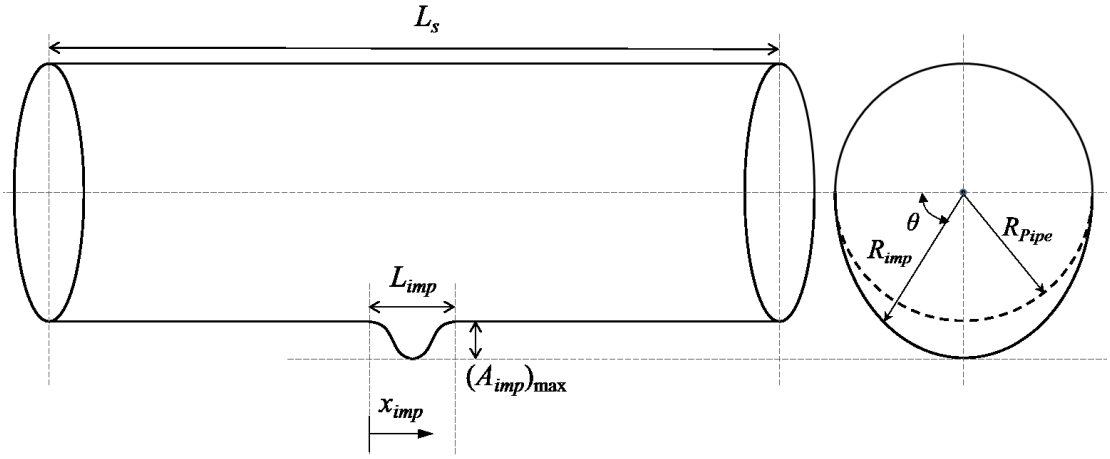

Figure 5-7: Imperfect pipe scheme and definitions of variables

5.3.1.2 Element Selection and Meshing

The S4R shell element (Simulia Corp.2013) is chosen from the Abaqus/Explicit element library and assigned to the pipes' body to simulate the plane stress condition developed in the pipe wall. The S4R element is a three-dimensional 4-node quadrilateral shell element with 6 degrees of freedom at each node.

Reduced integration is used by lower order integration approximation to obtain the stiffness matrix of the S4R element which makes it a quite computationally inexpensive element. S4R is a uses the isoparametric formulation with linear (first-order) shape function to interpolate the displacement field within the element based on the nodal displacements resulting in a considerable reduction of computational cost.

The S4R element allows for arbitrarily large rotations and finite membrane strains (in-plane strains) in the large-deformation analysis which makes it a good choice for large-strain nonlinear geometric analysis (e.g. buckling analysis). Stress in the thickness direction of the S4R element is zero, however, it accounts for the through-thickness deformations due to the Poisson's ratio effect which makes it suitable for plastic analysis involving large deformations and necking.

S4R is a general-purpose element that accounts for transverse shear deformations. It uses classical shell theory (that does not consider the transverse shear deformations) for thin shells and shear flexible theory for thick shells which makes it robust and accurate for solving both thin and thick shell problems being subjected to any desired loading conditions.

The S4R shell element avoids the so-called hourglassing problem through assigning a very small artificial stiffness to the degree of freedom associated with hourglass deformation mode. Hourglass is plausible to occur when using reduced integration elements and is a situation similar to a rigid body motion where no internal strain energy is obtained for the element resulting in meaningless outputs.

As the size of the finite elements is reduced in a model, the number of elements and accordingly the accuracy of the solution is increased. However, this will be accompanying by a significant increase of computational efforts. Therefore, there is always a trade-off between the accuracy of the solution and the time of analysis to define the mesh size. Mesh study is a common method that is used to achieve the fine mesh size for an FE model. In this method, FEA with various mesh sizes are performed and the fine mesh size is obtained where the response of the analysis perfectly matches the analyses with smaller elements. That is, the fine mesh size is associated with the mesh size below which no considerable change is observed in the general load-deformation response of the FEA. The fine element sizes for the FEA of X65 and X70 specimens were obtained from the previous mesh studies (Dorey 2001; Sen 2006). And, a mesh study was performed to obtain the fine mesh size for the X80 specimens. However, smaller (finer) mesh sizes were defined in the FEA of full-scale tests (as reported in Table 5-4) in order to achieve more accurate strain values at the fracture location.

Another practice to increase the accuracy of the solution with a reasonable computational cost is to assign a very fine mesh to the critical regions and use a coarse mesh size for the rest of model. However, previous studies (Mohareb et al. 2001; Dorey 2001) showed that having different mesh sizes along the length of pipe in FEA will lead to a local buckling artificially created right at the boundaries between the coarse

and fine meshed regions. Therefore, a structured mesh pattern was used to generate uniform square elements (i.e. aspect ratio of unity) of the same size (Table 5-4) between the two ends of pipe models.

Table 5-4: Mesh size for different pipe models

Specimen Name	Mesh Size
X65D92Y94p80T32	20mmx20mm
X80D54Y90p60T27	25mm×25mm
X80D54Y83p60T26	25mm×25mm
X70D92Y89p80T18	16mm×16mm

5.3.1.3 Material Stress-Strain Calibration

The experimental data obtained from material tests were used to calibrate the stress-strain curve for the pipe specimens through the methodology proposed in Section 4.6. Figure 5-8 to Figure 5-10 demonstrate the stress-strain curves of steel material calibrated for X65, X80, and X70 pipe specimens using experimental data (diagrams show stress-strain curve up to only 25% strain). Since the objective of all full-scale tests was to study the local buckling strain, limited material test data were available for the full-scale pipe specimens and no special procedure like what explained in Section 4.4 had been followed to measure the rigorous static stress-strain behavior of the material. Although the calibration of post-necking stress-strain is highly dependent on the slope of the pre-necking stress-strain curve which accordingly determines the final fracture prediction by FEA, it was assumed that the static stress-strain curve follows the same family of slopes as the experimentally obtained curve up to the onset of diffused necking as typically shown in Figure 5-8. Power law was calibrated similar to Section 4.6 to reflect the post-necking stress-strain behavior. The calibrated equation

of power law for each specimen is given in the corresponding diagram (Figure 5-8 to Figure 5-10). The calibrated stress-strain curves were fed into the FE models to perform a plastic analysis up to the final fracture initiation.

5.3.1.4 Damage Evolution and Ductile Fracture Model

As it was shown in previous chapters, fracture strain of the pipeline steels is dependent on two parameters; namely, stress triaxiality and Lode Angle. To predict the onset of ductile fracture in the FEA, the *Johnson*'s cumulative damage criterion introduced by Eq. (3-14) is used in its following form as the fracture criterion in which the equivalent plastic strain to fracture is stated as a function of stress triaxiality and the normalized third deviatoric stress invariant.

$$\Phi_S = \int_0^{\bar{\varepsilon}_f^p} \frac{d\bar{\varepsilon}^p}{\bar{\varepsilon}_f^p(\eta,\xi)} = 1 \qquad (5\text{-}3)$$

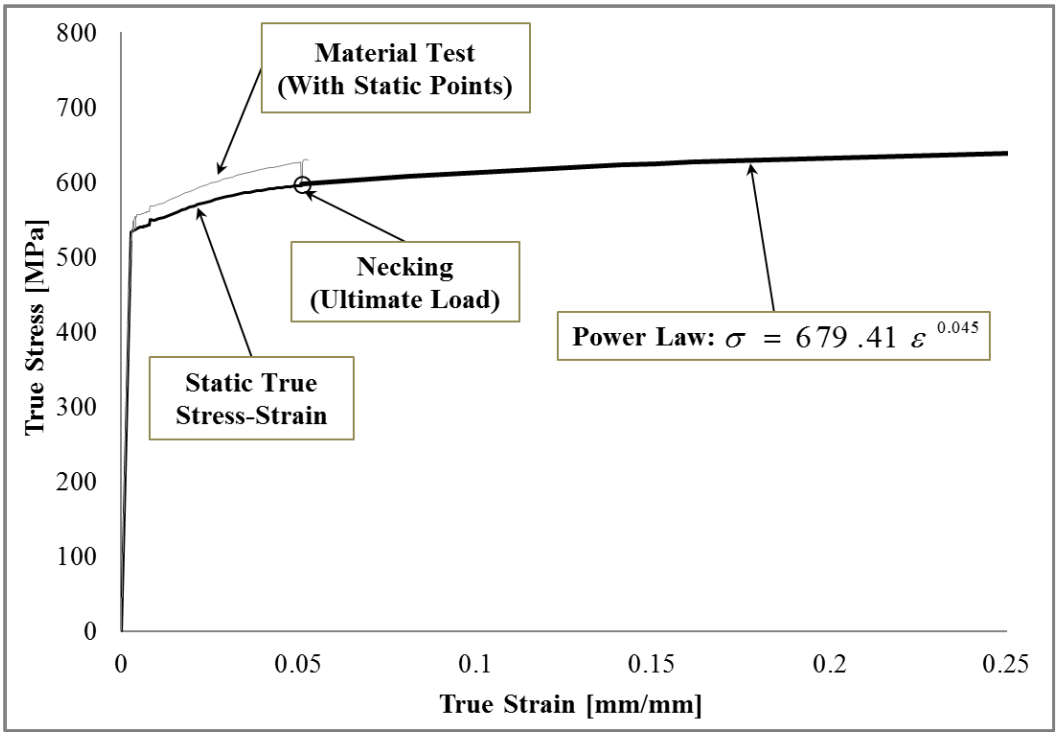

Figure 5-8: Stress-strain curve calibrated for X65 cold bend specimen

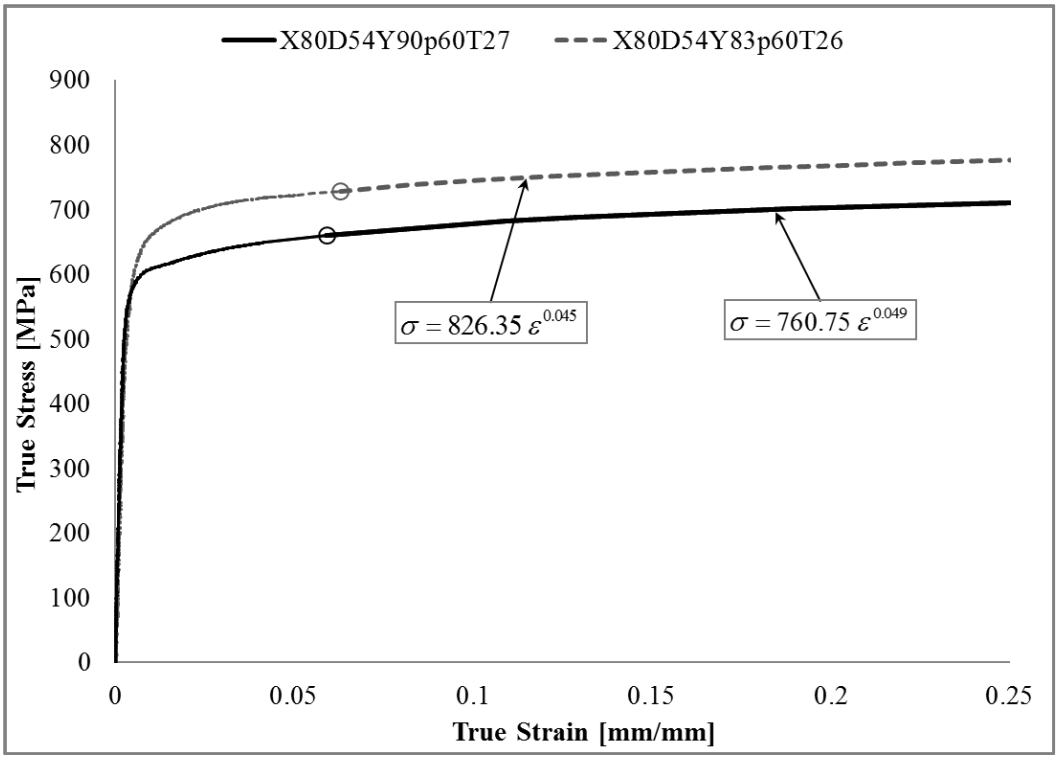

Figure 5-9: Stress-strain curve calibrated for X80 line specimens

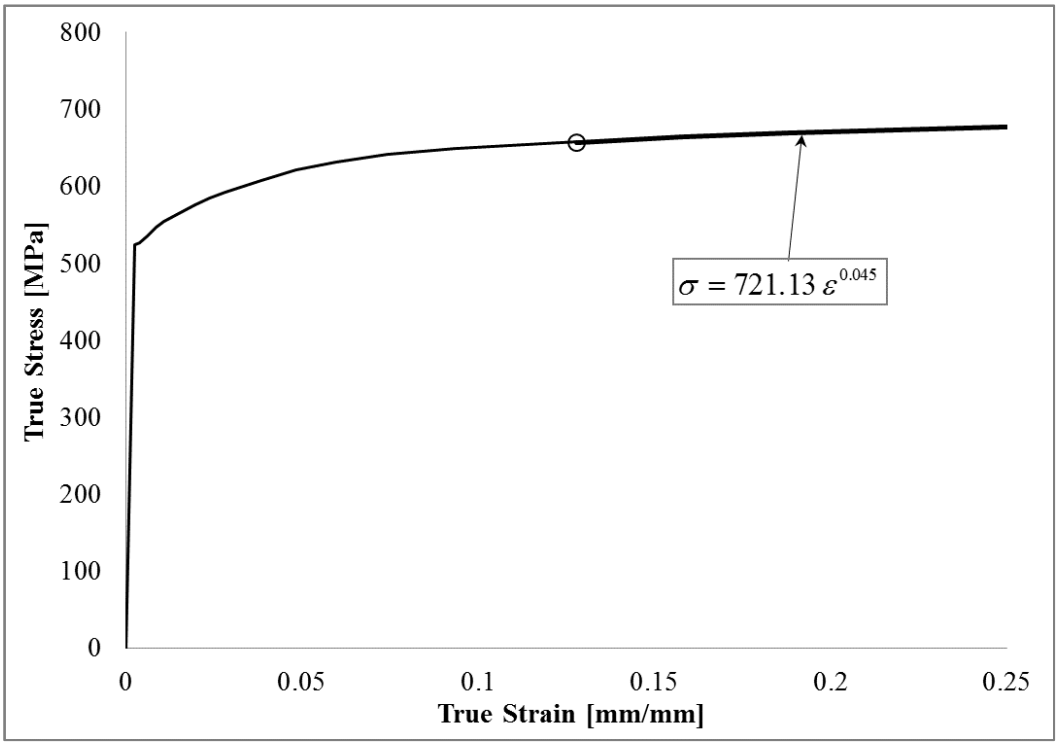

Figure 5-10: Stress-strain curve calibrated for X70 line specimen

in which, Φ_S will be hereafter referred as fracture index, the $\bar{\varepsilon}_f^p(\eta,\xi)$ is the inverse of integrating function and denotes the fracture locus in the $(\bar{\varepsilon}_f^p,\eta,\xi)$ space. The equivalent plastic strain to fracture for X65 steel material that was calibrated in the previous chapter (Table 4-7) is incorporated into Eq. (5-3) and used for the X65 cold bend pipe. The general fracture toughness that was derived for pipelines' high-strength steels and was proposed in Eq. (4-12) is assumed as the fracture strain for X80 line pipes. And, fracture locus postulated by *Kofiani et al.* (2013) for X70 steel (Table 4-1) is considered for the X70 line specimen.

The fracture criterion given by Eq. (5-3) is used in conjunction with Von Mises plasticity model. Once this criterion is convinced and the integration accumulates to unity at any point in an element, material fails at that point and the ductile fracture initiates in the FE simulation. At this point, it is assumed that the element which meets the fracture criterion loses its entire load-carrying capacity and "element removal" technique is used to remove the failed element from the analysis while preserving its mass. For the S4R type of shell elements, the element removal becomes effective when all the through-thickness integration point of an element convinces the fracture criterion. When an element is removed, stress tensor associated with that element is set to zero which makes it act like new free surface is formed. In terms of fracture mechanic problems, element removal could fairly predict the crack growth in the continuum body after the formation of ductile crack provided that a very dense mesh is used at the fracture location since the coarse mesh results in an unreal crack blunting (Lee 2005). However, the intention here is the prediction of ductile macro-crack formation and its propagation is not of interest as it is reasonably assumed that the final rupture of pipe wall coincides with the ductile fracture initiation.

As mentioned in Section 3.2, the ductile fracture phenomenon is the result of void nucleation and coalescence to form micro-cracks followed by the growth of these micro-cracks and conversion to macro-cracks. By default, Eq. (5-3) is used by Abaqus only to predict the damage initiation point due to the onset of void nucleation stage in ductile material, and then, Eq. (3-26) borrowed from damage mechanics is used to progressively degrade the material stiffness representing the damage evolution due to

micro-crack formation stage, until, the material loses its total stiffness and element removal approach eliminates the fully degraded element from the mesh to simulate the macro-crack formation. However, the milestone of fracture strain models studied in Section 3.4, which is the case for the current research, is that the void nucleation and coalescence starts to happen in a ductile material as soon as plastic deformations start due to post-yielding loading. This process is highly accelerated by the initiation of diffuse necking until the localized necking and large plastic deformations meet the fracture criterion of Eq. (5-3) where the ductile crack is formed. Therefore, the D_d variable in Eq. (3-26) is taken equal to unity in the simulations to trigger the failed element removal after the Eq. (5-3) is convinced.

5.3.2 Other Parts of Model

Other components of the tests set-up were modeled in the FE models as required to create a close simulation of physical loads and boundary conditions.

Collars were considered at the both ends of all pipes as a segment of their body with the same material definition and element type assigned to them but with a double thickness value to moderate the effect of rigid end condition of pipes on load transition.

End plates were considered as a relatively thick flat plates with an elastic material with the same elastic modulus as the pipe steel since only a very small amount of out-of-plane elastic deformations were developed in them under internal pressure load (Sen 2006). S4RS type shell elements with small membrane strains assigned to the end plates to account for the in-plane rigidity of the end cross-sections of the pipe specimens.

Moment arms were modeled with a beam cross-section and it was fairly assumed that they behave rigidly during the test for the modeling purposes. A very stiff elastic artificial material with the elastic modulus equal to 2E+20 Mpa was assigned to the moment arms to address their rigid behavior in the analysis. The 2-node B31 type linear beam elements were assigned to the moment arms. Moment arms were necessary to be included in the models for the first three specimens due to the compressive axial force that was developed in these specimens while imposing the curvature by the hydraulic jack. However, moment arms were not included in the FE model for the last X70

specimen since the axial load was conserved constant to the known desired amount by the axial MTS machine for this pipe during the test (Section 5.2.2).

5.3.3 Constraints and Contact

The Proper form of constraints was required to be defined so as to attach all the individual parts of the models to each other in the FE assembly so that suitably interact during the FE analysis and simulate the internal load transition (developed by external loads) between all components in the real test conditions.

End plates were tied to the both ends of the pipes. “Tie” feature rigidly fuses the surface of the end plates with the nodes of pipe ends in such a way that there will be no relative translational or rotational motion between them. Also, “Multi-Point Constraint” or “MPC” feature was used to constrain the displacement and rotation of all nodes in end plates to the motion of the pivot point where the axis of pipe and moment arms meet each other.

Moreover, moment arms were tied to the pivot points for the FE models of the first three specimens. Moment arms were introduced as a “rigid body” to constrain all their nodal degrees of freedom (translational and rotational) so that no relative motion could take place between the nodes.

As the bending curvature is increased in the pipe, the closure of the local buckle might be the case of failure on the compressive side of the cross-section. In this case, a very discontinuous form of nonlinearity is introduced into the analysis due to the contact of the inner surface of the pipe with itself. “General contact” feature in Abaqus was used to address the contact constraint in the FE models using the penalty method which allows for the relative motion between the contact surfaces according to the contact properties. Mechanical properties of contact are defined base on tangential behavior due to friction between the contact surfaces, and the normal behavior at the contact surface. The coefficient of friction of steel on steel is equal to 0.3 and is introduced as the tangential penalty at the contact surface. To avoid the surface penetrations, “Hard” contact approach is used to maximize the penalty stiffness in the normal direction which relates the normal force at contact surface to the penetration distance.

5.3.4 Symmetry, Boundary Conditions, and Loading

The pipe specimens are axisymmetric and theoretically, a quarter of their geometry could be only modeled. However, it was quite necessary to model the half of the geometry to obtain the correct post-buckling deformations. That is, after large deformations, the local buckle starts to move out of its cross-sectional plane where wrinkling starts to form.

As mentioned earlier, two types of FE models were created for the first three specimens and the last one. Figure 5-11 and Figure 5-12 show the FEA models and boundary conditions for the X65 cold bend pipe and the X70 line pipe specimens respectively.

The loading procedure explained in Section 5.2.2 was exactly followed in the FE models to simulate true experimental loading condition. In the last step of loading procedure for the models with moment arms, the bending curvature was exerted on the pipes through applying an increasing horizontal displacement (jack displacement) to the free end of the moment arms (with the roller type BC) similar to the approach used in the physical tests. Whereas, displacement control rotations were directly applied to the pivot points in the FEA of the last specimen for which no moment arms were modeled.

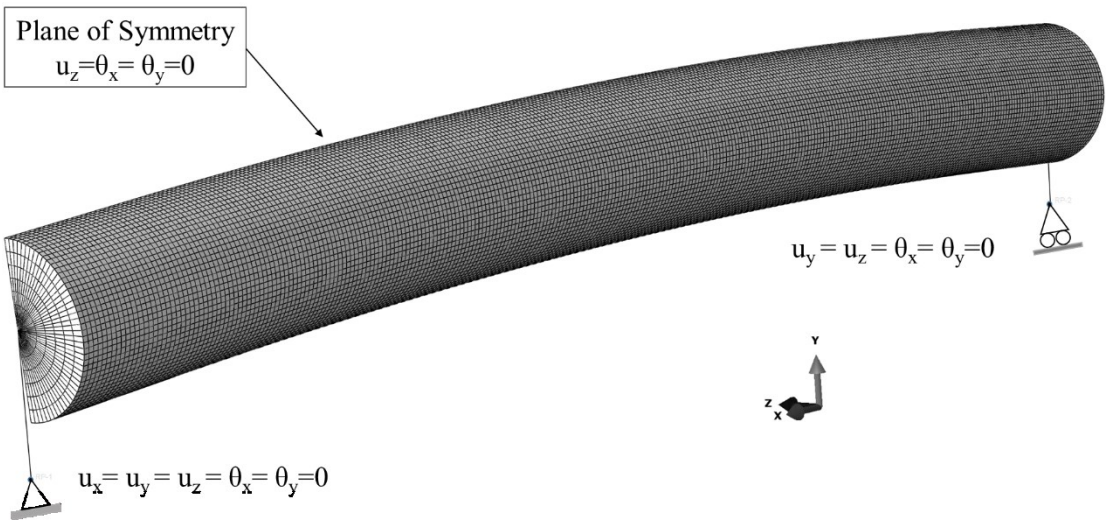

Figure 5-11: FE model and BC of the X65 cold bend specimen

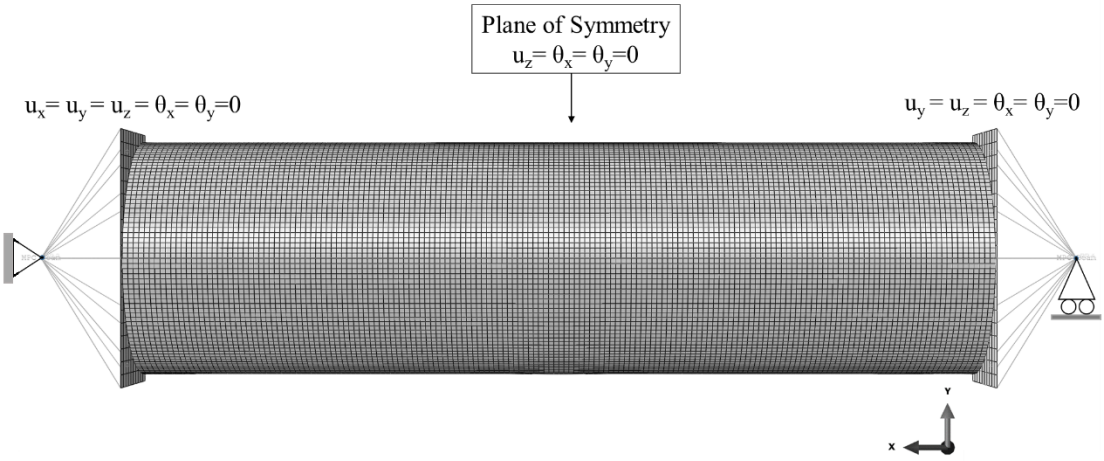

Figure 5-12: FE model and BC of the X70 line pipe specimen

5.3.5 Explicit Solver and Quasi-Static Analysis

The explicit solution method is more efficient and robust than the classical implicit method in solving high nonlinear three-dimensional static problems involving very large plastic deformations, material failure and solution discontinuities like wrinkling or contact interaction. The explicit solver is capable of accommodating the ductile fracture initiation criterion and crack formation discussed in the Section 5.3.1.4 without any convergence issue.

The explicit solver is a true dynamic method that solves for the general dynamic equation of motion based on defining the nodal lumped mass matrix and using the explicit central-difference numerical integration algorithm through small stable time increments. Hence, despite the Newton-Raphson or Riks solvers for the implicit method, no iterations and convergence check is necessary for the explicit approach.

In explicit dynamics, the vector of nodal accelerations, $\ddot{u}_{(t)}$, is first calculated explicitly at any given time through the following equation

$$\ddot{u}_{(t)} = M^{-1}\left(P - I\right)_{(t)} \qquad (5\text{-}4)$$

where M is the nodal lumped mass matrix, P is the vector of external force, and I is the vector of internal force which is zero during the very first time increment (Δt). In fact, the out-of-balance forces, $\left(P - I\right)_{(t)}$, make the stress waves to be initiated from the nodes subjected to external loads and internally propagate between the neighboring elements through the whole model.

Having the nodal accelerations at each time step, element strains are found by the integration rules and state of stress is found using constitutive law. Herein, very small stable time increments are required for integration purposes to obtain accurate solutions. The stable time increment is defined as the minimum time required for the stress waves to travel across any element in the model.

Using the explicit dynamic solution method for solving a static problem demands very small time increments to perform a quasi-static analysis and reduce the effect of inertial forces ($M\ddot{u}$) on the solutions to a negligible level. Simulation of the quasi-static tests in their real physical time period is too expensive and computationally impractical as it requires millions of stable time increments to finish the analysis. Therefore, special techniques are necessary to be engaged to artificially accelerate the time of analysis while keeping the solutions accurate. Loading rate and material density are artificially increased to obtain economical solutions for quasi-static analysis. Increasing the loading rate reduces the total time scale of the analysis, and increasing the material density by a factor of f_{mass}^2 decreases the stable time increments by a factor of f_{mass} .

Accelerating the time of analysis using the two above-mentioned artificial approaches leads to the dominant effect of inertia on the equation of equilibrium and analytical solutions. Therefore, a number of analyses were run for each model and the following examinations were made to obtain the optimal scale factors for the loading rates and mass to keep the inertial impact insignificant in the shortest analysis time.

1- Smooth step amplitude curve offered by Abaqus was used to gradually apply the external loads and avoid the disruption of stress wave propagation in time.
2- The load-deformation response of the explicit models was compared to that of experiments and parallel static analysis of the model using Newton-Raphson solver in Abaqus/Standard V.6-13. Excessive acceleration of the analysis would result in a disturbed deformed configuration or load-deformation curve of the FE model due to inertial effect. For instance, localized buckling close to the external excitations can be developed due to excessive increase of load rating.
3- The kinetic energy of the deforming material was compared to its internal energy during the analysis. It was assumed that the analysis is performed at a quasi-static level once the kinetic energy stands less than 5% of the internal energy during the major part of the analysis.

5.4 Summary

Four full-scale bending experiments were described. The pipe specimens were mutually categorized in 30" and 48" nominal sizes with almost similar material properties at each category and pressurized to 80% and 60% of the SMYS respectively. Under increasing monotonic curvature, one pipe at each category failed due to rupture of the tensile wall on the opposite side of the wrinkling. The other specimens were unloaded after formation of the bulging buckle.

In addition, the FE models of all full-scale tests were developed using Abaqus V.6-13. FE techniques and features were engaged to simulate the real conditions of the physical tests. The material model discussed in the previous chapter was used to model the plasticity and ductile fracture of the material. And, "contact" was modeled to capture any self-contact of the pipe wall due to increased bending curvature.

CHAPTER 6: FEA RESULTS AND DISCUSSION

6.1 Introduction

In this chapter, the FEA results of full-scale testes are presented and verified by the experimental data. The verified FE models are then used to study the ultimate failure modes of the wrinkled buried pipelines due to monotonically-increasing curvature, the key design variables that are responsible for the post-buckling rupture of the tensile wall, and the BC of the bent pipes that are critical in triggering the post-buckling rupture.

6.2 Numerical Results for X65 Cold Bend Specimen

From the results obtained by FEA, the bending moment at the middle of X65 cold bend pipe (where pipe possess initial deflection) and the global curvature developed in the pipe length is calculated by the following equations (Sen 2006)

$$m_b = 2R_{pin}\left(l_e \cos\left(\theta_{FEA}\right) + L_{v0} + \Delta_{vFEA}\right) \quad (6\text{-}1)$$

$$\phi_g = \frac{2\theta_{FEA}}{L_s + 2l_e \sin\left(\theta_{FEA}\right) - \Delta_{roller}} \quad (6\text{-}2)$$

where R_{pin} is the reaction force of the pinned end of the moment arm, θ_{FEA} is the average angle of pinned and roller ends (θ_{FEA}=| $\theta_{pin} - \theta_{roller}$ |/2), Δ_{vFEA} is the vertical deflection of the middle of the pipe obtained from FEA, and Δ_{roller} denotes the horizontal displacement of the roller end of the moment arm at each loading step (Figure 5-11).

Figure 6-1 compares the moment-curvature response of the test and FEA up to the fracture point. It is illustrated that the load-deformation response of the FE model closely mimics the experimentally captured behavior from elastic region to large plastic

deformations while predicting the onset of local buckling and post-buckling behavior. This clearly indicates the capability of the stress- strain calibration methodology proposed in Section 4.6 (also Section 5.3.1.3) to simulate the true mechanical behavior of the steel material under large plastic deformations until the material failure. Furthermore, the fracture strain calibrated for X65 steel material in the previous chapter coupled with the cumulative fracture criterion (Section 5.3.1.4) successfully predicts the fracture initiation point seen in the test as demonstrated in Figure 6-1.

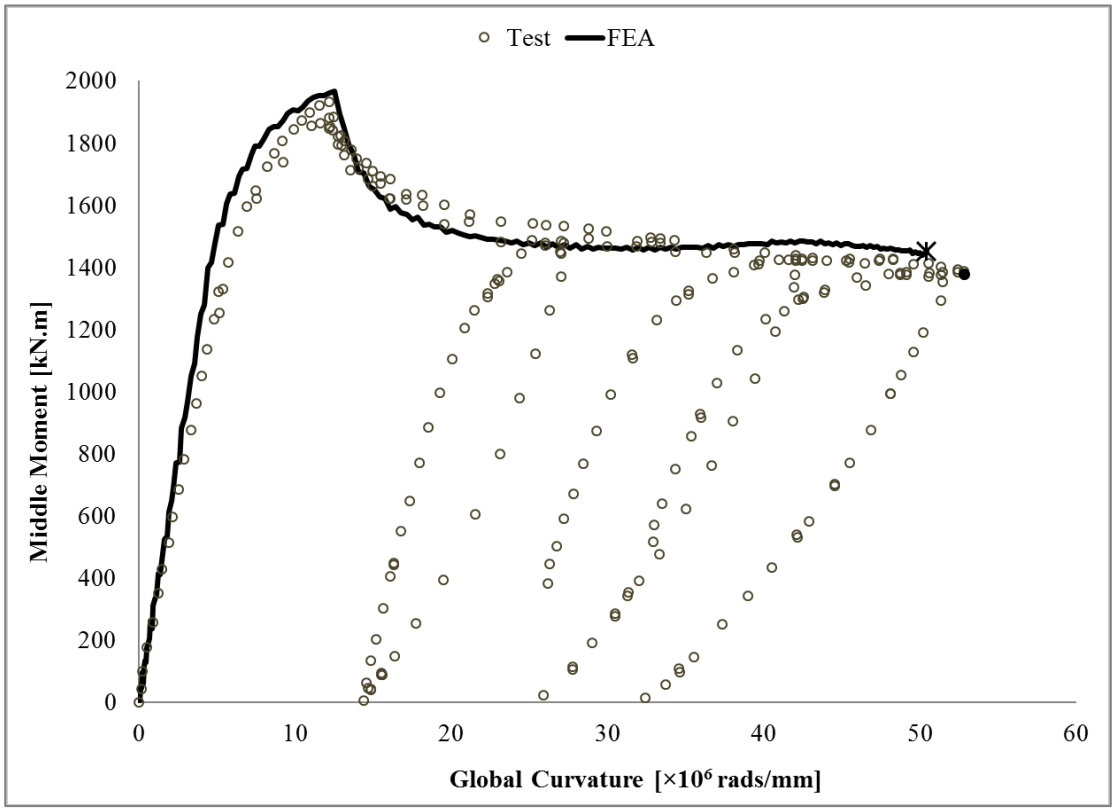

Figure 6-1: Comparison between the experimental load-deformation plot and FEA response up to the rupture for X65 cold bend specimen

In Figure 6-2, the deformed configuration of the cold bend pipe obtained from the FEA is compared to the specimen's deformed shape once the ductile crack initiation triggers the rupture. The FE model perfectly simulates the experimental deformations. The local curvature and the size of bulging buckle on compression side at rupture, and more

importantly, the location of rupture on tensile side of the cross-section are exactly reproduced by FE simulation.

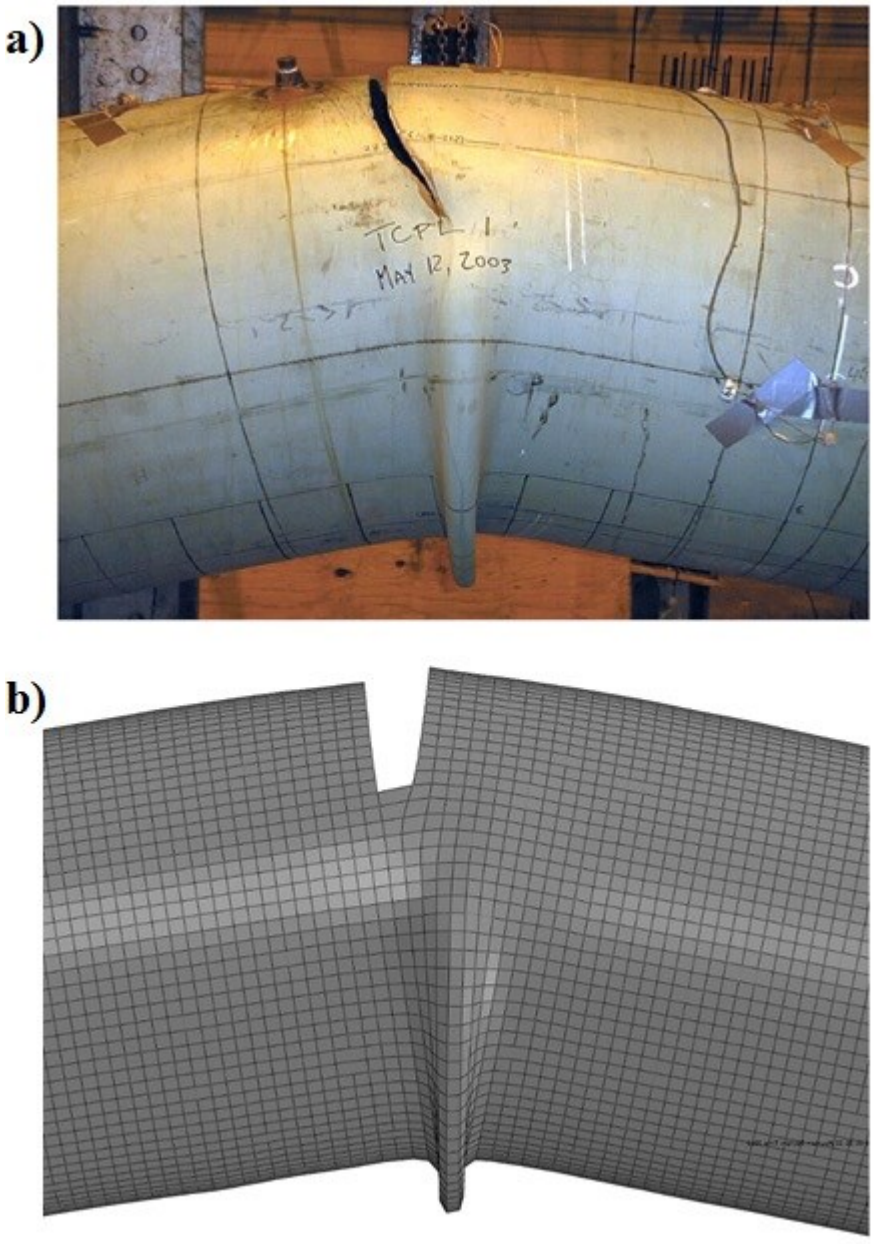

Figure 6-2: Comparison between the final deformed configuration and rupture of X65 cold bend specimen; obtained from a) test (Sen 2006), and b) FE simulation

Figure 6-3 illustrates the contour of the fracture index over the cross-section immediately before the ultimate rupture. It is recognized that despite the considerable deformations due to buckling, the fracture index on the compressive side of the cross-section is insufficient to trigger the rupture on the compressive side.

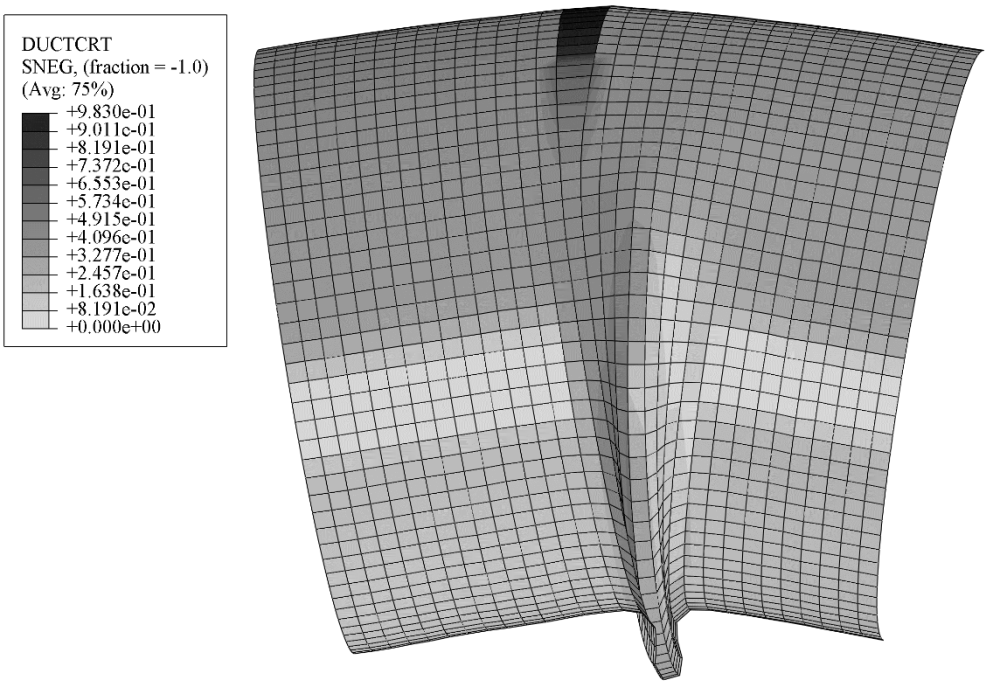

Figure 6-3: Fracture index contour of X65 specimen before rupture (inside view)

6.2.1 Post-buckling Failure Modes of Pressurized Pipes

Not only does internal pressure affect the onset and type of the wrinkling, but also, it changes the post-buckling load-displacement response of a pipe. The verified FE model for the X65 pipe is used to study the failure modes under different values of internal pressure. Figure 6-4 compares the FE load-displacement of the pipes with 40% and 70% internal pressure with that of the 80%. It can be recognized that the decrease of internal pressure results in the lower post-buckling load-carrying capacity which is decreasing with a higher reduction rate (more unstable behavior). Hence, in the case of lower internal pressures, the equivalent plastic strain on the tensile side of the buckled

cross-section is not sufficiently accumulated to satisfy the fracture criterion up to the point that the both sides of the wrinkle come into a hard contact with each other and the bulging buckle closes. The closure of buckle restrains the axial displacement of the compressive side which allows the buckled cross-section to strongly resist the applied curvature again by contact support of the inner surface and increases the cross-sectional load-carrying capacity. Therefore, the closure of buckle appears as a sharp rise in the moment-curvature behavior of the pipe and introduces a new increasing loading path. This phenomenon has been verified by the experimental observations through the full-scale tests conducted by *Sen* (2006).

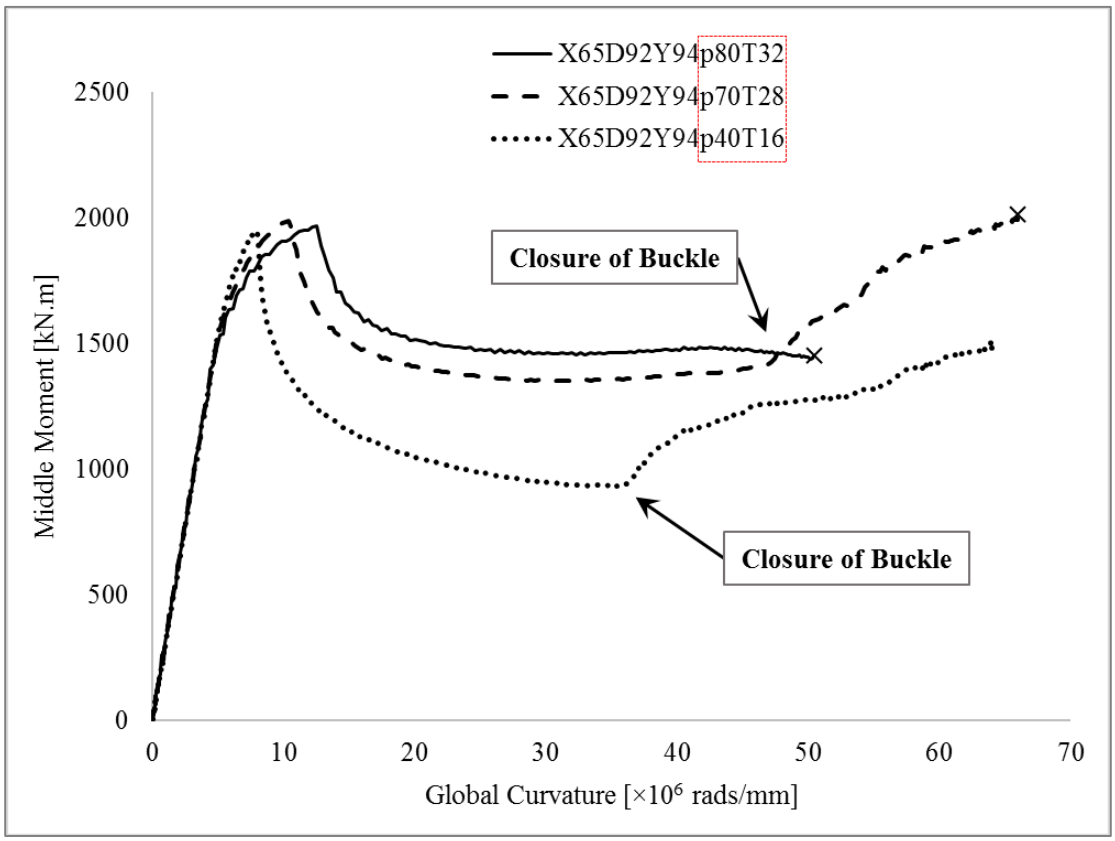

Figure 6-4: Load-displacement comparison of the cold bend pipe subjected to p/p_y ratios of 80%, 70% and 40%

In the case of 70% internal pressure, the new increasing loading path triggers the rupture of the tensile wall on the opposite side the wrinkling after the buckle closes

(Figure 6-5), unlike the ultimate rupture for the 80% internal pressure that occurred along the stable post-buckling loading path before the closure of buckle. On the contrary, in the case of the very low internal pressure of 40%, excessive cross-sectional distortion is created by the formation of successive wrinkles on the compressive side as indicated in Figure 6-6. In this situation, the fracture index on the tensile side is quite negligible and on the compressive side only accumulates to less that 0.4 which is insufficient to spark the rupture of the wall ($\Phi_S < 1$). This clearly indicates that the post-wrinkling rupture of the compressive wall is unlikely to occur due to increasing curvature even after severe distortion of the wrinkled wall.

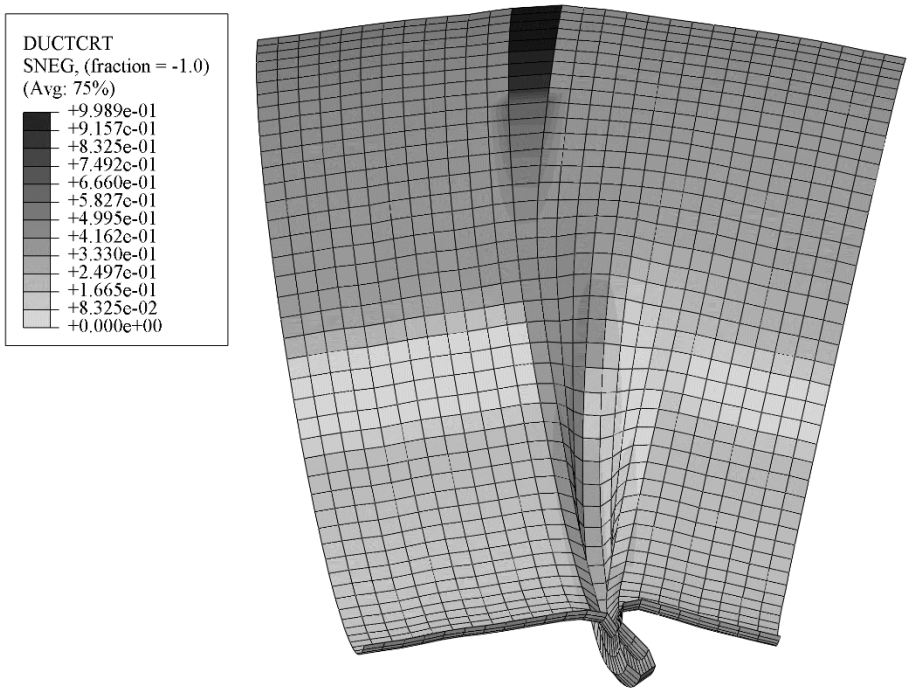

Figure 6-5: Fracture index contour of X65 pipe with p/p_y ratio of 70% before rupture (inside view)

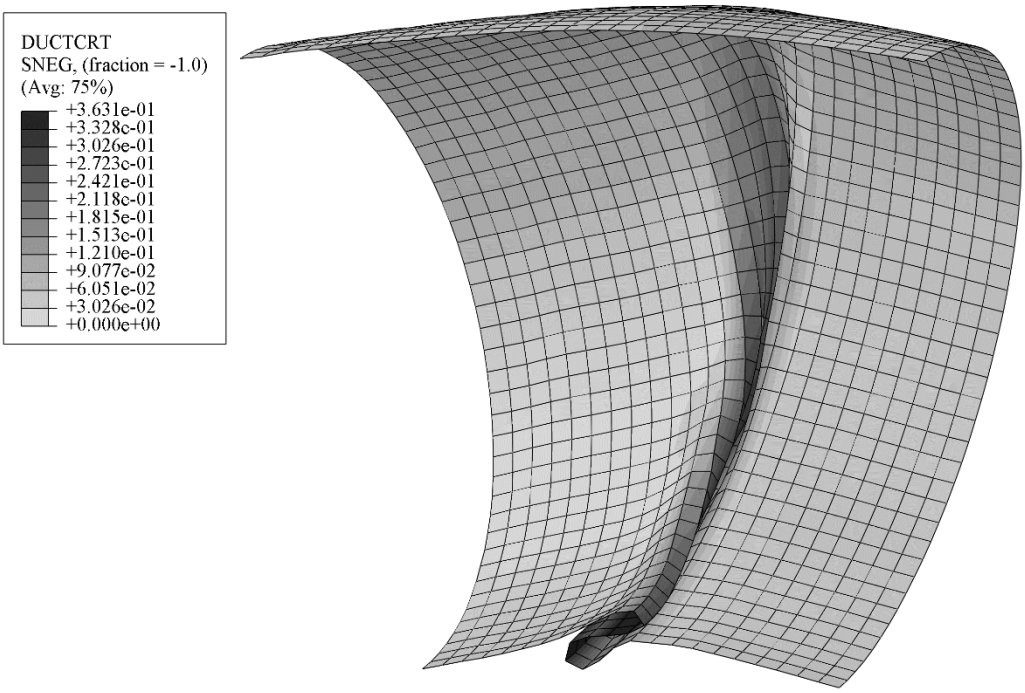

Figure 6-6: Compression failure mode and the fracture index contour of the X65 pipe with p/py ratio of 40% under highly increased curvature (inside view)

6.3 Numerical Results for X80 Line Pipe Specimens

Figure 6-7 draws a comparison between the load-displacement results obtained by FEA and test for the X80D54Y90p60T27 specimen. Both experimental and numerical curves are in a good agreement with each other on pre-buckling and post-buckling regions and show an increased load degradation in the late post-buckling loading path at almost the same point. Although the analytical load is more rapidly decreasing in comparison to the experimental load, the proposed calibration method for the stress-strain curve is on the conservative side in terms of design purposes and the ductile crack initiation is well predicted by the fracture criterion introduced in the FEA. Figure 6-8 demonstrates the final deformed configuration and the formation of rupture on the tensile side of the buckled cross-section which is comparable to the experimental failure shown in Figure 6-9. The contour of the fracture index immediately before the rupture is shown in Figure 8. As it can be seen, no rupture is plausible to occur on the

compressive side of the cross-section at the buckled wall until the increase of curvature triggers the strain localization in the tensile wall on the opposite side of the buckle.

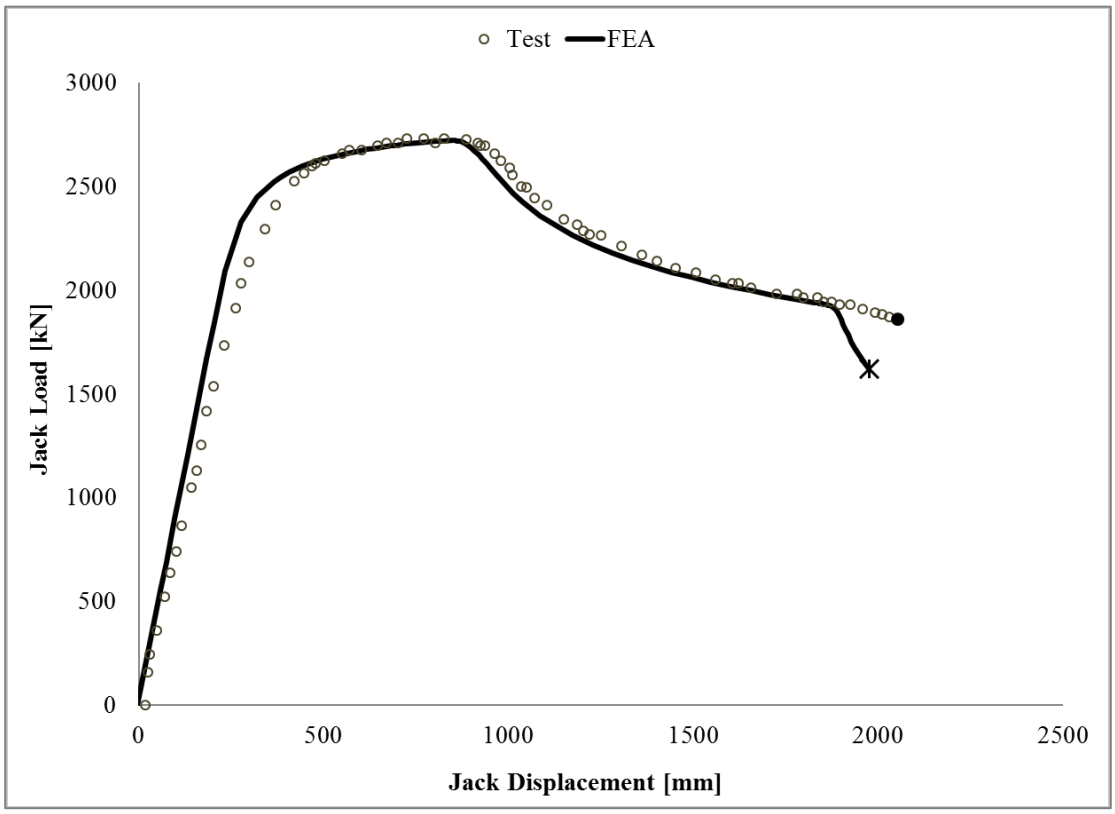

Figure 6-7: Comparison of the experimental load-deformation plot of the X80D54Y90p60T27 pipe with FEA response until the rupture

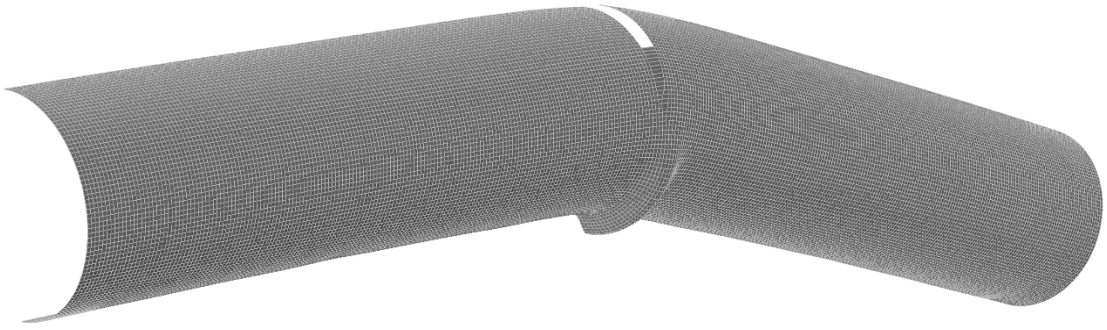

Figure 6-8: Deformed configuration and rupture on the opposite side of buckle obtained from FE simulation of the X80D54Y90p60T27 line pipe

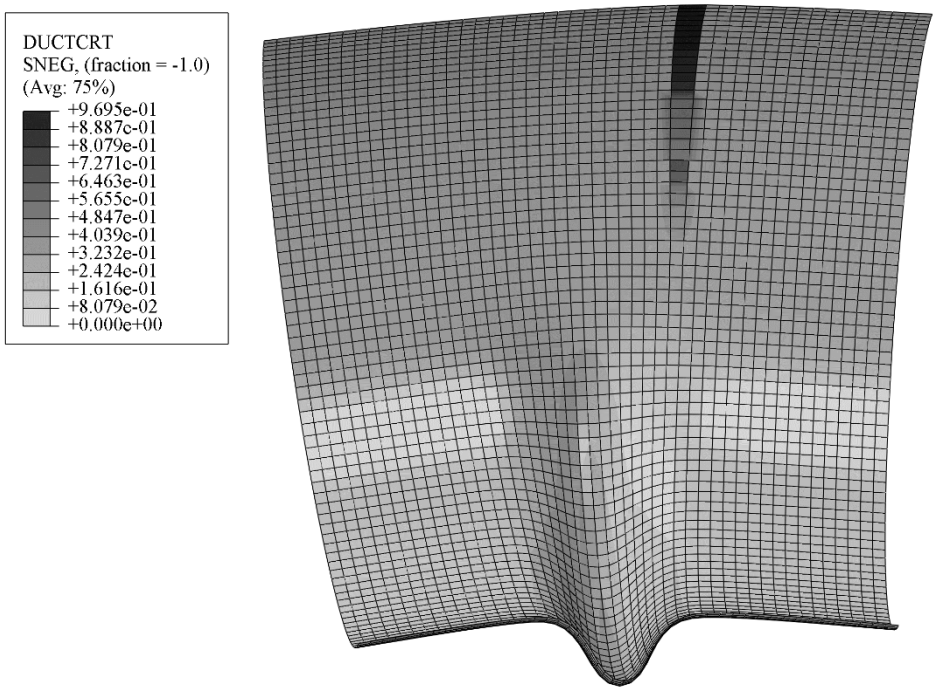

Figure 6-9: Fracture index contour for X80D54Y90p60T27 pipe before rupture (inside view)

It was previously mentioned that the specimen with lower *Y*/*T* ratio (83%) was unloaded after the formation of the buckle. Hence, the FE model for this pipe is verified by the experimental data until the local buckle is formed and is employed to investigate the ultimate failure mode under the increase of imposed curvature and deformations.

The analytical load-deformation for the X80D54Y83p60T26 specimen is compared to the experimental response in Figure 6-10. It is shown that the FE is capable of acceptably regenerating the experimental load-deformation behavior up to the post-buckling branch. From the extension of FEA, it is revealed that no rupture occurs on the tension side of the pipe before the bulging buckle on the compressive side closes. However, after the closure of buckle, the load-carrying capacity starts to increase leading to localized necking and final rupture on the opposite side of the buckle as shown in Figure 6-11. It is also understood from this figure that the strain accumulation on the compressive side is not sufficient to spark the rupture in the compressive wall.

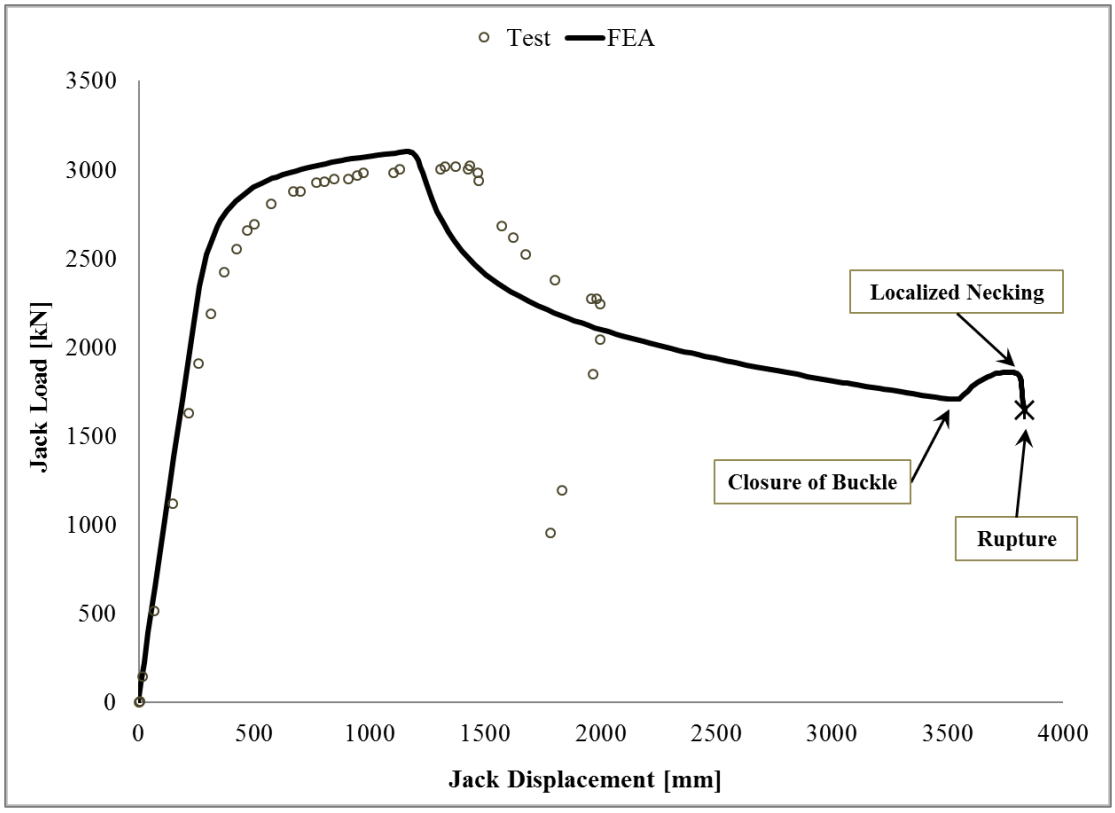

Figure 6-10: Comparison of the experimental load-deformation plot of the X80D54Y83p60T26 pipe with FEA response

6.3.1 Effect of *Y*/*T* Ratio

Both X80 pipe specimens have almost the same geometry and are subjected to the same loading conditions but they differ in material plasticity, i.e. they possess different *Y*/*T* ratio in particular. It was postulated that only the specimen with higher *Y*/*T* ratio failed due to the post-buckling rupture before the closure of buckle. The reason is that the higher *Y*/*T* ratio leads to the rapid increase of plastic strain in the wall while the pipe is experiencing bending deformations in the post-buckling equilibrium state.

Figure 6-12 illustrates the history of fracture index accumulation for both X80 pipes at the necking point versus the horizontal displacement of the moment arm. This plot shows that the fracture index for the specimen with higher *Y*/*T* ratio has a quite steeper slope at the early stage of the loading. For this specimen, localized necking initiates

quite soon after the onset of the buckling which is accompanied by large localized plastic strains and manifests itself as the sudden increase of the slope of fracture index with respect to the applied load. However, the fracture index is only accumulated to 0.19 in the pipe with lower Y/T ratio until the closure of buckle where the new load path is developed and sparks the localized necking and abrupt plastic deformations.

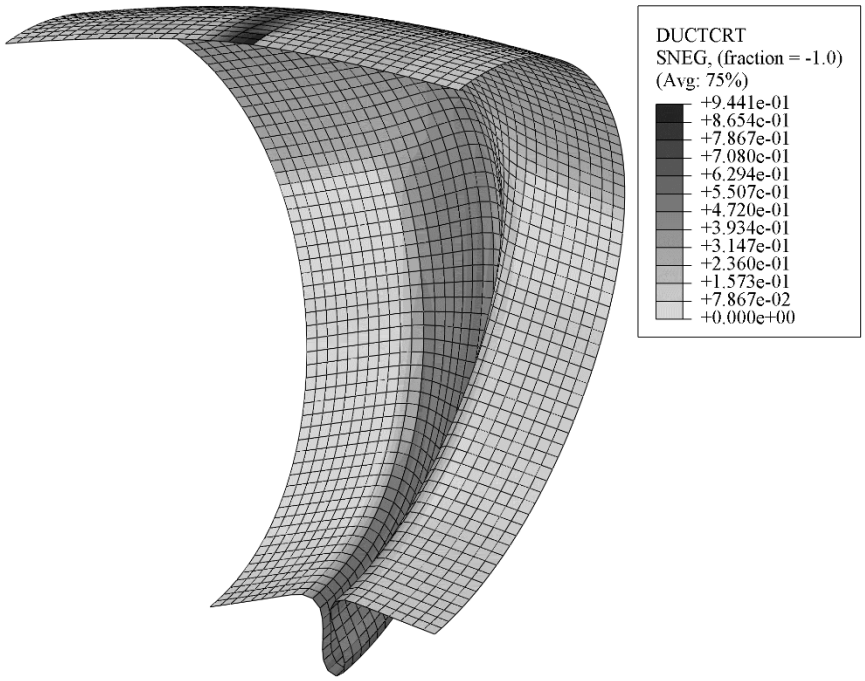

Figure 6-11: Fracture index contour for X80D54Y83p60T26 pipe before rupture (inside view)

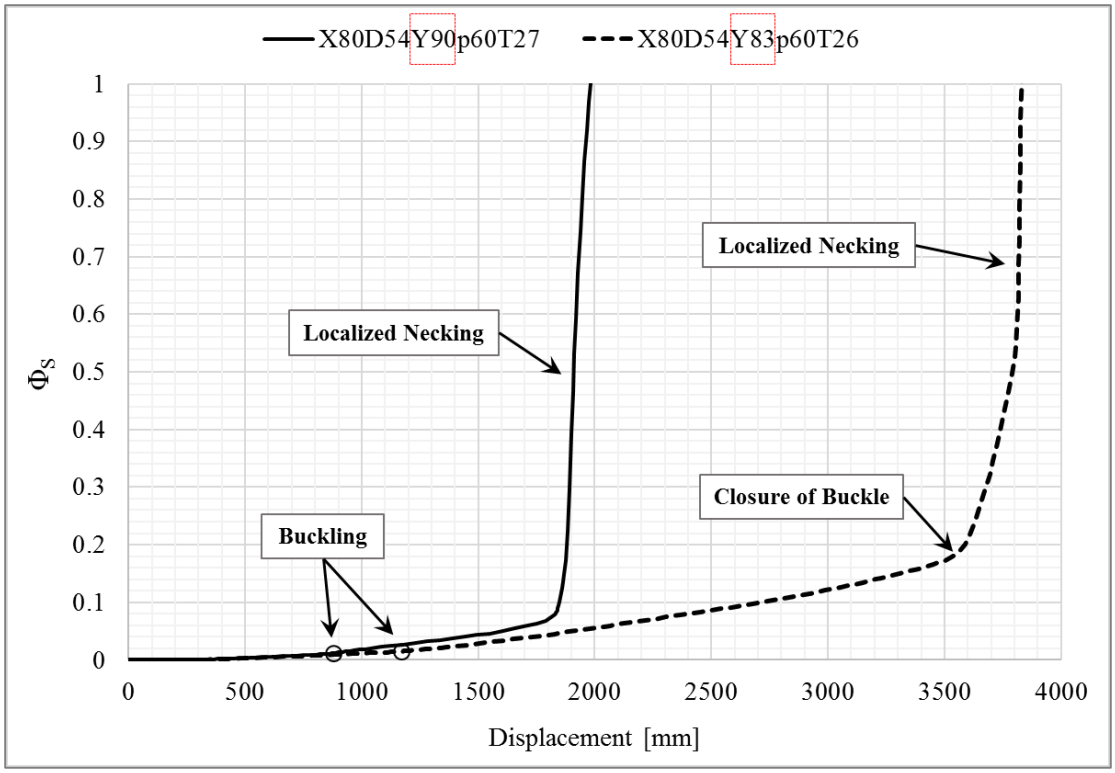

Figure 6-12: Comparison of fracture index accumulation for X80 specimens

6.3.2 Coupled Effect of *Y*/*T* Ratio and Internal Pressure

It was presented in the previous section that the *Y*/*T* ratio plays a key role on the rupture of buckled pipelines. Also, it was demonstrated earlier that the internal pressure is another significant parameter that can change the final failure modes of the buckled steel pipes under monotonically-increasing curvature. Using the verified FE model for the X80 pipes, a quick comparative study is undertaken herein to investigate the coupled effect of the *Y*/*T* ratio and internal pressure on the modes of failure and the rupture of the tensile wall.

Figure 6-13 compares the numerical load-displacement response for the pipe with the *Y*/*T* ratio of 90% under the decreased rates of internal pressure by 5% reductions. It is shown that a slight decrease of the internal pressure results in the post-buckling rupture of the tensile wall to be deferred and occur due to the revived load-carrying capacity after the closure of buckle. Further reduction of the internal pressure switches the final

failure mode from the rupture on the tension side to an excessive distortion of the wrinkled wall on the compressive side without the occurrence of any rupture.

On the contrary, the internal pressure is increased by 5% increments for the pipe with *Y*/*T* ratio of 83% as indicates in Figure 6-14. It can be seen that the increase of internal pressure results in a more stable equilibrium state on the post-buckling loading path and precipitates the occurrence of post-buckling rupture. That is, the increase of internal pressure converts the ultimate mode of failure from the rupture after the closure of buckle i.e. the revival of the load-carrying capacity to the rupture of wall promptly after the formation of the bulging buckle.

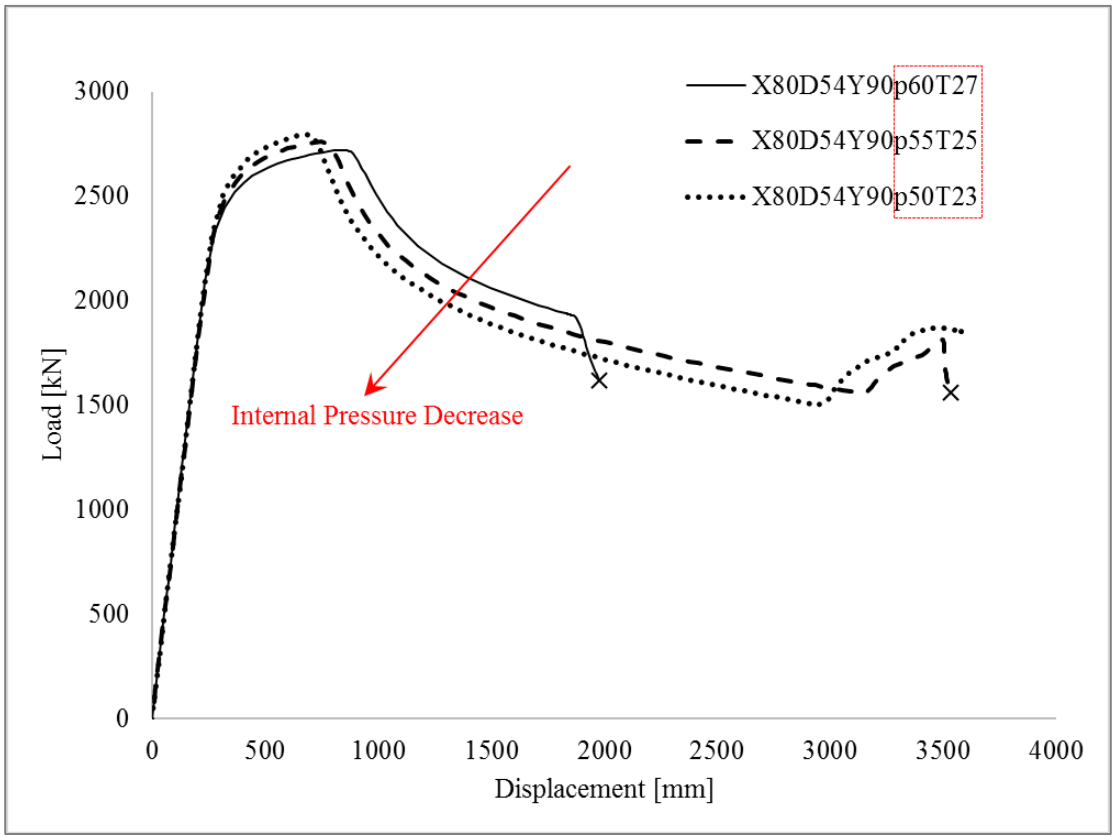

Figure 6-13: Numerical load-displacement comparison of the X80 specimen with *Y*/*T* of 90% being subjected to different p/p_y ratios

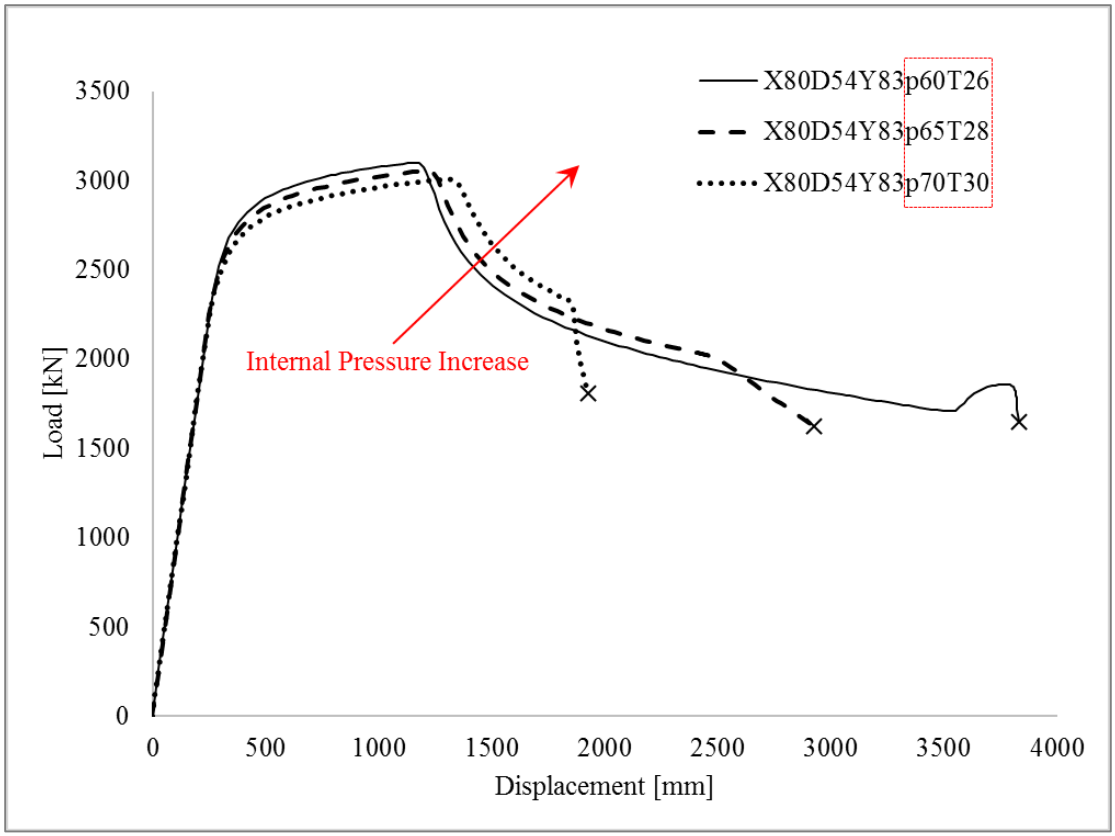

Figure 6-14: Numerical load-displacement comparison of the X80 specimen with Y/T of 83% being subjected to different p/p_y ratios

6.4 Numerical Results for X70 Line Pipe Specimen

The end moment for the X70 line specimen was obtained directly from the FEA results and the following equation was used to calculate the global curvature of the pipe at each loading step

$$\phi_g = \frac{|\theta_{pin}| + |\theta_{roller}|}{L_s} \qquad (6\text{-}3)$$

where the θ_{pin} and θ_{roller} are the rotations at the pivot points (Figure 5-12). Figure 6-15 indicates the moment-curvature plot obtained from FEA in comparison to that of the

experiment. It is shown that the FE simulation closely mimics the experimental response until after the formation of the local buckling where the test was stopped. The post-buckling behavior and final failure mode of the pipe are predicted by the extension of the FEA. Although this pipe was highly pressurized to 80% of the SMYS, no rupture was predicted by the FE simulation until the closure of the buckle at which the fracture index only accumulates to 0.08 on the tensile side of the buckled region. Similar to the X80 specimen with the lower Y/T ratio, rupture is triggered for this pipe shortly after the creation of new load path due to the closure of buckle.

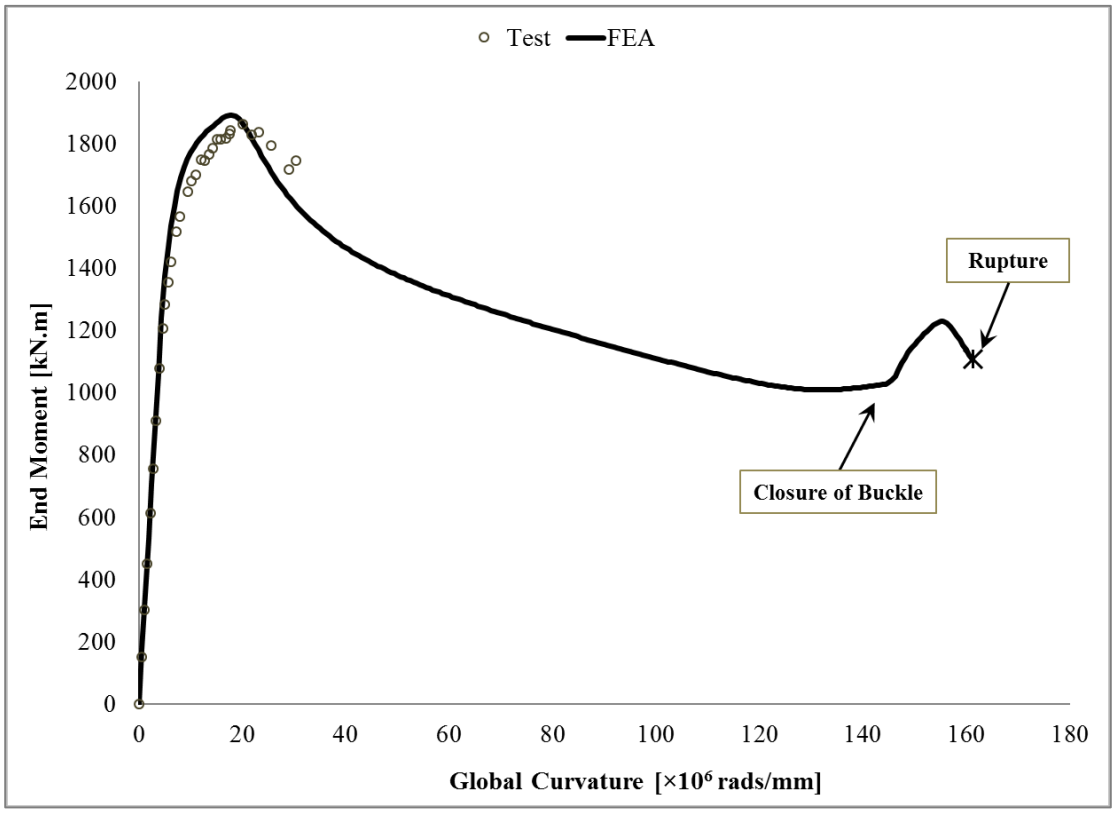

Figure 6-15: Comparison of the experimental load-deformation plot of the X70D92Y89p80T18 pipe with FEA response

Figure 6-16 demonstrates the contour of the fracture index before the rupture occurrence. In spite of large post-buckling deformations, it is shown that the growth of the fracture index on the compressive side is quite insufficient to provoke the rupture

at the buckling location; and, the rupture of the tensile wall on the opposite side of the wrinkling is doomed to be the final failure.

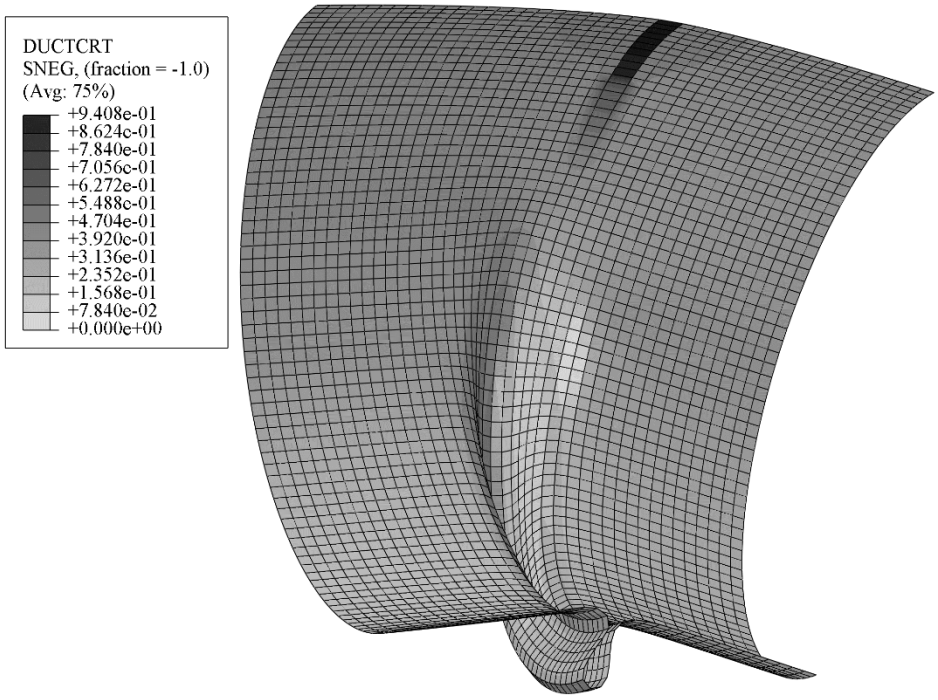

Figure 6-16: Fracture index contour of X70 line pipe with p/p_y ratio of 80% before rupture (inside view)

6.4.1 Effect of Tensile Axial Load

Rupture (fracture) is always associated with the development of extreme principal tensile stresses in a continuum body which reveals the strong effect of the tensile axial load on the rupture of the wrinkled pipelines.

It can be figured that the X65 and X70 pipes possess quite similar dimensions, material properties, and internal pressure. The X65 specimen experiences rupture before the closure of the buckle, whereas, the rupture occurs in the X70 specimen due to the closure of buckle and the revival of the load-carrying capacity of the buckled cross-section. The major distinct difference between these two tests is the amount of axial tensile load that is developed in the specimens. The X65 specimen experiences a

considerable normalized tensile load (T_A/T_{Ay}) of 32% due to the effect of internal pressure during the whole test procedure, whereas, the normalized tension is adjusted to 18% for the X70 specimen by means of the axially aligned MTS machine. This reveals the strong effect of axial tensile load on the rupture of the wrinkled cross-section. To examine this matter, the compressive load applied by the MTS is eliminated from the verified FE simulation. In this case, 36% normalized axial load is developed in the pipe wall due to the internal pressure acting on the end plates. The change in the load-deformation behavior and final failure mode of the pipe is shown in Figure 6-17. It can be seen that the increase of axial tension results in a more stable post-buckling behavior (a higher degree of load-carrying capacity) which for the pipe with 36% axial load rapidly leads to the post-buckling rupture before the closure of the buckle (similar to the X65 specimen) unlike the pipe with 18% axial load that fails in a rupture due to the closure of buckle and the revival of the load-carrying quality. As a result, the pipelines that are subjected to negative temperature gradient e.g. the pipelines that are constructed in arctic regions during summer time are more vulnerable to the rupture at the wrinkled segment due to the formation of primary tensile axial force.

6.5 Critical Boundary Conditions for Rupture of the Buckled Pipelines

In engineering practice, every structure should be analyzed and designed to withstand any probable loading situations that they might experience during their lifetime. In order to find the critical load combinations, the BC of structural elements is usually conceived by the physics of the problem and modeled in their idealized form for the purpose of structural analysis. However, a large amount of complexity is involved in the soil-pipe interactions and underground excitations that make it very challenging to discover the proper idealized BC for buried pipelines. Therefore, the most critical boundary conditions are normally assumed for the experimental and analytical simulations of buried pipes based on to the physical mechanism of soil-pipe interactions, and more importantly, the type of failure under examination; whether it is buckling due to compression or rupture associated with tension.

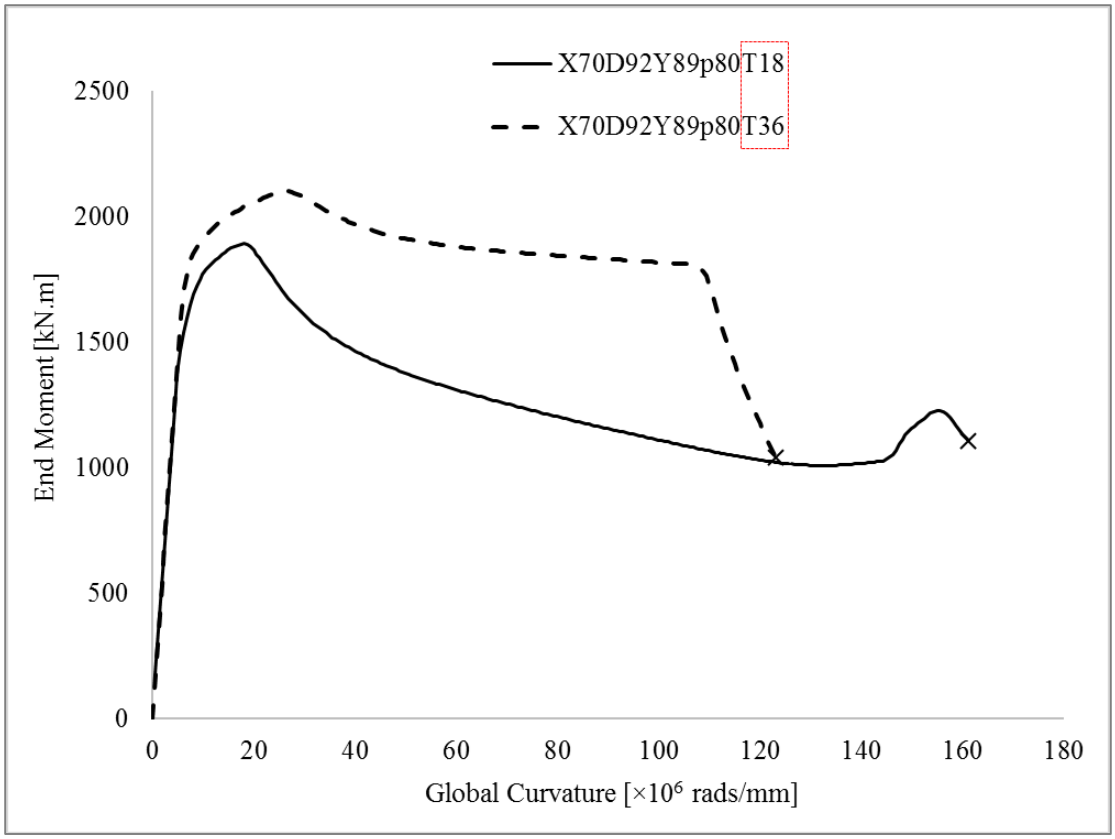

Figure 6-17: Numerical load-displacement comparison of the X70 specimen being subjected to different axial tensile load

Figure 6-18 illustrates the simplified spring model of soil-pipe interactions due to the local differential ground movements which result in the increase of curvature along a segment of the pipeline. The increase of curvature from the straight line to the deflected segment is accompanied by the creation of bumps in the vicinity of the boundaries due to the catenary action of the continuous line as shown in Figure 6-18. Since the surrounding soil applies the same local resistance against the deflection of the line at both sides of the bump location, “hinge action” is assumed at the boundaries of the deflected segment. As the curvature is imposed to a segment of the line, the frictional resistance forces are developed by the friction between the line and its surrounding soil medium that have two opposing effects. The Presence of these frictional forces constrains the axial displacement of the pipe and decreases the compressive strains leading to buckling. Therefore, they are conservatively neglected in the case of

buckling studies and the pipe is allowed to freely displace in its axial direction while being deflected under the imposed curvature. This assumption results in the simply-supported BC which is the most critical BC for the buckling of pipe wall under the compressive stresses. Therefore, a test set-up similar to Figure 2-1 (or Figure 5-1) and simplified BC as shown in Figure 5-12 (or Figure 5-11) have been used in almost every previous experimental and analytical studies of the CBS.

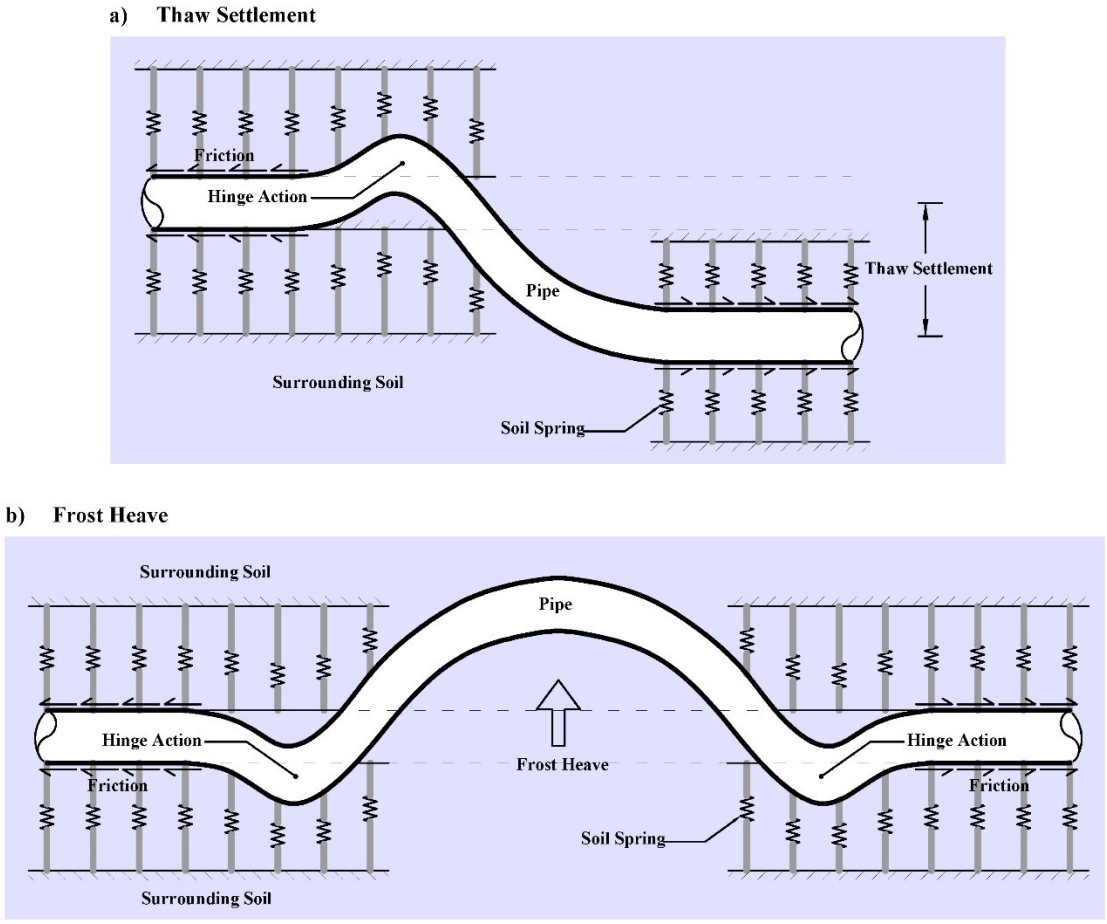

Figure 6-18: Mechanism of soil-pipe interactions due to imposed curvature;
a) Thaw settlement; b) Frost heave

It was discussed in the earlier sections that once the two sides of a local buckle come into a hard contact to each other, the load-carrying capacity of the buckled pipe is revived and an increasing moment-curvature loading path is created. In fact, the closure

of buckle restrains the axial displacement of the pipe on the compressive side of the cross-section which allows the buckled pipe to resist the increasing curvature. It was also proved that the rupture of pipe wall can be triggered on the tensile side of the buckle location a short while after the closure of buckle and restoration of the load-carrying quality. In addition, it was presented in Section 6.4.1 that the existence of tensile axial load plays a key role in precipitating the rupture of wrinkled pipes. Therefore, in spite of CBS limit, the effect of frictional forces that restrain the axial displacement of the deflected segment of the line and develop tensile stress in the wall must be taken into merit considerations once dealing with the rupture limit state of the wrinkled pipes.

Field studies show that the buried pipelines can be subjected to very localized curvature and deformations (Das 2003). It can be observed from Figure 6-18 that the deflected segment of the line is increased in length in comparison to its initial state. As the bigger frictional forces act along the line, the larger elongation is developed in the deflected segment of the line. This elongation leads to the tensile axial force in the pipe wall. Hence, it is understood from the physics of the problem that the most critical BC for the deflected segment of the line that needs to be considered while assessing the rupture limit state of the wrinkled pipes is the so-called pinned-pinned condition. That is, the hinge ends with restraint to the axial displacement. The critical BC is more likely to form due to the transverse excitations on discontinuous regions like frost heave in arctic regions (Figure 6-18) or liquefaction in the seismic regions, slope instability at the crest of sloped lines, near-fault ground movements (Vazouras et al. 2010), and road/river crossings.

The described critical BC for rupture is examined using the verified FE model of the X70 line specimen. To do so, the buckling BC is switched to the critical BC for rupture by restraining the axial degree of freedom at both ends of the pipe (U_x=0 in Figure 5-12) after the bulging buckle forms and grows on the compressive side of the wall. Figure 6-19 compares the obtained load-displacement response of the pipe due to the described critical BC and the conventional buckling BC. It can be seen that restraining the axial displacement of the pipe acts quite similar to the closure of the buckle due to the buckling BC and creates a new increasing load-displacement branch by

reinvigorating the load-carrying capacity of the buckled cross-section. Therefore, the critical BC changes the mode of failure from rupture after the closure of buckle to a premature rupture shortly after the formation of the buckle as explained in Section 6.2.1. Figure 6-20 draws a comparison between the axial load and displacement of the end of the pipes due to the critical BC and buckling BC. As the axial displacement of the pipe is restrained for the critical BC case, a tensile axial force is developed in the pipe which is increasing with the increase of the imposed curvature. This axial tension represents the effect of frictional forces restraining the axial displacement of the line at the boundaries of the deflected segment.

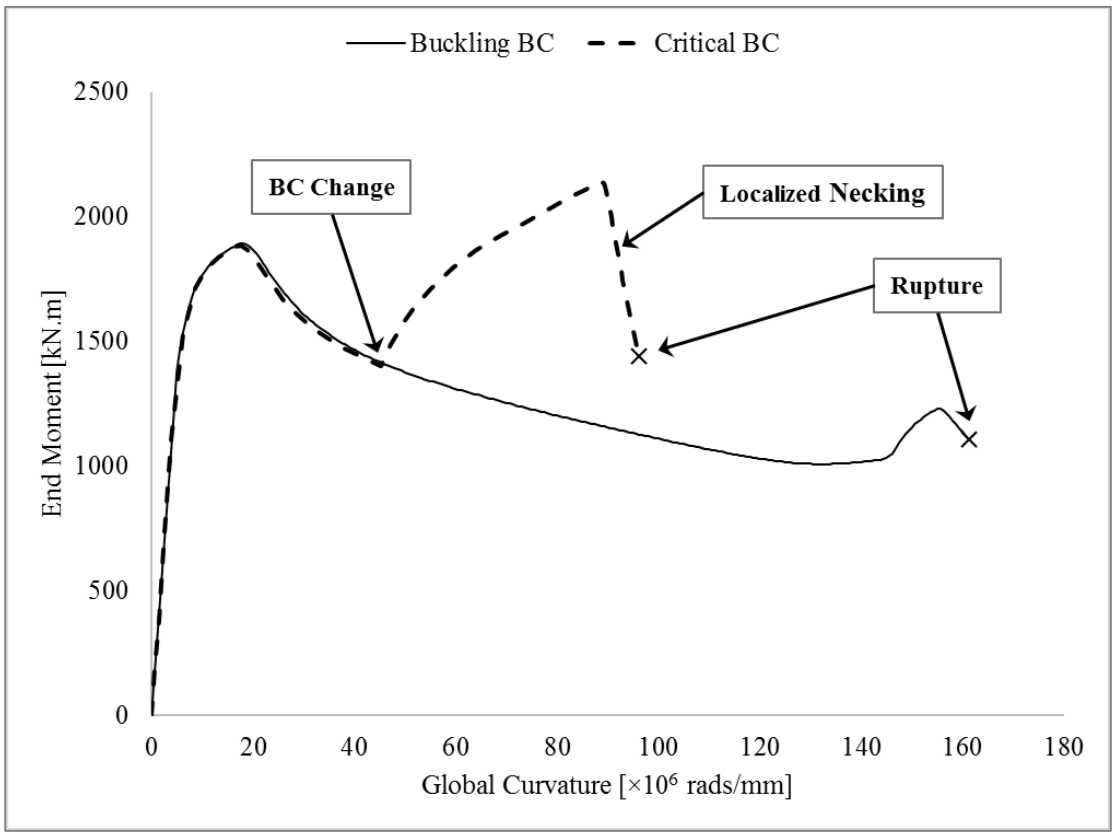

Figure 6-19: Comparison of load-displacement behavior of the X70 pipe subjected to critical buckling and rupture BC

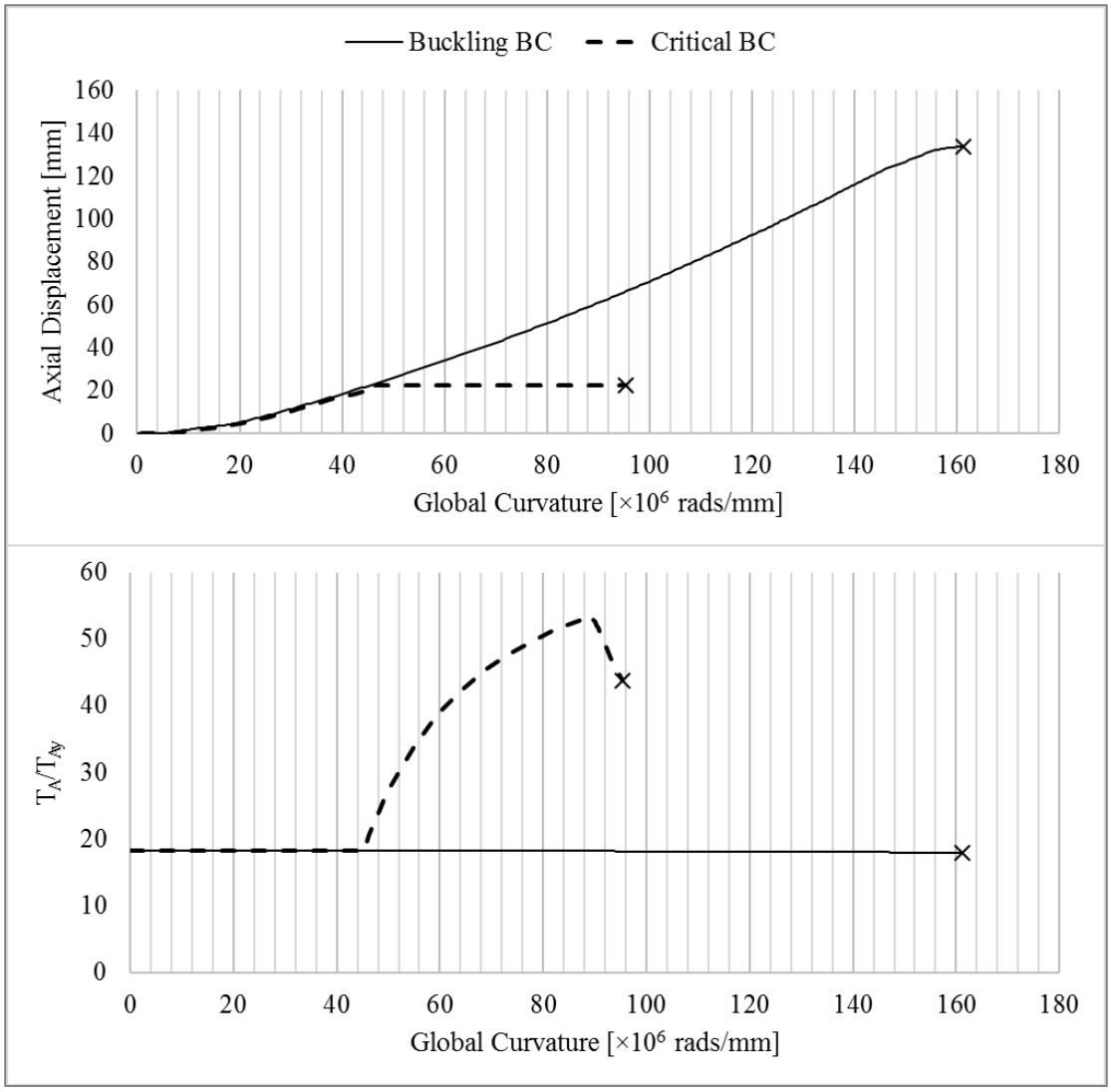

Figure 6-20: Comparison of axial displacement and tensile load developed in the X70 pipe being subjected to critical buckling and rupture BC

6.6 Summary

The results of the FE simulation of the full-scale tests was presented in this chapter. It was shown that the FE models accurately simulate the physical test behavior. The obtained results suggest that the proposed plasticity calibration closely simulates the post-necking material behavior. Also, the cumulative fracture criterion along with the

ductile fracture toughness successfully predicts the ductile fracture initiation in the steel pipes.

The verified FE models were then engaged in studying the modes of failure of wrinkled pipes, the key factors affecting the post-buckling rupture, and the critical rupture BC in association with the increased curvature. It was postulated that the rupture of the tensile wall on the opposite side of the wrinkling is the only burst scenario that is plausible under increased monotonic curvature and no rupture is likely to occur at the wrinkling location in the compressive wall even after abrupt distortion. From the FEA results, the internal pressure, Y/T ratio, and tensile axial load were identified as the crucial factors that significantly contribute to the ultimate failure mode of wrinkled pipes which can be the rupture of the tensile wall or the distortion of the compressive wall. Depending on the values of these key variables, rupture can occur on the post-buckling loading path or after the closure of buckle where the moment-carrying capacity of the pipe is revived. That is, the increase of these variables dramatically increases the chance of rupture.

In addition, the BC of the deflected segment of buried pipelines under increasing curvature was studied through a simple phenomenological soil-pipe model. It was deduced that in the situations where the frictional forces become big enough to restrain the axial displacement of buried pipelines (e.g. the pipelines that are subjected to frost heave, liquefaction, slope instability at the crest of sloped ground, strike-slip near-fault ground movements, and road/river crossings), the so-called pinned type BC is developed at the boundaries of the deflected segment which is the most critical condition to the post-buckling rupture of the wall. Similar to the closure of the buckle, the pinned-pinned BC increases the load-carrying capacity and develops an increasing axial tensile load in the buckled region.

CHAPTER 7: PARAMETRIC STUDY AND DESIGN GUIDELINES

7.1 Introduction

The material model and FE models were previously verified by full-scale experimental data. It was also discovered through FEA that the internal pressure, Y/T ratio, tensile axial load, and BC significantly affect the final failure mode of wrinkled pipes. In this chapter, a thorough parametric study is conducted through numerical analysis to discover the coupled effect of these key design parameters and derive some useful design guidelines on rupture of bent buckled pipes on the tension side of the wrinkled region. Herein, the material model for X65 steel grade that was carefully calibrated in Chapter 4 is used to predict the rupture. However, it is shown that the obtained results could be applicable to any steel grade since non-dimensional parameters are used to find the governing correlations. Furthermore, this study only deals with the plain line pipes and the girth-welded or cold bend pipes are beyond the scope of the current study.

The parametric study is accomplished through three phases and a total of 266 FEA runs. Both of the critical BC for rupture (98 FE models) and Buckling BC (168 FE models) discussed in Section 6.5 are examined here as the upper and lower bounds for the real constraints being applied to the buried pipelines. In the first step, the effect of important geometric parameters versus critical design factor (normalized internal pressure equal to the ratio of hoop stress to SMYS) is discovered to eliminate the insignificant parameters and reduce the total computational costs. Then, the limiting design factor is found for the critical BC as a function of Y/T ratio in association with the strain-based design. And finally, the critical design factor is studied for the buckling BC through involving the tensile axial force in the study.

7.2 Phenomenological Study of the Problem: Key Parameters

The rupture of a wrinkled steel pipe on the tension side due to the internal pressure and monotonically-increasing curvature (Figure 7-1a) can be explained using a simple truss model shown in Figure 7-1b. Formation of a bulging buckle on the compressive side

of the cross-section due to compressive bending stress could be idealized as a plastic hinge (Tajika et al. 2011; Igi et al. 2011) located at the centroid of the wrinkling, and the post-buckling effect of hydrostatic internal pressure could be assumed as a hypothetical element which resists the ovalization of the cross-section. The stiffness of the hypothetical element is associated with the rate of internal pressure. It can be readily understood that in the presence of the internal pressure, the tensile strain is accumulated on the opposite side of the wrinkled area. The higher the rate of internal pressure, the larger the accumulated strain under increasing curvature. Hence, the rate of internal pressure is identified as the main design variable in triggering the rupture. In other words, the tension side on the opposite side of the wrinkled region would rupture only if the rate of internal pressure (the stiffness of the hypothetical element) transcends a limiting value. For the pipes subjected to an internal pressure lower than this limiting value, the formation of successive buckles (in members AH and DH in Figure 7-1b) is reached before the strain accumulation on the tension side adequately grows to initiate the ductile crack formation.

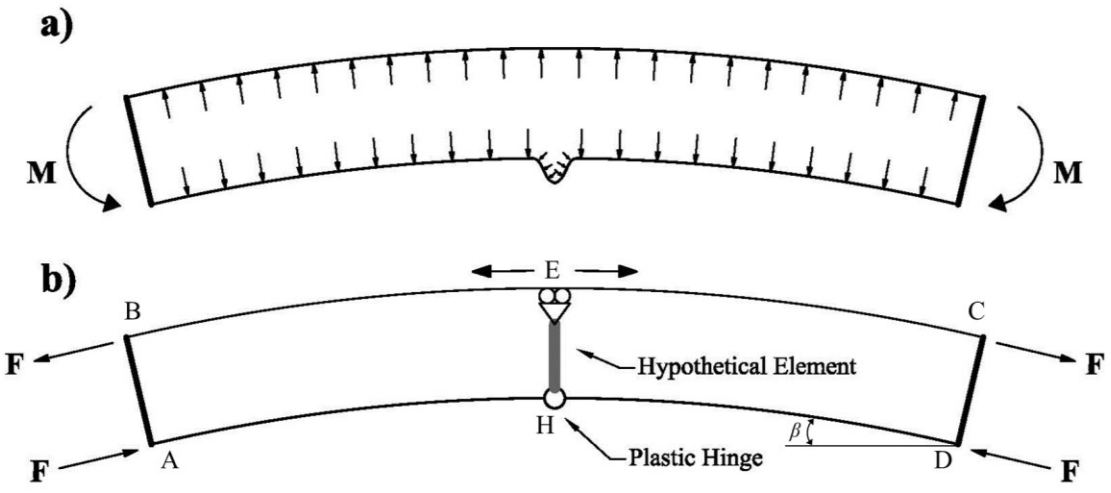

Figure 7-1: Strain accumulation on the opposite side of wrinkle; a) Wrinkled pipe under internal pressure and increasing curvature; b) Phenomenological truss model of the wrinkled pipe

On the other hand, the rate of plastic strain accumulation in the pipe wall is heavily dependent on the tangent modulus (the post-yield slope of the stress-strain curve) which

can be fairly quantified by the Y/T ratio. The larger Y/T ratio for the material results in the higher rate of plastic strain accumulation that leads to a catastrophic rupture.

Although the existence of the axial tensile load delays the formation of buckling, it delays the closure of bulging buckle; and directly contributes to the strain accumulation on the tensile side of the cross-section.

7.3 1st Phase of the Parametric Study: Geometry Effect

As the first step, different pipe sizes and D/t ratios are examined for rupture due to internal pressure and increasing curvature and under the critical rupture BC. Table 7-1 indicates the matrix of variables.

Table 7-1: Matrix of parameters: the 1st phase of parametric study for critical BC

D [mm]	***D/t*** -	***p/p_y*** [%]
500	50	≤100
750	70	
1000	90	

Various design factors up to 100% are tried to find the critical internal pressure value above which the post-buckling rupture of the pipe wall occurs on the opposite side of the wrinkling. Internal pressure value is related to design factor through the following equation

$$p = \frac{2t\left(p/p_y\right)F_y}{D} \qquad (7\text{-}1)$$

Table 7-2 summarizes the geometric characteristics of the FE models for each pipe size. Figure 7-2 illustrates a typical FE model and BC. Similar to Section 6.5, the BC is switched from simply-supported (buckling BC) to pinned-pinned (critical rupture BC) mode after the bulging buckle is completely formed and the compressive strain is reached to 1~3 times the CBS calculated by Eq. (2-1).

Table 7-2: Geometric description of FE models

D	L_s	$(A_{imp})_{max}$	L_{imp}	L_{Collar}	Mesh Size
mm	mm	mm	mm	mm	mm×mm
500	1500	0.75	200	100	8×8
750	2250	1.00	300	150	12×12
1000	3000	1.25	400	200	16×16

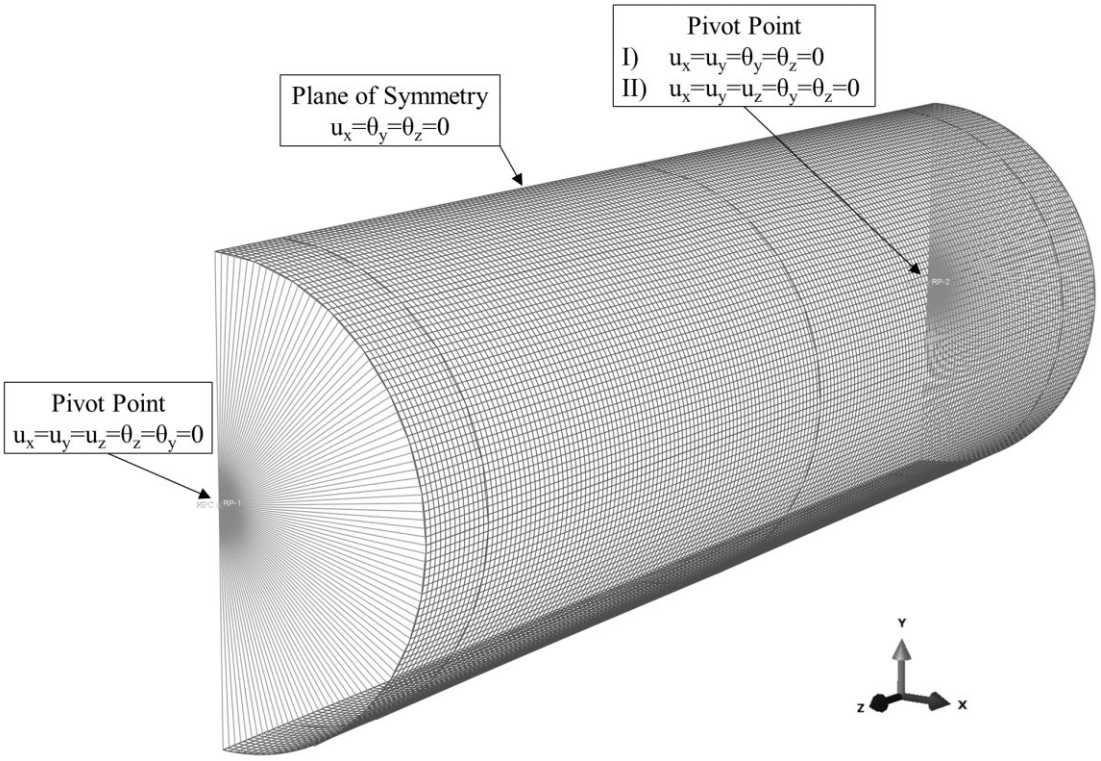

Figure 7-2: FE Model and BC

For each set of variables, very large post-buckling deformations were imposed by increasing curvature until the final failure was achieved by either a rupture on the opposite side of the wrinkling or the failure at the boundaries.

To achieve the goal that is finding the critical internal pressure to rupture, a trial and error method was used to optimize the number of FEA as shown in Figure 7-3. For instance, in the case of the set of variables associated with D=750 mm and D/t=90, the design factor equal to 80% was considered as the first trial. Since rupture was observed for this set of variables, the design factor was reduced by 20% reductions until the failure mode was changed to the successive buckles on the compressive side of the pipe wall and no rupture on the tensile side. Then, an increment of 10% was applied to the design factor until the failure mode switched back to the rupture. This procedure was continued until the increment/reduction became as low as 2.5% where the critical internal pressure to rupture was found for each set of parameters.

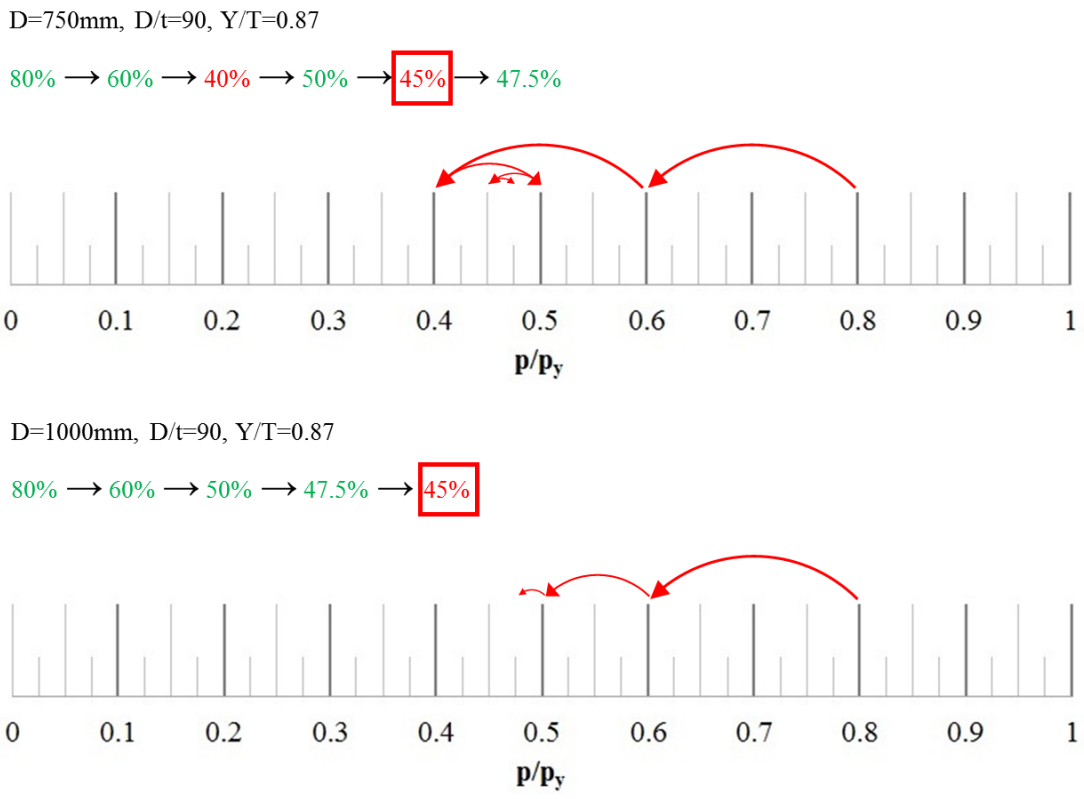

Figure 7-3: Strategy of changing internal pressure values

At this stage of the parametric study, 58 FEA were conducted. Figure 7-4 illustrates the critical design factor versus D/t ratio obtained for different pipe sizes. It is observed

that the pipe size has no effect on the final failure mode of the wrinkled pipe. Moreover, the critical internal pressure is linearly changing versus D/t ratio. However, the dependence of the critical design factor on D/t ratio appears to be very slight as an increment of 20 units for D/t ratio only reduces the critical design factor by 2.5%.

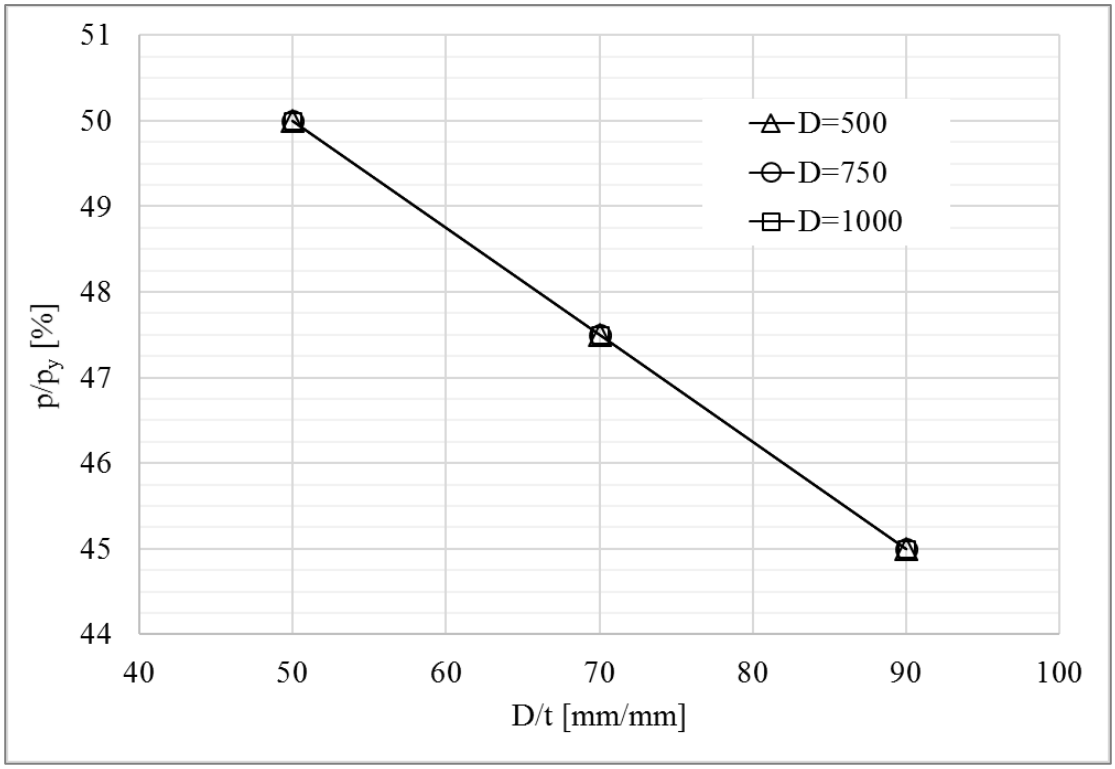

Figure 7-4: Critical p/p_y vs D/t for different pipe sizes

Figure 7-5 compares the moment-curvature response of the D90Y87p47.5 series for different pipe sizes obtained from FEA. Obviously, as the pipe diameter is increased, the ultimate load to rupture is increased, and the final curvature is decreased. However, the same critical internal pressure associated with the rupture limit is obtained for the pipes with different diameters but the same D/t ratio.

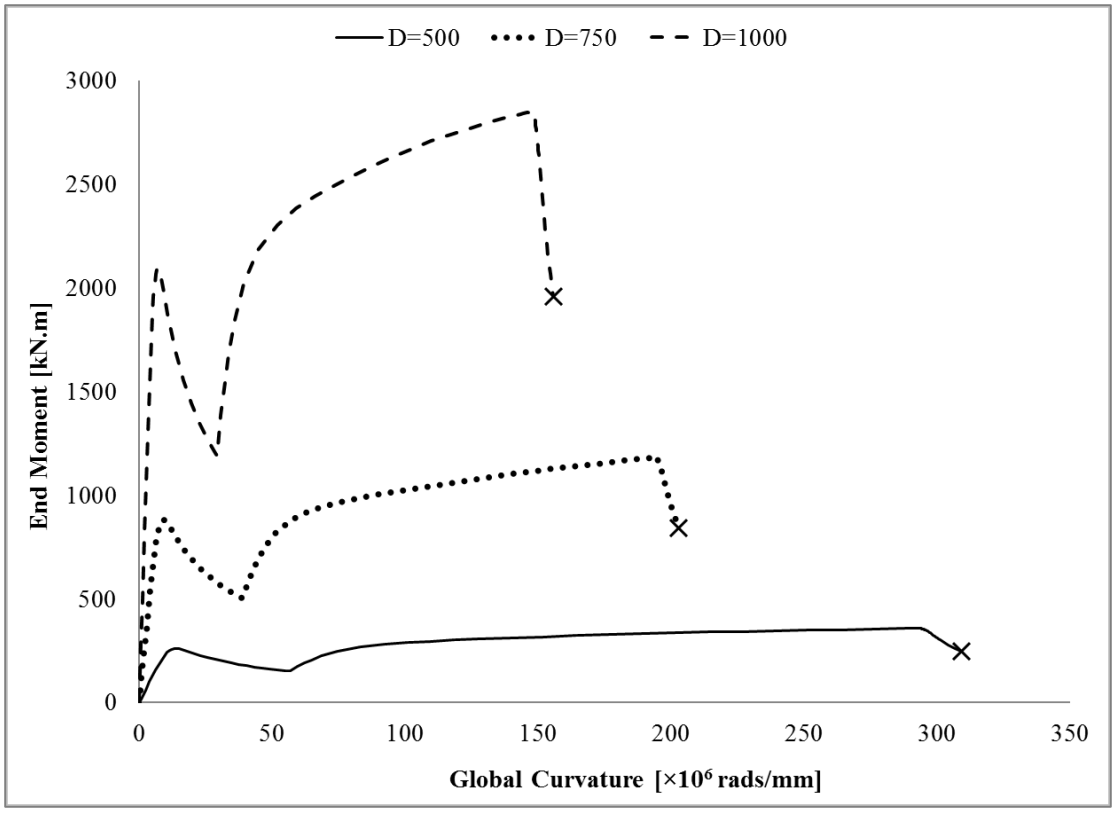

Figure 7-5: End moment vs global curvature for D90Y87p47.5 series

7.4 2nd Phase of the Parametric Study: Critical Design Factor

In this phase, the effect of *Y*/*T* ratio is examined on the burst of wrinkled pipes. Table 7-3 summarizes the mechanical strength requirements for API X65/CSA Gr448 steel grade specified by codes. It is learned that the maximum *Y*/*T* ratio allowed by the pipeline codes is 93 %. On the other hand, the SMYS from Table 7-3 divided by the experimental tensile strength of the material (628 Mpa) results in the minimum *Y*/*T* ratio of 72%. Therefore in this study, a set of values ranged from 72% to 93% are assigned to the *Y*/*T*. Table 7-4 demonstrates the matrix of parametric study at this stage.

In order to artificially generate the stress-strain curves with different *Y*/*T* ratios, the ultimate strength (F_u) of the material obtained from the test is kept constant and the yield strength (F_y) is changed.

Table 7-3: Code specifications for X65/Gr448 steel material

Grade	Yield Strength (F_y or Y) [MPa]		Tensile Strength (F_u or T) [MPa]		Y/T [%]	
	min	**max**	**min**	**max**	**min**	**max**
X65 [1]	450	600	535	760	-	93
448 [2]	448	600	531	760	70 *	93

[1] API-5L (2012)

[2] CSA-Z245.1 (2014)

* CSA-Z662 (2011)

Table 7-4: Matrix of parameters: the 2nd phase of parametric study for critical BC

D/t -	p/p_y [%]	Y/T [%]
50	≤100	72
		77
70		80
		87 (Test)
90		93

The following form of the *Ramberg-Osgood* equation suggested by CSA-Z662 (2015) code is used to create the engineering stress-strain curve associated with each Y/T value

$$\varepsilon^{ENG} = \frac{\sigma^{ENG}}{E} + \left(0.005 - \frac{F_y}{E}\right)\left(\frac{\sigma^{ENG}}{F_y}\right)^{n_{RO}} \quad (7\text{-}2)$$

in which, the *Ramberg-Osgood* hardening constant (n_{RO}) can be related to the uniform strain through the following empirical equation (Wang et al. 2004a)

$$\varepsilon_u = \frac{2}{n_{RO}} \qquad (7\text{-}3)$$

Table 7-5 reports the mechanical properties of the materials with different *Y*/*T* ratios which were calculated by combining the *Ramberg-Osgood* equation and Eq. (7-3). It can be seen that the increase of the *Y*/*T* ratio (or the hardening constant) results in the decrease of the uniform strain at necking. That is, the plastic strain localization is reached earlier for the materials with the higher *Y*/*T* ratio. Figure 7-6 shows the engineering stress-strain curves for the materials with different *Y*/*T* ratios generated using the *Ramberg-Osgood* equation. It is worthy of attention that the stress-strain curve of real materials obtained from physical tests can be different from the idealized curves shown in Figure 7-6. That is, a material with the same steel grade and *Y*/*T* ratio can follow a different form of stress-strain relationship. However, the final results for two different materials with the same *Y*/*T* ratio is still the same.

Table 7-5: Mechanical properties of the materials with different *Y*/*T* ratios

Y/T	***F_u***	***F_y***	***n_{RO}***	***ε_u***
%	MPa	MPa	-	mm/mm
72	628	452	12.23	0.164
77		483	15.00	0.133
80		502	17.12	0.117
87 (Test)		549	-	0.085
93		584	42.14	0.047

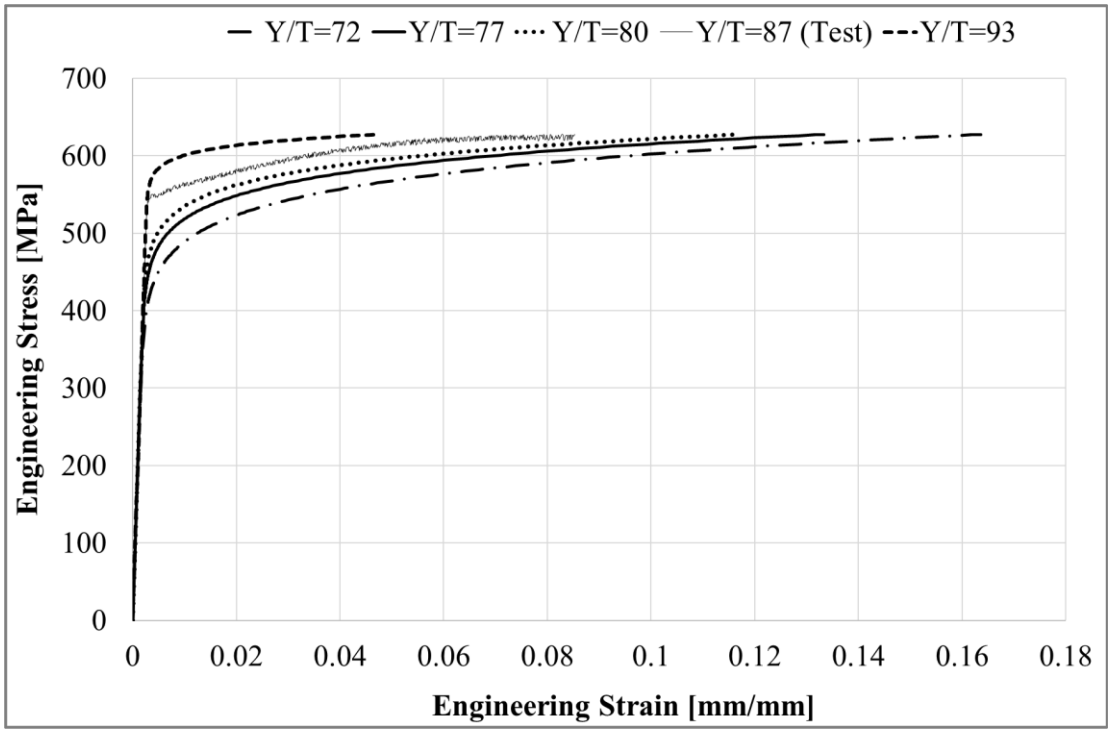

Figure 7-6: Engineering stress-strain curves for the materials with different *Y*/*T* ratios

Using the engineering stress-strain curves, the procedure introduced in Section 4.6 can be now used to obtain the true stress-strain curves associated with the materials with different *Y*/*T* ratios. The power law is calibrated to predict the post-necking stress-strain relationship. Table 7-6 includes the power law constants calibrated for the materials with different *Y*/*T* ratios. Figure 7-7 shows the true stress-strain curves obtained for the materials with different *Y*/*T* ratios.

Identical strategy as what explained in the previous section is engaged here in changing the rate of design factor during this phase of the parametric study. However, the initial trial is selected based on the critical design factors obtained for the same set of variables with the adjacent *Y*/*T* ratio as illustrated in Figure 7-8.

The post-buckling deformations are applied through the increase of the monotonic curvature until either a “rupture on the tensile side” or the “formation of successive buckles on the compressive side” was reached as the final failure modes. Figure 7-9 shows the compression failure of the D90Y80p75 pipe by the formation of the successive buckles before the rupture is triggered. The successive buckle formation

leads to the distribution of the bending tensile strains over the length of the pipe which avoids the strain localization and rupture. This can be easily understood by introducing successive plastic hinges and hypothetical elements in the simplified truss model shown in Figure 7-1b.

Table 7-6: Power law constants obtained for the materials with different *Y*/*T* ratios

Y/T	***A***	***n***
72	1019.80	0.182
77	977.13	0.155
80	918.26	0.126
87 (Test)	830.96	0.083
93	770.81	0.053

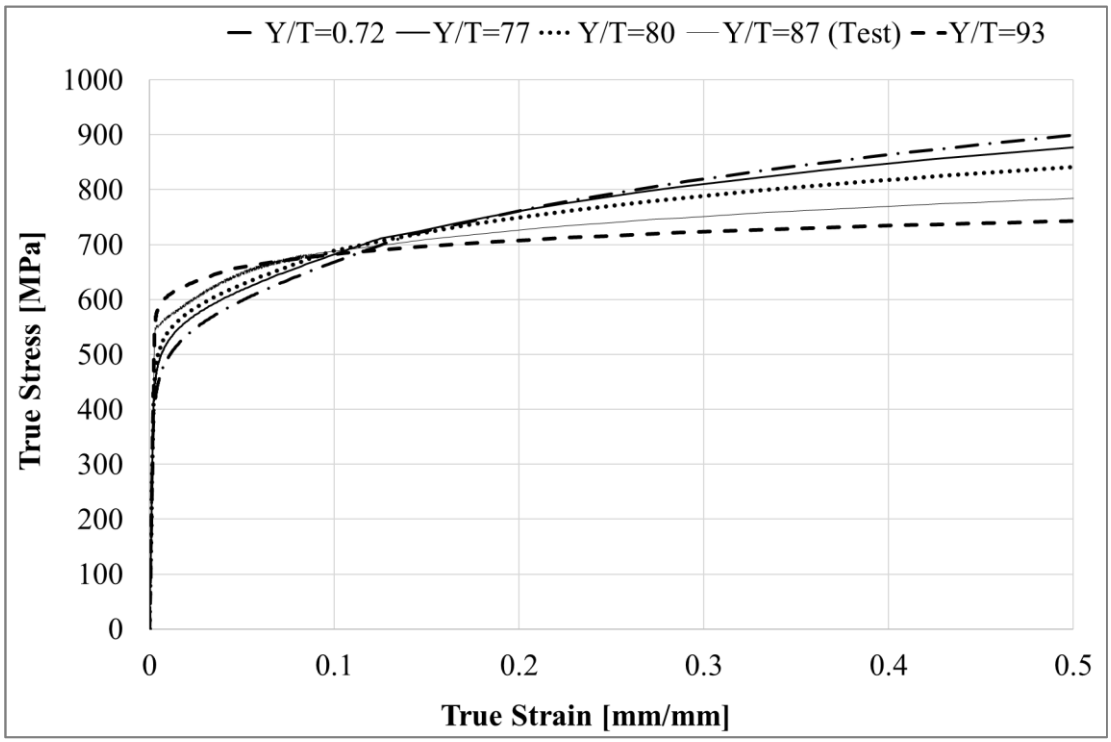

Figure 7-7: True stress-strain curves for the materials with different *Y*/*T* ratios

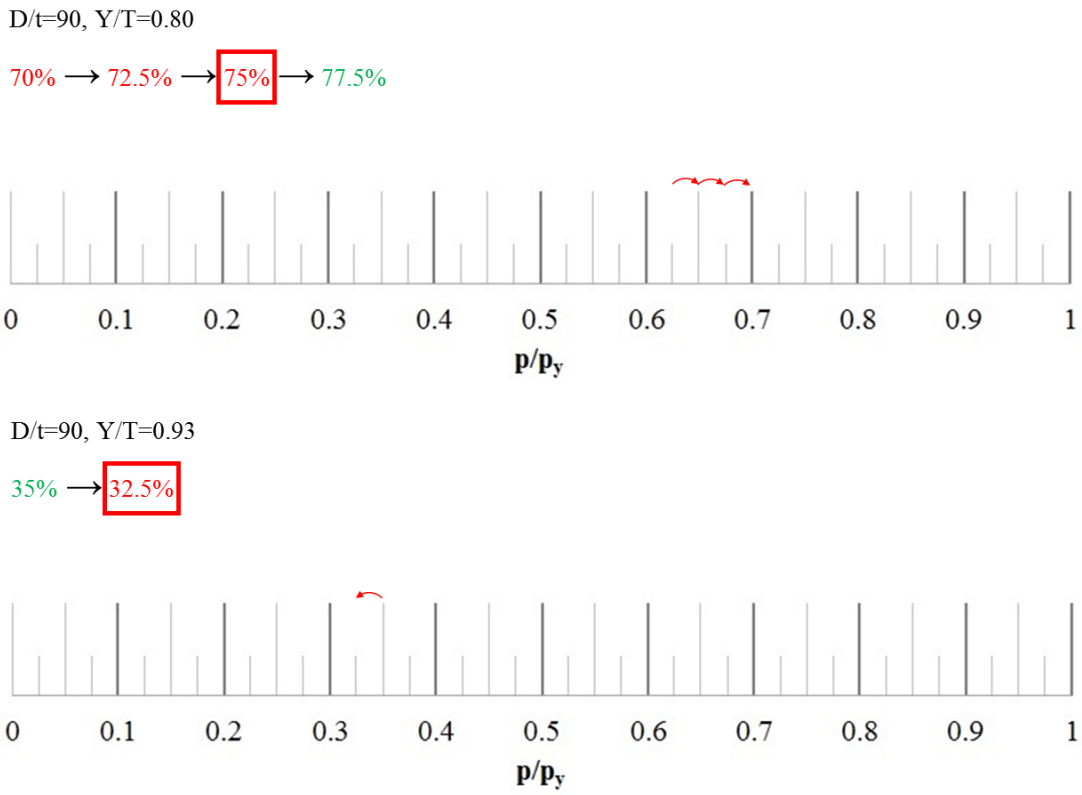

Figure 7-8: Strategy of changing internal pressure in the 2nd phase of parametric study

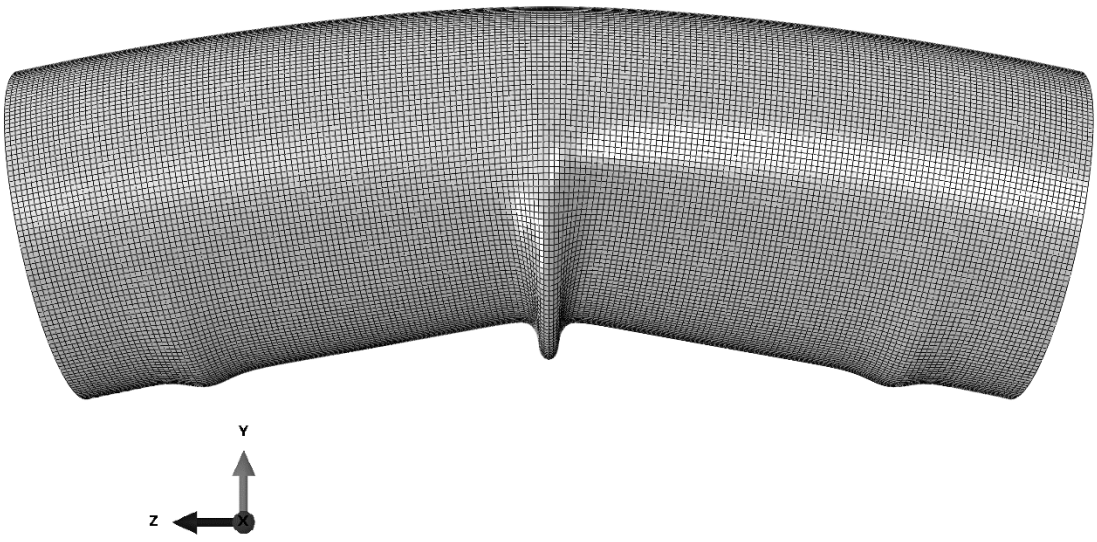

Figure 7-9: Successive buckle formed along the pipe for the D90Y80p75 set

Figure 7-10 shows the results of the 2nd phase of parametric study as the critical design factor against D/t ratio for different Y/T levels. It is observed that for the higher Y/T ratios, the critical design factor is increased by the increase of D/t ratio, but, the opposite relationship governs as the Y/T ratio is decreased. This observation is due to the nonlinear contribution of the D/t ratio, internal pressure and yield strength to the CBS shown in Eqs. (2-1) to (2-3), which delays or precipitates the formation of the successive buckles on the compressive side of the cross-section (buckling in members AH and DH in Figure 7-1b). In either event, the effect of D/t ratio on the critical design factor seems quite insignificant. Whereas, a small rise in Y/T ratio markedly increases the critical design factor to the point that no rupture failure was obtained for the case of Y/T ratio equal to 72%.

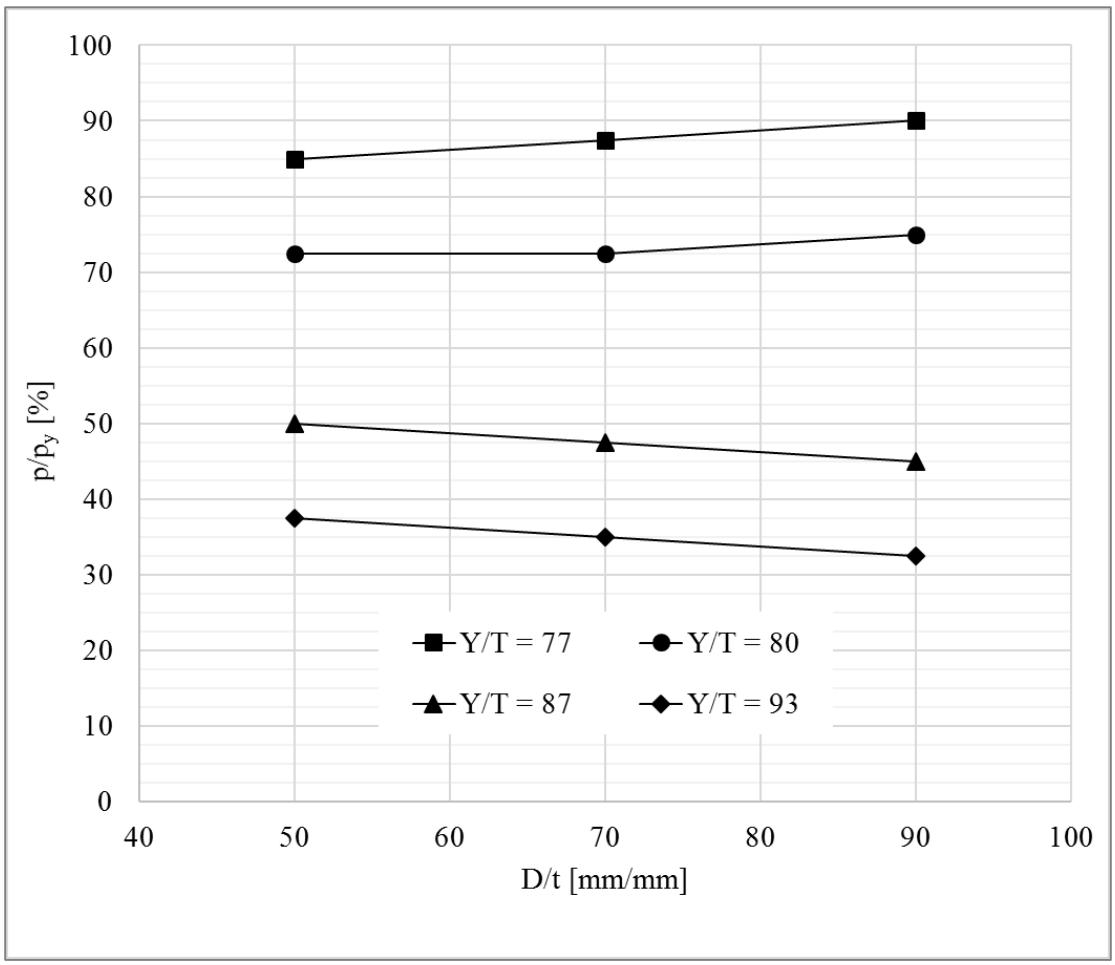

Figure 7-10: Critical p/p_y vs D/t for different Y/T ratios

Thus, it seems more helpful to rearrange the results with respect to the Y/T ratio as depicted in Figure 7-11. In this figure, the exponential reduction of design factor with the increase of Y/T ratio is highly distinctive. As the D/t ratio impact is so negligible, the lower envelope of the critical design factor is used to eliminate the effect of D/t ratio and specify a conservative limit.

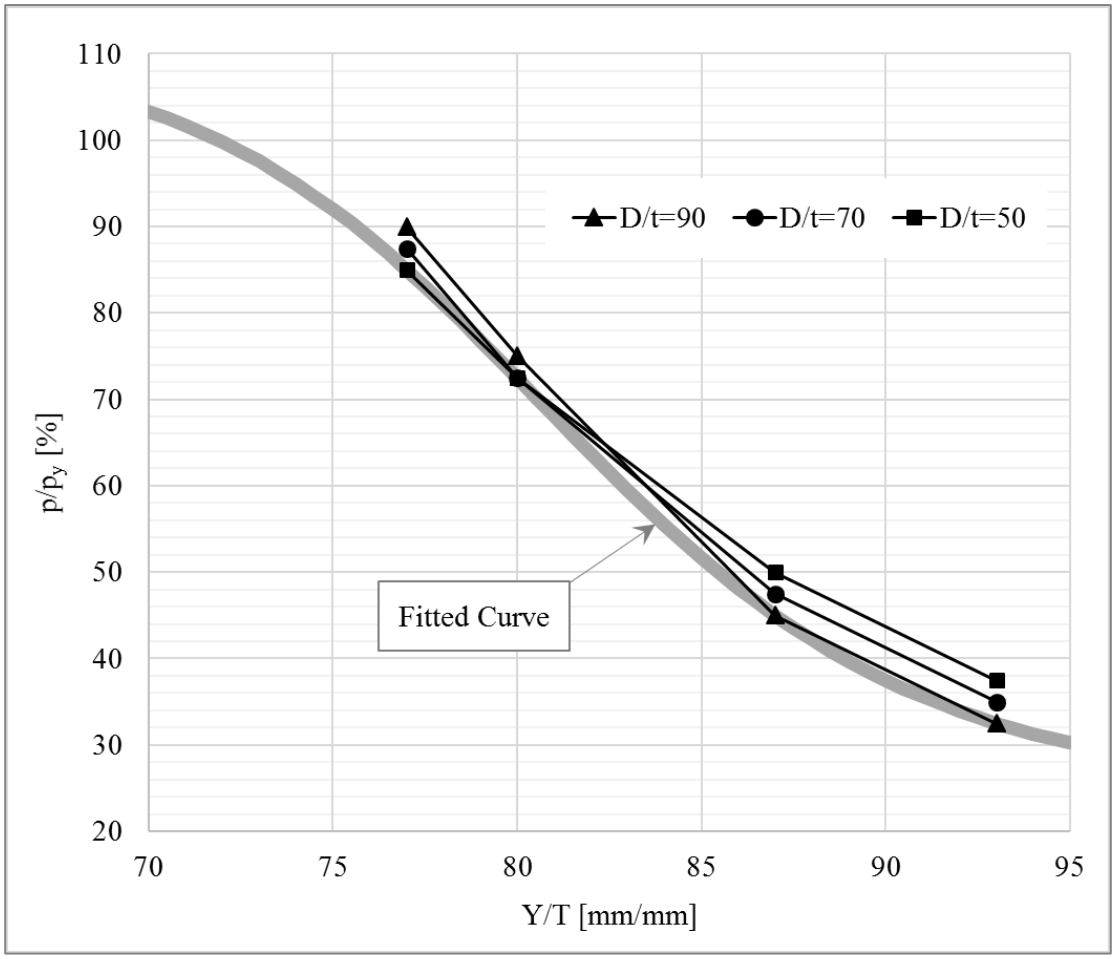

Figure 7-11: Critical p/p_y vs Y/T for different D/t ratios

The following sigmoidal logistic function is used to fit the design factor limit versus the Y/T ratio

$$\left(\frac{p}{p_y}\right)=\frac{k_1-k_2}{\left(1+\left[\frac{1}{k_3}\left(\frac{Y}{T}\right)\right]^{k_4}\right)^{k_5}}+k_2 \qquad (7\text{-}4)$$

where the $k_{1\sim5}$ are the constants of the logistic function. k_1 and k_2 are the values of the function at 0 and $+\infty$ respectively. k_3 is the value of the function at the inflection point. k_4 is called the Hill's slope and adjusts the slope of the curve at the inflection point. And, k_5 is the asymmetry factor. Table 7-7 indicates the constants of the fitted curve for the design factor envelope which is shown in Figure 7-11.

Table 7-7: Constant of logistic function calibrated for critical p/p_y (Critical BC)

k_1	k_2	k_3	k_4	k_5
109.88	24.46	81.21	16.702	1.0

The fitted sigmoid curve specifies a limit to the design factor for the transition from the compressive failure to the rupture of the pipe wall due to large imposed bending tensile strains. That is, the post-buckling rupture is likely to occur due to the large increasing curvature provided that the internal pressure transcends the critical design factor limit. Although the rupture limit was obtained for the X65 steel grade, it could be generalized to all steel grades since the design factor and Y/T ratio are dimensionless quantities. Also, the design factor limit should address the rupture of pipes subjected to the buckling BC as it was derived based on the critical rupture BC. Figure 7-12 compares the proposed design limit state to all the pipe specimens with buckling BC and rupture failure that was discussed in the previous chapters. It can be seen that the proposed limit state fairly covers the rupture of the plain pipe specimens with buckling BC and different steel grades. This includes the specimens that failed in the rupture before and after the closure of bulging buckle. However, it should be noted that all specimens with buckling BC are subjected to considerable axial tensile force.

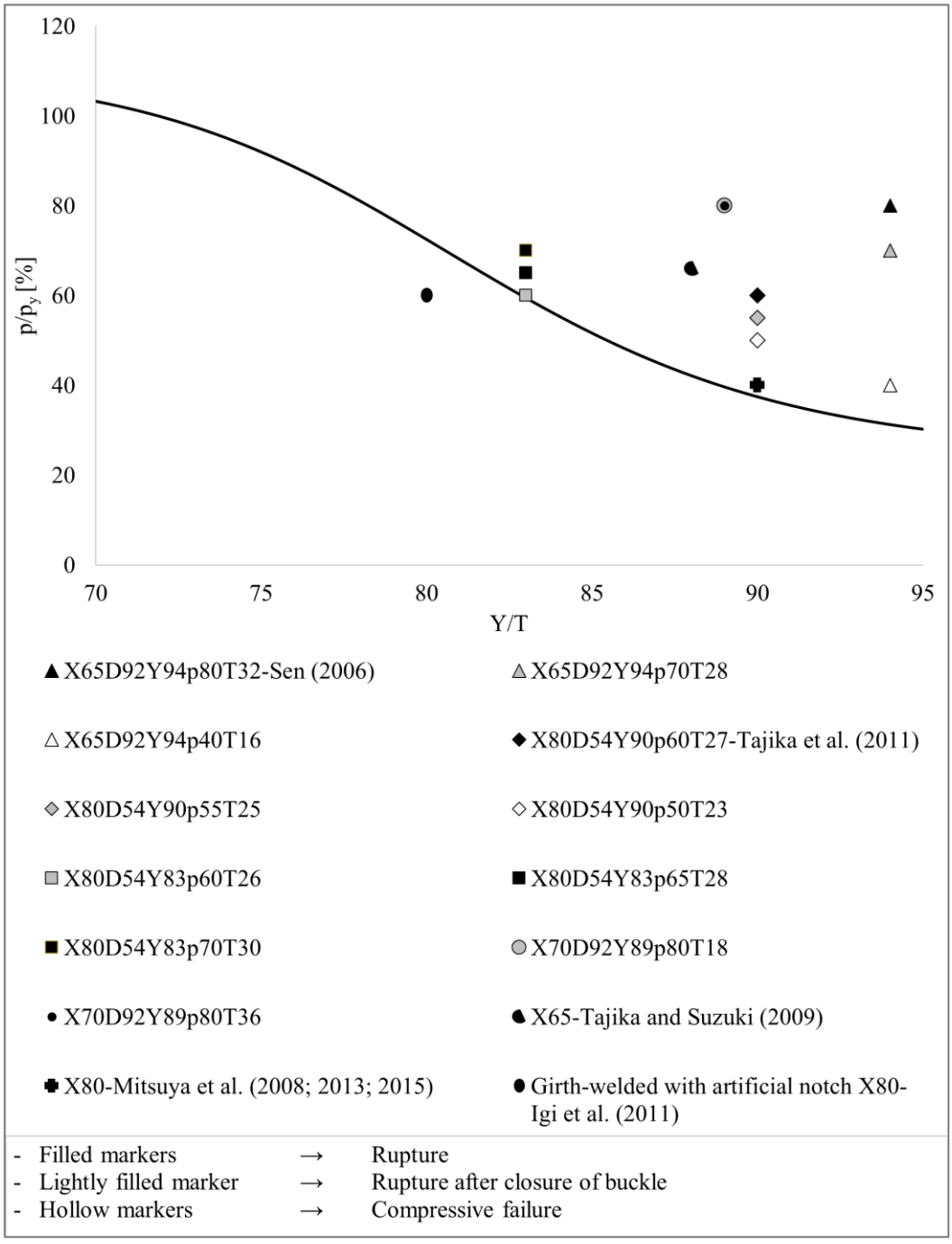

Figure 7-12: Critical design factor obtained for rupture BC in comparison to the pipe specimens with buckling BC discussed in the previous chapters

As a further matter, it is known that the pipeline codes (API-5L 2012; CSA-Z662 2015) limit the design factor to 80%. Hence, the design factor limit state of the wrinkled pipes can be defined by a piecewise function as demonstrated in Figure 7-13 (the solid black line).

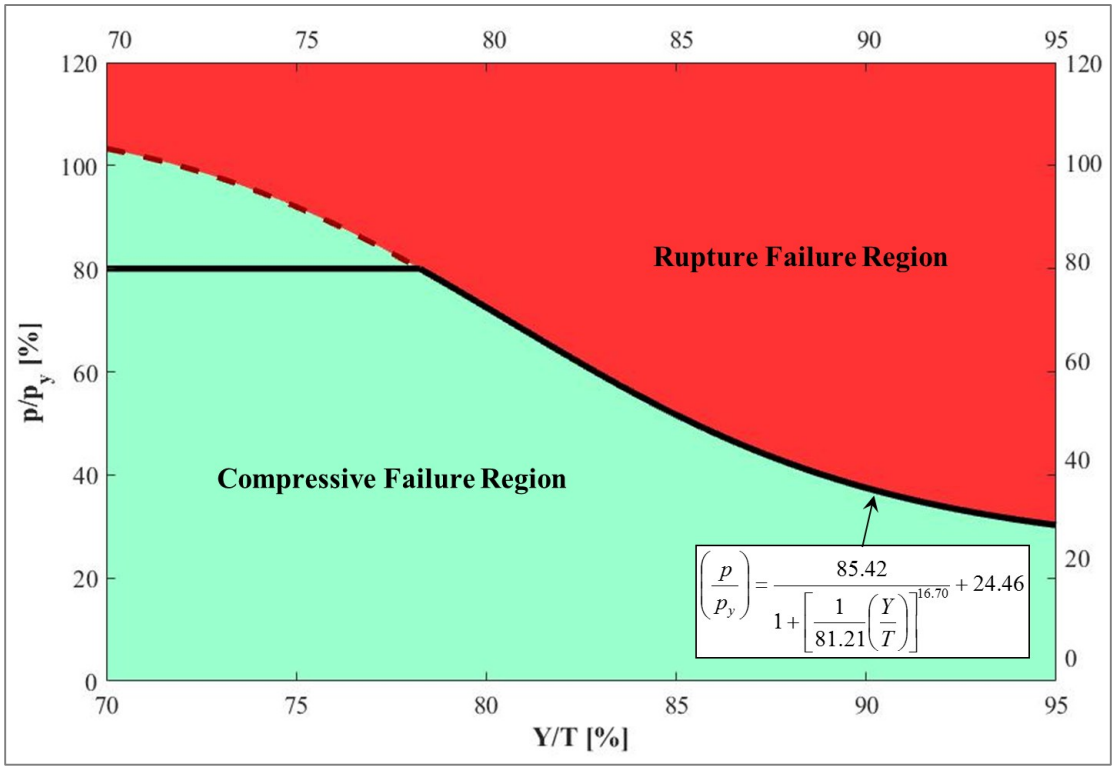

Figure 7-13: Rupture limit state for critical BC

7.5 3rd Phase of the Parametric Study: Effect of BC and Tension

It was discussed in Section 6.5, that the critical rupture BC develops an increasing axial tensile load in the deflected segment of the pipelines while experiencing an increasing curvature. Hence, the rupture limit that was obtained for the critical rupture BC can deal with the rupture of the pipe specimens with buckling BC subjected to a level of axial tensile stress as it was shown in the 2nd phase of the parametric study. Although the critical rupture BC creates an axial tensile force in the line, it only serves as the

minimum design requirement. In this regards, the effect of axial tensile load on the post-buckling rupture of the wrinkled pipes is studied in this phase to accommodate the rupture limit for the pipelines that are subject to additional tensile loads. The buckling BC is used herein to understand the pure effect of axial tensile load on the design factor limit. The results in this section are used to investigate the average tensile load that is applied to the line by the critical rupture BC as the minimum axial load for which the wrinkled buried pipelines should be designed. Table 7-8 indicates the matrix of parametric study for this phase. The normalized axial tensile load parameter (ratio of tensile load to the yield force) is varied between 0 to 30%.

Table 7-8: Matrix of parameters: parametric study for buckling BC

<table>
<tr><th>D/t
-</th><th>p/p_y
[%]</th><th>Y/T
[%]</th><th>T_A/T_{Ay}
[%]</th></tr>
<tr><td rowspan="2">50</td><td rowspan="6">≤100</td><td>72</td><td rowspan="2">0</td></tr>
<tr><td>77</td></tr>
<tr><td rowspan="2">70</td><td>80</td><td rowspan="2">10</td></tr>
<tr><td rowspan="2">87 (Test)</td></tr>
<tr><td rowspan="2">90</td><td rowspan="2">20</td></tr>
<tr><td>93</td><td>30</td></tr>
</table>

Similar to the previous phases, an increasing monotonic curvature is imposed to the pipe for each set of parameters until the post-buckling rupture is reached or an excessive distortion of the wall on the compressive side with no rupture on the tension side appears as the final compressive failure. Figure 7-14 to Figure 7-16 demonstrate the final results for critical design factor versus Y/T ratio for D/t ratio equal to 90 to 50 respectively. Each chart includes the critical design factor obtained for the range of normalized axial tension. Comparing these charts reveal that the higher the D/t ratio slightly increases the critical design factor. It is also obvious that the critical design factor is markedly reduced by the increase of axial tensile stress. The obtained results

suggest that no rupture is likely to occur for the wrinkled pipes without any axial tension. And, the post-buckling rupture can only be triggered for extremely large Y/T ratios (e.g. Y/T=93%) for the case of 10% normalized tensile load. The reason is that for the slight axial loads, the exceedingly high internal pressure is required to provoke the rupture failure where the accordion type buckling tend to form due to the inelastic buckling on the compressive side of the cross-section (successive buckles in members AH and DH in Figure 7-1b). Figure 7-17 shows the accordion type buckling as the ultimate failure mode for the D50Y93p95T00 pipe obtained from the FE simulation. From the results obtained for the 20% and 30% normalized axial load, it can be seen that the critical design factor is changing in a sigmoidal manner versus the change of Y/T ratio. Table 7-9 reports the constants of the logistic functions shown in Figure 7-14 to Figure 7-16 that are fitted to the data for 20% and 30% normalized axial load wherever enough data exist.

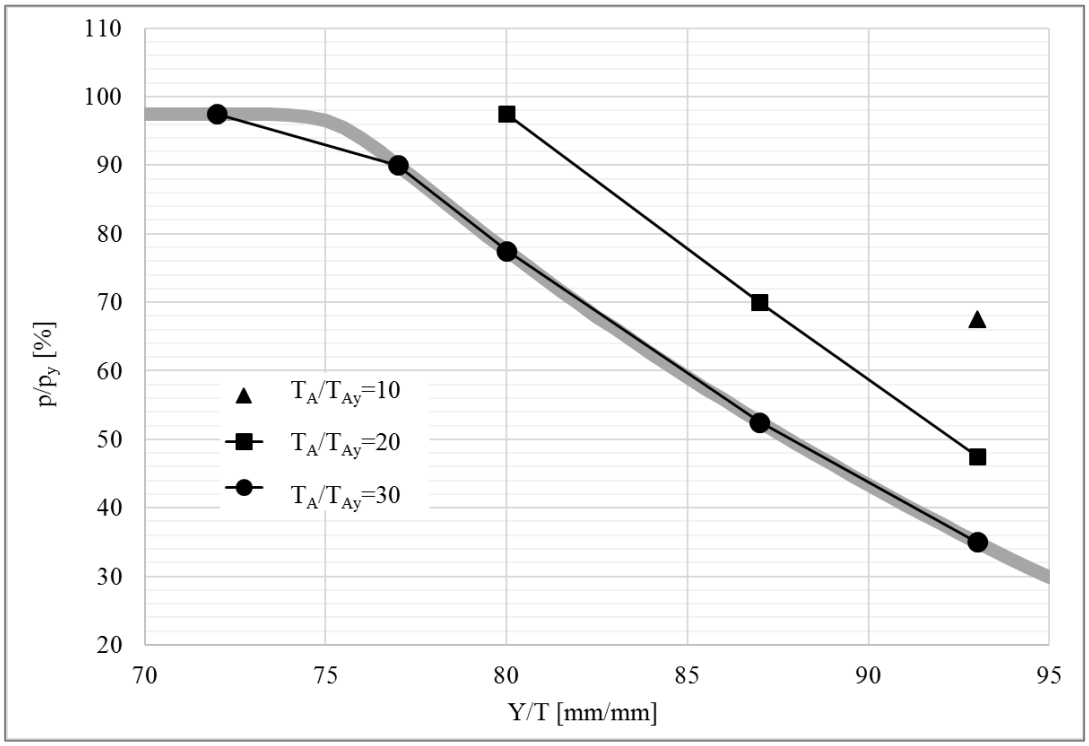

Figure 7-14: Critical p/p_y vs Y/T for different T_A/T_{Ay} ratios in case of D/t=90

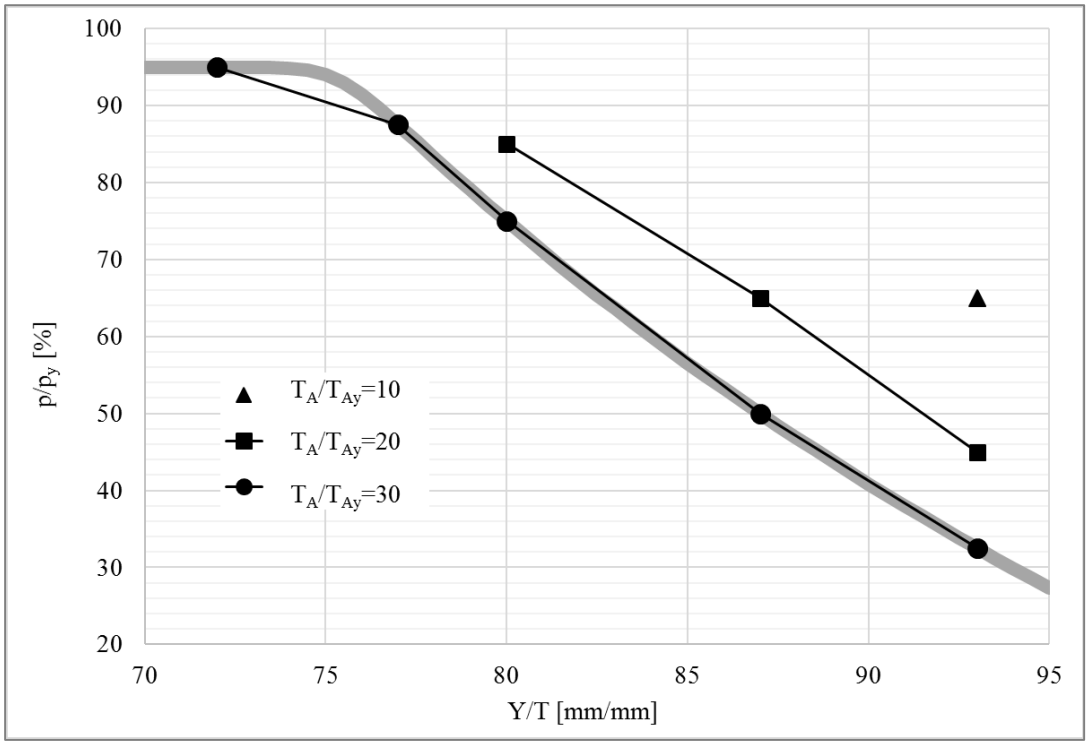

Figure 7-15: Critical p/p_y vs Y/T for different T_A/T_{Ay} ratios in case of D/t=70

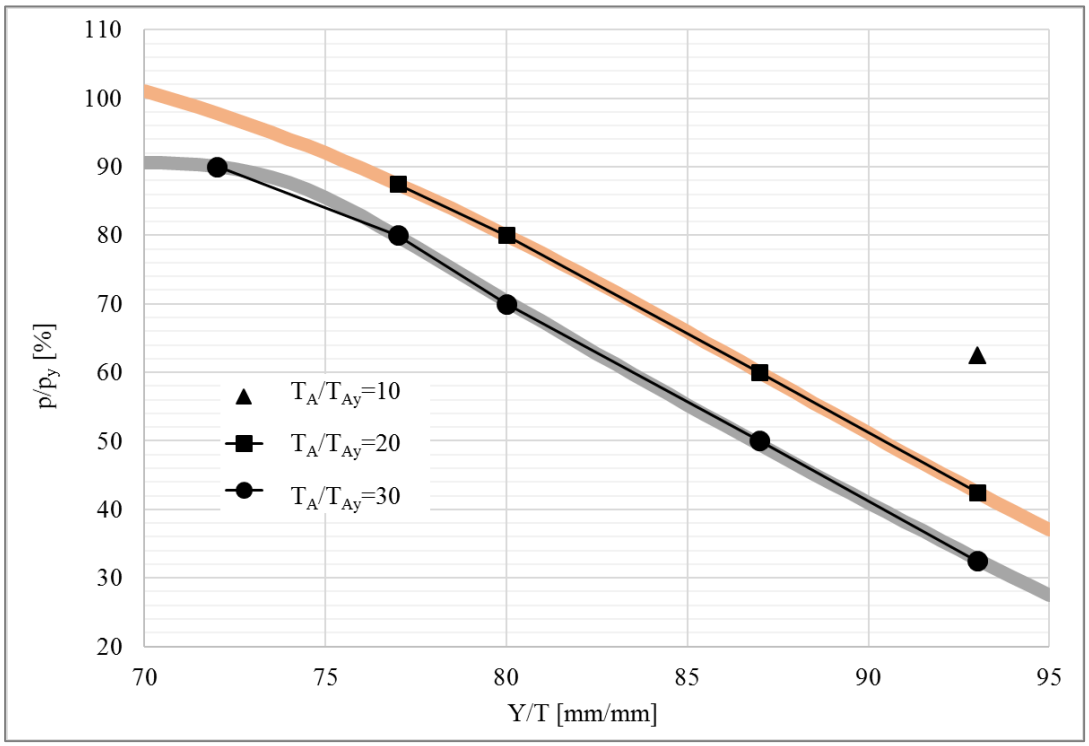

Figure 7-16: Critical p/p_y vs Y/T for different T_A/T_{Ay} ratios in case of D/t=50

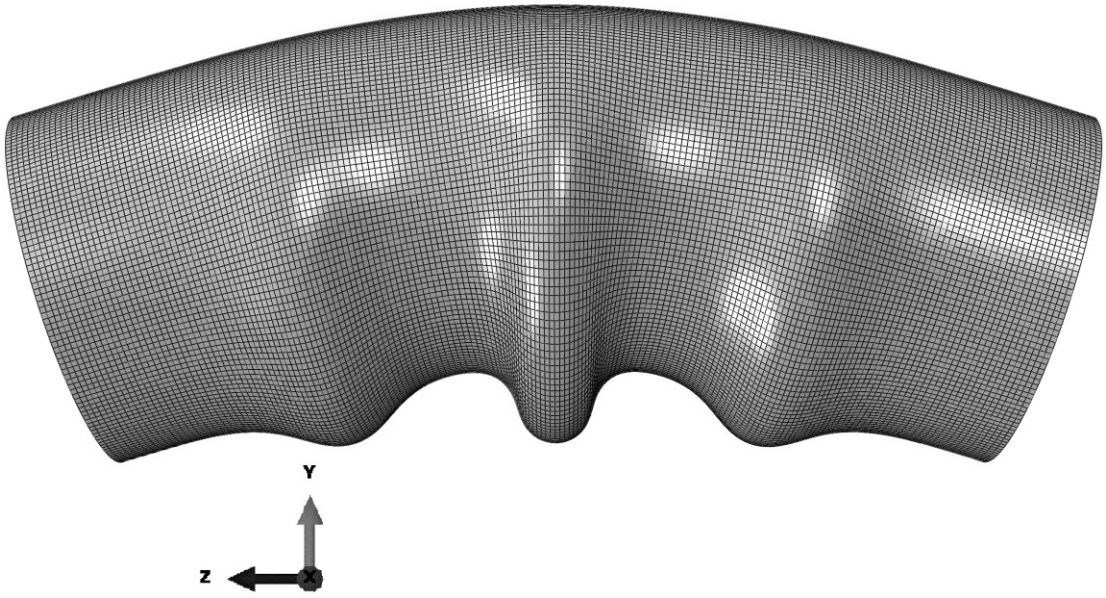

Figure 7-17: Accordion buckle for the D50Y93p95T00 set

Table 7-9: Constant of logistic functions calibrated for critical p/p_y (Buckling BC)

D/t	T_A/T_{Ay}	k_1	k_2	k_3	k_4	k_5
90	**30**	97.50	-111.89	75.379	140.19	0.01204
70	**30**	95.00	-114.39	75.379	140.19	0.01204
50	**20**	116.07	-14.27	90.07	8.102	1.0
50	**30**	90.76	-87109.33	73.77	65.619	4.378E-05

Figure 7-18 demonstrates the final results for different T_A/T_{Ay} levels rearranged with respect to the D/t ratio. It is shown that the critical design factor is decreasing by the increase of the Y/T ratio until the effect of D/t ratio becomes so marginal for high Y/T ratios. In any case, the results for the D/t=50 provides the overall envelope for the critical design factor.

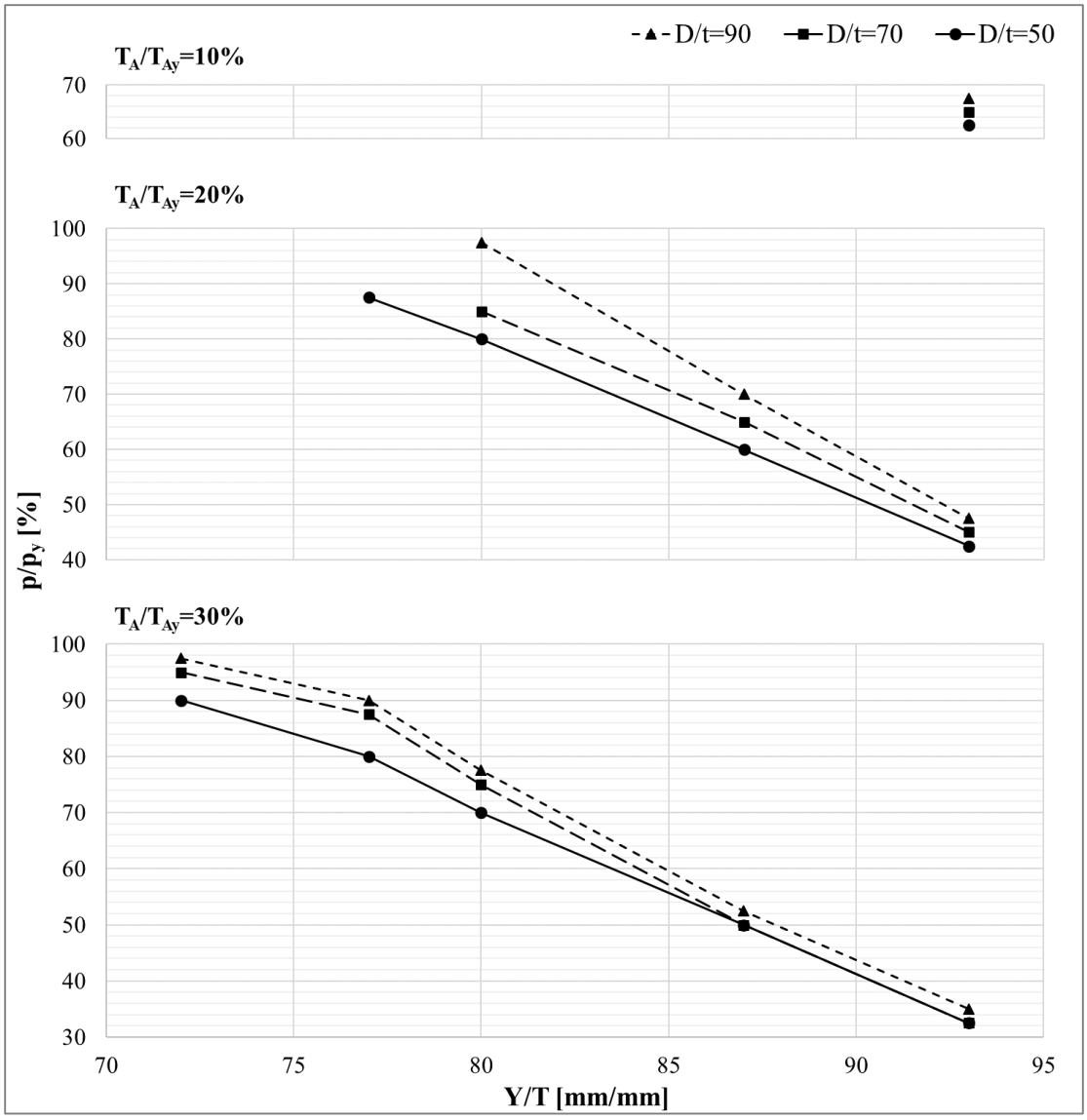

Figure 7-18: Critical p/p_y diagrams for different D/t and T_A/T_{Ay} ratios

From the discussions, it can be understood that the Y/T and T_A/T_{Ay} ratios are the two major key factors to the design factor limit. Therefore, the critical design factor can be expressed as a three-dimensional function of the Y/T and T_A/T_{Ay} ratios. Herein, the quadratic surface equation is used to fit a surface to the obtained results as follows

$$\left(\frac{p}{p_y}\right) = P_1 + P_2\left(\frac{Y}{T}\right) + P_3\left(\frac{T_A}{T_{Ay}}\right) + P_4\left(\frac{Y}{T}\right)^2 + P_5\left(\frac{Y}{T}\right)\left(\frac{T_A}{T_{Ay}}\right) + P_6\left(\frac{T_A}{T_{Ay}}\right)^2 \quad (7\text{-}5)$$

where the $P_{1\sim6}$ are the constants of the quadratic equation. Table 7-10 summarizes the constants of the quadratic equations that are fitted to the data for different D/t ratios through solving an optimization problem. Figure 7-19 shows the proposed rupture limit state as the envelope of critical design factor on the (Y/T, T_A/T_{Ay}) plane that was obtained based on D/t=50.

Table 7-10: Constants of fitted quadratic surfaces

D/t	**P_1**	**P_2**	**P_3**	**P_4**	**P_5**	**P_6**
90	292.40	0.80	-6.64	-0.032920	0.050480	0.010630
70	-5.00	4.62	2.15	-0.041200	-0.030600	-0.018000
50	64.38	2.98	0.53	-0.031780	-0.016600	-0.005303

7.6 Minimum Design Tensile Load

In this section, the results for the critical BC obtained in the 2nd phase of the parametric study is compared to the results for buckling BC to estimate the minimum axial tensile force for which the wrinkled buried pipelines should be designed. Figure 7-20 compares the rupture limit that was obtained for the critical BC to the critical design factor envelops for buckling BC associated with the 20% and 30% normalized axial tension. It can be said that the curve for the critical BC is roughly fluctuating between the curves for the buckling BC with 20% and 30% normalized load. That is, depending on the Y/T ratio of the steel material, the critical rupture BC approximately develops 20~30% normalized tension in the wrinkled pipelines under increasing curvature. The linear interpolation approach is used to obtain the average tension that is developed by the critical BC as a function of the Y/T ratio. Figure 7-21 depicts the average normalized tension associated with the critical BC as the minimum design requirement for sage operation of the wrinkled buried pipes. For instance, it is assumed that a buried steel

pipeline is made of a material with Y/T=90% and is primarily subjected to the 10% normalized compression. If this pipe buckles, the minimum normalized tension of 33.4% is developed in this pipe due to the effect of critical BC. Hence, by substituting the Y/T=90 and T_A/T_{Ay}=23.4 into the Eq. (7-3), the internal pressure in this pipe should be reduced to less than 49.6% of the yield pressure to assure the safe operation of the pipe and avoid the catastrophic rupture due to the increasing curvature.

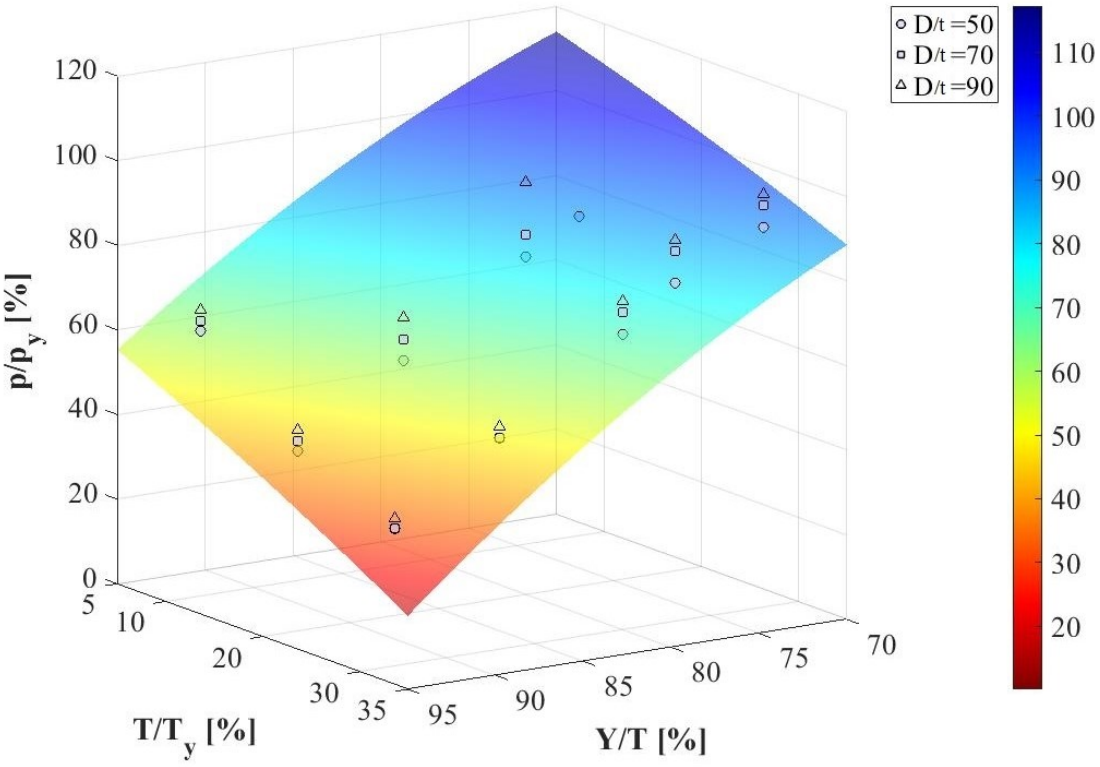

Figure 7-19: Rupture limit state for buckling BC
[critical design factor envelope on the (Y/T, T_A/T_{Ay}) plane for D/t=50]

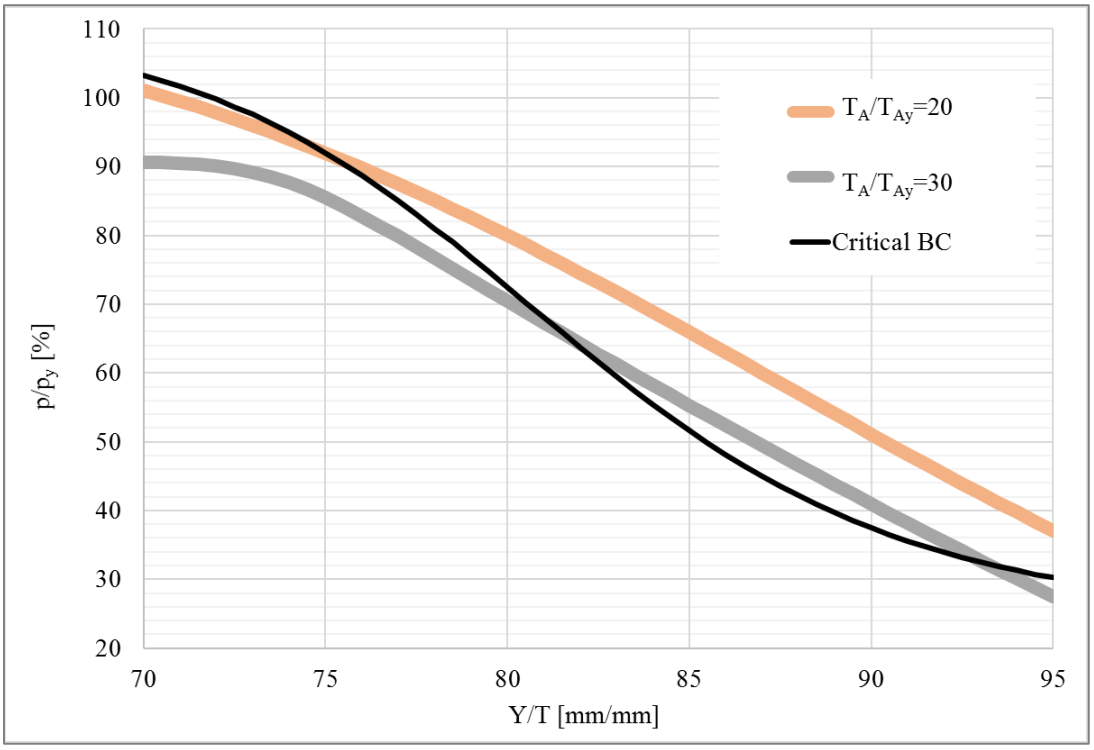

Figure 7-20: Comparison of the rupture limit for critical BC and Buckling BC

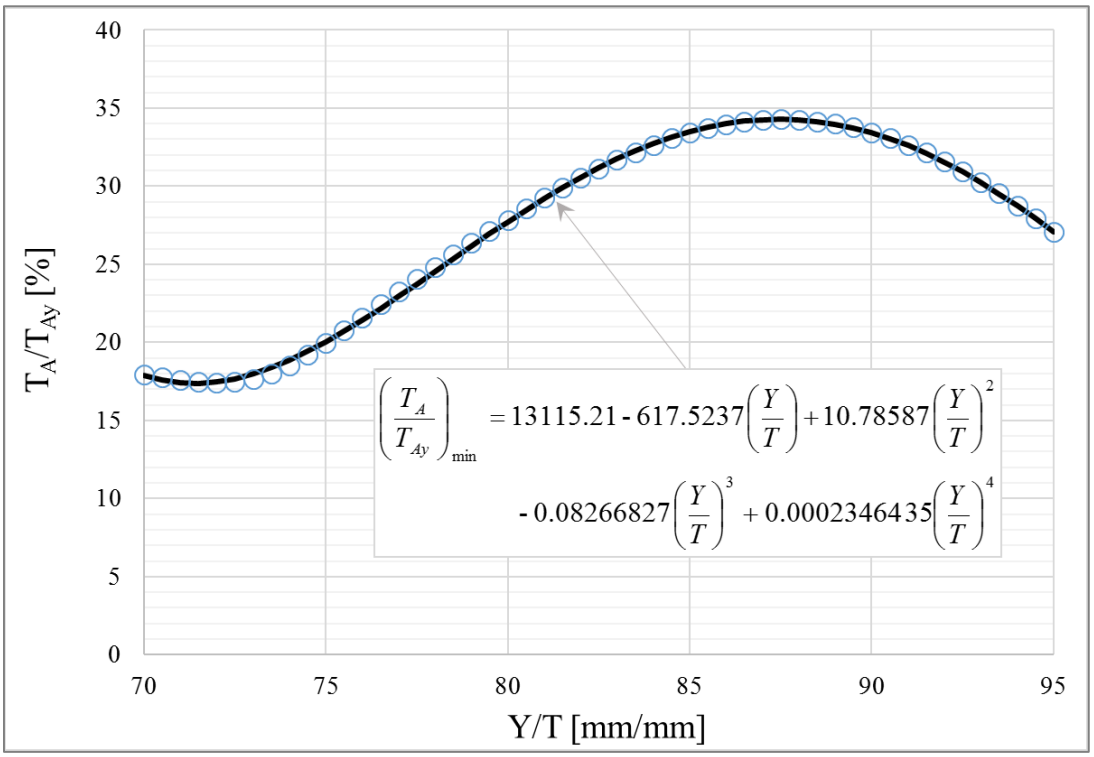

Figure 7-21: Minimum design tensile load

7.7 Summary

Coupled effect of design variables on post-buckling rupture of wrinkled buried pipelines was studied through a step-by-step parametric study. First, it was shown that the D parameter alone has no effect on the ultimate failure mode, whereas, the D/t ratio has a marginal impact on the occurrence of rupture. Then, the coupled effect of internal pressure, Y/T ratio, and D/t ratio was studied for the wrinkled pipelines that are subject to the critical pinned-pinned BC. The envelope of the results (with respect to D/t ratio) was used to introduce the critical design factor (normalized internal pressure) as a sigmoid function of the Y/T ratio. The critical design factor is the transition between the compressive failure and rupture failure. That is, in the wrinkled pipelines subjected to the internal pressure values that transcend the critical design factor, the post-buckling rupture is triggered due to an increased curvature.

Next, the coupled effect of internal pressure, Y/T ratio, axial tensile load, and D/t ratio was investigated for the bent pipelines with simply-supported BC to account for the effect of primary tension load. In this case, it was shown that the decrease of the D/t ratio slightly reduces the critical design factor. And, the critical design factor was obtained as a three-dimensional function of the Y/T ratio and normalized tension. Finally, the minimum design tension load which is equivalent to the effect of critical pinned BC was obtained by drawing a comparison between the critical design factor envelopes for different BC.

CHAPTER 8: SUMMARY, CONCLUSIONS, AND RECOMMENDATIONS

8.1 Summary

Steel pipelines commonly possess a high degree of ductility that enables them to carry a large amount of post-buckling deformations while retaining their operational safety and structural integrity. To benefit from this outstanding feature, the post-buckling behavior of the steel pipes should be full well understood to preserve the buckled pipelines in a safe operation mode and avoid any premature ultimate failure.

Rupture is one of the major failure limits to the integrity of the pipelines that endangers our environment as well as the public safety and property. It has been shown that the underground wrinkled pipelines are unlikely to rupture at the wrinkling location under monotonic loading conditions (Das 2003) unless they are subject to a very unique and changing BC accompanied by extremely large plastic deformations toward tearing the wrinkled wall (Ahmed 2011).

The current research work tackled the rupture of the wrinkled buried pipelines on the tension side of the wrinkled portion due to a monotonically-increasing curvature (Sen 2006; Tajika et al. 2011; Igi et al. 2011; Tajika and Suzuki 2009; Mitsuya et al. 2008; Mitsuya and Motohashi 2013; Mitsuya and Sakanoue 2015). The main focus was given to the understanding of the post-buckling behavior and ultimate failure modes of the wrinkled pipes and the derivation of design guidelines to safeguard the wrinkled pipes from fracture caused by bending tensile strains.

First, a series of small-scale experiments consisted of the dogbone coupons, notched round bars, and grooved plates were carried out on X65 steel grade to study the plasticity and ductile fracture of steel pipelines. Then, the test results were used through a hybrid experimental-numerical approach to calibrate a right material model that not only simulates the real post-necking behavior of the material, but also, acceptably predicts the ductile fracture initiation in steel pipelines.

Next, the FEA of a number of pertinent full-scale tests on steel pipes was performed to validate the material model and the FE simulation techniques. After that, the FE models

were used to study the critical BC and the crucial design variables that are responsible for the rupture of wrinkled pipelines undergoing monotonic curvature.

Finally, a comprehensive parametric study was conducted to discover the coupled impact of different key parameters on the post-buckling rupture of the pipe wall, and, corresponding design guidelines were derived and proposed as the rupture limit state for in-service wrinkled buried pipelines.

8.2 Conclusions

The following conclusions can be drawn in accordance with the experimental, analytical and numerical results acquired by the current research work

1- The experimental results obtained from small-scale fracture tests on X65 steel grade showed that the fracture strain is highly dependent on the stress triaxiality and Lode angle (i.e. the deviatoric stress invariants).

2- Parallel FE simulation of the material tests revealed that the post-necking stress-strain relation of the material can be successfully modeled by fitting the power law to the post-yield experimental stress-strain data through solving an optimization problem.

3- A hybrid experimental-numerical approach was used to calibrate the M-C fracture criterion based on the results of RB and GP tests where the ductile fracture toughness of the X65 steel was obtained in the form of the equivalent plastic strain to fracture as a function of stress triaxiality and Lode angle.

4- The fracture strain of the X65, X70 and X100 steel grades were averaged and a general fracture strain was proposed for the steel pipelines based on the *Xue*'s model.

5- FE simulation techniques and the proposed plasticity calibration were successfully engaged in modeling the physical response of four different full-scale tests. It was shown that the equivalent fracture strain can accurately predict the rupture in the pipe wall through the cumulative fracture criterion.

6- Internal pressure, Y/T ratio, and tensile axial load were identified as the three key variables that are jointly governing the ultimate post-buckling failure mode of buried pipelines.

7- It was postulated by FEA that the burst of wrinkling on the compressive side of the cross-section is extremely unlikely to occur under increased monotonic curvature. And, the ultimate failure mode can be either excessive compressive deformations, or the rupture of the tensile wall on the opposite side of the wrinkled location depending on the values of the three key parameters.

8- It was assumed from a phenomenological model of a buried pipeline that the pinned condition can be developed at the boundaries of the bent segment of the line, by which, the axial displacement is restrained and an increasing tension load is introduced. The analysis of the post-buckling rupture revealed that the pinned-pinned BC restores the load-carrying capacity of the buckled pipe and is the most critical BC leading to the rupture of the wall. Therefore, this critical BC serves as the minimum design requirement that needs to be considered for the safe analysis of in-service wrinkled buried pipelines.

9- The parametric studies indicated that the geometric design factors (i.e. D and D/t ratio) have negligible effect on the final failure mode of the wrinkled buried pipelines.

10- The critical design factor envelope was proposed for the pinned-pinned BC as the following sigmoidal function of Y/T ratio for retaining the wrinkled buried pipelines in a safe operating mode

$$\left(\frac{p}{p_y}\right)_{Cr} = \frac{85.42}{1+\left[\frac{1}{81.21}\left(\frac{Y}{T}\right)\right]^{16.70}} + 24.46 \qquad (8\text{-}1)$$

11- The effect of primary tension load on the critical design factor was studied using the simply-supported BC. The design factor envelope was proposed by using a quadratic surface as

$$\left(\frac{p}{p_y}\right)_{Cr} = 64.38 + 2.98\left(\frac{Y}{T}\right) + 0.53\left(\frac{T_A}{T_{Ay}}\right) - 0.03178\left(\frac{Y}{T}\right)^2 - 0.0166\left(\frac{Y}{T}\right)\left(\frac{T_A}{T_{Ay}}\right) - 0.0053\left(\frac{T_A}{T_{Ay}}\right)^2 \quad (8\text{-}2)$$

12- By comparing the critical design factor envelopes for different BC, the minimum design tensile load was obtained in association with the critical BC. That is, the design tension load is equivalent to the increasing tension which is developed by pinned-pinned condition and should be added to the primary axial load carried by the wrinkled pipelines.

8.3 Recommendations for Future Research

This research was designed in relation to a series of other works that aimed at the rupture of wrinkled pipes. The post-buckling rupture of the wrinkled buried pipelines was fully addressed in the current research. The findings of this research highlighted a number of new research topics for the future studies in order to better understanding of the behavior and final failure modes of the wrinkled pipelines that are itemized in the following

1- A comprehensive full-scale experimental program on the post-buckling rupture of the pressurized pipes under pinned-pinned BC and increasing monotonic curvature is recommended for future works to accurately verify the results obtained in the current research.
2- A risk analysis of the post-buckling rupture failure is recommended as a determining factor for retaining the wrinkled pipelines in service.
3- It was understood from the FEA results that the *Y*/*T* ratio can affect the CBS in the case of inelastic buckling which has not been addressed in the codes. Therefore, research on the effect of *Y*/*T* ratio on the CBS is proposed as a future research.

4- Since the outcome of this research is associated with the plain pipes, the study of the post-buckling rupture of the girth-welded pipelines with weld defects and wrinkling formed at the girth weld location is suggested as later research topic.

5- It has been postulated that once the wrinkling forms in the plain segment of a pipeline, the rupture is unlikely to be initiated from the defects of the girth weld even if the crack size in the welded zone is relatively large (Igi et al. 2011; Igi and Suzuki 2007). A thorough investigation of this subject and comparison with the limits obtained by this research is proposed for the future studies to assure the serviceability of the wrinkled pipelines.

6- As the wrinkle formation and fracture are most likely to happen in the location of cold bends, the post-buckling rupture of cold bend pipes with residual strains caused by different bent angles and under the opening and closing modes is put forward to be addressed by the future efforts.

7- It was shown that the higher the internal pressure increases the chance of post-buckling rupture of the tensile wall. On the other hand, the tearing failure of the wrinkling in the compressive wall has been shown to be more likely in the case of low internal pressure (Ahmed 2011). As such, seeking a unified design guideline that accounts for both of these post-buckling rupture modes is recommended as a future research.

8- Research on the effect of material grade, anisotropy introduced by UOE process, and internal pressure fluctuations on the rupture of pipe wall is suggested as future research topics.

REFERENCES

Ahmed, A. U., Aydin, M., Cheng, J. R., and Zhou, J. (2011). "Fracture of Wrinkled Pipes Subjected to Monotonic Deformation: An Experimental Investigation." *Journal of Pressure Vessel Technology,* 133(1), 1-9.

Ahmed, A. U., Das, S., and Cheng, J. R. (2010a). "Numerical Investigation of Tearing Fracture of Wrinkled Pipe." *Journal of Offshore Mechanics and Arctic Engineering,* 132(1), 1-10.

Ahmed, A. U., Cheng, J. R., and Zhou, J. (2010b). "Development of Failure Criteria for Predicting Tearing of Wrinkled Pipe." *8th International Pipeline Conference,* American Society of Mechanical Engineers, Calgary, Canada, 9-17.

Ahmed, A. U. (2011). "Failure criteria for tearing of telescoping wrinkles". PhD. University of Alberta, Edmonton, Canada.

American Petroleum Institute. (2012). "Specification for Line Pipe". *API Specification 5L,* Forty-fifth Edition.

American Society for Testing and Materials. (2014). "Standard test methods and definitions for mechanical testing of steel products". *ASTM A370.*

Bai, Y. (2007). "Effect of Loading History on Necking and Fracture". PhD. Massachusetts Institute of Technology, Cambridge, USA.

Bai, Y., Teng, X., and Wierzbicki, T. (2009). "On the application of stress triaxiality formula for plane strain fracture testing." *Journal of Engineering Materials and Technology,* 131(2).

Bai, Y., and Wierzbicki, T. (2010). "Application of extended Mohr–Coulomb criterion to ductile fracture." *Int.J.Fract.,* 161(1), 1-20.

Bai, Y., and Wierzbicki, T. (2008). "A new model of metal plasticity and fracture with pressure and Lode dependence." *Int.J.Plast.,* 24(6), 1071-1096.

Bao, Y. (2003). "Prediction of ductile track formation in uncracked bodies". PhD. Massachusetts Institute of Technology, Cambridge, USA.

Bao, Y., and Wierzbicki, T. (2004a). "A comparative study on various ductile crack formation criteria." *Journal of Engineering Materials and Technology,* 126(3), 314-324.

Bao, Y., and Wierzbicki, T. (2004b). "On fracture locus in the equivalent strain and stress triaxiality space." *Int.J.Mech.Sci.,* 46(1), 81-98.

Bridgman, P. W. (1952). "Studies in large plastic flow and fracture". McGraw-Hill, New York.

Canadian Standards Association. (2015). "Oil and gas pipeline systems". *CSA Z662,* Seventh Edition.

Canadian Standards Association. (2011). "Oil and gas pipeline systems". *CSA Z662,* Sixth Edition.

Canadian Standards Association. (2014). "Steel Pipe". *CSA Z245.1,* Ninth Edition.

Cheng, R., Sen, M., Behbahanifard, M., and Murray, D. W. (2004). "Local buckling behavior and design of cold bend pipes." *Rep. No. 2004-1,* University of Alberta, Edmonton, Canada.

Chiou, Y., and Murray, D. (1993). "Towards rational deformation limit states for buried pipelines." *The Third International Offshore and Polar Engineering Conference,* ISOPE, Singapore, 18-24.

Das, S., Cheng, J. J. R., and Murray, D. W. (2007a). "Prediction of the fracture life of a wrinkled steel pipe subject to low cycle fatigue load." *Canadian Journal of Civil Engineering,* 34(9), 1131-1139.

Das, S., Cheng, J. R., and Murray, D. W. (2007b). "Behavior of wrinkled steel pipelines subjected to cyclic axial loadings." *Canadian Journal of Civil Engineering,* 34(5), 598-607.

Das, S., Cheng, J. R., and Murray, D. W. (2002). "Fracture in wrinkled linepipe under monotonic loading." *2002 4th International Pipeline Conference,* ASME, Calgary, Canada, 1613-1618.

Das, S., Cheng, J., and Murray, D. W. (2007c). "Prediction of fracture in wrinkled energy pipelines subjected to cyclic deformations." *Int.J.Offshore Polar Eng.,* 17(03), 205-212.

Das, S. (2003). "Fracture of wrinkled energy pipelines". PhD. University of Alberta, Edmonton, Canada.

Dassault Systèmes Simulia Corporation. (2013). "Abaqus Analysis User's Guide." *Version 6.13-4*, Providence, RI, USA.

Del Col, P. R. (1998). "Behaviour of Large Diameter Line Pipe Under Combined Loads". MSc. University of Alberta, Edmonton, Canada.

Dorey, A. B., Murray, D. W., and Cheng, J. (2006a). "Critical buckling strain equations for energy pipelines—A Parametric Study." *Journal of Offshore Mechanics and Arctic Engineering,* 128(3), 248-255.

Dorey, A. B., Murray, D. W., and Cheng, J. (2006b). "Initial imperfection models for segments of line pipe." *Journal of Offshore Mechanics and Arctic Engineering,* 128(4), 322-329.

Dorey, A. B. (2001). "Critical buckling strains in energy pipelines". PhD. University of Alberta, Edmonton, Canada.

EVRAZ Inc. (2015). "Chemical and Mechanical Test Report: Stock Certification for Pipe No.11, Heat No. M15879." Camrose, Canada.

Faleskog, J., Gao, X., and Shih, C. F. (1998). "Cell model for nonlinear fracture analysis–I. Micromechanics calibration." *Int.J.Fract.,* 89(4), 355-373.

Fathi, A. (2012). "Effects of material anisotropy on the buckling resistance of high strength steel pipelines". PhD. University of Alberta, Edmonton, Canada.

Gao, X., Faleskog, J., and Shih, C. F. (1998). "Cell model for nonlinear fracture analysis–II. Fracture-process calibration and verification." *Int.J.Fract.,* 89(4), 375-398.

Gao, X., and Kim, J. (2006). "Modeling of ductile fracture: significance of void coalescence." *Int.J.Solids Structures,* 43(20), 6277-6293.

Gioielli, P. C., Minnaar, K., Macia, M. L., and Kan, W. C. (2007). "Large-scale testing methodology to measure the influence of pressure on tensile strain capacity of a pipeline." *The Seventeenth International Offshore and Polar Engineering Conference,* ISOPE, Lisbon, Portugal.

Gurson, A. L. (1977a). "Continuum theory of ductile rupture by void nucleation and growth: Part I—Yield criteria and flow rules for porous ductile media." *Journal of Engineering Materials and Technology,* 99(1), 2-15.

Gurson, A. L. (1977b). "Porous rigid-plastic materials containing rigid inclusions; yield function, plastic potential and void nucleation." *Proceedings of the Fourth International Conference on Fracture,* 357-364.

Gurson, A. L. (1975). "Plastic Flow and Fracture Behavior of Ductile Materials Incorporating Void Nucleation, Growth and Interaction". PhD. Brown University, Providence, USA.

Igi, S., and Sakimoto, T. (2010). "Tensile Strain Capacity of X80 Linepipe in Full Scale Test." *The Twentieth International Offshore and Polar Engineering Conference,* ISOPE, Beijing, China.

Igi, S., Sakimoto, T., Suzuki, N., Muraoka, R., and Arakawa, T. (2010). "Tensile strain capacity of X80 pipeline under tensile loading with internal pressure." *2010 8th International Pipeline Conference,* ASME, Calgary, Canada.

Igi, S., Sakimoto, T., Tajika, H., Endo, S., Muraoka, R., and Suzuki, N. (2011). "Strain Capacity of 48" OD X80 Pipeline in Pressurized Full-scale Bending Test." *The Twenty-first International Offshore and Polar Engineering Conference*, ISOPE, Hawaii, USA.

Igi, S., and Suzuki, N. (2007). "Tensile strain limits of X80 high-strain pipelines." *The Seventeenth International Offshore and Polar Engineering Conference,* ISOPE, Lisbon, Portugal.

Japan Gas Association. (2001). "Guideline for Design of High Pressure Gas Pipeline against Soil Liquefaction in Earthquake (in Japanese)".

Johnson, G. R. (1980). "Materials Characterization for computations involving severe dynamic loading." *Proc. Army Symp. Of Solid Mechanics,* DTIC Document, 62-67.

Johnson, G. R., and Cook, W. H. (1985). "Fracture characteristics of three metals subjected to various strains, strain rates, temperatures and pressures." *Eng.Fract.Mech.,* 21(1), 31-48.

Khoo, H. A. (2000). "Ductile fracture of steel". PhD. University of Alberta, Edmonton, Canada.

Kiran, R., and Khandelwal, K. (2014). "Gurson model parameters for ductile fracture simulation in ASTM A992 steels." *Fatigue & Fracture of Engineering Materials & Structures,* 37(2), 171-183.

Kofiani, K. N. (2013). "Ductile Fracture and Structural Integrity of Pipelines & Risers". PhD. Massachusetts Institute of Technology, Cambridge, USA.

Kofiani, K., Nonn, A., and Wierzbicki, T. (2013). "New calibration method for high and low triaxiality and validation on SENT specimens of API X70." *Int.J.Pressure Vessels Piping,* 111-112 187-201.

Kofiani, K., Wierzbicki, T., Nonn, A., Kalwa, C., and Walters, C. (2012). "Experiments and fracture modeling of high-strength pipelines for high and low stress triaxialities." *The Twenty-second International Offshore and Polar Engineering Conference,* ISOPE, Rhodes, Greece, 511-518.

Kossakowski, P. (2012). "Prediction of ductile fracture for S235JR steel using the Stress Modified Critical Strain and Gurson-Tvergaard-Needleman models." *J.Mater.Civ.Eng.,* 24(12), 1492-1500.

Lee, Y. (2005). "Fracture Prediction in Metal Sheets". PhD. Massachusetts Institute of Technology, Cambridge, USA.

Lemaitre, J. (1992). "A course on damage mechanics." Springer-Verlag Berlin Heidelberg.

Lemaitre, J. (1985). "A continuous damage mechanics model for ductile fracture." *Journal of Engineering Materials and Technology,* 107(1), 83-89.

Lemaitre, J. (1984). "How to use damage mechanics." *Nucl.Eng.Des.,* 80(2), 233-245.

McClintock, F. A. (1968). "A criterion for ductile fracture by the growth of holes." *Journal of Applied Mechanics,* 35(2), 363-371.

Mitsuya, M., and Motohashi, H. (2013). "Rupture of Induction Bend Pipe under Opening Mode Bending." *The Twenty-third International Offshore and Polar Engineering Conference,* ISOPE, Anchorage, USA, 512-519.

Mitsuya, M., Sakanoue, T., Yatabe, H., and Hashimoto, Y. (2008). "Deformation behavior and limit state of high-grade induction bend pipes subjected to large ground deformation." *The Eighteenth International Offshore and Polar Engineering Conference,* ISOPE, Vancouver, Canada, 166-173.

Mitsuya, M., and Sakanoue, T. (2015). "Rupture prediction for induction bends under opening mode bending with emphasis on strain localization." *Int.J.Pressure Vessels Piping,* 135-136 1-11.

Mohareb, M. E., Kulak, G., Elwi, A., and Murray, D. (2001). "Testing and analysis of steel pipe segments." *J.Transp.Eng.,* 127(5), 408-417.

Mohareb, M. E. (1995). "Deformational behaviour of line pipe". PhD. University of Alberta, Edmonton, Canada.

Nahshon, K., and Hutchinson, J. (2008). "Modification of the Gurson model for shear failure." *European Journal of Mechanics-A/Solids,* 27(1), 1-17.

Oh, C., Kim, Y., Baek, J., and Kim, W. (2007a). "Development of stress-modified fracture strain for ductile failure of API X65 steel." *Int.J.Fract.,* 143(2), 119-133.

Oh, C., Kim, Y., Baek, J., Kim, Y., and Kim, W. (2007b). "Ductile failure analysis of API X65 pipes with notch-type defects using a local fracture criterion." *Int.J.Pressure Vessels Piping,* 84(8), 512-525.

Rakin, M., Gubeljak, N., Dobrojević, M., and Sedmak, A. (2008). "Modelling of ductile fracture initiation in strength mismatched welded joint." *Eng.Fract.Mech.,* 75(11), 3499-3510.

Ramberg, W., and Osgood, W. R. (1943). "Description of stress-strain curves by three parameters." *Rep. No. 902,* National Advisory Committee for Aeronautics, Washington DC, USA.

Rice, J. R., and Tracey, D. M. (1969). "On the ductile enlargement of voids in triaxial stress fields∗." *J.Mech.Phys.Solids,* 17(3), 201-217.

Rogers, H. (1960). "The tensile fracture of ductile metals." *AIME Trans,* 218(3), 498-506.

Sadasue, T., Igi, S., Kubo, T., Ishikawa, N., Endo, S., Glover, A., Horsley, D., and Toyoda, M. (2004). "Ductile cracking evaluation of X80/X100 high strength linepipes." *2004 International Pipeline Conference,* ASME, Calgary, Canada, 1661-1669.

Sen, M., Cheng, J., Murray, D., and Zhou, J. (2008). "Mechanical properties of cold bend pipes." *Journal of Pressure Vessel Technology,* 130(2), 251-257.

Sen, M., Cheng, J., Murray, D., Zhou, J., Adams, K., Yoshizaki, K., Fukuda, N., Como, M., and Cerelli, E. (2004). "Full-Scale Tests of Cold Bend Pipes." *2004 International Pipeline Conference,* ASME, Calgary, Canada, 419-426.

Sen, M. (2006). "Behaviour of cold bend pipes under combined loads". PhD. University of Alberta, Edmonton, Canada.

Sen, M., and Cheng, R. (2010). "Finite element analysis of cold bend pipes under bending loads." *2010 8th International Pipeline Conference,* ASME, Calgary, Canada, 257-267.

Tajika, H., Igi, S., Sakimoto, T., Tsuyama, S., Muraoka, R., Arakawa, T., and Suzuki, N. (2011). "Full-Scale Bending Test of 48" X80 Linepipes." *The Twenty-first International Offshore and Polar Engineering Conference,* ISOPE, Hawaii, USA.

Tajika, H., and Suzuki, N. (2009). "Bending Capacity and Seismic Integrity of X65 ERW Line Pipe." *The Nineteenth International Offshore and Polar Engineering Conference,* ISOPE, Osaka, Japan, 527-533.

Talatahari, S., and Mohajer Rahbari, N. (2015). "Enriched Imperialist Competitive Algorithm for system identification of magneto-rheological dampers." *Mechanical Systems and Signal Processing,* 62-63 506-516.

Tvergaard, V. (1982a). "Ductile fracture by cavity nucleation between larger voids." *J.Mech.Phys.Solids,* 30(4), 265-286.

Tvergaard, V. (1982b). "On localization in ductile materials containing spherical voids." *Int.J.Fract.,* 18(4), 237-252.

Tvergaard, V. (1981). "Influence of voids on shear band instabilities under plane strain conditions." *Int.J.Fract.,* 17(4), 389-407.

Tvergaard, V., and Needleman, A. (1984). "Analysis of the cup-cone fracture in a round tensile bar." *Acta Metallurgica,* 32(1), 157-169.

Vazouras, P., Karamanos, S. A., and Dakoulas, P. (2010). "Finite element analysis of buried steel pipelines under strike-slip fault displacements." *Soil Dyn.Earthquake Eng.,* 30(11), 1361-1376.

Wang, Y., Cheng, W., and Horsley, D. (2004a). "Tensile strain limits of buried defects in pipeline girth welds." *2004 International Pipeline Conference,* ASME, Calgary, Canada, 1607-1614.

Wang, Y., Cheng, W., McLamb, M., Horsley, D., Zhou, J., and Glover, A. (2004b). "Tensile Strain Limits of Girth Welds with Surface-Breaking Defects Part I an Analytical Framework." *Pipeline Technology, Proceedings of the 4th International Conference on Pipeline Technology,* Ostend, Belgium, 9-13.

Wang, Y., Horsley, D., Cheng, W., Glover, A., McLamb, M., and Zhou, J. (2004c). "Tensile strain limits of girth welds with suface-breaking defects-Part II: Experimental correlationa and validation." *4th International Conference on Pipeline Technology, Ostend, Belgium,* Ostend, Belgium.

Wang, Y., Liu, M., Horsley, D., and Zhou, J. (2006). "A quantitative approach to tensile strain capacity of pipelines." *2006 International Pipeline Conference,* ASME, Calgary, Canada, 545-552.

Wang, Y., Rudland, D., Denys, R., and Horsley, D. (2002). "A preliminary strain-based design criterion for pipeline girth welds." *2002 4th International Pipeline Conference,* ASME, Calgary, Canada, 415-427.

Wierzbicki, T., Bao, Y., and Bai, Y. (2005a). "A new experimental technique for constructing a fracture envelope of metals under multi-axial loading." *Proceedings of the 2005 SEM annual conference and exposition on experimental and applied mechanics,* 1295-1303.

Wierzbicki, T., Bao, Y., Lee, Y., and Bai, Y. (2005b). "Calibration and evaluation of seven fracture models." *Int.J.Mech.Sci.,* 47(4), 719-743.

Wierzbicki, T., and Xue, L. (2005). "On the effect of the third invariant of the stress deviator on ductile fracture." Impact and Crashworthiness Laboratory, Massachusetts Institute of Technology, Cambridge, United States.

Wilkins, M., Streit, R., and Reaugh, J. (1980). "Cumulative-Strain-Damage Model of Ductile Fracture: Simulation and Prediction of Engineering Fracture Tests." *Rep. No.*

UCRL-53058, Lawrence Livermore National Lab., CA (USA); Science Applications, Inc., San Leandro, CA (USA), Livermore, USA.

Xue, L. (2007a). "Damage accumulation and fracture initiation in uncracked ductile solids subject to triaxial loading." *Int.J.Solids Structures,* 44(16), 5163-5181.

Xue, L. (2007b). "Ductile Fracture Modeling-Theory, Experimental Investigation and Numerical Verification". PhD. Massachusetts Institute of Technology, Cambridge, United States.

Xue, Z., Pontin, M., Zok, F., and Hutchinson, J. W. (2010). "Calibration procedures for a computational model of ductile fracture." *Eng.Fract.Mech.,* 77(3), 492-509.

Zhang, W., and Cai, Y. (2010). "Continuum damage mechanics and numerical applications." Springer Heidelberg Dordrecht London.

Zhou, Z., and Murray, D. (1995). "Analysis of postbuckling behavior of line pipe subjected to combined loads." *Int.J.Solids Structures,* 32(20), 3015-3036.

Appendix A: Porous Plasticity

Gurson (1975; 1977a; 1977b) derived an associated plastic flow rule for homogeneous and porous ductile solid media modeled as a void-matrix aggregate (Figure A-1a). By studying a spherical volume element of radius "r_m" with elastic-perfectly plastic material containing a concentric spherical void of radius "r_v" (Figure A-1b), that is large enough to be statically representative of properties of aggregate, a macroscopic yield function for the porous solid was proposed dependent on the hydrostatic stress and microscopic void volume fraction (f), which is the ratio of the volume of the void to that of the volume element (r_v^3 / r_m^3). *Gurson*'s yield function will shrink to the von Mises yield function when hydrostatic stress and void volume fraction are both zero. *Tvergaard* (1981; 1982a; 1982b) modified the *Gurson*'s yield function by introducing the constant factors of q_1, q_2, and q_3 to account for the effect of void interaction effects in the porous media.

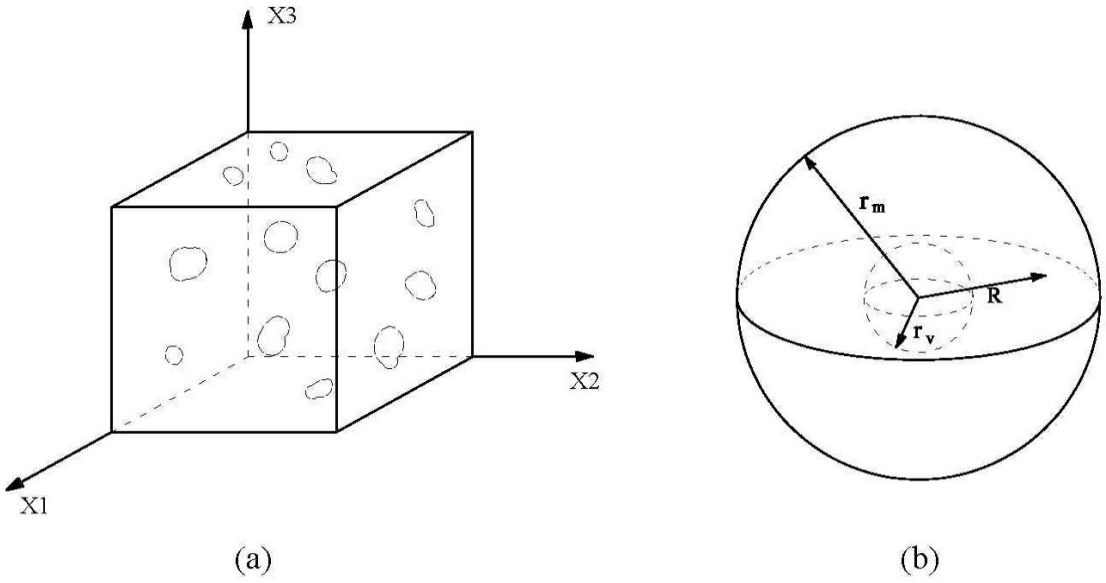

Figure A-1: *Gurson*'s material and void model
a) *porous media*; b) *Spherical void model*

According to the experimental observations, the stress-carrying capacity of a material at ductile fracture point vanishes due to the coalescence of voids and formation of a macroscopic crack. However, this phenomenon is unrealistically predicted by Gurson's equations at a very high level of the void volume fraction. Hence, *Tvergaard and Needleman* (1984) replaced the void volume fraction, f, with a modified function, $f^*(f)$, to limit the application of the *Gurson*'s model only for the void volume fraction values below a critical void volume fraction (f_c) and to amplify the void growth by an accelerated void growth factor (K) above the critical void volume until the fracture void volume (f_F) is reached. This critical void volume fraction is associated with a local failure resulting from necking of ligament between adjacent voids. Finally, *Gurson-Tvergaard-Needleman* (GTN) plasticity model is introduced as

$$\Phi = \left(\frac{\bar{\sigma}}{\sigma_{ym}}\right)^2 + 2q_1 f^* \cosh\left(\frac{3q_2}{2}\frac{\sigma_m}{\sigma_{ym}}\right) - \left(1 + q_3 f^{*2}\right) = 0 \qquad \text{(A-1)}$$

in which, $\bar{\sigma}$ and σ_m are equivalent stress and hydrostatic stress at the macroscopic level, and σ_{ym} denotes the equivalent plastic stress flow in the damage-free matrix of material at a microscopic level which could be taken equal to the material hardening stress as a function of equivalent plastic strain, $\sigma_{ym}\left(\bar{\varepsilon}^p\right)$. q_1, q_2, and q_3 are the void interaction parameters. The void volume fraction function, f^*, is defined as

$$f^* = \begin{cases} f & f_0 \le f \le f_c \\ f_c + K\left(f - f_c\right) & f_c \le f \le f_F \\ \bar{f}_F & f_F \le f \end{cases} \qquad \text{(A-2)}$$

where f_0 is the initial void volume which is the material characteristic, $K = \dfrac{\bar{f}_F - f_c}{f_F - f_c}$, and $\bar{f}_F = \dfrac{q_1 + \sqrt{q_1^2 - q_3}}{q_3}$.

The change in the void volume fraction is attributed to the growth of existing voids and the nucleation of new voids. Therefore,

$$df = df_{gr} + df_{nucl} \qquad \text{(A-3)}$$

where the crack growth rate could be formulated in terms of plastic volumetric strain (ε_{kk}^{p}) based on the mass conservation law and void nucleation rate is taken to be proportional to the rate of equivalent plastic strain as

$$\begin{cases} df_{gr} = (1-f)d\varepsilon_{kk}^{p} \\ df_{nucl} = \mathrm{A}_N d\bar{\varepsilon}^{p} \end{cases} \qquad \text{(A-4)}$$

Proportionality constant, A_N, in the latter equation, is defined based on Gaussian distribution as

$$\mathrm{A}_N = \frac{f_N}{s_N\sqrt{2\pi}} \exp\left[-0.5\left(\frac{\bar{\varepsilon}^{p} - \varepsilon_N}{s_N} \right)^2 \right] \qquad \text{(A-5)}$$

in which, f_N is volume fraction of nucleated voids and ε_N is the mean strain of void nucleation with standard deviation s_N. Study on the parameters of the GTN model shows that this model maps the von Mises yield function before nucleation strain (ε_N) is reached. The rate of strength dramatically decreases with an increase of f_N value and

void growth is accelerated as f_c is reached up to the point of complete loss of load-carrying capacity by reaching to f_F (Kiran and Khandelwal 2014).

The most demanding task in the application of the GTN model is to calibrate the model for a given material by finding the optimal solution for the model parameters. Nine parameters including q_1, q_2, q_3, f_0, f_N, ε_N, s_N, f_c and f_F in GTN model are required to be calibrated. In most cases, some reasonable fixed values are assigned to a number of parameters of the model and the others are obtained by different methodologies from experimental observations, parallel finite element analysis, and microstructural analysis. It was shown that using q_1=1.5 instead of unity considerably improved the *Gurson*'s yield function response in numerical studies of periodically distributed holes. Also, as the system loses stress-carrying capability after fracture void volume (f_F), the reasonable assumptions (Tvergaard and Needleman 1984) could also be made for some other parameters as

$$\left\{q_1 = 1.5,\ q_2 = 1,\ q_3 = q_1^2 = 1.25\right\} \quad \Rightarrow \quad \bar{f}_F \to \frac{1}{q_1}.$$

Kiran and Khandelwal (2014) categorized GTN model parameters for metals obtained from the literature into three categories; I) Damage only occurs due to growth of pre-existing voids inside the material and new voids do not nucleate during the loading of material (f_0>0, ε_N=0, f_N=0); II) No voids exist in the material before loading and damage occurs because of new void nucleation and growth (f_0=0, ε_N & f_N >0); III) Damage is caused by growth of pre-existing voids and nucleation and growth of new voids (f_0, ε_N & f_N >0). For the second scenario, they postulated that the non-uniqueness of the optimal parameters, that is, an exponential correlation exists between volume fraction and strain of the void nucleation point as

$$f_N = C_1 \exp\left(C_2 \varepsilon_N\right) \qquad \text{(A-6)}$$

where C_1 and C_2 are constant. The GTN model was calibrated for structural steel ASTM A992 using experimental data from the uniaxial tensile tests of round bars with

different notch radii to attest the validity of the model for different triaxial stress values. The calibrated GTN model for ASTM A992 was shown to be capable of predicting the ductile fracture of plates with holes inside and plates with reduced section (Kiran and Khandelwal 2014). *Kossakowski* (2012) conducted tensile strength tests in parallel to numerical analysis to calibrate the GTN model for S235JR Steel. *Rakin et al.* (2008) calibrated the GTN model for high-strength low-alloyed (HSLA) steel. *Xue et al.* (2010) performed tensile round bar test, mode I and mode II fracture tests to calibrate the GTN model for DH36 steel. Under shear stress condition, voids do not change in volume but only deform. *Nahshon and Hutchinson* (2008) incorporated J_{3D} deviatoric stress invariant and modified the *Gurson*'s model by introducing a new change of void volume fraction for damage at very low-stress triaxialities which are associated with shear fracture.